Instituut voor
Kern- en Stralingsfysica
Departement Natuurkunde
Faculteit Wetenschappen

KATHOLIEKE UNIVERSITEIT
LEUVEN

Search for non Standard Model physics in nuclear β-decay with the WITCH experiment

Promotor:
Prof. Dr. N. Severijns

Proefschrift voorgedragen tot
het behalen van de graad van
doctor in de wetenschappen, 2007

Door:

Sam Coeck

Leuven - 2007

If we knew what it was we were doing, it would not be called research, would it?
Albert Einstein

To my parents and my wife Anja,
for their never ending support.

Acknowledgement

Throughout the past years many people have helped me to realize everything that is described in the text that lies before you. I now consider it time to express my gratitude towards them in a small word of thanks.

First of all I have to thank my parents for giving me the opportunity to study in the field of my choice and for their eternal support in everything work and non-work related. Without them this work would never have materialized.

Secondly I am indebted to my promotor prof. Nathal Severijns for given me a chance to work under his guidance. I will also not forget all present and former group members of the nuclear orientation group that have worked by my side for these past years. They thought me what the term *team spirit* means and provided the correct atmosphere for discussion and reflection. Together with our colleagues from CERN they were also at the basis of many successful missions to CERN. The members of the technical staff also deserve a special word of thanks for their tireless effort in providing everything we needed *asap*.

Finally I would like to thank Anja for always supporting me. Words can not express how much she has mend to me these last years.

September 2007
Sam

Contents

Introduction

For a long time the dream of many physicists has been to find *the theory of everything*, a single theory explaining every physical phenomenon we see around us, from the very big like galaxies, to the very small like the atomic nuclei. Although many efforts have been made, no such theory has been found up to now. What is known is that all these phenomena can be explained by only four forces:

- gravity, which makes sure we stay on the ground and makes apples fall on our heads;
- electromagnetism, which gives us light, cell phones and computers;
- the strong interaction, which keeps quarks together in nucleons and binds nucleons to form an atomic nucleus;
- the weak interaction, which causes some particles, like the neutron, to transform into other particles, in casu the proton.

Although phenomena caused by the weak interaction were discovered already a long time ago, it is probably the most mysterious of the four fundamental forces to many physicists. Maybe it is because it can not be imagined as a simple every day attraction or repulsion like the other three fundamental forces, or is it because on top of that it shows other peculiar properties?

Unlike α- and γ-radiation, β-radiation - maybe the best known example of a weak interaction process - has a continuous energy spectrum instead of a discrete one, a fact that led Pauli to postulate the existence of a new particle now known as the neutrino. Another surprise to the physics community came when Wu *et al.*, hinted by the theoretical work of Lee and Yang, showed that parity is not conserved in the weak interaction, and even more that it is maximally violated.

Today the theories describing the four forces are combined in what is known as *the Standard Model*. Still it is believed not to be the final *theory of everything* as it contains many free parameters and assumptions that are needed to describe the experimental results. In the Standard Model the weak interaction is said to have a specific appearance, described by a V-A (Vector *minus* Axial-vector) Hamiltonian, in agreement with experiments performed mainly in the 1950's. Although consistent with the experimental results, there is still room for deviating appearances of the weak interaction as right-handed

V+A terms or additional scalar (S) or tensor (T) terms. The experimental field of researching these additional terms received renewed interest when in the 1990's atom and ion traps made their appearance in nuclear physics. This triggered a number of experiments to again venture into the field of low energy weak interaction research.

One of those new experiments is WITCH (**W**eak **I**nteraction **T**rap for **CH**arged particles). Its primary aim is to improve the present limits on the contribution of scalar terms in the weak interaction Hamiltonian, although the physics that can be researched with this setup goes much further than this.

The aim of this work is to present the WITCH experiment and the current status and achievements of the project. A first chapter will focus on the weak interaction physics studied with WITCH and the observables linked to this. In the second chapter a concise overview of the whole experimental setup will be given. The following chapters discuss some important components of the setup, namely the diagnostics detectors, the pulsed drift section and the Penning traps, in detail. In the subsequent chapters the first measurements, which proof the principle of the experiment, will be discussed and some future improvements and measurements are suggested.

Three published articles are incorporated in the text:

- **Microchannel plate response to high intensity ion bunches**
  S. Coeck, M. Beck, B. Delauré, V.V. Golovko, M. Herbane, A. Lindroth, S. Kopecky, V.Yu. Kozlov, I.S. Kraev, T. Phalet, N. Severijns,
  Nuclear Instruments and Methods in Physics research A, **557** (2006) 516-522 [Coe06].

- **A Pulsed Drift Cavity to capture 30 keV ion bunches at ground potential**
  S. Coeck, B. Delauré, M. Herbane, M. Beck, V.V. Golovko, S. Kopecky, V.Yu. Kozlov, I.S. Kraev, A. Lindroth, T. Phalet, B. Vereecke, S. Versyck, D. Beck, P. Delahaye, F. Wenander, N. Severijns,
  Nuclear Instruments and Methods in Physics research A, **572** (2007) 585-595 [Coe07a].

- **Ab initio simulations on the behavior of small ion clouds in the WITCH Penning trap system**
  S. Coeck, B. Delauré, M. Herbane, V.Yu. Kozlov, I.S. Kraev, M. Tandecki, F. Wauters, M. Beck, P. Delahaye, A. Herlert, S. Sturm, N. Severijns,
  Nuclear Instruments and Methods in Physics research A, **574** (2007) 370-384 [Coe07b].

They are presented in separate chapters *as published*, with additional comments or results at the end of each of these chapters.

Chapter 1

Nuclear weak interaction physics

In this first chapter, a short overview of the weak interaction physics that will be studied with WITCH will be given. The focus is on low energy weak interaction processes as these can be probed by experiments like WITCH.

1.1 β-decay

Probably the best known example of a weak interaction process occurring at low energies is that of nuclear β-decay in which the nucleus emits or absorbs a β-particle. Three different forms of β-decay are commonly observed:

- β^--decay: $n \rightarrow p + e^- + \bar{\nu}_e$
- β^+-decay: $p \rightarrow n + e^+ + \nu_e$
- EC-decay: $p + e^- \rightarrow n + \nu_e$

In 1934 Fermi was the first to propose a Hamiltonian describing the β-decay process by assuming it to be analogous to the Hamiltonian of electromagnetic processes. Later Gamow and Teller extended Fermi's Hamiltonian to contain all possible Lorentz invariant interactions. Following the theoretical work of Lee and Yang [Lee56] and the famous experiment of C.S. Wu [Wu57] parity violating terms were also added to the Hamiltonian. The most general Hamiltonian density is then given by

$$\begin{aligned}
\mathcal{H}_\beta \quad = \quad & (\bar{p}n)\left(\bar{e}\left(C_S + C'_S\gamma_5\right)\nu\right) \\
& + \left(\bar{p}\gamma_\mu n\right)\left(\bar{e}\gamma^\mu\left(C_V + C'_V\gamma_5\right)\nu\right) \\
& + \frac{1}{2}\left(\bar{p}\sigma_{\lambda\mu}n\right)\left(\bar{e}\sigma^{\lambda\mu}\left(C_T + C'_T\gamma_5\right)\nu\right) \\
& - \left(\bar{p}\gamma_\mu\gamma_5 n\right)\left(\bar{e}\gamma^\mu\gamma_5\left(C_A + C'_A\gamma_5\right)\nu\right) \\
& + \left(\bar{p}\gamma_5 n\right)\left(\bar{e}\gamma_5\left(C_P + C'_P\gamma_5\right)\nu\right) \\
& + h.c.
\end{aligned} \tag{1.1}$$

	Selection rules	Operators
Fermi	$\Delta I = 0$ $\Delta T = 0$ $\Delta\pi = 0$	S/V
Gamow Teller	$\Delta I = 0,\pm 1$ $(0 \nrightarrow 0)$ $\Delta T = 0,\pm 1$ $(0 \nrightarrow 0)$ $\Delta\pi = 0$	T/A

Table 1.1 – *Fermi and Gamow-Teller selection rules and operators.*

with

$$\sigma_{\lambda\mu} = -\frac{1}{2}i(\gamma_\lambda\gamma_\mu - \gamma_\mu\gamma_\lambda). \tag{1.2}$$

The five different terms in the Hamiltonian can be distinguished from each other on the basis of their transformation properties under a proper Lorentz transformation. Conventionally the terms are named according to their transformation properties: Scalar (S), Vector (V), Tensor (T), Axial-vector (A) and Pseudo-scalar (P). C_i and C'_i are called the coupling constants and determine the relative strength of each of the terms. The presence of the C'_i terms accounts for the parity violating properties of β-decay.

Two types of β-decays can be distinguished: allowed transitions, for which

$$\begin{aligned} \Delta I &= 0, \pm 1 \\ \Delta T &= 0, \pm 1 \\ \Delta \pi &= 0 \end{aligned} \tag{1.3}$$

(ΔI, ΔT and $\Delta\pi$ respectively being the difference in spin, isospin and parity between the initial and final states) and forbidden decays. Within the allowed approximation two forms of nuclear β-decay can be distinguished: Fermi decay and Gamow-Teller decay. Their respective selection rules are given in Table 1.1.

1.1.1 Standard Model

Within the Standard Model a $V - A$ form of the weak interaction is assumed. No Scalar or Tensor terms are present[1]. In addition, maximum parity violation is assumed. In terms of the coupling constants this is translated into

$$\begin{aligned} &C_V = C'_V = 1 \\ &C_A = C'_A = -1.27 \\ &C_S = C'_S = 0 \\ &C_T = C'_T = 0 \end{aligned} \tag{1.4}$$

The analysis in Ref. [Sev06] has shown that when no prior assumptions are made except that the coupling constants are real (no time-reversal violation),

[1]The pseudoscalar term can be neglected if the nucleons are treated as being non-relativistic.

the present experimental limits on the coupling constants are given by

$$\begin{aligned} -1.40 < \quad & C_A/C_V & < -1.17 \\ 0.87 < \quad & C'_V/C_V & < 1.17 \\ 0.86 < \quad & C'_A/C_A & < 1.16 \\ -0.065 < \quad & C_S/C_V & < 0.070 \\ -0.067 < \quad & C'_S/C_V & < 0.066 \\ -0.076 < \quad & C_T/C_A & < 0.090 \\ -0.078 < \quad & C'_T/C_A & < 0.089. \end{aligned} \tag{1.5}$$

It is clear that there is still considerable room for experimental improvements of these limits.

1.1.2 Other weak interaction investigations

Although the best known process caused by the weak interaction is low energy β-decay, many other phenomena caused by the weak interaction can be observed at higher energies, for instance when colliding high energy particles or when looking at the decay of π or K particles. Although the two energy regimes for experiments are completely different[2], measurements on nuclear β-decay and higher energy processes yield complementary information on the nature of the weak interaction [Sev06].

The presence of exotic Scalar or Tensor type interactions that could possibly be observed in nuclear β-decay would imply the existence of a new boson that mediates this force. Such new boson(s) could then be searched for directly in high energy collision experiments. Possible candidates for such a Scalar boson could for instance be a charged Higgs particle or leptoquarks.

One of the main advantages of precision experiments in nuclear β-decay over high energy experiments is the fact that the former are largely model independent in the interpretation of the experimental results, while the latter rely on a large amount of theoretical input to predict the signature that has to be searched for.

1.2 Correlation coefficients

The coupling constants C_i and C'_i have to be determined from experiments. They can, however, not be observed directly. For this reason observables containing these factors have to be derived from the general Hamiltonian of equation 1.1. Therefore Jackson, Treiman and Wyld [Jac57] set out to derive an expression for several decay rate distributions in the case of allowed decays and taking into account the Coulomb corrections. Their result for nonoriented nuclei is given by

$$\omega(\boldsymbol{\sigma}|E_\beta, \Omega_\beta, \Omega_\nu)dE_\beta d\Omega_\beta d\Omega_\nu =$$

[2]Not only the energy scales but often also the sizes and price tags of the experiments are vastly different.

$$\frac{F(\pm Z, E_\beta)}{(2\pi)^5} p_\beta E_\beta (E_0 - E_\beta)^2 dE_\beta d\Omega_\beta d\Omega_\nu \frac{\xi}{2} \left\{ 1 + a\frac{\mathbf{p}_\beta \cdot \mathbf{p}_\nu}{E_\beta E_\nu} + b\frac{m_\beta}{E_\beta} \right.$$
$$\left. + \boldsymbol{\sigma} \cdot \left[G\frac{\mathbf{p}_\beta}{E_\beta} + H\frac{\mathbf{p}_\nu}{E_\nu} + K\frac{\mathbf{p}_\beta}{E_\beta + m_\beta}\left(\frac{\mathbf{p}_\beta \cdot \mathbf{p}_\nu}{E_\beta E_\nu}\right) + L\frac{\mathbf{p}_\beta \times \mathbf{p}_\nu}{E_\beta E_\nu}\right]\right\} \tag{1.6}$$

where E_β, $\mathbf{p}_\beta$ and Ω_β denote respectively the total energy, momentum and angular coordinates of the β-particle and similarly for the neutrino. $\boldsymbol{\sigma}$ represents the spin vector of the β-particle. The upper sign refers to β^--decay whereas the lower sign refers to β^+-decay. ξ is a normalization factor proportional to the decay rate and contains the nuclear matrix elements M_F and M_{GT}:

$$\begin{aligned} \xi &= |M_F|^2(|C_S|^2 + |C'_S|^2 + |C_V|^2 + |C'_V|^2) \\ &+ |M_{GT}|^2(|C_A|^2 + |C'_A|^2 + |C_T|^2 + |C'_T|^2). \end{aligned} \tag{1.7}$$

The function $F(\pm Z, E_e)$ is the so-called Fermi-function which corrects the expression for the Coulomb interaction between the β-particle and the daughter nucleus with charge Z.

The coefficients a, b, G, H, K and L are called correlation coefficients and depend on the coupling constants C_i and C'_i as well as on the nuclear matrix elements. The β-ν-angular correlation coefficient a has proven to be highly sensitive to possible admixtures of Scalar and Tensor type interactions while the coefficients H, K and L have not shown any practical importance up till now. Another important term is the Fierz interference term b, because it is present in all correlation measurements, irrespective of the correlation coefficient that is measured.

Including first order (i.e. up to order αZ) Coulomb corrections[3] the β-ν-angular correlation coefficient a is given by

$$\begin{aligned} a\xi &= |M_F|^2\left[|C_V|^2 + |C'_V|^2 - |C_S|^2 - |C'_S|^2 \mp \frac{\alpha Z m_e}{p_\beta} 2Im(C_S C_V^* + C'_S C'^*_V)\right] \\ + & \frac{|M_{GT}|^2}{3}\left[|C_T|^2 + |C'_T|^2 - |C_A|^2 - |C'_A|^2 \pm \frac{\alpha Z m_e}{p_\beta} 2Im(C_T C_A^* + C'_T C'^*_A)\right] \end{aligned} \tag{1.8}$$

and the Fierz interference term is written as

$$b\xi = \pm 2\Gamma Re\left[|M_F|^2(C_S C_V^* + C'_S C'^*_V) + |M_{GT}|^2(C_T C_A^* + C'_T C'^*_A)\right] \tag{1.9}$$

with

$$\Gamma = (1 - \alpha^2 Z^2)^{1/2}. \tag{1.10}$$

Since the contribution of the Fierz interference term can not be neglected when measuring the β-ν-angular correlation coefficient, it is more convenient to define a parameter $\tilde{a}$ that is given by

$$\tilde{a} = \frac{a}{1 + \frac{m_e}{E_\beta} b}. \tag{1.11}$$

[3]This approximation has been shown to be correct at the level of 10 % of the correction [Vog83].

Interaction	a
V	1
A	-1/3
S	-1
T	1/3

Table 1.2 – *The β-ν-angular correlation coefficient a for pure forms of the weak interaction.*

Within the Standard Model, however, the Fierz interference term is predicted to be equal to 0 as each term in Eq. 1.9 contains either a Scalar or Tensor type coupling constant (see also Eq. 1.4) such that $\tilde{a} \equiv a$. A precise determination of the Fierz term can also yield limits on the contribution of exotic currents in the weak interaction. Note however that for instance for a pure Fermi transition the Fierz term would be trivially equal to 0 if the Scalar currents are right handed ($C_S = -C'_S$). Hardy and Towner [Har05] found that

$$\frac{C_S C_V + C'_S C'_V}{|C_V|^2 + |C'_V|^2 + |C_S|^2 + |C'_S|^2} = -(0.00005 \pm 0.00130) \qquad (1.12)$$

from a careful analysis of the $\mathcal{F}t$ values of various $0^+ \rightarrow 0^+$ superallowed pure Fermi transitions. This result puts a stringent limit on the possible combinations of C_S and C'_S. If plotted in a (C_S, C'_S) graph, this limit would be represented as a narrow band of allowed values, but this band would stretch from $(-\infty, +\infty)$ over $(0, 0)$ to $(+\infty, -\infty)$. A measurement on a would, however, impose a limit represented by a circle in this plane. Both limits thus yield complementary information on the possible existence of Scalar type currents in the weak interaction.

The values of a for pure V and A (Standard Model) interactions and pure S and T interactions are shown in table 1.2. Any admixture of for instance an S-type interaction into the Standard Model V interaction in the pure Fermi decay will thus lead to an a parameter that differs from the Standard Model value.

Expressions for other correlation coefficients can be found in [Sev06].

1.3 β-ν-angular correlation coefficient determination

To measure the β-ν-angular correlation coefficient a directly one would have to measure the electron and neutrino momentum $\mathbf{p}_\beta$ and $\mathbf{p}_\nu$. As the neutrino is very hard to detect this is almost impossible. Instead one can detect the daughter nucleus that recoils during the decay as a consequence of the conservation of energy and momentum. This recoil process is illustrated in Fig. 1.1. One can infer the kinematics of the reaction, and thus the angular correlation coefficient a, through this in different ways:

- β-recoil coincidence measurement;

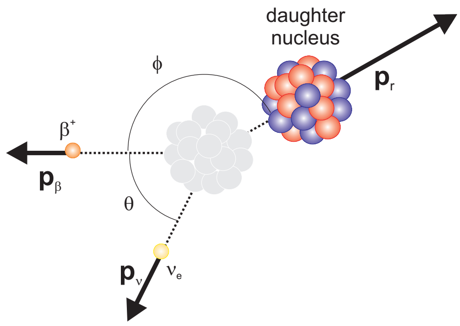

Figure 1.1 – *The emission of the β-particle and the neutrino causes the nucleus to recoil.*

- detection of secondary radiation;
- measurement of the recoil energy spectrum.

Examples of the first two will be given in section 1.5 but first the focus will be on the last possibility, as this is the option chosen for the WITCH experiment.

1.3.1 Daughter recoil spectrum

The β-ν-angular correlation coefficient can be inferred from the shape of the recoil spectrum. This can be understood by having another look at Fig. 1.1 and by writing the β-ν-angular correlation in terms of the angular distribution function W of the angle θ between the momentum of the β-particle and the neutrino as:

$$W(\theta) = 1 + \frac{p_\beta \cdot p_\nu \cdot \cos(\theta)}{E_\beta E_\nu}\tilde{a}. \tag{1.13}$$

When a is large (e.g. $a = 1$ for pure V interaction), $W(\theta)$ will be large for small angles θ while $W(\theta)$ will be large for large angles θ when a is small (e.g. $a =$ -1 for pure S interaction). When the emission angle between the β-particle and the neutrino θ is small, conservation of energy and momentum dictates that the recoil energy of the daughter nucleus is large. If on the other hand the angle θ is large, the recoil energy will be small. This is illustrated in Fig. 1.2 for a purely Vector and a purely Scalar β-decay. Thus through equation 1.13, we can see that large values of a will produce on average more high energy recoils than low values of a.

In Fig. 1.3 calculated recoil energy spectra are shown for the four pure decay modes listed in table 1.2. A clear difference in the shape of these recoil spectra, depending on the β-ν-angular correlation coefficient a, can be observed. The maximum recoil energy for the decay of the nucleus ${}^A_Z X$ with decay energy Q is given by

$$T_{R,max} = \frac{(Q \pm m_e c^2)^2 - m_e^2 c^4}{2M_{at}({}^{A}_{Z\pm1}X)c^2} \tag{1.14}$$

where the upper sign corresponds to β^--decay and the lower sign to β^+-decay.

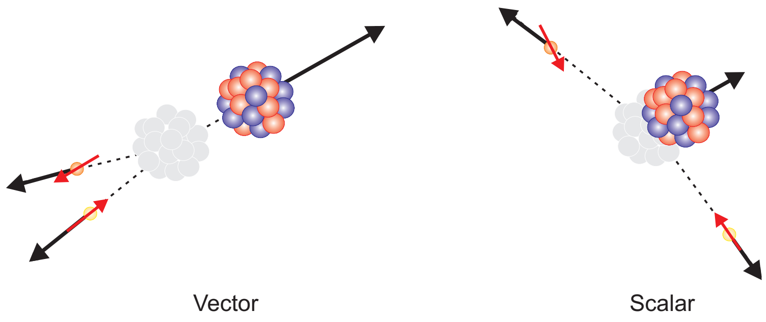

Figure 1.2 – *Illustration of the difference in recoil energy between a purely Vector β-decay and a purely Scalar one.*

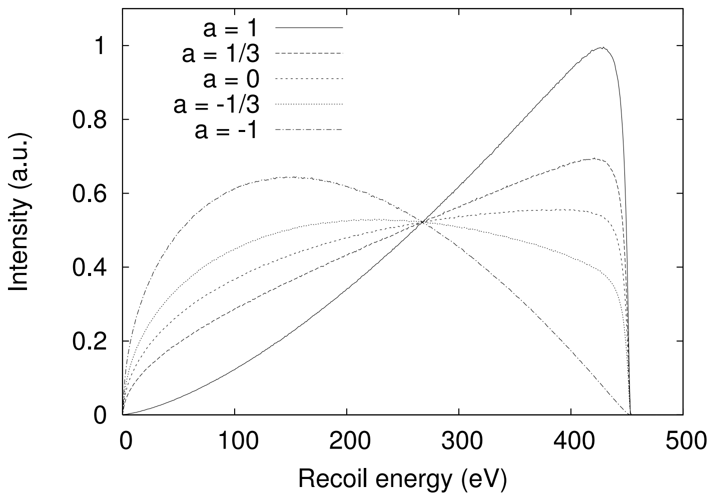

Figure 1.3 – *Differential recoil spectra for ^{35}Ar for different a parameters.*

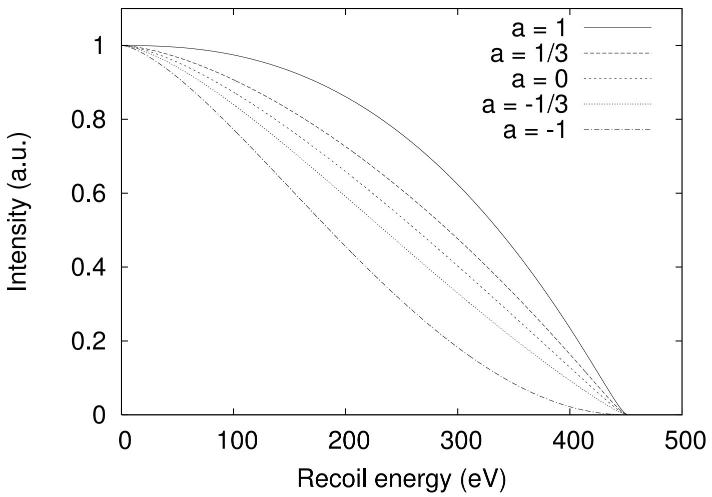

Figure 1.4 – *Integral recoil spectra for ^{35}Ar for different a parameters.*

For reasons that will become clear after the explanation on the working principle of the WITCH setup, we also define the integral recoil spectrum S(E) of the differential recoil spectrum s(E) as

$$S(E) = \int_E^\infty s(E_r)dE_r = \int_0^\infty s(E_r)dE_r - \int_0^E s(E_r)dE_r \tag{1.15}$$

The integral spectra corresponding to the differential ones from Fig. 1.3 are shown in Fig. 1.4 and it is the integral spectrum that will be measured at WITCH.

1.4 Additional effects

1.4.1 Practical problems

The biggest problem in determining the a-parameter through the recoiling daughter nucleus lies in the preparation of the radioactive source. Since the recoil energy is typically only of the order of 100 eV, scattering of the recoil poses a serious threat for systematic errors. For this reason, prior to the arrival of atom and ion traps, only elements that can form a gaseous source where used for this type of measurement. Now the range of interesting isotopes has expanded to the alkali metals for atom traps and basically any isotope for ion traps, thus increasing the potential of a successful measurement in this field.

1.4.2 Mixed transitions

One of the prime isotopes suited for performing a precision measurement at WITCH is ^{35}Ar (see section 2.9). The primary decay mode is a $3/2^+ \rightarrow 3/2^+$

mixed Fermi/Gamow-Teller transition. To obtain an expression for a for such a mixed transition we start by defining the mixing ratio ρ as

$$\rho = \frac{C_A M_{GT}}{C_V M_F}. \tag{1.16}$$

The Standard Model β-ν-angular correlation coefficient for mixed transitions can then be written as

$$a_{SM} = \frac{1-\rho^2/3}{1+\rho^2}. \tag{1.17}$$

By including possible non Standard Model terms, a can, under the assumptions of maximal parity violation and no time reversal violation for the V- and A-interactions, be approximated as [Sev06]

$$\begin{aligned} a \approx a_{SM} \quad & - \quad \frac{1}{(1+\rho^2)^2}\left[\left(1+\frac{1}{3}\rho^2\right)\frac{|C_S^2|+|C_S'|^2}{C_V^2}\right. \\ & + \quad \left.\frac{1}{3}\rho^2(1-\rho^2)\frac{|C_T^2|+|C_T'|^2}{C_A^2}\right] \\ & + \quad \frac{\alpha Z m}{p_e}\frac{1}{1+\rho^2}\left[\mp Im\left(\frac{C_S+C_S'}{C_V}\right)\right. \\ & \pm \quad \left.\frac{\rho^2}{3} Im\left(\frac{C_T+C_T'}{C_A}\right)\right] \end{aligned} \tag{1.18}$$

where the upper sign again refers to β^--decay and the lower sign to β^+-decay. It is clear that for a precision measurement on a mixed transition the mixing ratio has to be precisely known. For ^{35}Ar the mixing ratio is known with good precision from the $\mathcal{F}t$ value (i.e. $\rho = -0.282 \pm 0.003$) and the Standard Model value for a is 0.903 with a relative error of 0.21% due to the error on the mixing ratio [Tan07].

In Fig. 1.5 a Standard Model recoil spectrum for ^{35}Ar and one in which a 5% (10%) Scalar contribution is included is shown. No other non Standard Model terms are included, but the Scalar currents are assumed to be right handed ($C_S = -C_S'$). The integral spectra are shown in Fig. 1.6. Note that the point where the difference in the integral spectra is largest for different a, corresponds to the point where the differential recoil spectra for different a cross (see Fig. 1.3).

1.4.3 Daughter charge state

When the nucleus of an atom decays through β-decay, the charge state which the daughter obtains depends on the charge state of the mother atom and the type of β-decay:

$$\begin{aligned} M^q &\rightarrow D^{q-1} + \beta^+ + \nu_e \\ M^q &\rightarrow D^q + \nu_e \\ M^q &\rightarrow D^{q+1} + \beta^- + \bar{\nu}_e \end{aligned}$$

In addition to this, a process called electron shake-off also contributes to the final charge state.

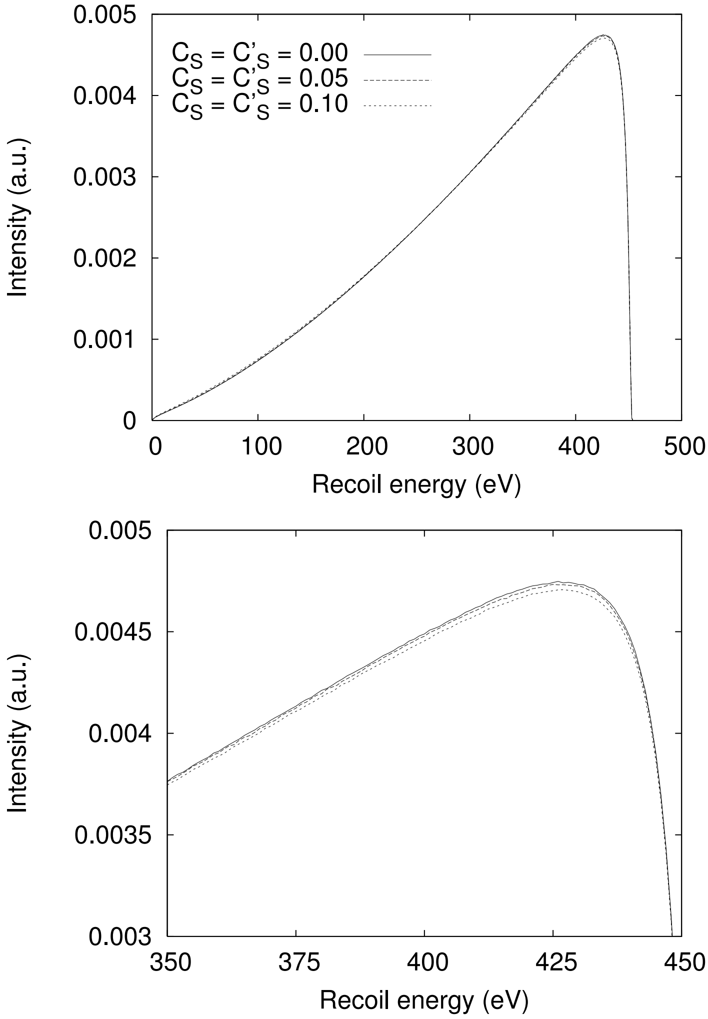

Figure 1.5 – *(top) Differential recoil spectra for ^{35}Ar assuming a pure Standard Model form, and with a 5% Scalar contribution ($a = 0.898$) and a 10% Scalar contribution ($a = 0.884$). (bottom) Zoom around the spectrum's maximum where the difference between the different curves is most easily observed.*

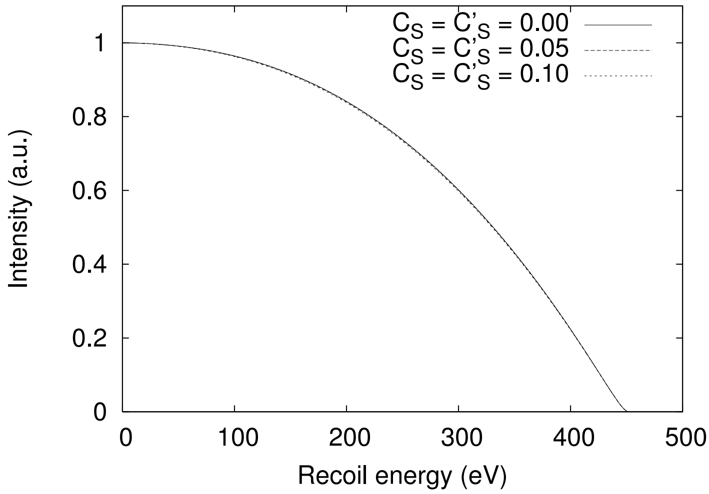

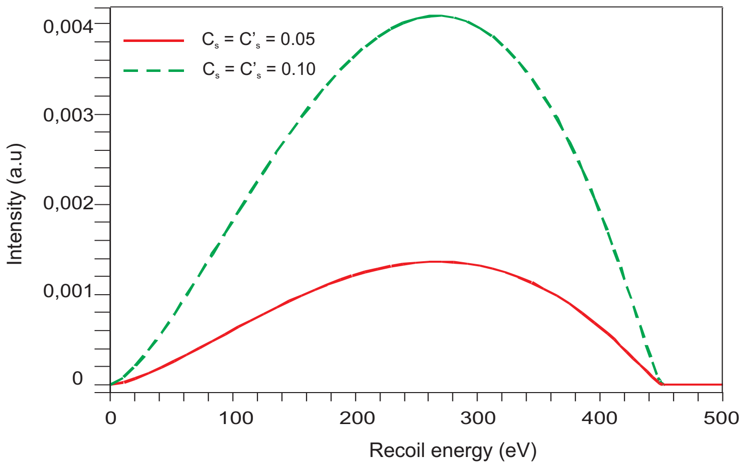

Figure 1.6 – *(top) Integral recoil spectra for ^{35}Ar assuming a pure Standard Model form, and with a 5% Scalar contribution and a 10% Scalar contribution. (bottom) Difference between the non-Standard Model spectra and the Standard Model one.*

For many isotopes the charge state distribution after β-decay is poorly or not known. In addition all available data are for a neutral mother atom, and the influence of the initial charge state has not been investigated.

When determining the energy of the recoiling nucleus with the retardation principle like in the WITCH experiment (more details will be given in chapter 2), the ions with charge state q will go into the spectrum at position E/q. This leads to a spectrum that actually consists of a number of overlapping spectra. An example of a spectrum containing several charge states is shown in Fig. 1.7 for ^{35}Ar. Note that since the final charge state distribution for the decay of $^{35}Ar^{+}$ is not known the values

$$\begin{aligned} 1^{+} &: 10\% \\ 2^{+} &: 3\% \\ 3^{+} &: 1\% \end{aligned}$$

are used purely for illustration (the remainder of the ^{35}Cl daughters is supposed to end up as neutrals).

For this reason only the upper half of the spectrum, which purely consists of 1^{+} events, can be used, especially if the charge state distribution is poorly known. Even in this case a systematic effect will be present if the charge state distribution is dependent on the β or recoil energy. This has been discussed in Ref. [Sci03] but the results given therein do not reach the precision required for precision measurements using β^{+} emitters and the effect has to be investigated further [Sci03]. Also for this effect the influence of the initial charge state of the decaying element has not been investigated yet.

1.4.4 Gamma recoil

Not only the emission of a β-particle or neutrino but also the emission of a γ-ray causes the nucleus to recoil. The recoil energy of a γ-transition of energy E for a nucleus of mass M is given by

$$T_{R\gamma} = \frac{E_{\gamma}^{2}}{2Mc^{2}}. \tag{1.19}$$

If the γ-ray follows the β-decay, a significant effect on the shape of the recoil spectrum is seen. For an angle θ between the direction of recoil caused by the β-decay (energy $T_{R\beta}$) and the direction of recoil caused by the γ-decay (energy $T_{R\gamma}$) the total recoil energy is given by

$$T_R = T_{R\beta} + T_{R\gamma} + 2\cos(\theta)\sqrt{T_{R\beta}T_{R\gamma}}. \tag{1.20}$$

As the direction of emission of the γ-ray is random, the angle θ is distributed according to

$$\theta = acos(2\mu - 1) \tag{1.21}$$

with μ uniformly distributed within $[0, 1]$. Combined with equation 1.20 this leads to a response function of uniformly distributed energies between

$$T_{R,min} = T_{R\beta} + T_{R\gamma} - 2\sqrt{T_{R\beta}T_{R\gamma}}$$

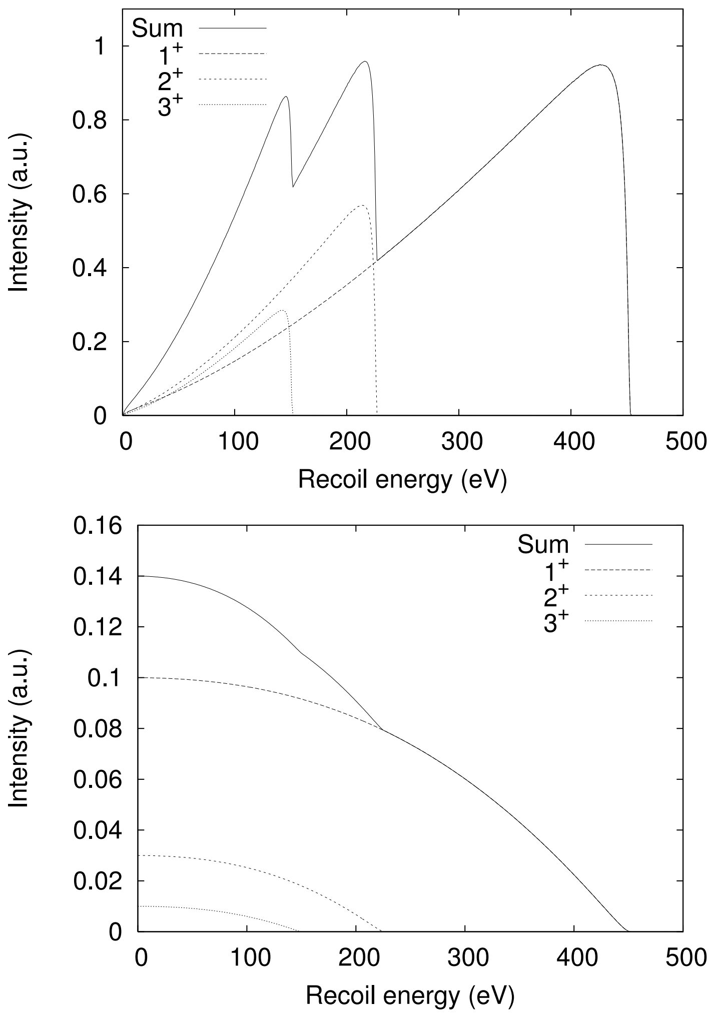

Figure 1.7 – *(top) Differential recoil spectrum for the decay of* $^{35}Ar^{+}$ *containing* 1^{+}, 2^{+} *and* 3^{+} *recoil ions. (bottom) Integral recoil spectrum for the decay of* $^{35}Ar^{+}$ *containing* 1^{+}, 2^{+} *and* 3^{+} *recoil ions.*

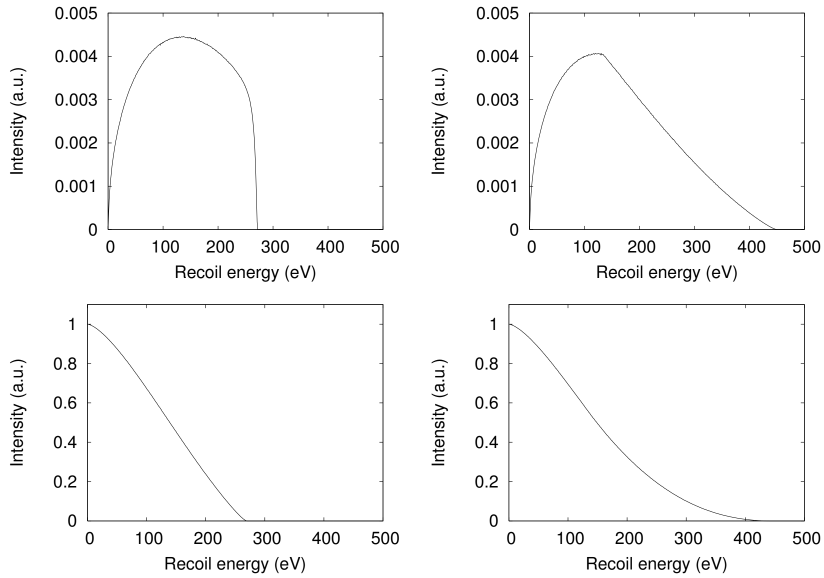

Figure 1.8 – *Influence of the γ-recoil on the recoil energy spectrum. [top](left) Original recoil spectrum. (right) Recoil spectrum including γ-recoil. [bottom](left) Original integral recoil spectrum. (right) Integral recoil spectrum including γ-recoil.*

and

$$T_{R,max} = T_{R\beta} + T_{R\gamma} + 2\sqrt{T_{R\beta}T_{R\gamma}}.$$

Figure 1.8 shows the influence on the recoil energy spectrum of the second most intense branch of the ^{35}Ar decay, which goes to an excited state in ^{35}Cl at 1.219 MeV with a 1.23(3) % branching. The maximum recoil energy after γ-decay is typically very close to the maximum recoil energy of the main branch that goes to the groundstate of the daughter isotope directly (i.e. 452 eV in this case). This means that the two recoil spectra will almost completely overlap. It is thus imperative that the relative branching ratios are precisely known and to take the γ-recoil into account when performing the analysis of a precision experiment.

If several γ-rays follow each other sequentially, all the recoils have to be combined. This will very much complicate the shape of the recoil spectrum, and especially if the different branching ratios are not very well known, hamper a precision measurement of the a-parameter through the shape of the recoil spectrum.

1.4.5 Internal conversion

Especially low energy and high multipolarity γ-transitions in high Z isotopes are often accompanied by a large fraction of internal conversion (IC) decays. In these decays the excess energy of the nucleus is transferred to one of the orbital electrons, which is subsequently removed from the atom. The energy available to the escaping electron is determined by the energy of the transition E_γ and the binding energy of the electron B_i and is given by

$$E_{IC} = E_\gamma - B_i. \tag{1.22}$$

The total recoil associated with this process is then determined by

$$T_R = T_{R\beta} + T_{RIC} + 2\cos(\theta)\sqrt{T_{R\beta}T_{RIC}} \tag{1.23}$$

with

$$T_{RIC} = \frac{\frac{E_{IC}^2}{c^2} + 2E_{IC}m_e}{2M} \tag{1.24}$$

again leading to a response function of uniformly distributed energies between

$$T_{R,min} = T_{R\beta} + T_{RIC} - 2\sqrt{T_{R\beta}T_{RIC}}$$

and

$$T_{R,max} = T_{R\beta} + T_{RIC} + 2\sqrt{T_{R\beta}T_{RIC}}.$$

Because of the very small decay energies involved in this process, the recoil associated with internal conversion is typically rather small. It can however still cause a significant Doppler broadening.

1.4.6 Electron capture

The decay of a nucleus through β^+-decay can be accompanied by electron capture decays (EC) where an orbital electron is captured by the nucleus which transforms a proton into a neutron and emits a neutrino. As in the final state of the EC decay only two particles are present, namely the neutrino and the recoiling daughter nucleus, the recoil of the nucleus is mono energetic. The kinetic energy of the recoiling nucleus can to good order be approximated as

$$T_R = \frac{(Q - B_i)^2}{2Mc^2} \tag{1.25}$$

with Q being the Q-value of the decay, B_i the binding energy of the electron that was captured and M the mass of the daughter atom ${}^{A}_{Z-1}X$. This recoil energy is always higher than the maximum recoil energy of the β^+-decay for the same nucleus.

In itself a measurement of the EC peak would be interesting since new physics can also be obtained from such measurement (see for instance chapter 11). For such measurements, decays with large electron capture branching but relatively short half lives are needed, thus severely limiting the number of suitable isotopes.

Measuring the EC peak is also of practical use because the EC peak can, when looking at a β-recoil spectrum, be used to determine the response function of the system (see chapter 2). For many interesting candidates for a measurement of the β-ν-angular correlation coefficient the EC intensity is, however, very low, hampering a precise online determination of the spectrometer response function.

1.5 Other experiments

1.5.1 Experiments from the past

Maybe one of the most successful experiments ever conducted in this field, was the measurement of the recoil spectrum of the pure Gamow-Teller decay of ^6He at Oak Ridge more than 40 years ago [Joh63]. Their result $a = -0.3343 \pm 0.0030$ still provides the best limit on the Tensor coupling constants C_T and C'_T.

Another successful experiment was performed at ISOLDE, CERN by Schardt and Riisager in 1993 and was repeated by Adelberger *et al.* in 1999. In this experiment the kinematic broadening of β delayed protons was measured for the pure Fermi decay of ^{32}Ar. Their result $\tilde{a} = 0.9989 \pm 0.0052_{stat} \pm 0.0039_{syst}$ improved the limits on a possible Scalar contribution on the weak interaction Hamiltonian [Ade99].

1.5.2 Present and future experiments

With the advent of atom and ion traps, a new range of experiments entered the field. The first successful correlation measurement in an atom trap was performed at TRIUMF by Gorelov *et al.*. They used a Magneto Optical Trap (MOT) as a radioactive source for their measurement of the TOF spectrum of the ^{38}Ar particles coming from the decay of $^{38}K^m$. Their result $\tilde{a} = 0.9981 \pm 0.0030^{+0.0032}_{-0.0037}$ provides the best limit from β-ν-angular correlation measurements on possible Scalar contributions to the weak interaction Hamiltonian and is in agreement with the Standard Model [Gor05].

Another experiment using a MOT is set up at Berkeley [Sci04]. Their measurements on ^{21}Na yielded $\tilde{a} = 0.5243 \pm 0.0091$, a value that differs by about 3σ from the Standard Model value of 0.558(3) [Nav91].

The Paul trap experiment at LPC-Caen and the WITCH experiment are the first experiments that aim at a correlation measurement using an ion trap. In the case of LPC-Caen the aim is to improve the limit on the contribution of Tensor currents by measuring the recoils of ^6He using a Paul trap [Ban05].

The aSPECT experiment [Glu05] is aiming for a measurement of the recoil energy spectrum of the recoiling protons after the β-decay of the free neutron, which is a mixed Fermi/Gamow-Teller transition. The spectrometer that is used in this experiment is similar to the one that is used at the WITCH experiment (see chapter 2).

Finally, at KVI-Groningen a whole program is currently being set up where, amongst others, β-ν angular correlations will be measured using a MOT [Ber03].

Chapter 2

Overview of the WITCH setup

In this chapter a short overview of the WITCH setup and its environment will be given. Many of the in-depth details are kept for later chapters where some of the main components of the system will be discussed. A complete overview of the entire setup is presented in Fig. 2.1. In short the radioactive beam received from ISOLDE is first cooled and bunched in REXTRAP before it is sent to WITCH. There it is first sent through the horizontal beamline into the vertical beamline where the ions are slowed down. Then they are injected into the high magnetic field of the Penning traps. In the traps the ion cloud is cooled and purified and held as radioactive source. Ions that decay in the decay trap can enter the retardation spectrometer where their energy is probed to finally end up on the recoil detector.

2.1 ISOLDE

The WITCH experiment is located at the On-Line Mass Separator ISOLDE facility [Kug92, Kug00] at CERN. Here radioactive isotopes are created by bombarding a target with protons from the PS-Booster accelerator at an energy of 1.4 GeV. Radioactive atoms created inside the target through nuclear reactions are subsequently extracted from the target and ionized in one of the various ion sources. The products are mass-separated and injected into the beamline of the experimental hall where they are guided to the different setups. Two mass separators are available: the GPS (General Purpose Separator) with a mass resolution of approximately 2400 and the HRS (High Resolution Separator) that has a resolution of 6000. The layout of the ISOLDE facility is shown in Fig. 2.2. ISOLDE is capable of delivering many different radioactive beams at good intensities, not limiting experiments like WITCH to one specific isotope (or one specific physics topic for that matter).

The protons hitting the ISOLDE target are pulsed and have a cycle time of 1.2 s. For many elements the release from the target is not constant but

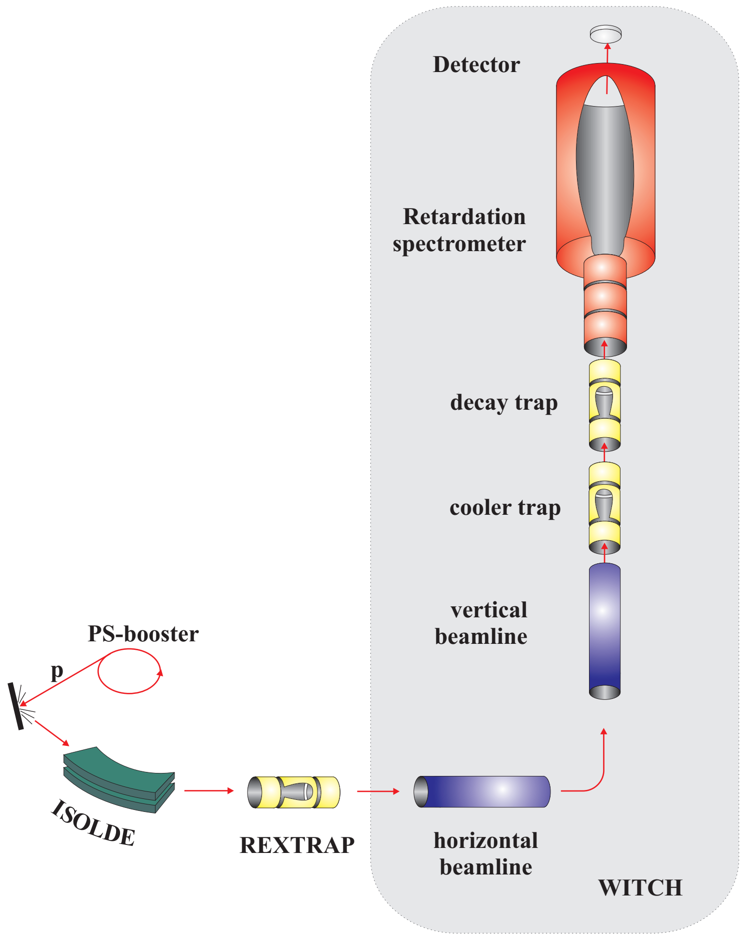

Figure 2.1 – *Schematic overview of the WITCH setup and its environment. Radioactive ions received from ISOLDE are first cooled and bunched in REXTRAP before they are passed on to the WITCH experiment. Here they are decelerated and then injected into the first of two Penning traps. After cooling and mass selective purification the ions are transferred and stored in the second Penning trap which serves as scattering free source for the experiments. The energy of the recoiling ions leaving this trap is probed in the retardation spectrometer before the ions are detected in the MCP ion detector.*

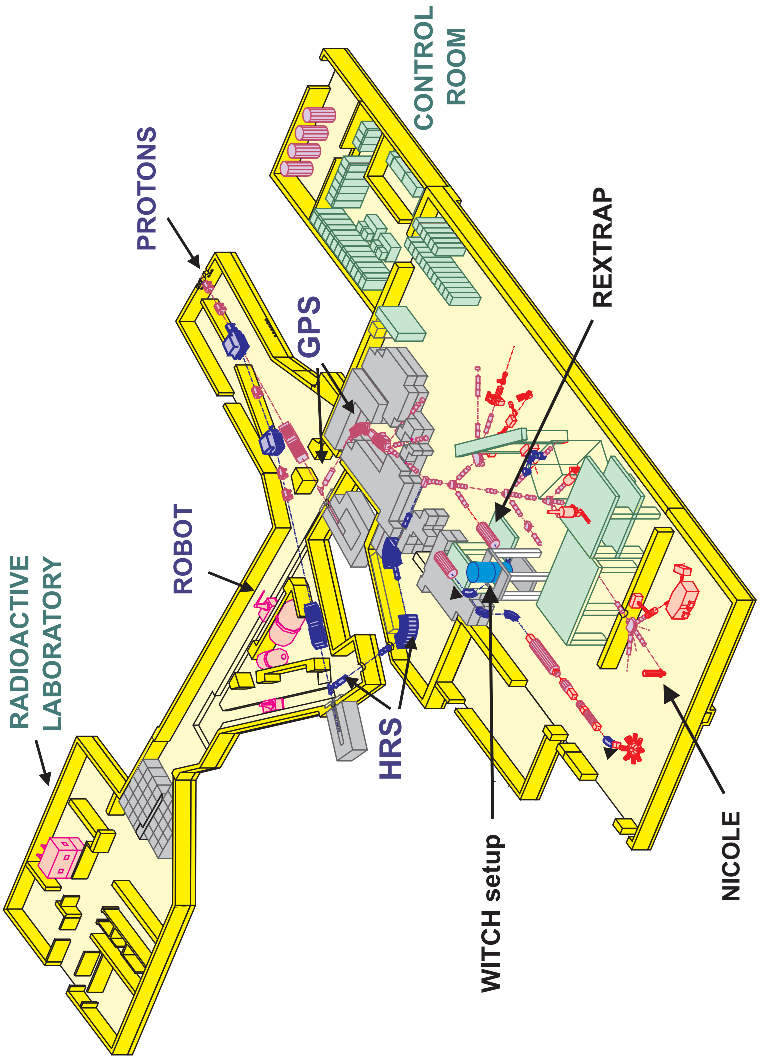

Figure 2.2 – *Overview of the ISOLDE facility in CERN. The location of the WITCH experiment in the experimental hall is indicated.*

rather reaches a maximum after a certain time from the impact of the proton pulse. For this reason it is often best to synchronize the experimental cycle with the proton cycle of ISOLDE.

2.2 REXTRAP

The REXTRAP Penning trap is the first step of the REX-ISOLDE post acceleration complex. In REXTRAP, ions that are delivered from the separator as a more or less continuous beam are accumulated and ejected as a short bunch. In addition the ions are also cooled and some mass dependent purification is performed. Not only does the cooling reduce the energy spread of the ions ejected from the trap, it also improves the transversal emittance which is a measure for the quality of the beam. Because of the need for a bunched beam, but also because of this improved beam quality, the WITCH experiment was set up downstream of the REXTRAP Penning trap.

Often typical parameters used for REXTRAP in combination with the REX accelerators are not optimal for the purposes of the WITCH experiment. One such example is the ejection of the ions from the trap: by making the ejection potential steeper the time structure of the ion pulse can be made significantly shorter, which increases the overall efficiency of the WITCH system (see chapter 4 for more information). This is shown in Fig. 2.3 where the "Time Of Flight (TOF)" structure of the $^{39}K^{+}$ ions as detected at the exit of REXTRAP is shown for different voltages applied to the central electrodes of the trap during ejection. The steeper the ejection potential, the shorter the bunch becomes, but also the higher the average ion energy and spread in ion energy. The steepest ejection potentials shown have been successfully used already and an even shorter pulse most often is not required for WITCH operation.

2.3 Beamline

The WITCH experiment has both a horizontal and vertical section in its beamline. In the horizontal beamline the ion beam is guided from the REXTRAP setup into the vertical part of the WITCH beamline. In the vertical beamline the ion beam is slowed down using a pulsed drift tube and is prepared for injection into the high magnetic field region where the Penning traps are located. To ensure optimal control of the ion beam's parameters numerous electrostatic elements are foreseen in both sections of the beamline.

2.3.1 Horizontal beamline

The horizontal beamline is the first part of the WITCH setup that the ions enter after their ejection from REXTRAP. An overview of the electrodes in the horizontal beamline is given in Fig. 2.4. Its main constituents are the two electrostatic kicker/bender combinations. A first bender bends the ions over an angle of 29° in the horizontal plane. This deflection is necessary to create some distance between the vertical part of the setup and the REX beamline.

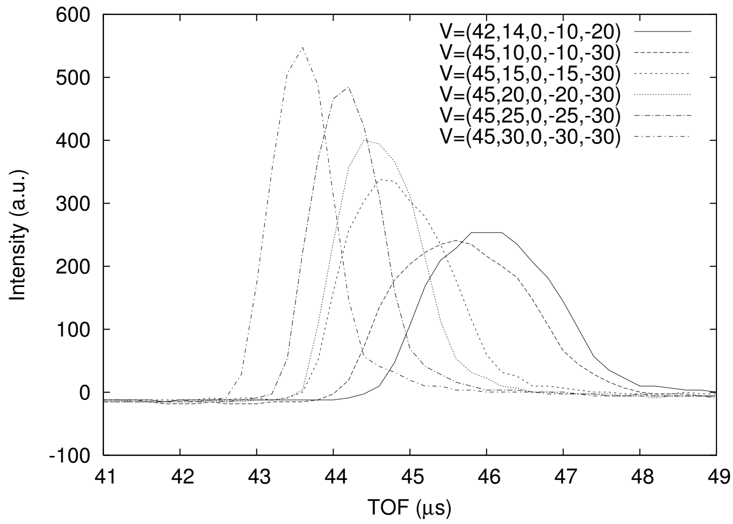

Figure 2.3 – *TOF structure of a bunch of* $^{39}K^{+}$ *ions as detected at the exit of REXTRAP for different ejection voltages. The voltages on the five central trap electrodes during the ejection are indicated in the grapg legend.*

Abbreviation	Function
HB	Horizontal beamline
VB	Vertical beamline
KICK	Kickers
BEND	Benders
STEE	Steerers
EINZ	Einzellens
RETA	Retardation electrode
PDT	Pulsed drift tube
DRIF	Drift electrode
MCPD	MCP detector
FCUP	Faraday cup detector
DIAP	Diaphragm
IONS	Off-line ion source
( )	Not installed

Table 2.1 – *Naming conventions used in figures 2.4 and 2.5.*

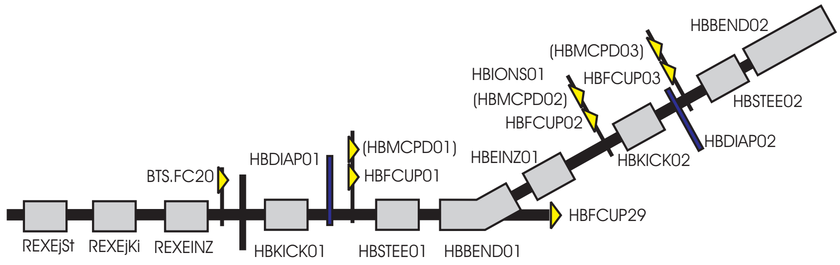

Figure 2.4 – *Overview of the electrode layout in the horizontal beamline using the naming conventions of table 2.1. The REXTRAP Ejection Steerers/Kickers (REXEjSt and REXEjKi), Einzellens (REXEINZ) and last faraday cup (BTS.FC20) are also shown.*

The second bender bends the ions over 90° from the horizontal plain into the vertical part of the setup. Both benders are preceded by a pair of electrostatic kickers that steer the beam into the bender, or in case needed, let the beam pass straight on. A beam-gate is connected to the kickers of the 29° bender. This fast switching device can quickly switch between sending ions into the bender and letting them pass straight through the beamline. This enables us to select ions on the basis of their Time Of Flight out of REXTRAP, thus avoiding that possible contaminants, like ionized Ne buffer gas, enter the WITCH setup.

The tuning of this part of the beamline, including the ejection electrodes of REXTRAP, is very critical since it determines the quality with which the beam can be injected into the vertical part of the beamline and eventually also into the magnetic field. Especially the tuning of the 90° bender has proven to be very critical in this respect. A change in the bender voltage of only 0.1% has been seen to have a significant effect on the tuning of the beam further downstream in the beamline. In the horizontal beamline only Faraday cups are foreseen for the moment for beam diagnostics. The first (position sensitive) MCP detector is located directly behind the 90° bender. More information on the beam diagnostics can be found in chapter 3.

Off-line ion source

A recent addition to the setup is the ion source for stable alkali ions [Rep07]. The source is an exact copy of the one that is used for REXTRAP [Gha96b] and is installed in the horizontal beamline replacing the diagnostics set HBMCPD02 and HBFCUP02. A set of movable electrostatic benders can bend the beam from the source into the beamline. As the source provides a DC ion beam, the beam has to be pulsed. To accomplish this the beam-gate device that is normally connected to the kickers of the 29° bender, can be connected to the ion source bender. The drawback of this method is the low beam intensities that can be obtained. If the source produces a DC current of 100 pA and a pulse length of only 3 μs is required, the ion pulse only consists of about 2000 particles instead of the roughly 10^6 that are obtained from REXTRAP. On the other hand this

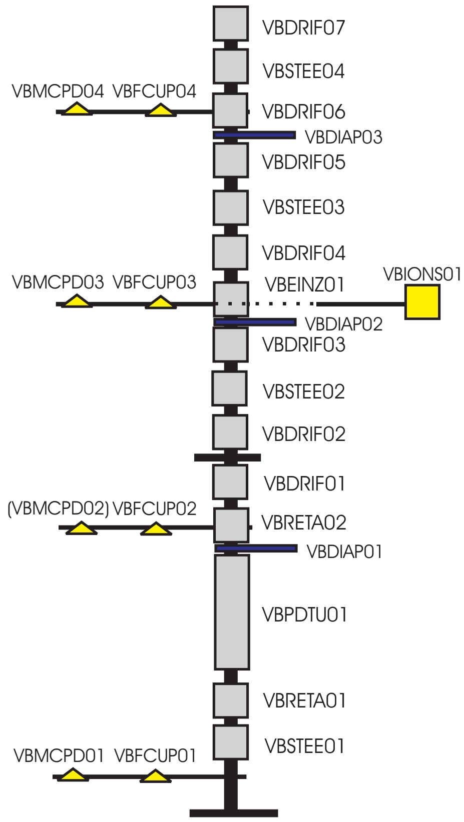

Figure 2.5 – *Overview of the electrode layout in the vertical beamline following the naming conventions of table 2.1.*

source does make the WITCH experiment less dependent on REXTRAP and as such greatly increases the amount of time the system can be used for off-line testing.

2.3.2 Vertical beamline

The layout of the vertical beamline is presented in Fig. 2.5. The most important component in this section is the Pulsed Drift Tube (PDT). This switchable electrode avoids the need for a high voltage platform for the Penning traps by slowing down the ions coming from REXTRAP at an energy of 30(60) keV to several hundred eV's. A full description of the PDT system, its operation and tests performed with the system are presented in chapter 4.

When the PDT is used, faraday cups can no longer be used for beam tuning upstream of this electrode since the repetition rate of the pulsed beam is limited to 1 Hz and the charge collected on the Faraday cup during this period is too small to be read by the electrometer (see chapter 3 for an alternative way of reading the faraday cups that could render them functional even in

Name	Voltage (V) (sim) [Del04] (60 keV)	Voltage (exp) (V) (30 keV)
REX ejec stee hor	0	17
REX ejec stee ver	0	18
REX ejec kick hor	0	24
REX ejec kick ver	0	-25
REXTRAP-lens	28500	15900

Table 2.2 – *Overview of the REXTRAP beam optical components and the simulated as well as experimental voltages for each component for a 30 (60) keV ion beam.*

this situation). That is why in this section MCP detectors (see chapter 3) are foreseen for tuning the beam. Additionally these detectors also provide the necessary timing information for the correct tuning of the beam-gate and PDT timing.

A small cross beam ion source is also foreseen in this section of beamline. This ion source can be used to ionize gasses (preferably noble gasses like Ar). The beam of this source can be pulsed by pulsing its extraction electrode and the beam can be shot straight into the traps at an energy of about 100 eV [Coe03].

2.3.3 Tuning the beamline

The tuning of the beam in WITCH starts with the beam ejected from REXTRAP. This tuning has to be done properly as otherwise it is almost impossible to obtain high efficiency for the transport further down the beamline. Table 2.2 gives an overview of typical voltages for the REXTRAP electrodes used for WITCH operation together with the simulated values [Del04]. Subsequently the tuning of the WITCH beamline elements starts. Generally as a fist step, one tries to get the beam from one diagnostics to the other by tuning the optical elements just in front of the detector. This method has only low precision since small deviations of the beam from the ideal path are not easily seen as the detector is very close. Once the beam arrives to a detector further downstream, preferably as far away as possible, one can go back to tuning elements early on in the beamline. Because the detector is now much further downstream the tuning becomes much more sensitive. This is illustrated in Fig. 2.6 for the tuning of HBEINZ01. This procedure can then be repeated several times in order to obtain a well tuned beam. During this procedure one attempts to avoid as much as possible asymmetric settings in the different steering elements in order to obtain a straight beam. By now the first step is often skipped because rough tuning values are known from previous tunings. Table 2.3 lists tuning voltages for the horizontal beamline and table 2.4 does the same for the vertical beamline.

For some of the beam optical elements it is important not only to look at the element itself but also at the elements that steer the beam in the same

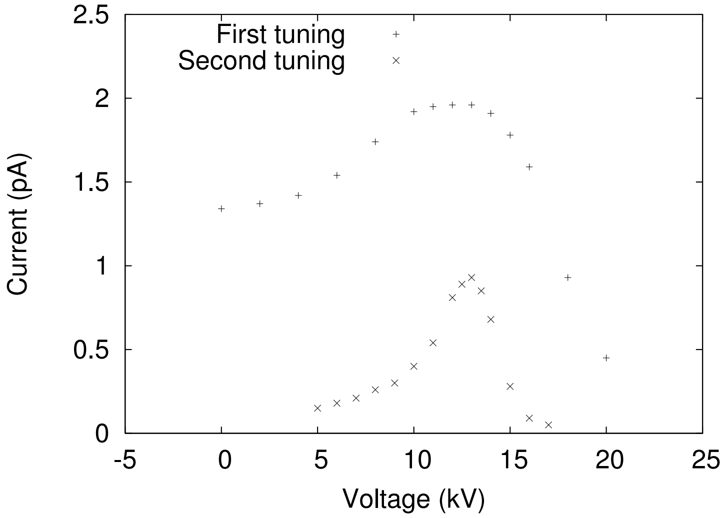

Figure 2.6 – *The sensitivity of the tuning of the HBEINZ01 electrode during the first rough tuning on HBFCUP03 and the second tuning on VBFCUP03. (The overall difference in current between the first and second scan is caused by a reduced current from the REXTRAP source for the second scan.)*

Name	Voltage (V) (sim) [Del04] (60 keV)	Voltage (exp) (V) (30 keV)
HBKICK01L	-2200*	-1220
HBKICK01R	2200*	1220
HBSTEE01U	0	0
HBSTEE01D	0	0
HBBEND01L	-4372*	-2090
HBBEND01R	4372*	2090
HBEINZ01	11500	12900
HBKICK02U	-2200*	-1260
HBKICK02D	2200*	1260
HBSTEE02L	0	0
HBSTEE02R	0	0
HBBEND02U	-4372*	-2185
HBBEND02D	4372*	2185

Table 2.3 – *Overview of all beam optical components of the horizontal beamline and the simulated and experimental voltages for each component for a 30 (60) keV ion beam.*
**Note that these voltages differ from the ones given in Ref. [Del04] following new simulations of the kickers and benders.*

Name	Voltage (V) (sim) [Del04] (60 keV)	Voltage (exp) (V) (30 keV)
VBSTEE01D	0	0
VBSTEE01U	0	0
VBSTEE01L	0	0
VBSTEE01R	0	0
VBRETA01	40000	0
VBPDT01P	52000	21000
VBPDT01N	-8000	-9150
VBRETA02	-2500	-4200
VBDRIF01	-2000	-3900
VBDRIF02	-1500	-1900
VBSTEE02D	-1500	-1900
VBSTEE02U	-1500	-1900
VBSTEE02L	-1500	-1900
VBSTEE02R	-1500	-1890
VBDRIF03	-1500	-1900
VBEINZ01	-1500	-1200
VBDRIF04	-400	-1400
VBSTEE03D	-1500	-1560
VBSTEE03U	-1500	-1560
VBSTEE03L	-1500	-1500
VBSTEE03R	-1500	-1480
VBDRIF05	-1500	-1700
VBDRIF06	-1500	-1300
VBSTEE04D	-1500	-380
VBSTEE04U	-1500	-380
VBSTEE04L	-1500	-380
VBSTEE04R	-1500	-380
VBDRIF07	-1500	-300
VBDRIF08-11	-1500	-200
VBDRIF12	-1500	0

Table 2.4 – *Overview of all beam optical components of the vertical beamline and the simulated as well as experimental voltages for a 30 (60) keV ion beam.*

or opposite direction or that re- or de-focus the beam before or after. Prime examples of this are the kicker and bender combinations: if the kicker voltage is changed, the bender voltage also has to be changed and for each kicker voltage a new optimum in the bender voltage can be found. There is however only one ideal combination. This combination can best be found by making a *2D* scan in which all possible combinations are scanned and the optimal one is selected.

Together with a more complete understanding of the diagnostics MCP's and the new position sensitive MCP's, both of which will be discussed in chapter 3, this systematic way of tuning has greatly improved the efficiency of the beam transport between REXTRAP and the WITCH cooler trap. A list of efficiencies is shown in table 2.5 where the comparison to previous efficiency values is also made [Koz06]. Overall a gain of a factor of 10 to 100 has been made compared to the year 2004, and a lot of progress is still foreseeable in this field.

The overall tuning efficiency of the system can be estimated by dramatically decreasing the beam intensity coming from REXTRAP and shooting the beam through the whole system to the main detector. By adjusting the collection time of REXTRAP the number of particles going into the WITCH system can be estimated. The intensity is decreased so much that only a few counts can still be detected with the main detector. Using this method a tuning efficiency of 10-20% has been shown.

2.4 Traps

To store the radioactive ions in a scattering free environment, WITCH uses a Penning trap, named after the Dutch physicist F.M. Penning. In this trap, ions can be stored through the combination of a strong (9 T) magnetic field and a weak electric field. In fact, the system uses not one but two of these traps. A first, referred to as the cooler trap, is used to cool and mass selectively purify the ion cloud that is obtained from ISOLDE through REXTRAP. The second trap, the decay trap, serves as the real source for the experiment. In this trap a cloud of up to 10^6 radioactive ions can be stored for several seconds without significant losses. As it is instructive to first give an overview of the working principle and possibilities of Penning traps (see chapters 5 and 6), a detailed description of the WITCH Penning trap system will be postponed to chapter 7.

2.5 Spectrometer

Directly measuring the energy of the recoiling ions is not a trivial task. While relatively simple energy sensitive detectors exist for high energy ions, electrons or γ's, no such simple detector is available for ions with a kinetic energy of the order of 100 eV. For this reason the WITCH experiment uses a somewhat bulkier retardation spectrometer. This type of spectrometer is also used for precision neutrino mass measurements [Lob85, Pic92, Kat04] and in the aSPECT system where it is needed to measure the energy spectrum of the recoiling proton originating from the decay of the neutron [Glu05]. In the spectrometer the

Parameter	Ideal	2004	2007
Horizontal beamline, ϵ_{HBL} (%)	100	100	100
Pulsed Drift Tube, ϵ_{PDT} (%)	100	8	50÷100
Injection into magnetic field, ϵ_{inj} (%)	100	1÷10	∼20
Cooler trap, ϵ_{cool} (%)	100	∼45	∼45
Transfer between traps, ϵ_{trans} (%)	100	∼80	∼80
Storage in decay trap, ϵ_{decay} (%)	100	100	100
Fraction from trap to spectrometer (solid angle, trapped after decay), $\epsilon_{2\pi/4\pi} \cdot \epsilon_{tad}$ (%)	40	/[a]	/
Shake-off to 1^+ charge state for β^+, ϵ_{s-0} (%)	∼10[b c]	/	/
Transmission through spectrometer, ϵ_{spectr} (%)	100	/	/
MCP, ϵ_{MCP} (%)	60	52.3	52.3
Total efficiency (%)	∼1	$\sim 0.6 \cdot (10^{-3} \div 10^{-2})$	∼0.1

Table 2.5 – *Overview of the efficiencies of the different parts of the WITCH system. Ideal and 2004 data are taken from Ref. [Koz06].*

[a] These efficiencies have not been studied experimentally yet. The ideal value is used for the total efficiency.
[b] This can be increased to ∼80% if a β^- decaying isotope is used.
[c] This number is only an estimate since the charge state distribution after the decay of $^{35}Ar^+$ is not known.

kinetic energy of a particle is probed by applying an electrostatic barrier and detecting the number of particles that can cross this barrier. A particle with kinetic energy T along the retardation electric field and charge q can only cross a barrier of height U_r if

$$T > q \cdot U_r. \tag{2.1}$$

Although the principle of the retardation spectrometer is simple, the implementation is not. The ions that recoil after their decay originate from the high magnetic field region of the Penning traps. As a consequence they do not only have an axial velocity component but also a radial one. This radial velocity component can not be probed by the retardation principle. Therefore a conversion of radial into axial velocity has to be made to be able to probe the full kinetic energy. This is realized by making an adiabatic transition from the high magnetic field region into a low magnetic field region. The ratio of the radial kinetic energies $T_{1,2\perp}$ in the two magnetic field regions $B_{1,2}$ is then given by [Jac75]

$$\frac{T_{1\perp}}{T_{2\perp}} = \frac{B_1}{B_2}. \tag{2.2}$$

For the specific case of the WITCH experiment the first magnetic field region is the 9 T field of the Penning traps and the second is in the spectrometer region where a field of 0.1 T is applied. In this way almost 99% of the radial kinetic energy can be converted into axial energy.

After the ions with sufficient energy have crossed the retardation barrier in the analyzing plane, they are picked off the magnetic field lines and focussed onto the detector. This is accomplished by using electrostatic acceleration electrodes instead of another magnetic field like is done in Ref. [Lob85, Pic92, Kat04, Glu05]. The full implementation of the retardation spectrometer is shown in Fig. 2.7.

The voltages on the spectrometer are set by a voltage supply that can sweep its output voltage between 0 and 500 V in maximally 40 steps. The trigger for changing the retardation voltage is generated by the Data Acquisition system. This ensures that the retardation voltage on the spectrometer can later be inferred from the measurement bin in time domain as it is stored by the Data Acquisition card that is connected to the detector. More details concerning this supply can be found in Ref. [Lin04].

2.5.1 Response function

A detailed analysis of the response function of the retardation spectrometer can be found in Ref. [Del04]. This has shown that the main contribution to the shape of the spectrometer response function, accept for an overall shift to lower energy, is the temperature of the ion cloud inside the decay trap. For a temperature T and recoil energy T_R the response function is Gaussian with

$$\sigma = \sqrt{2 T_R k_B T} \tag{2.3}$$

with k_B the Boltzmann constant. Even at room temperature this results in a response function at the endpoint of the ^{35}Ar recoil spectrum ($T_R = 452$ eV)

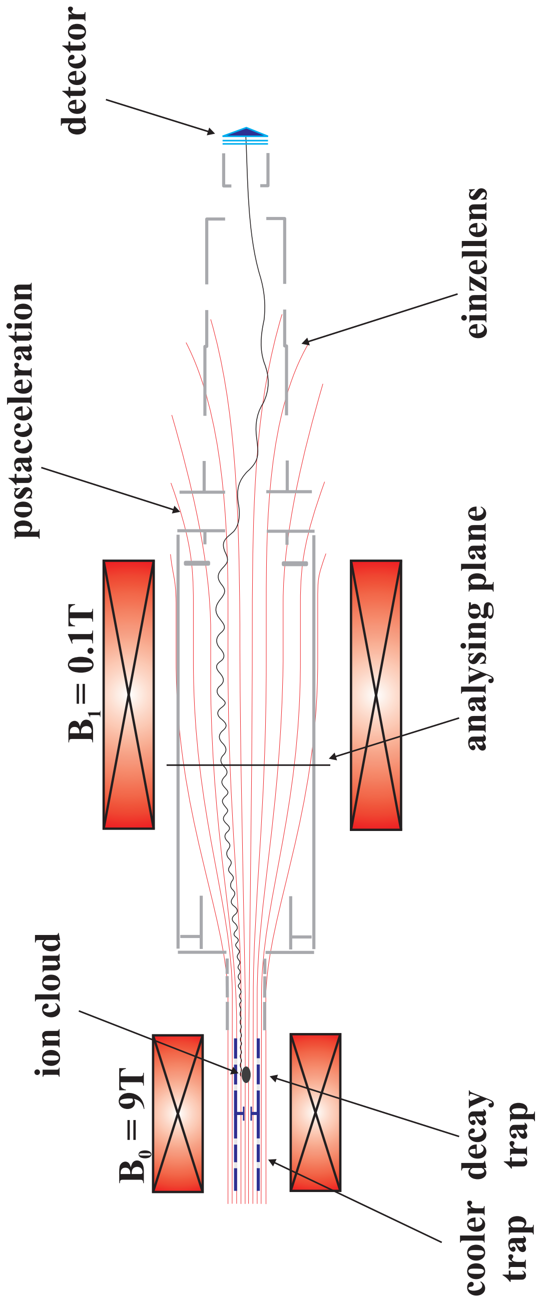

Figure 2.7 – *Drawing of the implementation of the retardation spectrometer in the WITCH system.*

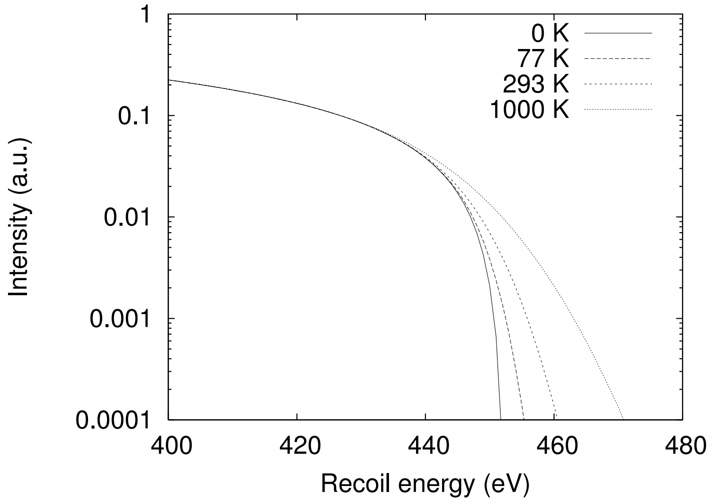

Figure 2.8 – *Influence of the broadening of the spectrometer response function on the shape of the upper part of the integral recoil spectrum of* ^{35}Ar *as a result of the thermal motion of the ions in the decay trap. For the 0 K curve an ideal monoenergetic response function was assumed.*

with $\sigma = 4.8$ eV. The effect of this on the shape of the integral recoil spectrum of ^{35}Ar is shown in Fig. 2.8. During a measurement the temperature of the ion cloud can be deduced from the width of the EC peak provided sufficient counts are present in this peak. If the cloud would not be in thermal equilibrium during the measurement it could, however, be that the width of the spectrometer response function is not constant throughout the measurement. This point will have to be investigated in more detail experimentally. Note that in addition it is possible that the reduction of number of ions present in the decay trap due to the radioactive decay, influences the response function. Also this will have to be studied in detail experimentally and through simulations.

The response function could be improved by cooling the traps and the buffer gas. Such system has already been developed [Web03] and the applicability for the WITCH system is under investigation.

2.5.2 Systematic effects

A full description of systematics effects caused by the implementation of the spectrometer has been given in Ref. [Del04] and will not be repeated here. However, one effect that needs to be mentioned here as it is of special importance for the rest of the text is the so called *trapped after decay* fraction.

As mentioned before the recoiling particles can have a high radial component in their velocity while they are in the high magnetic field region. In addition the Penning trap itself also has an electric field to contain the ions. This prevents ions with very small axial velocity from escaping the trap and thus from reaching the spectrometer. The fraction of ions that does not remain trapped after decay is given by

$$\epsilon_{tad} = 1 - \sqrt{\frac{qU_C}{T_r}} \tag{2.4}$$

with U_C the voltage difference between the center of the trap and the place with the highest potential between the center of the trap and the entrance of the spectrometer. As can be seen the fraction of trapped ions is lowest when the trapping potential is as shallow as possible. This has to be accounted for when setting up the decay trap for an experiment. As the chance for a recoiling particle to stay trapped in the decay trap is dependent on the particle's energy and thus influences the shape of the measured recoil energy spectrum, this effect has to be well investigated both with simulations and in the setup itself.

2.6 Detector

WITCH requires a detector that can detect low energy ions with high efficiency, good timing resolution and at high count rates. For this purpose an MCP detector was selected. This type of detector can detect low energy ions with an efficiency of ~50% at count rates of the order of 1 MHz. Although the principle of the experiment only requires a counting detector it is advantageous to obtain more information from the detector that could provide insight into possible systematic effects influencing the spectrum measurement. Important additional information that can be obtained is the position of each ion on the detector. This would for instance allow one to check that all recoil ions fall within the detector. Especially during the early phases of the experiment's operation this could provide crucial information on how to improve or alter the system to obtain the necessary precision for a final measurement.

To accomplish this, an MCP detector with resistive anode, identical to the one described in Ref. [Lie05] (DLD40), is used. This detector has an active area of 47 mm diameter and a position resolution of 110(26) μm has already been achieved [Lie05]. Note that such high position resolution is not required at WITCH since the position information of the detector is not directly used for the analysis of the spectrum shape. The efficiency of this detector has been shown to be 52.3(3)% [Lie05]. The front side of the detector is at a potential of -7 kV to ensure that all ions are accelerated towards the detector and that the detection efficiency does not depend on the ion's initial kinetic energy.

The timing signals from which the position information can be obtained, are digitized through a 4-channel TDC (Time to Digital Convertor). The data are read into the Labview computer program through a Camac interface. Simultaneous with the position encoding, the height of the MCP signal is also processed by a QDC (charge to Digital Convertor) in the same Camac electronics crate. This enables us to obtain both the position and the pulse height for a single event. The disadvantage of the system in its present form is the rather long time needed for the time and charge digitization and for sending the data to the computer. As this takes about 500 μs, not all events detected by the

MCP can be processed in this way.

An alternative for this detector would be a *channeltron* detector [Yaz06]. This detector has as main advantages a very high detection efficiency (close to 100%) and the very high count rate it can handle (10^8 counts/sec is possible). An important disadvantage is that no position information can be obtained from the detector itself.

2.7 Data Acquisition

The current data acquisition system (DAQ) consists of two independent and parallel branches:

1. A first part that is used purely for counting events from the main MCP detector. This is done using a Multi-Channel Scaler that stores the number of detected events per time bin. The time bins are synchronized with the spectrometer power supply so that they can later be converted into energy bins.

2. The second part that stores as much information about a single event as possible: the position on the MCP, the pulse height of the detector, the time when the event occurred and the number of the event since the start of the counting. The latter is necessary since at the present time this part of the acquisition is actually too slow to store all events.

A detailed overview of this DAQ system is given in Fig. 2.9. By splitting the DAQ in this way one can measure the recoil spectrum with the full ion intensity as detected by the MCP and obtain position and pulse height information for some fraction of the events. In the future a faster DAQ system, which is capable of a full event-by-event storage of all information, will have to be conceived. In this respect, it could be interesting to have a system that can also store the shape of the MCP signal through a fast digitizer board [DaC05]. Such a system would make it possible to separate multiple hits and possibly allow the separation between ion and β-particle signals (see section 2.11). More details about the DAQ system of the experiment can be found in Ref. [Lin04].

2.8 Experimental cycle

The WITCH experiment does not work with a continuous beam of ions but with a pulsed beam. Therefore the same experimental cycle is repeated for each individual ion pulse. A schematic view of the timing cycle of the experiment is shown in Fig. 2.10. The whole cycle is triggered by the proton pulse hitting the ISOLDE target. After this, the cooling and accumulation in REXTRAP starts. The first step in the cycle of WITCH is the triggering of the beam-gate and the PDT. Once this done the ions are injected into the traps and the whole trap cycle can start. This cycle is discussed separately in section 7.2. For now it is sufficient to note that the measurement can only start after the transfer of the ions from the cooler trap into the decay trap. During the time the ions

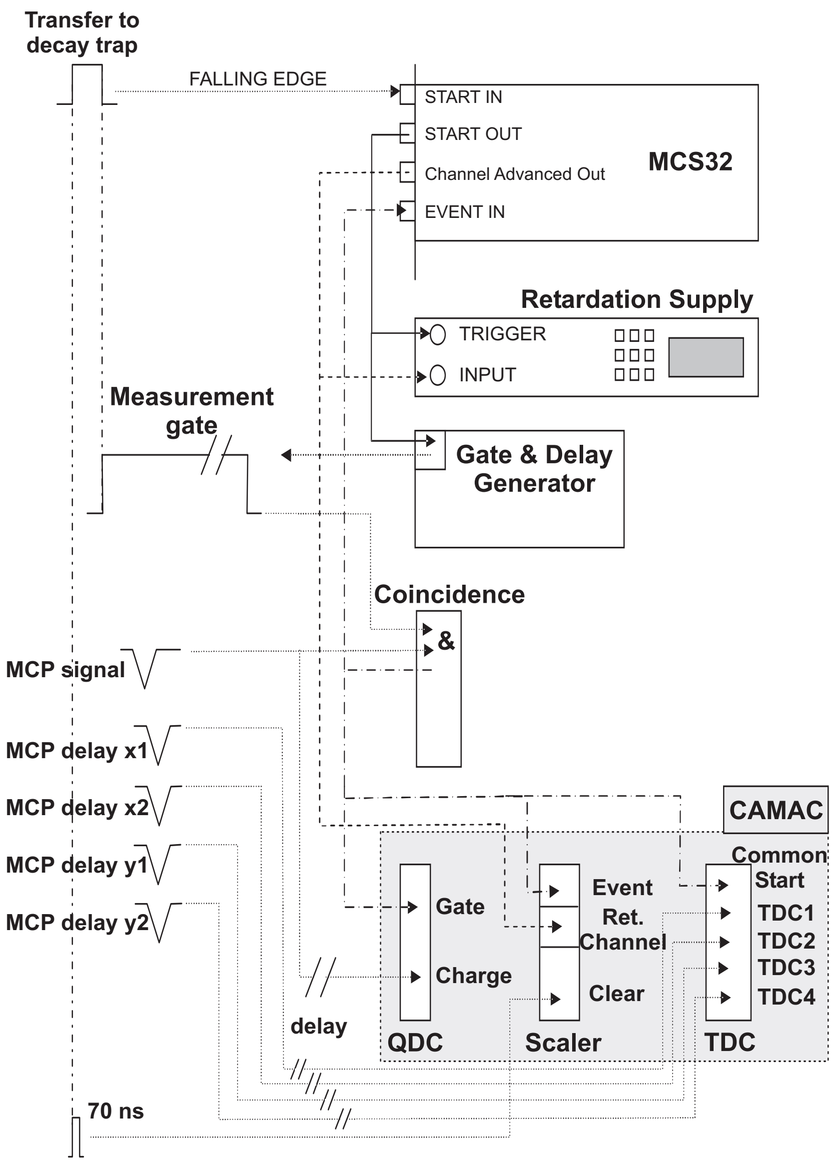

Figure 2.9 – *Detailed overview of the data acquisition system at it is used for the moment at WITCH.*

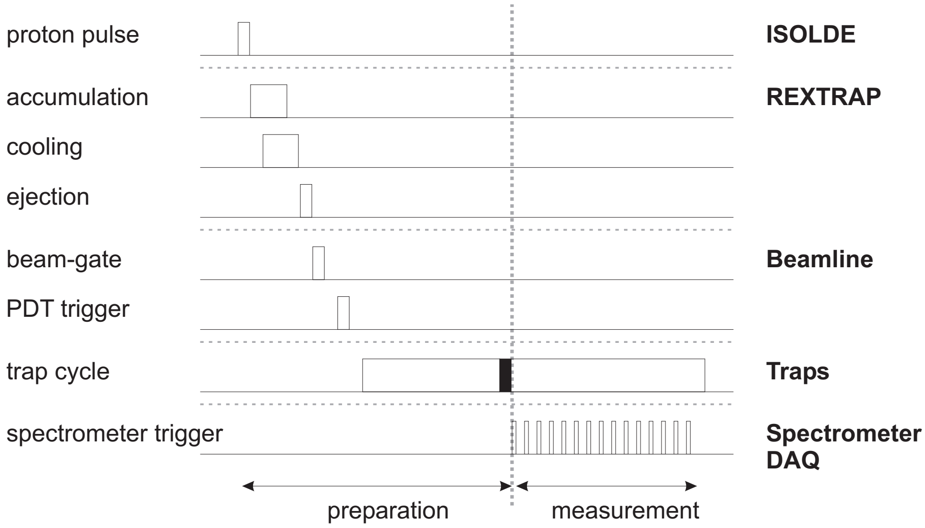

Figure 2.10 – *Overview of the experimental cycle of the WITCH setup. The moment of transfer from the cooler trap into the decay trap is indicated in black. Drawing is not to scale.*

are in the decay trap the real measurement is performed and the energy of the recoiling ions is determined.

For scanning the retardation potential two possibilities exist:

- The potential can be scanned from 0 to the maximum during each cycle (shown in Fig. 2.10).
- The potential can be changed between cycles and it is kept constant during each cycle.

The first option has as advantage that no extra normalization of the number of ions that is present in the traps is needed. Disadvantages are that the spectrometer voltage has to be switched during the measurement, a procedure that may induce unwanted effects, and that the measured integral recoil spectrum has to be corrected for the half-life of the decaying isotope, which thus has to be known with high precision. The second option can only be used if the trap load can be properly normalized. For the moment this is not yet possible and therefore the first option is used. In the future this will become possible thanks to the installation of an extra detector in the system. The details of this detector will be discussed in section 7.4. After the measurements, the traps can again be emptied, a procedure that is further discussed in section 7.2.

2.9 Isotope candidates

Thanks to its location at the ISOLDE mass separator, the WITCH experiment has a wide range of radioactive isotopes at its disposal. This allows us to put stringent requirements on what isotope to use for each specific physics goal. Some requirements are determined simply by the principle of the system, and are the same for a whole range of experiments:

1. The **production yield** at ISOLDE [Isolde] should be sufficiently high. Due to the fact that the WITCH experiment does not rely on event-by-event reconstruction of the decay events it relies heavily on high statistics. The production yield should preferably be of the order of 10^6 particles/s or higher.

2. The **half-life** of the isotope should be of the order of seconds. Since, for each cycle, the traps can only be loaded by approximately 10^6 particles, it is important that a large fraction of the particles decays, again to allow sufficient statistics to be taken in a reasonable amount of time. The lower limit for the half-life is determined by the time needed to prepare the ion cloud before it is transferred into the decay trap and is of the order of 0.2 s.

3. Minimal **isobaric and isomeric contamination** should be present in the ISOLDE beam. Although isobaric mass selective purification can be performed in either REXTRAP or in the WITCH cooler trap, the contaminants would fill up either trap, limiting the amount of *useful* ions that can be trapped. In addition, long lived contaminants, even if they can be removed from the beam in either trap, could contaminate the system for a long time with their radioactivity.

4. An isotope with low **ionization potential** is preferred as this limits problems with neutralization in both REXTRAP and the WITCH cooler trap. Note that this is not a strict requirement but rather a preference.

For the determination of the β-ν-angular correlation coefficient a a few additional requirements have to be taken into account:

1. If one wants to investigate the possible presence of a Scalar term in the weak interaction Hamiltonian, one should select a decay that has a high and well known Fermi component in the decay.

2. The endpoint of the recoil energy spectrum should be of the order of 100 eV to maximally $\sim$500 eV to enable a precise measurement using the retardation spectrometer as it is now.

3. To avoid contamination of the spectrum an isotope with a clean decay spectrum should be selected as all decay branches give rise to different recoil spectra and these all overlap in the final spectrum. Most importantly the upper part of the recoil spectrum should be clean of any other decay branches. This also excludes additional branches that have consequent γ-decays.

4. The daughter of the decaying isotope should be stable or sufficiently long lived in order not to disturb the measurement. Note that also here ele-

ments with a half-life of the order of months/years would contaminate the system for a long time.

5. When using an isotope that undergoes β^+-decay, the EC peak can be used to check the response function of the system during the measurement. On the other hand with a β^+-decaying isotope one has to rely on *shake-off* to obtain a recoiling ion, a process that only has a roughly 10% efficiency. For a β^--decay about 80% of the recoiling particles have a 1^+ charge state, but no EC peak is present.

A non-exhaustive list of possible isotope candidates is given in Table 2.9. In this list only $0^+ \rightarrow 0^+$ superallowed transitions and mirror nuclei that have a high Fermi contribution in their β-decay ($|\rho|^2 < 0.1$) with 0.2 s$< t_{1/2} <$ 10 s are shown.

From this list ^{35}Ar has been selected as the prime candidate for a measurement of the β-ν-angular correlation coefficient a, mostly due to its high production yield at ISOLDE. The decay scheme of ^{35}Ar is shown in Fig. 2.11.

2.10 Data analysis procedure

The most convenient way to analyze data from a technically complex experiment like WITCH is probably through the use of Monte Carlo simulations. This type of analysis consists of several steps:

- Generate a set of spectra with *infinite* statistics for the different parameters to be fitted, through Monte Carlo simulations describing the experiment.
- Perform a Maximum-likelihood fit of the experimental spectrum to the generated spectra. This gives us the fitting values for the experimental spectrum.
- To estimate the statistical errors on the fitted parameters, a large set of additional spectra can be simulated with the fitted parameters as input and comparable statistics as the initial experimental data set. All these additional spectra are then fitted to the spectra with *infinite* statistics and from the distribution of the fit values the statistical error bars can be determined.
- The systematical errors can be obtained by making small changes in the experimental parameters that are included in the simulation routine and looking for their influence on the final result.

The main difficulty in this analysis procedure lies in the full description of the experiment in the simulations. For the case of the WITCH experiment the Monte Carlo simulations should be full particle tracking simulations of the recoiling ions and the β-particles. Maybe the most difficult part in this respect is determining the correct starting conditions. This requires exact knowledge of the properties of the ion cloud inside the decay trap. Some simulations that have already been performed in this respect will be presented in chapter 6.

mother	state	$t_{1/2}$ (s)	yield (ions/μC)	daughter	state	$t_{1/2}$ (s)	ΔE (MeV)	$T_{R,max}$ (eV)	P_{EC} %	BR %	a_{SM}
^{26}Al	isom	6.345	$6.8 \cdot 10^4$	^{26}Mg	gs	stable	4.23255(17)	280.7	0.082	> 99.997	1
	gs	$7.4\ 10^5$y	*		exc	476 fs	2.20	53.2		97.3	
^{34}Cl	gs	1.527	$1.3 \cdot 10^3$	^{34}S	gs	stable	5.49178(20)	387.9	0.080	> 99.988	1
	isom	1920	$2.2 \cdot 10^5$		exc	325 fs	3.511	138		28.5	
^{38}K	isom	0.924	$6.3 \cdot 10^6$	^{38}Ar	gs	stable	6.044440(11)	429.1	0.085	> 99.998	1
	gs	458	$7.9 \cdot 10^7$		exc	470 fs	3.7456	144.2		99.8	
					gs	stable	5.9131	408.9		<0.6	
^{42}Sc	gs	0.681	*	^{42}Ca	gs	stable	6.42563(38)	444.2	0.099	99.9941(14)	1
	excit	61.7	$1.5 \cdot 10^3$		exc	250 fs	3.8528	139.5		100	
^{46}V	gs	0.423	0	^{46}Ti	gs	stable	7.05071(89)	496.6	0.101	$99.9848^{+0.0013}_{-0.0042}$	1
^{50}Mn	gs	0.283	$7.6 \cdot 10^5$	^{50}Cr	gs	$1.8\ 10^{17}$y	7.63243(23)	542.3	0.107	99.9423(30)	1
	isom	105	*		exc	1.25 ps	4.6983	185.6		8.0	
^{33}Cl	gs	2.511	$1.4 \cdot 10^2$	^{33}S	gs	stable	5.5826(4)	414.5	0.074	98.45(14)	0.887(3)
					exc	1.17 ps	4.742	287.1		0.48	
^{35}Ar	gs	1.775	$4.3 \cdot 10^7$	^{35}Cl	gs	stable	5.9661(7)	452.6	0.072	98.36(7)	0.903(2)
					exc	150 fs	4.7458	271.3		1.23	

Table 2.6 – *Table of interesting isotopes for a β-ν-angular correlation coefficient measurement with the WITCH experiment. Only $0^+ \rightarrow 0^+$ superallowed transitions [Har05] and mirror nuclei [Tan07] that have a high Fermi contribution in their β-decay ($|\rho|^2 < 0.1$) and with $0.2s < t_{1/2} < 10s$ are included.*
**No information available on the same target [Isolde].*

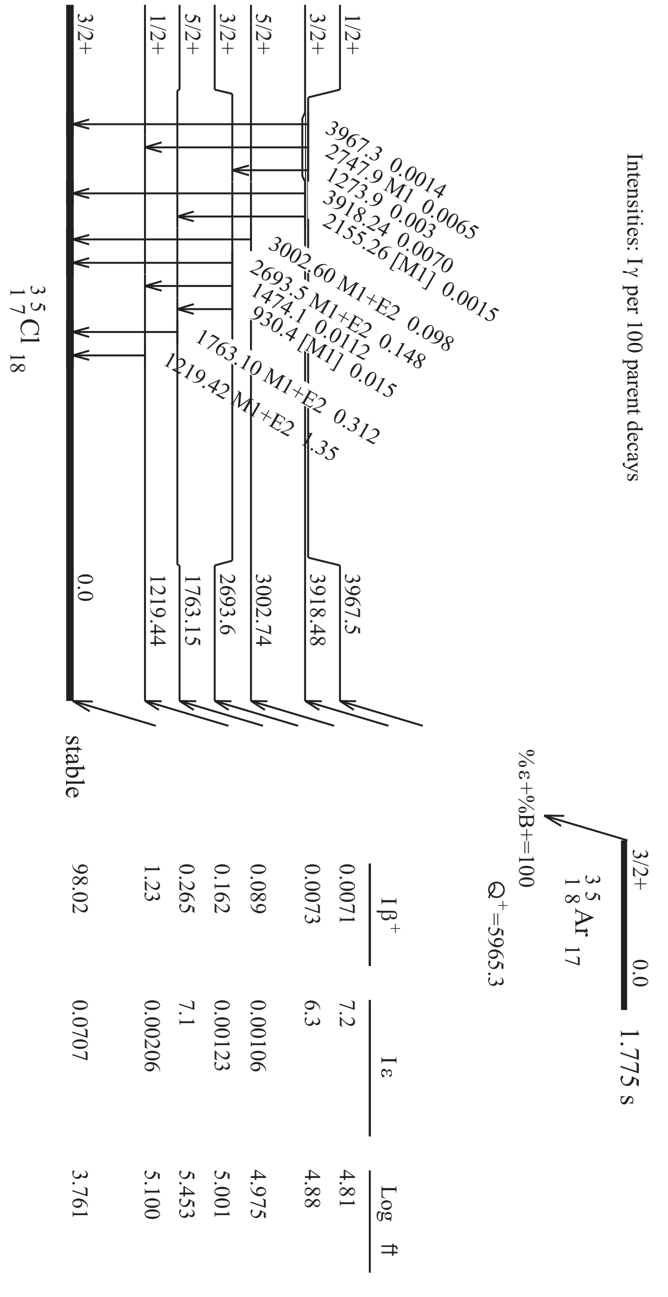

Figure 2.11 – *Decay scheme of* ^{35}Ar *(taken from Ref. [NNDC]).*

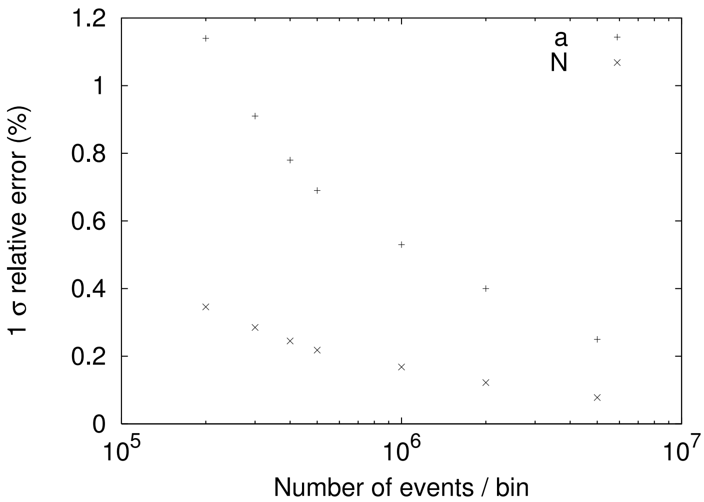

Figure 2.12 – *Simulated obtainable precision as a function of the number of particles.*

2.11 Achievable precision

The precision that can be achieved on the β-ν-angular correlation coefficient a from a measurement on ^{35}Ar can be estimated by running the third step of the afore mentioned analysis procedure. As no full particle tracking simulation routine that takes into account all known effects exists as yet for the WITCH-experiment, the simulations were done for a very much simplified and idealized system. In addition the width of the response function of the spectrometer was assumed to be exactly known and to correspond to a cloud at room temperature. The only free parameters in the fit where the β-ν-angular correlation coefficient a and the number of recoils N that went into the spectrometer. A plot of the obtainable precision under these assumptions as a function of the number of decays for ^{35}Ar is shown in Fig. 2.12. For this analysis the measurement started at 230 eV and proceeded in 25 steps of 10 eV. The number of events is quoted as the number of 1^+ charge state events reaching the detector per bin if the retardation voltage would be 0 V.

2.11.1 β background

Not only the recoiling ions will reach the detector, a number of β-particles emitted in the decay can also make it to the detector. As the energy of these β-particles is typically of the order of MeV for the isotopes of interest for WITCH, they will not be influenced by the retardation voltage. They thus provide a constant background (not taking into account the half-life of the decay) for the recoil spectrum. Although the solid angle of the detector as seen from the decay trap is quite small, the β-particles are, just like the ions, all focussed into the

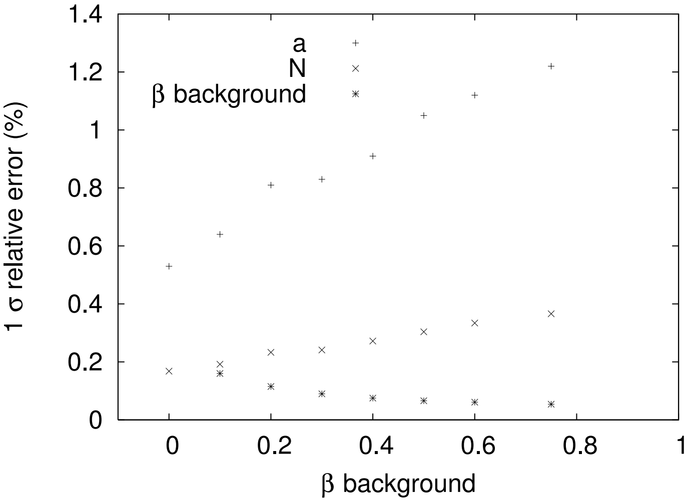

Figure 2.13 – *Simulated achievable precision for* 10^6 *ion events including a* β*-background.*

spectrometer by the high magnetic field present in the trap region. This causes a non-negligible amount of β-particles to reach the detector.

Simulations estimating this background have been performed in GEANT4 and have been extensively discussed in Ref. [Koz06] and Ref. [Koz05]. Here it is estimated that for every 10 000 recoil ions going into the spectrometer (β^+-decay) 1290 β-particles reach the detector. First experimental hints concerning the amount of β-particles detected by the recoil detector can also be obtained from the first recoil measurements performed with the WITCH system on ^{124}In. From these measurements, discussed in chapter 8, it can be estimated that for every 10 000 recoil ions reaching the detector without retardation about 1 000 β-particles reach the detector (β^--decay) suggesting that for a β^+-decay the ratio is actually closer to 1/1.

Although this β background does not influence the shape of the recoil spectrum, it does worsen the statistical precision that can be obtained from the measurement. To investigate the influence of this background on the precision that can be achieved a similar analysis was used as discussed above, but now a constant background was included and the contribution of this background was added to the list of parameters to be fitted. The precision that can be obtained for $N = 10^6$ decays and the same conditions as before as a function of the β-background contribution, given as fraction of the number of recoils N as it was defined above, is shown in Fig. 2.13.

It is clear that an increased background leads to a smaller obtainable precision or correspondingly a longer measurement time to obtain a certain precision.

2.11.2 Width of the response function

Although the width of the spectrometer response function influences the shape of the measured recoil spectrum, simulations on the precision that can be obtained for a cloud at 77, 293 or 1000 K show no effect of the ion cloud temperature on the achievable precision in the range tested. Note however that these simulations assume that the shape and width of the response function of the spectrometer are exactly known. If the temperature of the ion cloud is off by roughly 2% (i.e. estimated to be 293 K while in reality it is 299 K) the fitted value of a will differ by about 0.1% in the case of ^{35}Ar.

Chapter 3

Microchannel plates and beam diagnostics

In this chapter the article entitled *Microchannel plate response to high intensity ion bunches* is presented. It shows the results of a detailed investigation of saturation effects when bombarding microchannel plate detectors such as the ones used for the beam diagnostics with high numbers of ions. Later in this chapter additional improvements to the diagnostics system for the WITCH beamlines are discussed. These improvements in the understanding of the beam diagnostics and the beam diagnostics themselves, made it possible to obtain a much better tuning of the WITCH beamline system as mentioned in chapter 2 and therefore should be considered as one of the major steps that led towards performing a first measurement (see chapter 8).

Microchannel plate response to high intensity ion bunches

S. Coeck, M. Beck, B. Delauré, V.V. Golovko, M. Herbane, A. Lindroth, S. Kopecky, V. Yu. Kozlov, I.S. Kraev, T. Phalet, N. Severijns

K.U.Leuven, Instituut voor Kern- en Stralingsfysica, Celestijnenlaan 200D, B-3001 Leuven, Belgium

Published in: *Nuclear Instruments and Methods in Physics research A **557** (2006) 516-522*

3.1 Abstract

In this paper, we discuss the response of microchannel plate detectors (MCP's) to high intensity bunches of ions with typical lengths of a few hundred microseconds. A dedicated experimental set-up was developed to measure this behavior. The MCP operating voltage and the ion beam intensity appear to be important factors in the saturation behavior of the detector. The results of the measurements are extended to the more realistic situation of TOF spectrum measurements for beam diagnostics purposes by using two consecutive pulses impinging on the detector in a time interval much shorter than the recovery time of the detector. A new method for measuring the recovery time of the MCP detector is proposed and results are compared to simple estimates from an RC model approach. Finally the results of the measurements are compared to Monte-Carlo simulations which use a reservoir model to simulate the MCP's behavior.

3.2 Introduction

Over the last years microchannel plate detectors (MCP's) have become rather popular in nuclear physics applications, not only as high precision detectors for detecting single ion events [Bec03, Ban05, Lie05, Bol96] but also in beam diagnostics applications [Bec03]. As single event detectors, MCP's have already been studied in great detail in a number of publications [Gao84, Hel85, Bre95, Obe97]. For beam diagnostics applications the position sensitivity of this type of detector is often used in combination with phosphor screens to monitor beam sizes and locations. However, because of their excellent timing properties, MCP's can also be used to monitor for instance the exact time structure of ion bunches. In order to achieve good accuracy in this case one has to account for saturation effects that appear when bombarding an MCP-type detector with high intensity ion bunches, which can alter the structure and intensity of the MCP signal. Not accounting for these effects could lead to misinterpretations of for instance pulse structures, TOF's, intensities, relative intensities of multiple pulses following each other with short time intervals, beam profiles when using a segmented anode detector, etc. It is therefore important to gain knowledge of these effects and more importantly on how to avoid them, prior to the use of MCP detectors for the above mentioned purposes.

3.3 Experimental set-up

Measurements of the response of an MCP to a bunch of ions were performed in a simple set-up which enabled control over many parameters. The set-up consists of four major parts: a cross beam ion source (Pfeiffer), the supply of which has been modified to be able to generate ion pulses, a metallic collimator which permits to determine the number of channels of the detector that are being used, two metallic grids to attenuate part of the ion beam and monitor the current produced by the ion source and, finally, an MCP detector (type MCP-MA25,

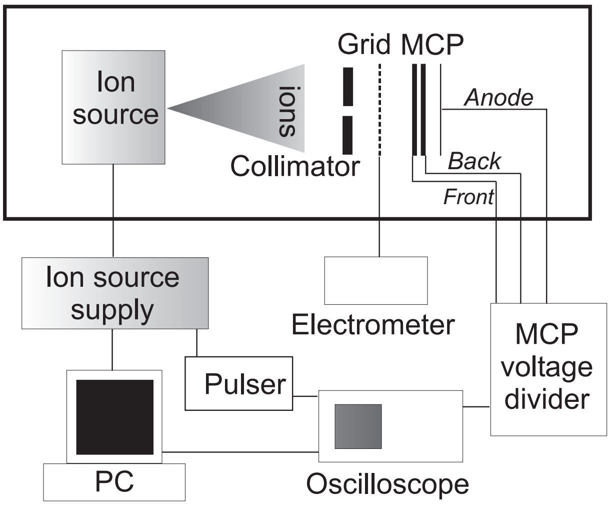

Figure 3.1 – *Schematic overview of the set-up used to measure the response of the MCP to high intensity ion pulses. The pulses are generated by an ion source which is controlled via the computer. The trigger for the pulses is given by a TTL pulse generator which also triggers the oscilloscope. The signal from the MCP is transferred to this oscilloscope via the MCP voltage divider and is then read by the computer via a NI Labview interface. The current on the grid was read by a Keithley 6512 Programmable Electrometer.*

manufactured by Delmar Ventures [Del], with an L/d ratio of 46). All signals from the MCP where first read by the oscilloscope where an averaging over 128 signals took place. This averaged signal was then read by the computer via a National Instruments Labview interface which summed 10 of these averaged signals before saving the data. The spectra presented here are thus each an average over 1280 ion pulses. An overview of the experimental arrangement, together with a schematic of the electronics used to control the experiment and to gather the data, is given in Fig. 3.1.

The cross beam ion source was used to ionize the rest gas inside the vacuum chamber thus creating a beam of positively charged ions with an energy of 150 eV. Pulsing was achieved by raising the voltage on the lens electrode inside the source above the ions energy level and periodically lowering it to a predefined value. The repetition rate of the ion source was set to 5 Hz in order to avoid saturation of the detector by consequent pulses. The metallic grids used had a 10% transmission rate with 1000 lines/inch and 25 μm spacing between the lines. A stack of two grids was inserted at 5 mm from the front of the MCP in order to avoid saturating it too much but still allowing the current to be read with good precision. The transmission of this stack was measured to be around 2% using a laser and a photodiode. During all measurements the current delivered by the ion source was kept stable to better than about 5%.

A collimator of 1 cm thickness was inserted at about 2 cm from the front plate of the MCP to control the number of MCP channels that was actually used. Due to the insertion of the metallic grid, which is at ground potential, between the collimator and the detector, the potential of the MCP's front face doesn't penetrate the collimator opening such that any (de)focussing effects are avoided. Thus the size of the beam spot on the detector is solely determined by the opening of the collimator. This was confirmed by simulations with the SIMION program [Dah00]. The beam from the ion source was defocussed and the distance between ion source and collimator was chosen sufficiently large (viz. 12 cm) to ensure a homogenous illumination of the detector. The number of channels used for a certain beam spot with radius r is obtained as

$$N = \frac{a_{open} \cdot \pi r^2}{\pi D^2} = \frac{2\pi}{\sqrt{3}}(\frac{r}{p})^2 \tag{3.1}$$

where a_{open} represents the open area fraction, i.e. the percentage of the MCP surface that is actually covered by the channels [Fra83], D the channel radius and p the channel pitch. The beam spot used here always had a radius of 2 mm. The MCP used is a Chevron type assembly of two MCP plates with a metallic anode. The channel radius D is 5 μm and the pitch p is 12 μm, corresponding to 17 500 channels being used for a 2 mm radius beam spot.

A special MCP voltage dividing scheme was used to permit separate control of the voltage on the front of the MCP (-3 kV for the measurements presented here) and the back of the detector. The voltage on the front of the MCP also determines the energy of the ions when striking the detector, since their initial energy is only 150 eV. The electronic scheme of this voltage divider is shown in Fig. 3.2.

The different components of the set-up were installed on an optical table to enable a precise positioning and easy interchange of all elements. The whole structure was inserted into a vacuum chamber which was pumped to a pressure of around $1 \cdot 10^{-6}$ mbar with a turbo molecular pump.

3.4 Experimental results

In order to quantitatively analyze the signals produced by the MCP detector when bombarding it with a bunch of ions, the data were fitted with the following equation

$$y = y_0 + A(e^{-\theta(t-t_0)} - e^{-\lambda(t-t_0)}) + B(e^{-\theta(t-t_0)} - e^{-\mu(t-t_0)}). \tag{3.2}$$

In this formula the first term represents a dc offset of the signal, the second term contains the difference of two exponential functions and reproduces the peaked shape of the signal and the third term was added to more accurately reproduce the tail of the peak which seems to decrease more slowly than described by the second term alone, especially for the highly saturated signals. This formula was found to reproduce the shape of all data very well. Although the values of the parameters (except for y_0) often have large error bars and can

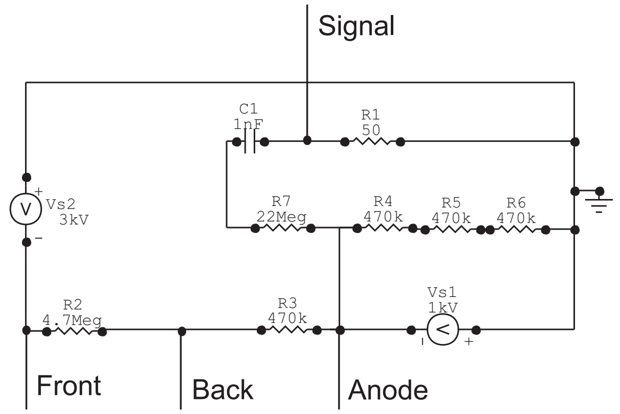

Figure 3.2 – *Electronic scheme for the MCP voltage divider which allows separate control over the voltages on the MCP front and the MCP back (thus determining the voltage difference over the MCP plates). Front, Back and Anode indicate the respective connections to the detector (see figure 3.1). Signal indicates the place where the actual signal is read.*

differ substantially when the parameter initializations in the fitting routine are changed, the combination of all parameters always reproduces the shape of a given pulse very well. A few examples of different pulse shapes that were fitted with this equation are shown in Fig. 3.3 (fit values and error bars are given for illustrative purposes only).

The fact that the front edge of the signal is not very sharp may be due to the slow lowering of the ion source lens voltage and is possibly not a real MCP related effect. It was checked that this slow pulse rise time is not an artefact of the used pick-up circuit by observing single ion pulses for which a pulse rise time in the order of several nanoseconds was observed.

3.4.1 Incoming beam intensity

The intensity of the incoming ion pulse is of course of major importance if one wants to study MCP saturation effects. In Fig. 3.4 the fitted shape of seven ion pulses with different beam intensities are shown for an MCP operating voltage of 1682 V (-3 kV on the front and -1.15 kV on the anode connections of the voltage divider described above). For the lowest intensity the detector is nearly unsaturated, i.e. the signal looks like the expected block signal, while with increasing intensity of the incoming ion pulses the signal is distorted from this square shape and becomes peaked.

It is important to note here that, contrary to what one might expect, it is not the absolute number of particles hitting the detector that determines the pulse shape, but the beam current. This follows from the observation that two pulses with different lengths but with the same beam current have the same shape, as is illustrated in Fig. 3.7. It should be noted though that this

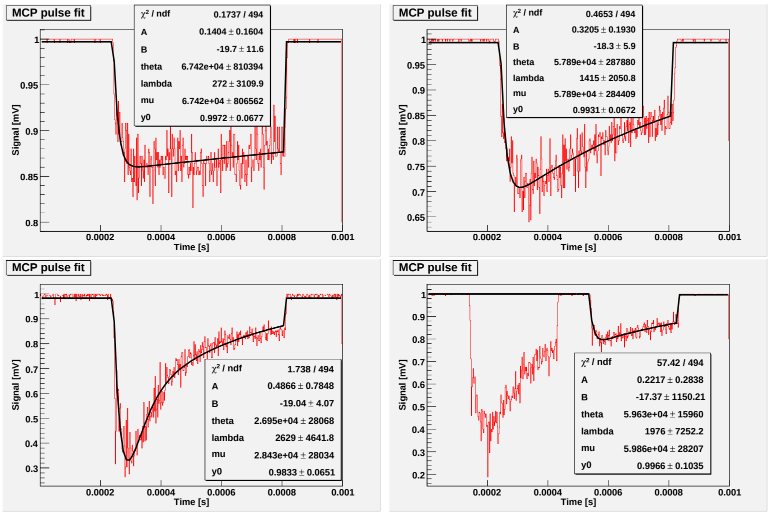

Figure 3.3 – *Some examples of fits of pulses with different shapes using Eq. 3.2. As can be seen Eq. 3.2 allows to obtain good fits for both non-saturated signals (e.g. upper left) and saturated signals (e.g. lower left). Only in this last case the third term in the formula is needed as can be seen from the fact that for all other cases $\mu = \theta$, such that the third term cancels. In the bottom right an example of two pulses hitting the detector shortly after each other is shown. This situation will be discussed in more detail below.*

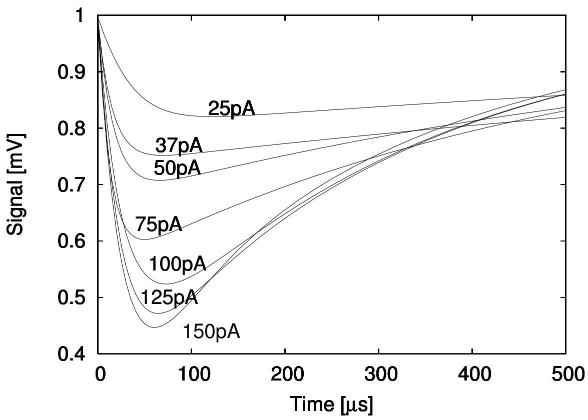

Figure 3.4 – *Evolution of the MCP pulse shape with changing beam intensity for an operating voltage of 1682 V (intensities are given as read on the grid). As was expected the MCP is driven further into saturation as the intensity of the ion beam increases, and the output signal becomes more and more peaked.*

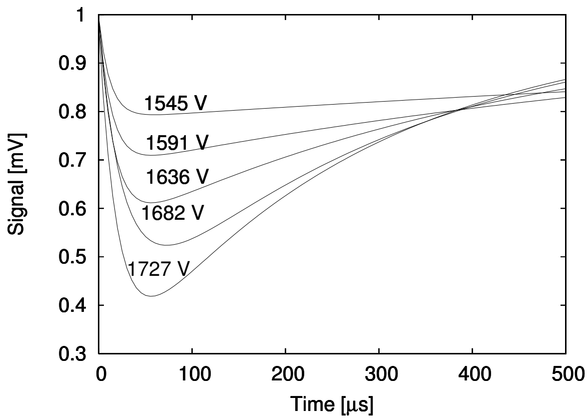

Figure 3.5 – *Evolution of the MCP pulse shape for a 100 pA ion beam (current read on the grid) as the voltage over the detector is increased from 1545 V to 1727 V. The effect is similar to that of increasing beam intensity: with a higher voltage being applied the MCP is pushed further into the saturation regime.*

remains only valid as long as the length of a pulse is significantly shorter than the recovery time of the detector, which is of the order of 10 to 100 ms (see section 3.4.3).

3.4.2 Voltage over the MCP plates

Since the number of electrons freed from the MCP by each incoming ion is essentially determined by the voltage difference between the front and back of the detector, this parameter also plays an important role in MCP saturation. This is illustrated in Fig. 3.5. One notices that as the voltage difference over the plates is increased the detector is driven further into saturation in a similar way as when the beam intensity is increased. To avoid saturation the voltage over the detector should thus not be too high.

Since the area of the signal is the simplest measure of the number of particles detected, this area is shown as a function of the number of particles that reach the detector[1] for different voltages in Fig. 3.6. Note that in this graph the curve for each voltage should pass through the origin. For the lowest voltage used, 1545 V, the area vs. number of particles is a straight line up about 7000 particles hitting the detector. Thus as long as the detector is not saturated, the area of the signal provides a good estimate of the number of particles detected, of course assuming a proper calibration. However, as soon as saturation is reached, the number of particles detected will be systematically underestimated by this method as is clearly visible for the larger voltages in figure 3.6.

[1]Derived from the current read by the electrometer (±5% uncertainty) and the measured transmission of the grids of 2%.

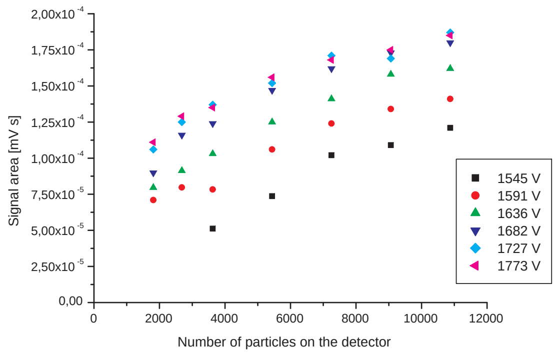

Figure 3.6 – *Area of the MCP signal (DC offset subtracted) as a function of the incoming number of particles for different MCP voltages.*

Several of the measurements presented were repeated after the detector had been used for some time already. The different measurements display the same behavior and no significant influence of detector aging was observed.

3.4.3 Double pulses

By letting two separate ion pulses impinge on the detector in a very short time interval (compared to the recovery time of the detector) one can simulate the response of the detector for the more realistic situation where two different species of ions with different times of flight hit the detector almost simultaneously. An example of this was already shown in the bottom right diagram of Fig. 3.3. In Fig. 3.7 the shape of the different pulses obtained under such conditions is plotted in one graph.

As can be seen, if the time between two pulses is very short in comparison with the detector's recovery time, the second pulse can be seen as a continuation of the first one, meaning that if the detector is driven into saturation by the first pulse, also the second one is completely altered in shape and height. To estimate the intensity of the ions in the second pulse or even the relative intensity compared to the ions in the first pulse one thus has to make sure that the detector is not driven into saturation.

The technique of using double pulses can also be used to get an estimate of the MCP recovery time. This is accomplished by using a high intensity beam so that the first pulse saturates the detector and then changing the time between the two pulses and comparing the two signals. The ratio of the areas of both peaks (which is proportional to the created electron charge) then provides an estimate for the recovery time of the detector. If one assumes that the MCP recovery is analogous to the charging of a capacitor [Wiz79], fitting these data should yield an exponential recovery. This is indeed what is observed, as is illustrated in Fig. 3.8. The time constant for the recovery τ is found to be

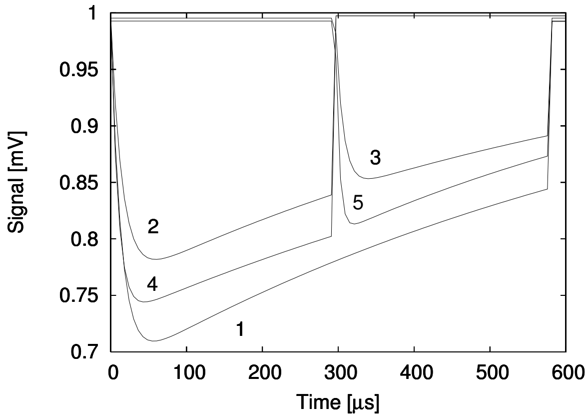

Figure 3.7 – *Signal shapes in the case of a double-pulse ion bunch for a 100 pA beam and an MCP operating voltage of 1636 V. Each time the two consecutive pulses are drawn directly behind each other, thus omitting the real time interval between them. 1: pulse shape for one long pulse of 580μs. 2: first of two 300 μs long pulses that are separated by 50 μs. 3: second of two 300 μs long pulses separated by 50 μs. 4: first of two 300 μs long pulses separated by 100 μs. 5: second of two 300 μs long pulses separated by 100 μs. As can be seen the second pulse each time appears as a continuation of the first when the time interval between the two pulses is neglected i.e. pulse 3(5) appears as the continuation of pulse 2(4). This will remain valid as long as the time between the two consecutive pulses is small compared to the recovery time of the detector.*

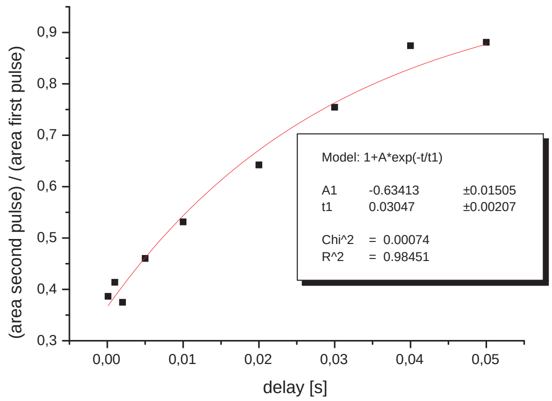

Figure 3.8 – *Measurement of the detector's recovery time by changing the delay between two consecutive pulses. The ratio of the areas of the first and second pulse is plotted. The value obtained for the recovery time constant is 30(2) ms.*

30 ± 2 ms. The expected RC time constant for a detector with a resistance of 320 MOhm and a capacitance between the front and back of the plates of 50 pF would be 16 ms, or a factor of two smaller than the experimentally obtained value. This would correspond to $k = 2$ in the formula

$$\tau = k\tau_{ch} = kR_{ch}C_{ch} = kR_{MCP}C_{MCP} \tag{3.3}$$

used by Fraser et al. in [Fra91] and [Fra93].

3.4.4 Avoiding saturation effects

By increasing the number of metallic grids one can increase the attenuation of the ion beam so as to avoid saturation, but this will of course be at the cost of signal height. As already mentioned one can also lower the voltage difference over the MCP plates to avoid saturation. The insertion of the metallic grids can be considered as a coarse reduction in beam intensity while the adaptation of the MCP voltage should be considered more as a finer tuning measure. A third option could be to limit the beam intensity directly, but this is often not desired especially in beam diagnostics applications for beam tuning. Increasing the beam spot size, in order to increase the number of channels that participate in the detection, is especially in beam tuning applications not interesting although it can be useful if one is simply interested in a TOF spectrum.

3.5 Simulations

A number of qualitative simulations were performed using the simple reservoir model described by Fraser et al. [Fra93]. In this model each channel of the detector is described as a reservoir of charge. With each event an amount of charge, according to a chosen Pulse Height Distribution (PHD), is depleted from the channel and between events the channel recovers its charge exponentially. With a Monte-Carlo routine a number of particles was simulated to hit the detector (a one-dimensional array of 17500 individual channels). The PHD used in this reservoir model was described as

$$P(x) = \frac{N}{1+A}\left\{\frac{1}{\sqrt{2\pi}\sigma_0}e^{-\frac{(x-x_0)^2}{2\sigma_0^2}} + \frac{A}{2}\left[1 - erf(\frac{x-x_0}{\sqrt{2}\sigma_0})\right]\right\} \tag{3.4}$$

This formula consists of a Gaussian distribution (center x_0 and width σ_0) and a step function with area A, N being a normalization constant [Sci03]. Charge was not only depleted from the channel the particle actually strikes but also from the neighboring channels, so as to take into account the fact that in reality a multi-stage detector was used. The results for the simulations where again fitted using equation 3.2 and are shown in Fig. 3.9. The qualitative resemblance between the simulated pulse shapes and the experimentally measured ones is very good. The only difference is the steeper front edge of the signal, but as mentioned before this is most likely related to the ion source properties and not to the MCP itself. Also simulations of two consecutive ion pulses (shown in the bottom right part of Fig. 3.9) agree very well with the experimental results given above.

3.6 Conclusion

A simple set-up was used to experimentally determine the effect of saturation of an MCP detector when exposed to short high intensity ion pulses. For a given beam spot size the shape of the detector's output signal was found to depend mainly on the beam intensity and the MCP operating voltage. The measurements where extended to the case of two consecutive pulses. This showed that the second pulse can be seen as a simple continuation of the first pulse if it arrives on the detector well within the detector's recovery time. This recovery time was measured by altering the delay between the two consecutive pulses. A value of 30(2) ms was found, as opposed to the value of 16 ms estimated from the simple RC model. Finally it was shown that Monte-Carlo simulations using the reservoir model reproduce the qualitative behavior of the measurements quite well.

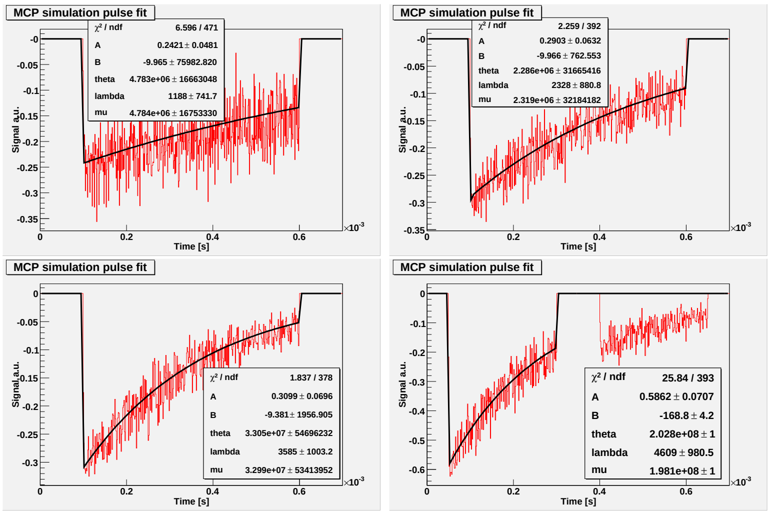

Figure 3.9 – *Qualitative simulations using the reservoir model from [Fra93] (top left: 2000 particles simulated, top right: 5000 particles, bottom left 7500 particles, bottom right: two consecutive pulses). As can be seen the simulations show the same qualitative behavior for an increasing number of particles or for double pulses as the measurements (compare to Fig. 3.3).*

3.7 Additional improvements to the diagnostics

3.7.1 MCP Read-out

Previously the output from the diagnostics MCP's was commonly connected to the oscilloscope, possibly through an amplifier, with a 50 Ω termination. This is necessary to avoid distortion of the fast MCP single ion signal (width < 10 ns) due to reflections in the cables. This termination, however, limits the output signal in amplitude as the output of the detector actually is a small current pulse. The bigger the resistance used, the bigger the signal on the oscilloscope, which reads a voltage and not a current. However due to the finite input capacitance of the oscilloscope, increasing the resistance in the system also increases its time constant. For this reason a termination piece of 1 kΩ is now commonly used (see Fig. 3.10) when using the diagnostics MCP detectors in combination with ion pulses. This termination still gives enough time resolution to see the structure in the ion pulse but gives a signal that is 20 times higher than with the previous system. This eliminates the need for an amplifier and allows one to use the detector at a lower operating voltage, thereby also limiting the risk of saturation effects.

If one is no longer interested in the time structure, one can even skip any additional termination and rely on the 1 MΩ termination of the oscilloscope, again increasing the signal height by a factor of 1000 but destroying the timing resolution. In this way even individual ion signals can be seen without the need

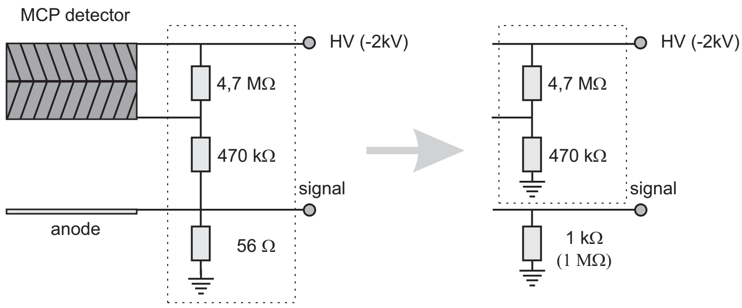

Figure 3.10 – *MCP readout scheme with improved sensitivity.*

for amplification.

3.7.2 Energy dependence

When using an MCP detector for detecting ion pulses containing a large number of ions, the height of the signal is determined by the number of particles and the average pulse height per particle striking the detector. As was shown above the average pulse height of the signals goes down and the signal height for the ion pulse becomes smaller once the detector becomes saturated. Not only saturation effects can affect the average pulse height, also the energy of the incident ions influences this parameter. As was for instance shown in Ref. [Hel85], the average pulse height or equivalently detector gain increases with increasing ion energy. Additionally, this effect depends on the mass of the ion [Ver06].

Especially the energy dependence of the detector gain is most disturbing for WITCH, as it complicates the comparison of beam intensity before and after the PDT due to the large change in beam energy (see chapter 4). This makes precise estimates of the PDT efficiency very difficult.

Several tests on this effect have been performed with the WITCH beam diagnostics detectors. In the future, additional tests will be performed, this time using the difference in Time Of Flight between the off line source and the detector to separate the different ion masses.

3.7.3 Position sensitive detectors

Detector choice

To facilitate the tuning of the beam in the horizontal but mainly in the vertical beamline, a system that can deliver information on the position of the beam in an easy and fast way was needed. As not only the position information but also the time structure of the ion pulse is of interest, MCP detectors again seemed like the best choice. Many possibilities to make this type of detectors position sensitive have been developed but many of them are limited to low count rates and are therefore not applicable in the WITCH beam diagnostic system. Two systems however are able to cope with this high count rate: an MCP detector in combination with a phosphor screen and an MCP detector with a segmented anode.

The advantage of a phosphor screen is the high spatial resolution. A disadvantage in case of the WITCH system is its relatively large size: a mirror behind the detector is needed to reflect the light to a CCD-camera located outside the path of the ion beam. Another disadvantage is that the spatial and timing information are no longer correlated due to the slow response of the phosphor screen.

A detector with a segmented anode does not have these problems but the spatial resolution is much worse and the read-out of the complete beam profile is less straightforward than with the phosphor screen. However, due to its much smaller size this option was finally chosen.

Implementation

Several prototype detectors were tested. First of all a classical anode consisting of small squares was used but it soon proved to be technically very difficult and time consuming to read all segments. The next step was to develop a system that consisted of wires in two perpendicular directions. With this system the beam profile in two perpendicular directions can be determined, but no full beam profile reconstruction is possible. This is, however, not strictly needed for the beam tuning where it is important to know the position of the center of the beam and the beam size. Both can be obtained from this system that consists of 4 major parts:

- Two metal plates between which the microchannel plates can be clamped in a chevron configuration.
- Two sets of 11 metallic wires. The sets are mounted perpendicular with respect to each other and are separated by a small teflon spacer. The wires are 0.25 mm in diameter and are spaced 2 mm apart.
- A full metal anode that collects all electrons passing through the wire set.
- An insulating teflon back plate.

A picture of the implementation of this type of anode is shown in Fig. 3.11. Each wire can be connected to the oscilloscope separately through a switching main frame. More details concerning this system can be found in [Ver06].

Replacing the anodes of the beam diagnostics MCP's by these segmented anodes has, together with the detailed understanding of the MCP's response discussed in the first parts of this chapter, been of major importance for improving the efficiency of the beam tuning at WITCH.

Further developments

A system that can read all segments of this detector at once is currently being investigated. The advantage of this is clear: one can obtain a full profile of the beam with a single ion pulse. One of the technical challenges in this respect is the extremely small currents/charges that have to be measured.

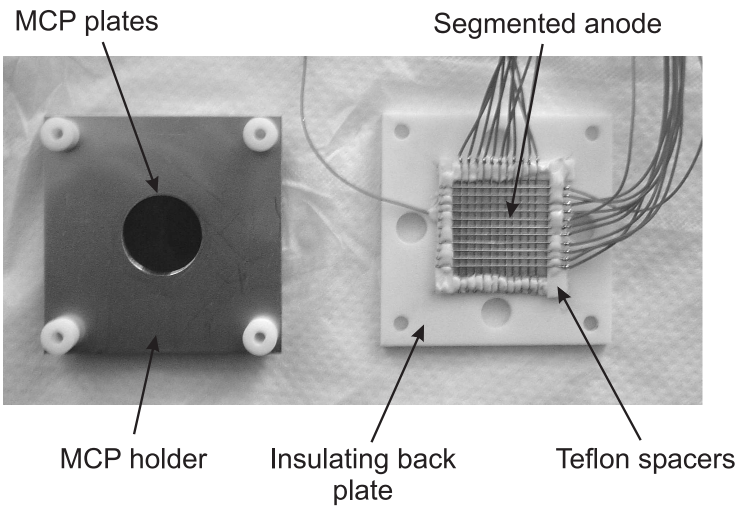

Figure 3.11 – *Picture of the position sensitive MCP detector for the beam diagnostics. The segmented anode is installed behind the MCP plates.*

3.7.4 Faraday cups

The most common way to use a Faraday cup is to directly connect it to a current measuring device and read the ion current that hits the cup. This works well for continuous ion beams or pulsed beams with high repetition rates. If one would, however, connect a low noise charge sensitive amplifier with some timing resolution to the Faraday cup it should be possible to actually see an ion pulse by connecting the output of the amplifier to an oscilloscope (see Fig 3.12). The big advantage of this type of system would be that all saturation or energy dependent effects of the detector, which is now a mere metal plate, can be avoided. The feasibility of this system is currently being looked into. It is

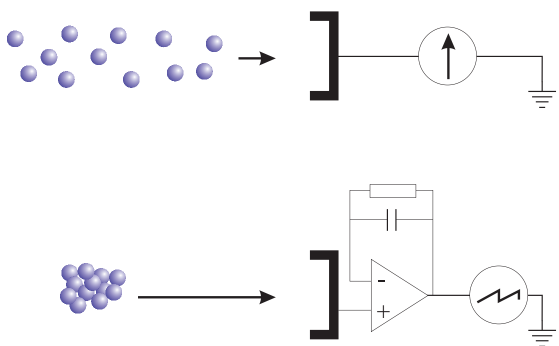

Figure 3.12 – *Method of using a Faraday cup to detect the ion beam intensity for continuous beams (top) and pulsed beams (bottom).*

already clear that this system would only work for systems that deal with high beam intensities (i.e. $> 10^4$ ions/pulse) as is the case at WITCH.

Chapter 4

The Pulsed Drift Tube

In this chapter the article entitled *A Pulsed Drift Cavity to capture 30 keV ion bunches at ground potential* is presented. The article explains in detail the working of the Pulsed Drift Tube (PDT) which is needed to reduce the energy of the 30 keV beam coming from REXTRAP to a few 100 eV, suitable for trapping the beam in the cooler trap, as well as early tests that were performed with this system. Apart from the beam diagnostics MCP detectors that were discussed in the previous chapter, the technical improvements to the WITCH PDT system and the optimization of its operational parameters constituted a second major technical development at WITCH over the last few years. At the end of the chapter some additional comments and more recent results are presented.

A Pulsed Drift Cavity to capture 30 keV ion bunches at ground potential

S. Coeck[a], B. Delauré[a,1], M. Herbane[a], M. Beck[a], V.V. Golovko[a], S. Kopecky[a], V. Yu. Kozlov[a], I.S. Kraev[a], A. Lindroth[a], T. Phalet[a], D. Beck[b], P. Delahaye[c], A. Herlert[c], F. Wenander[c], N. Severijns[a]

[a]*K.U.Leuven, Instituut voor Kern- en Stralingsfysica, Celestijnenlaan 200D, B-3001 Leuven, Belgium*
[b]*GSI-Darmstadt, Plankstr. 1, D-64291 Darmstadt, Germany*
[c]*ISOLDE-CERN, CH-1211 Geneva, Switzerland*

[1]*Present adress: Vlaamse Instelling voor Technologisch Onderzoek, Boeretang 200, B-2400 Mol, Belgium*

Published in: *Nuclear Instruments and Methods in Physics research A* ***572*** *(2007) 585-595*

4.1 Abstract

To capture radioactive ion beams of tens of keV in an ion trap, the use of a pulsed drift cavity allows one to avoid placing the complete setup on a high voltage (HV) platform. By pulsing down the voltage on a long electrode while the ion bunch is inside it, the electric potential zero level can be shifted down over a range equal to the initial beam energy, thus allowing the ions to be captured in a trap at ground potential. The pulsed drift cavity of the WITCH setup, which is completely HV-platform free, is described here. It is demonstrated that bunched beams with energies of typically 30 to 60 keV, as will become available to all users at the ISOLDE facility after the installation of an RFQ buncher, can be transported over distances of tens of meters to the experiments and by means of a pulsed drift cavity directly be injected into a purification Penning trap. Simulation work showing the efficiency of such a system is discussed and tests showing the feasibility of such a system are presented. An estimate of the pulse down time is made from TOF spectra. An outlook on how the system can be improved is presented too.

4.2 Introduction

Radioactive ions at ISOL (Isotope Separator On-Line) facilities, like ISOLDE/ CERN [Kug92], are usually accelerated to energies in the range of 30-60 keV and guided to the different experimental setups through a beamline system at ground potential. If detection of energetic decay products such as α, β or γ-radiation is pursued, it is sufficient to implant the mother nuclei into a foil. However in this case all low-energetic decay products, such as beta-recoil nuclei, remain contained in the host material. With the introduction of ion and atom traps, in which particles can be stored in a vacuum environment, this interesting region of observables has now become accessible too, permitting for instance mass measurements [Bol96], recoil energy and charge state determination of β-daughters [Bec03, Bec03b, Koz06, Gor05, Ban05, Sci03], and in principle many other interesting measurements for nuclear structure, weak interaction and atomic physics studies.

In order to capture radioactive ion bunches in a trap, they are typically slowed down to some tens of eV. This is usually done via an electrostatic retardation. In general this implies that the complete setup (electrodes, vacuum chambers, electronics, etc.) has to be placed at the same high voltage (HV) as the one used to accelerate the ions after their production. On the HV platform all electrodes of the setup can operate at low voltages.

Implanting the radioactive ions into a foil and then heating this foil to release and subsequently surface-ionize the ions in order to provide a beam with suitable energy, makes it possible to capture the ions at ground potential as was already demonstrated at the precision mass measurement Penning trap ISOLTRAP [Bol96] at the ISOLDE facility. However this approach is applicable for a limited number of elements only.

In the case of bunched beams an alternative for the HV platform is the pulsed drift cavity, which acts as an electro-dynamical elevator. While the ion bunch travels through a long electrode the voltage of this electrode is ramped down very fast over a range that equals the initial ion energy. This technique was first described in [Gha96] and later in [Gha02]. This approach has also been used at the ISOLTRAP setup at ISOLDE/CERN [Her01]. Later it was also implemented in the transparent Paul trap experiment [Ban05] at the Ganil accelerator facility. Both setups use two pulsed drift cavities. The first cavity, which is placed on a HV platform and immediately after the radio frequency quadrupole (RFQ) cooler/buncher in the setup, switches over several tens of keV. Just in front of the ion trap, which is placed at ground potential, a second switching is performed changing the beam energy by a few keV. As bunched beams become more and more a standard with the increasing number of RFQ bunchers that are being used to improve the properties of ion beams [Ban05, Her01, Nie01, Sik03], it is worth investigating how far one can go with this pulsed drift cavity approach. At the ISOLDE facility it is planned to install an RFQ buncher at the high resolution separator (HRS) line [Pod04]. The WITCH [Bec03, Bec03b, Koz06] pulsed drift cavity system can thus serve as a test case for such ISOL facilities equipped with a RFQ buncher. By first transporting the beam at 30 or 60 keV over a distance which can be of the order of 30 m, the increase in time spread due to an initial energy spread of up to 100 eV is still less then 0.3μs, even for a ^{238}U ion bunch. After passing through a pulsed drift cavity, the beam can be sent directly into an ion trap setup at ground potential, thus avoiding the need for a second RFQ buncher near the setup itself.

4.3 The WITCH-experiment

This paper describes the pulsed drift cavity system of the WITCH setup (Fig. 4.1) which is installed at the ISOLDE/CERN-facility. The WITCH experiment aims to measure the recoil energy spectrum of the daughter nuclei in nuclear beta decay to search for physics beyond the Standard Model [Bec03, Bec03b, Koz06]. The system uses 30 or 60 keV ion bunches that are delivered by the REXTRAP cylindrical cooler and buncher Penning trap [Ame98]. The time spread of an ion bunch with around 10^6 $^{39}K^+$ ions used for the measurements and simulations presented here, has a FWHM of about 6.75 μs. The energy spread is assumed to be less than 10 eV [Ame03]. After the ions are ejected from REXTRAP they first enter the horizontal beamline section of the WITCH setup and are then sent through an electrostatic 90° bender into the vertical part of the beamline. It is in this vertical section of the setup that the pulsed drift cavity is located. After the pulsing the ions are guided by a set of static electrodes into the 9 T high magnetic field region where the Penning traps are located. In the first of these two Penning traps (the cooler trap) the ions are cooled and the ion cloud is mass selectively purified. The cloud is then transferred into the second Penning trap (the decay trap) where it is held to let the radioactive ions decay. Through their decay energy the ions can leave the Penning trap, which thus serves as the scattering free radioactive source of the experiment. The energy

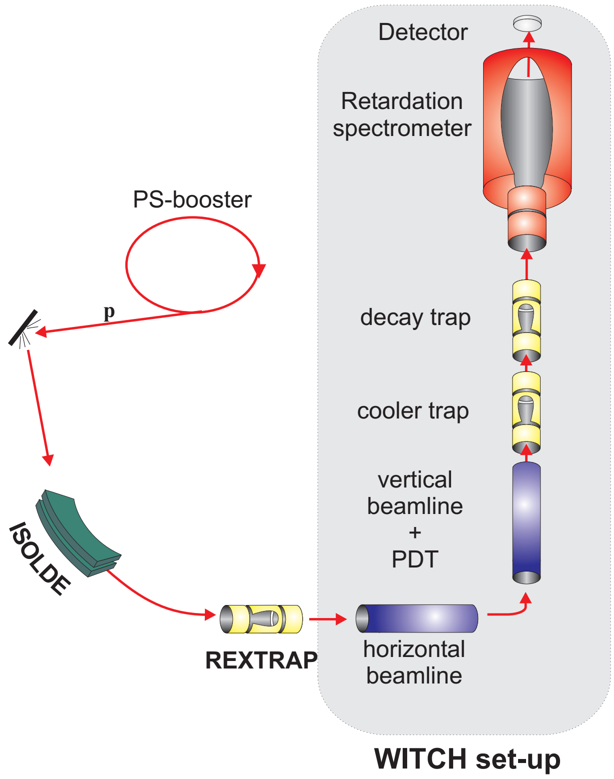

Figure 4.1 – *Overview of the complete WITCH setup. The pulsed drift cavity (PDT) is located in the vertical beamline section.*

of the recoil ions is then probed by the retardation spectrometer.

The pulsed drift cavity system of the WITCH setup differs in two ways from the already mentioned ISOLTRAP [Her01] and LPC-GANIL [Ban05] systems. First of all the switching is performed in a single step. Secondly the incoming 30 or 60 keV beam is retarded electrostatically before it enters the pulsed drift cavity.

4.4 PDT system

The pulsed drift cavity of the WITCH experiment, which shall be called the pulsed drift tube (PDT) in the remainder of this text, is located inside the vertical beamline (see Fig. 4.2) of the setup, which is the last stage before the two Penning traps. It is a 693 mm long solid stainless steel tube with 59.5 mm internal diameter. The vertical beamline contains a series of cylindrical stainless steel electrodes with inner diameter of 59.5 mm and four sets of X-Y steerer plates. To insulate the electrodes Macor® spacers are used. The drift electrodes behind the pulsed drift tube are set to -750 V and thus define the energy with which the ions are injected into the magnetic field.

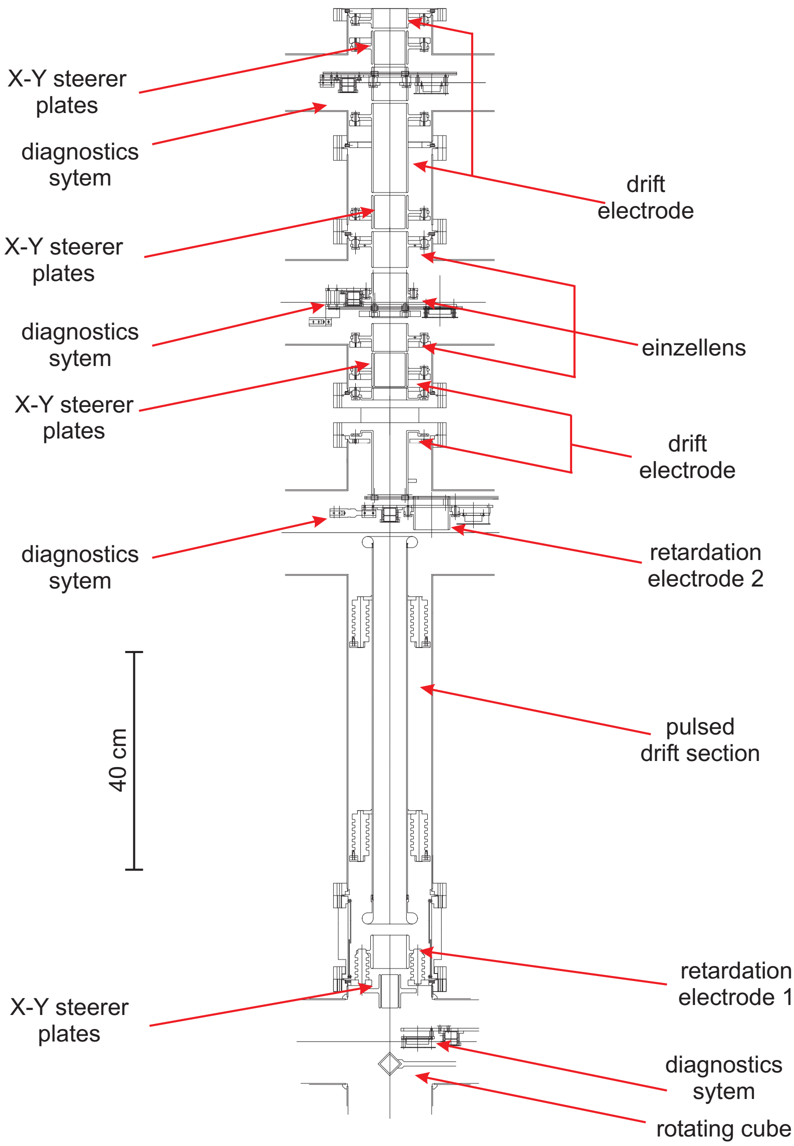

Figure 4.2 – *Vertical beamline of the WITCH-setup with the pulsed drift tube. The diagnostics for monitoring the ion beam are indicated separately.*

The ion bunches are retarded in two steps when entering the pulsed drift tube. This retardation is defined by the voltages on the first static retardation electrode (60 mm length, in front of the PDT) and on the pulsed drift tube itself. These voltages are not independent since together they determine the total focussing of the ion beam. Typical values are 18 kV and 26 kV respectively for a 30 keV beam. The optimal voltage settings are a balance between bunch length and beam focus in order to reach maximal efficiency. A strong retardation results in a slower ion beam in the pulsed drift tube which increases the time length of a bunch that can be pulsed. It is, however, also accompanied by a strong de-focussing of the beam in the long PDT electrode, implying a loss of ions when they would hit the electrode wall. After the pulsing, the ions are guided into the magnetic field of the Penning traps, via a series of shorter drift electrodes, at an energy of 750 eV. At four positions along the beam path, the ion bunches can be monitored by means of a Faraday cup or an MCP detector. The three diagnostics sets located behind the PDT (Fig. 4.2) consist of a small trolley which holds the Faraday cup, the MCP detector and the drift electrode, and which moves on vacuum bearings. The drift electrode serves to fill the open space that would otherwise be created when the diagnostics is removed and that would act as an einzellens, possibly inducing unwanted focussing effects.

The ramping down of the pulsed drift tube is realized by means of an electronic scheme with a Behlke solid state HV switch (HTS650-03-LC) as key component. This system is very similar to the one described in [Her01]. Although initially designed for operating voltages up to 60 kV, the system has been used only at 30 kV so far because of leakage current problems through the HV switch itself. The electronic scheme is the same for both voltages, but for some of the components the value that is used depends on the desired operating voltage. Figure 4.3 presents the layout of the scheme that was used for all tests that will be described below.

The positive voltage V_{PDT} is delivered by a FUG HCN 6,5M65000 (65 kV, 100 μA) power supply. The negative voltage V_{neg} is supplied by a ISEG CPn100 105 24 5 UC (-10 kV, 1 mA) power supply. The capacitor C_{buf} stores the charges that leave the PDT just after the HV switch is closed. A resistor, R_2, is installed in series with the HV switch to limit the peak current during the discharging of the PDT to a value below 30 A, so as to protect the HV switch. The fall time of the voltage over the pulsed drift tube is determined by the RC circuit formed by the capacitance of the pulsed electrode (including the cable) and the sum of the resistances of the switch and R_2. For the WITCH system the calculated time constant is $\tau_{PDT} = 0.186$ μs, taking into account the measured capacitance of 100 pF of the PDT-electrode. Ramping down the electrode over a range of 30 kV takes 1.2 μs (1.5 μs) to reach a voltage that deviates less than 50 V (10 V) from the relaxation voltage. For 60 keV those times are 0.1 μs longer. Note that the relaxation voltage is roughly 0.1% of the switching range (30 or 60 kV) higher than the voltage delivered by the negative power supply due to the charging of C_{buf}. This can, however, be compensated for by adjusting one of the two power supplies. The time to charge the cavity again is determined by the resistance R_1 and the capacitance of the pulsed drift

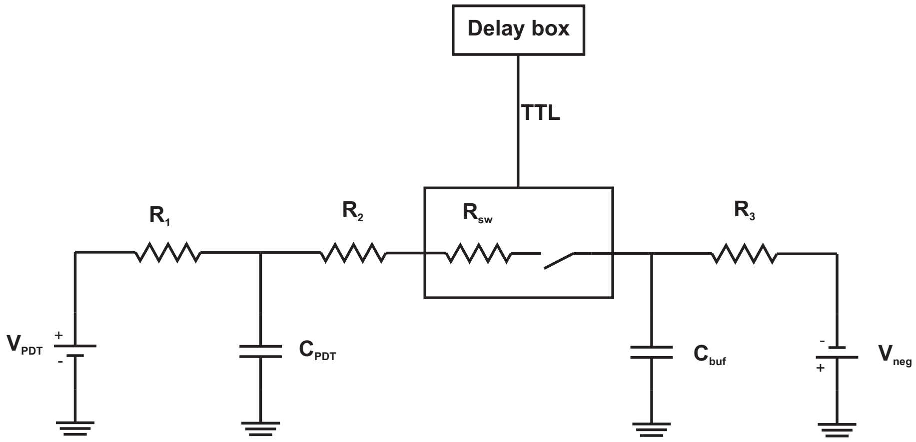

Figure 4.3 – *Electric scheme of the PDT switching system for an operating voltage of 30 kV. R_1=500 MΩ, C_{PDT}=100 pF, R_2=1500 Ω, R_{sw}=360 Ω, R_3=2000 Ω, C_{buf}=94 nF*

tube C_{PDT}. To reach a level deviating less than 1 V from the applied voltage, slightly less than 1 s is needed. For the purposes of the WITCH setup, where measurement cycles of the order of seconds are typical, this is fine. The HV switch is triggered by a TTL signal which is sent from a delay box as described in [Lin04]. The switching system is placed next to the beamline. The electrical feedthrough which connects the switch system to the PDT penetrates directly into the Faraday cage of the switching system, thus avoiding the use of coaxial cables which would worsen the timing properties of the system.

4.5 SIMION simulations

In order to design and understand the beam transport through the vertical beamline including the pulsed drift tube, a large amount of simulation work has been performed with the SIMION program [Dah00]. This program calculates ion trajectories by means of a Runge-Kutta algorithm of fourth order with adaptive step size. Electric potentials can be calculated for a user-defined electrode geometry by a relaxation method with nearest neighbor approach.

All ion trajectory simulations presented below have been performed for an ion bunch of 10^4 $^{39}K^+$ions, not including the repulsive Coulomb force. The ion energy was set to 29.930 keV to allow comparison with experimental results. A gaussian time distribution of the incoming ion bunch has been assumed. The FWHM of this distribution was determined from measurements with the MCP detector just in front of the PDT electrode. In order to study the timing effects of the PDT the simulations only considered ions traveling parallel to the axis.

The ion trajectory simulations have been performed in SIMION potential arrays with 2 mm per grid unit (gu) scaling. To investigate the influence of this scaling factor, a series of simulations has been performed with a potential array

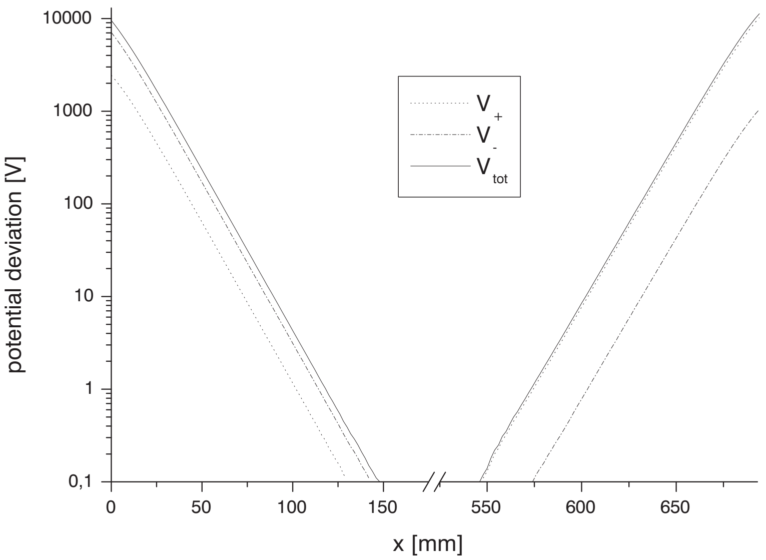

Figure 4.4 – *Deviation of electric potential on the axis of the PDT electrode from the applied voltage, before (V_+) and after (V_-) switching. Note that the electrode starts at position 0 mm and ends at 693 mm. V_{tot} represents the sum of the two deviations.*

of 0.25 mm/gu. This yielded changes in the energies of less than 1%.

4.5.1 Finite length effect

To allow for an efficient trapping in the first of the two Penning traps a maximal ion energy spread of about 50 eV is allowed. Due to the finite length of the pulsed drift tube the potential at the edges deviates from the applied voltage. The useful length of the cavity to obtain pulsed ions with an energy spread of less than 50 eV is thus reduced, even if the electrode could be pulsed down infinitely fast. To estimate the effect of this on the ion energies the deviation of the potential from the applied value was calculated along the axis of the pulsed drift tube, before (ΔV_+) and after the pulse down (ΔV_-). If at a given position the value of $\Delta V_{tot} = |\Delta V_-| + |\Delta V_+|$ is below the acceptable threshold (50 V for this study) an ion at that position is considered to be well bunched. Figure 4.4 shows these three energy contributions along the axis of the pulsed drift electrode.

If the pulsed drift cavity is switched over 30 kV, the useful length is 512 mm (for a 10V threshold), 533mm (50V) or 570.5mm (100V). For a 50 eV spread this corresponds to an effective length of 80% of the actual length. If the switched voltage range is 60 kV the useful length decreases by roughly 9 mm for all cases. If the diameter of the PDT would be 40 mm instead of 59.5 mm the useful length for a 50 eV threshold would increase to 590 mm or 85 % of the actual length.

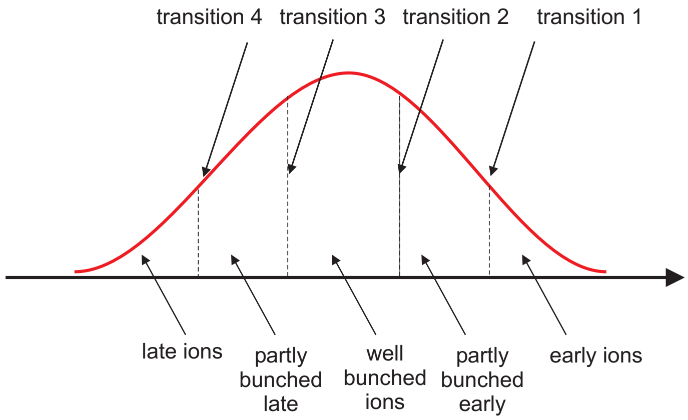

Figure 4.5 – *Division of the ion bunch into five separate groups. The early ions have already passed the PDT when it is pulsed down while the late ions have not yet reached the PDT. Both groups therefore experience no effect of the pulsing. The partly bunched early (late) ions experience a partial bunching because they are near the back (front) of the PDT at the time of pulsing.*

4.5.2 Drift energy dependence

Due to the large time spread of the REXTRAP ion bunch (i.e. about 6.75 μs) and the radial blow up when the beam is retarded to energies below 4 keV it is not possible to pulse the complete ion bunch in the WITCH PDT. To describe the performance of the PDT it is convenient to divide the ion bunch into five groups, as indicated in Fig. 4.5. Due to the difference in kinetic energy of these five groups inside and after the pulsed drift tube, they can be separated in a TOF measurement, as can be seen from Fig. 4.6. Here the TOF of the ions is plotted versus SIMION's time of birth (TOB) in the simulations. This TOB is equivalent to the time at which the ion passes a certain point in the WITCH beamline. Therefore an experimental TOF spectrum obtained with an MCP detector in front of the pulsed drift tube was used to provide the TOB values.

In Fig. 4.6 the early and the late ions are represented by linear dependencies between TOF and TOB on the outermost left and right side respectively. The well bunched ions are situated in the linear regions in the center. The partly bunched ions are located in the two transition regions separating the three regions discussed. From the curves it is clear that the time window for the well bunched ions is largest for the highest PDT voltages. In this case the drift energy of the ions in the pulsed drift tube is minimal, since they have been retarded most before entering the pulsed drift electrode. However as mentioned before one has to find a balance between this minimum in drift energy and a not too large radial blow up of the beam.

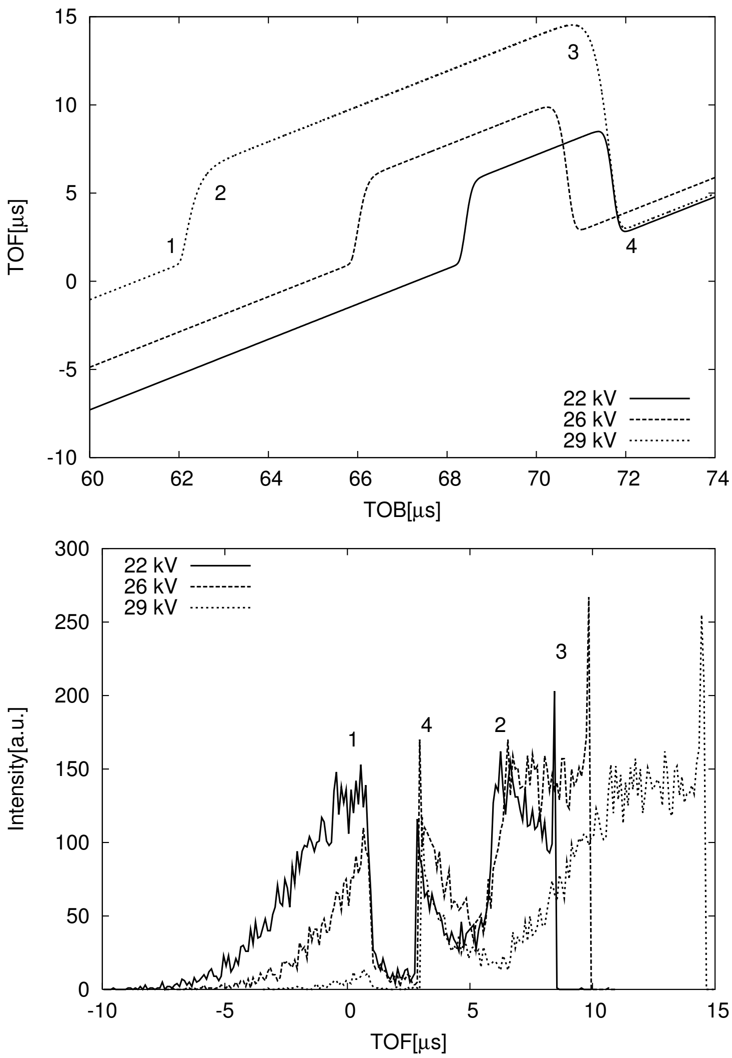

Figure 4.6 – *(top) Influence of V_{PDT} in the simulated TOF-graph for a prompt pulsing system ($\tau_{PDT} = 10^{-5}\mu s$ for voltages of 22 kV, 26 kV and 29 kV). The numbers (1 to 4) correspond to the transitions defined in Fig. 4.5. Well bunched ions are in the region between transitions 2 and 3. (bottom) Corresponding TOF spectra. These are shown here to illustrate the transition from the top graph to the experimentally observed spectra (see for instance Fig. 4.12).*

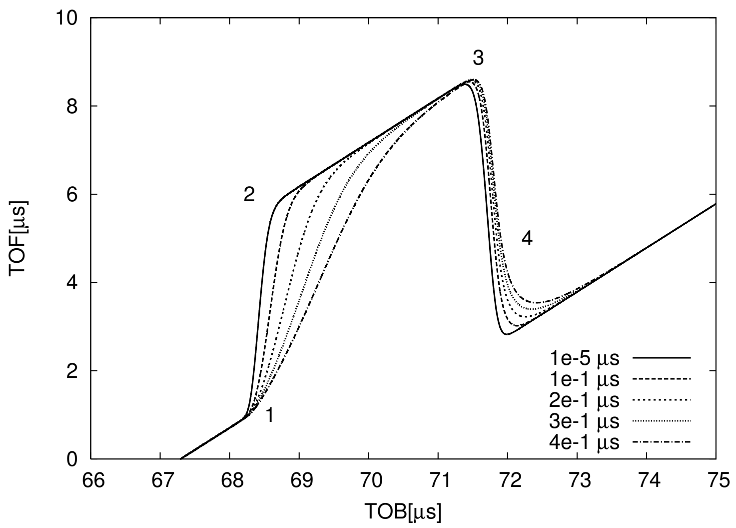

Figure 4.7 – *Simulated TOF-graph for different pulse down time constants τ_{PDT} for a voltage V_{PDT}=22 kV.*

4.5.3 Pulse down time constant

Apart from the energy of the ions inside the pulsed drift tube, the pulsing time constant τ_{PDT} is an important factor in determining the efficiency of the pulsed drift tube. The influence of τ_{PDT} on the TOF of the ions is shown in Fig. 4.7 for V_{PDT} = 22 kV. The partly bunched early ions (the ions near the rear of the PDT at the moment of pulsing) are most affected by the ramp speed. This can be seen from the fact that transition 2 fades away and the time window of the well bunched ions becomes more narrow when τ_{PDT} increases. A second effect of increasing the pulsing time constant is that transition 4 shifts slightly to larger TOF-values.

In order to estimate the fraction of ions that is well bunched it is important to look at the energy of the ions, as it is this observable that defines which ions can be considered as well bunched (e.g. kinetic energy spread $<$ 50 eV). Figure 4.8 shows the energy of the ions as a function of their time of birth for different time constants with V_{PDT}=22 kV. The behavior is similar to what has been observed in the TOF-case.

From this figure the time window of the well bunched ions can be estimated. To reach an energy spread of less than 50 eV and assuming a switching time constant of 0.2 μs, the time window is 2 μs. Taking into account the fact that the ion bunch is gaussian distributed with σ=2.88 μs, and assuming that the time window is centered around the maximum of the gaussian time distribution, the efficiency for ions to be well bunched is 27% at V_{PDT}=22 kV. Note that maximal efficiency would be reached with prompt pulsing (37%). This would correspond to a time window for the well bunched ions of 2.8 μs. This result is consistent with a calculation of the time window for 8 keV drift energy

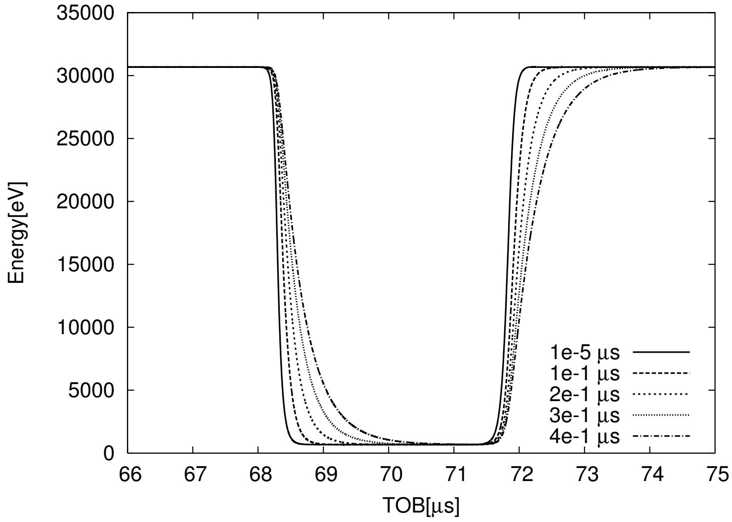

Figure 4.8 – *Kinetic energy of the ions after the pulsed drift tube for different time constants τ_{PDT} of the switching system and V_{PDT}=22 kV.*

inside the pulsed drift tube having a useful length of 80% of the real length. A switching system which pulses twice as fast as the present one, would result in a gain of 7 % if the time constant is the expected one. For V_{PDT}=26 kV the corresponding gain would be 6 % (from 43% to 49%) while for V_{PDT}=29 kV the gain would be even smaller (around 2 %, from 82% to 84%).

Figure 4.9 shows the time window of the well bunched ions for different (V_{PDT},τ_{PDT}) combinations. This shows again the importance of having slow ions passing through the pulsed drift tube (i.e. a large value for V_{PDT}). In addition it indicates that a faster switching system will not drastically improve the efficiency.

All pulsed drift tube characteristics discussed so far apply for $^{39}K^+$ ions. For ions with different mass the time window for the well bunched ions will change as the ion velocity decreases for increasing mass. Figure 4.10 shows the time window of the well bunched ions for five different masses. In order to study the efficiency of the pulsed drift tube as a function of the ion mass one should know the mass dependence of the time distribution of the initial ion bunch. This has not yet been investigated systematically with the REXTRAP setup.

4.5.4 TOF histogram

Since the TOF spectrum is the observable that is most easily accessible with the MCP detectors currently installed in the WITCH setup, it is interesting to the simulate TOF histograms of the ions arriving at the detector, as shown in Fig. 4.11. The presence of the early, late, well bunched and partly bunched ions can be easily understood by comparison with the TOF curves shown in Fig. 4.6. In order to estimate the time constant τ_{PDT} from an experimental TOF

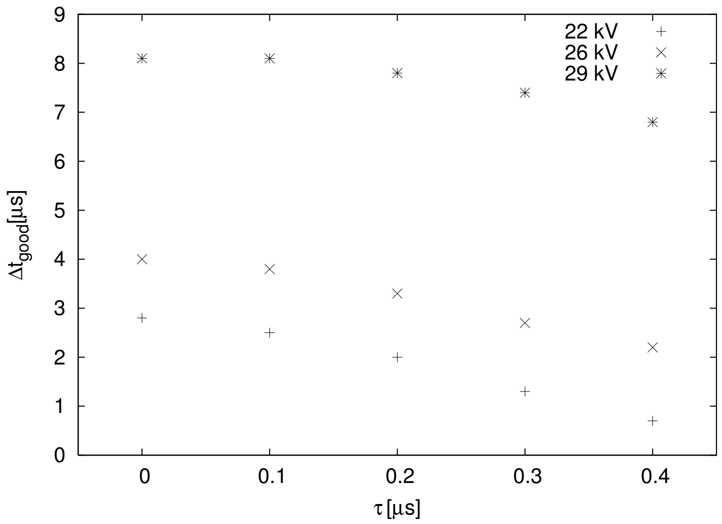

Figure 4.9 – *Time window for well bunched ions, Δt_{good}, as a function of the time constant τ_{PDT} for different PDT voltages.*

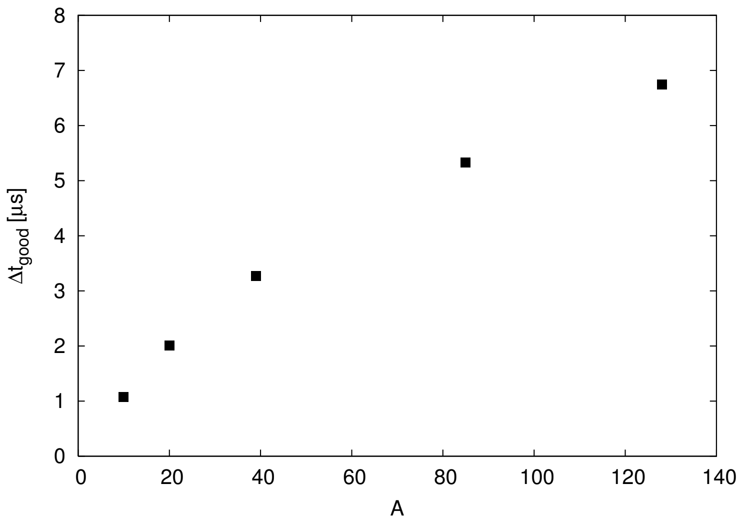

Figure 4.10 – *Simulated time window, Δt_{good}, for the well bunched ions for different ion masses (V_{PDT}=26 kV).*

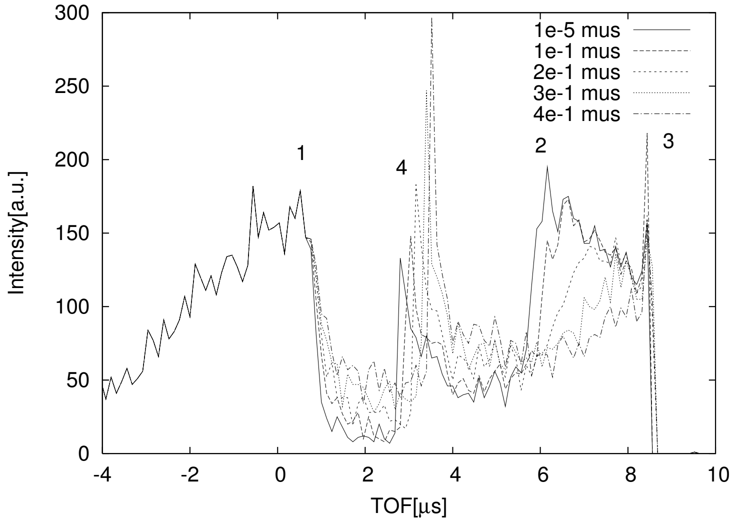

Figure 4.11 – *Simulated TOF histogram for different decay time constants τ_{PDT} and V_{PDT}=22kV. The numbers correspond to the different transition regions indicated in figure 4.5. The region between transitions 2 and 3 corresponds to the well bunched ions (see also figure 4.6).*

spectrum it is important to investigate how the shape of the TOF spectrum of the well bunched ions changes for various V_{PDT} and τ_{PDT}. This is also shown in Fig. 4.11. Two observations can be made. First of all transition 2 fades away for increasing τ_{PDT}. The intensity maximum for transition 2 first shifts to higher TOF values but then slowly fades away ending up in a situation where transition 2 is not visible any more (starting from $\tau_{PDT} = 0.3$ μs). Another effect of increasing τ_{PDT} is that transition 4 shifts to slightly higher TOF. By comparing simulated TOF spectra with experimental ones it is possible to estimate the real time constant.

4.6 Comparison of experimental tests with simulations

The pulsed drift tube of the WITCH setup has been tested with ions of different masses, specifically ^{20}Ne, ^{39}K, ^{36}Ar and ^{128}Xe. A microchannel plate with metal anode, placed roughly 40 cm behind the pulsed drift tube, was used to detect the ions. The signal was amplified by a Lecroy 821 amplifier and read out via a Tektronix TDS224 oscilloscope. The values measured by the oscilloscope were read into a data acquisition PC. All MCP spectra shown here are summed over 39 cycles, during which an ion bunch is first ejected from REXTRAP and then sent through the pulsed drift tube.

Since ion bunches ejected from REXTRAP contain of the order of 10^6 ions with different masses, saturation effects in the MCP detector have been observed [Coe06]. It is thus not possible to use the areas under the peaks in the MCP spectra observed before and after the pulsed drift tube to estimate the efficiency of the system. Instead, the time structure of the MCP spectra is studied. Although saturation effects of the MCP also alter the shape of the TOF spectra the structure for different pulsing conditions is still easily recognized. Comparison of experimental and simulated data provides an indication for the ramp down speed of the system and also shows the system's behavior for different masses.

The specific structure of the TOF spectrum after the PDT, as shown in Fig. 4.7, has been observed experimentally in a qualitative way. By tuning the voltage of the first retardation electrode just in front of the pulsed drift tube it is possible to change the ion optics through the pulsed drift electrode and make sure that the majority of the non-pulsed, 30 keV ions do not reach the MCP (see section 4.7). These will therefore not always be visible in the figures shown below.

Most of the tests have been performed with $^{39}K^{+}$ ions. Figure 4.12 shows TOF-spectra obtained for different voltages applied to the PDT. The structure of the well bunched ions in the TOF-spectrum is in good agreement with simulations (see Fig. 4.11). In order to estimate the ramp down speed of the pulsed drift tube, the experimental TOF spectrum for V_{PDT}=22 kV has to be compared to the simulated curves in Fig. 4.11. The experimental spectrum (Fig. 4.12) shows a maximum intensity for the well bunched ions at a TOF value of about 7 μs. At the right one observes a sharp peak that corresponds to transition 3. The presence of a maximum and the position of this transition in the TOF spectrum indicates that the time constant should be between 0.1 μs and 0.3 μs as shown in the SIMION simulations. This confirms that the timing of the PDT is indeed as expected (i.e. $\tau_{PDT} = 0.186\mu s$, see section 4.4).

Figure 4.13 shows experimental TOF spectra after the pulsed drift tube for different ion masses: ^{20}Ne, ^{36}Ar,^{39}K and ^{128}Xe. Note the peak around 3 μs for the spectrum of the ^{36}Ar ions (transition 4). This peak corresponds to 30 keV non-pulsed early ions. It is clearly seen that for different masses the well bunched ions (between transitions 2 and 3) are situated at different TOF values after switching the pulsed drift tube. Secondly it can be seen that the time window of the well bunched ions increases with increasing mass, as was also observed in the simulations (see Fig. 4.10).

4.7 Effect of the phase space

One might think that it is advantageous to use the PDT with as high a value of V_{PDT} as possible in order to increase the efficiency. However, as already mentioned, a higher voltage on the PDT induces a larger divergence of the beam when it enters the electrode. Therefore a complete study of the PDT must not only include time spread related effects but also the size and divergence of the incident ion beam. Ions entering the PDT off-axis or at some angle behave different from ions that fly along the axis, and can eventually even be lost when striking one of the electrodes. To be able to compare simulations of such effects

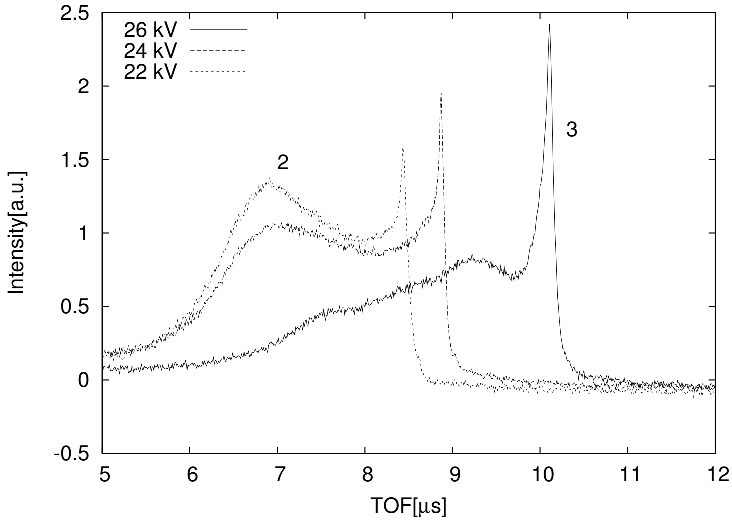

Figure 4.12 – *Measured TOF spectra for different PDT voltages and switching over 30 kV: 22kV →-8 kV, 24kV →-6 kV, 26kV →-4 kV.*

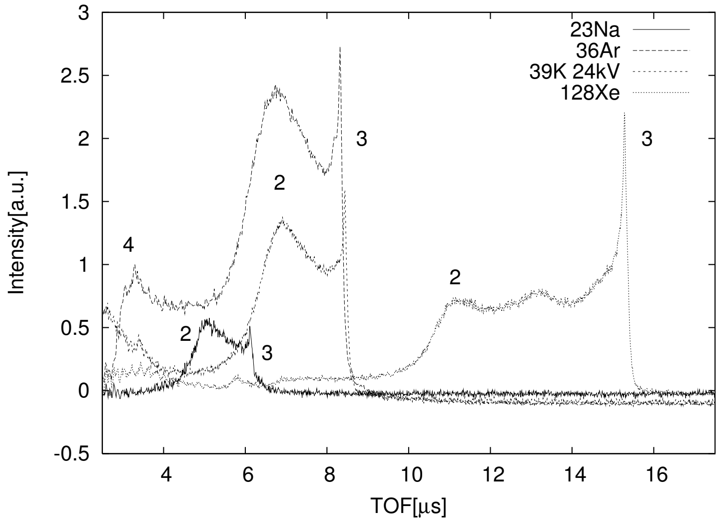

Figure 4.13 – *Experimental TOF spectrum for ions with different masses observed after the PDT.*

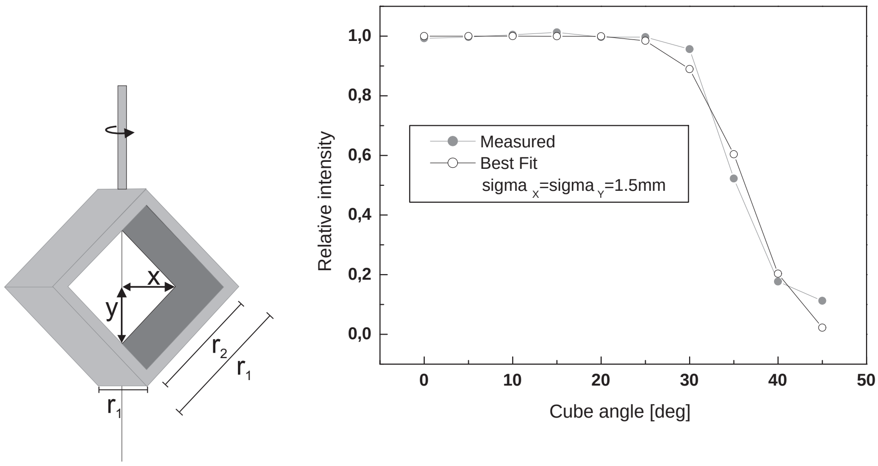

Figure 4.14 – *(left) Rotating cube used to measure the size of the beam in front of the PDT. (right) Best agreement between observed and simulated intensities transmitted through the rotating cube as a function of the rotation angle is obtained for a gaussian beam profile with σ = 1.5 mm.*

with the measured values and spectra, it is important to know the properties of the incident ion beam. The emittance of the beam and its size fully characterize the incident beam.

The transversal emittance of REXTRAP has been measured to be about 10π mm mrad [Ame05]. To measure the size of the beam entering the WITCH vertical beamline, the diagnostic system located about 250 mm below the PDT electrode, was used (see Fig. 4.2). It consists of a hollow stainless steel cube of which two opposite sides are open to allow the beam to pass (Fig. 4.14 (left)), and a Faraday cup mounted directly behind it to measure the transmitted beam intensity. When the cube is rotated along an axis parallel to the opened faces, the apparent aperture offered to the beam reduces, its size being given by a simple geometrical relation. Figure 4.14 (right) shows the experimental data as well as a fit to these considering a two-dimensional gaussian beam profile with σ = 1.5 mm. This is the typical size of the beam after transport from REXTRAP to the lower part of the vertical beamline.

4.7.1 PDT Efficiency

In this section results of SIMION simulations of the PDT efficiency for ion bunches with the characteristics described above are shown. No time spread of the ion bunches has been included (see previous sections). Simulations were performed for different PDT voltages. Finally, experimental results will be presented and compared to the simulations.

All simulations were performed for a bunch of 10^4 $^{39}K^+$ ions of 30 keV longitudinal energy[1]. In the axial direction all ions start from the same position which corresponds to the center of the diagnostics cube. Radially their initial coordinates are distributed within a disc of 1.8 mm radius (FWHM). The radial velocities were generated such that the ions are uniformly distributed over an erect emittance ellipse of 10π mm mrad, corresponding to the spatial focus at that position. PDT voltages V_{PDT} of 24, 25, 26, 27, 28 and 29 kV are considered. The voltage was always switched exponentially over a range of 30 kV with a time constant of 0.2 μs.

Figure 4.15 shows the ion trajectories obtained from SIMION for the six different cases considered. Each time the voltages of the electrodes before and after the PDT were optimized to get at the same time a maximum transmission and an almost parallel beam with the smallest possible size after the PDT (i.e. at the entrance of leftmost electrode shown).

As stated before, the ion bunch blows up more for high voltages on the PDT. The efficiency drops to about 93.5 % for 29kV, but remains at 100 % for the other voltages considered. It is to be noted, however, that for an incident ion bunch with a larger divergence, the blow-up is more important and losses can occur for lower values of V_{PDT} as well. The shape of the bunch after the PDT also plays a major role in the further manipulation of the ions. In general the beam has to be as parallel and as narrow as possible to allow injection with good efficiency into the high magnetic field of a Penning trap setup.

4.7.2 Experimental tests

In order to also experimentally test the phase space dependence of the PDT operation, the same conditions as for the measurements described in section 4.6 were used. However, to avoid saturation effects for the MCP detector, two semi-transparent grids were inserted just in front of the MCP [Coe06]. An example of a TOF spectrum recorded under these conditions is shown in Fig. 4.16.

For the corresponding SIMION simulation 10^4 ions were generated in a similar way as described in section 4.7.1, but now a gaussian time spread with σ=2.88 μs was included. For the emittance of REXTRAP the then measured value of 20π mm mrad [Rex05] was used in the simulations. This emmitance is different from the optimal value for which the general simulations were performed but still allows one to compare the simulation results to experimental data in order to verify the correctness of the simulation method. It should also be noted that to obtain good agreement between experimental results and simulations, the ions were generated with an offset angle of 1.5 degrees relative to the PDT axis. In fact, due to this offset angle, the early, the well-bunched and the late ions follow different paths during their passage through the different electrodes, the conditions for the early and late ions being such that most of them miss the detector (see Fig. 4.16). This offset can easily be explained through a non-optimal tuning of the beam through the horizonal beamline and

[1]Previously the REXTRAP HV was conventionally set to 29.93 kV; in the mean time this has changed to 30 kV exactly.

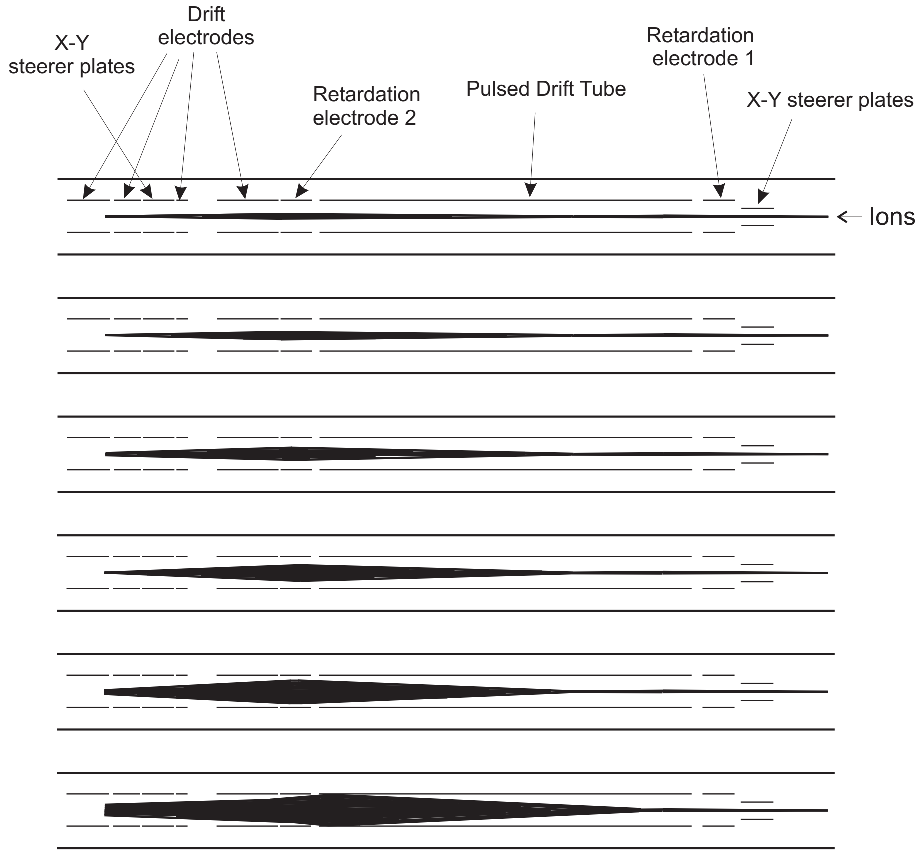

Figure 4.15 – *Drawing of the SIMION ion trajectories showing the effect of the PDT high voltage on the ion bunches (ions enter the PDT from the right). The voltage on the PDT ,V_{PDT}, is 24, 25, 26, 27 ,28 and 29 kV respectively (top to bottom). The size of the ion beam continually increases with V_{PDT} leading to losses for the highest values of V_{PDT} when ions start colliding with the electrode surfaces.*

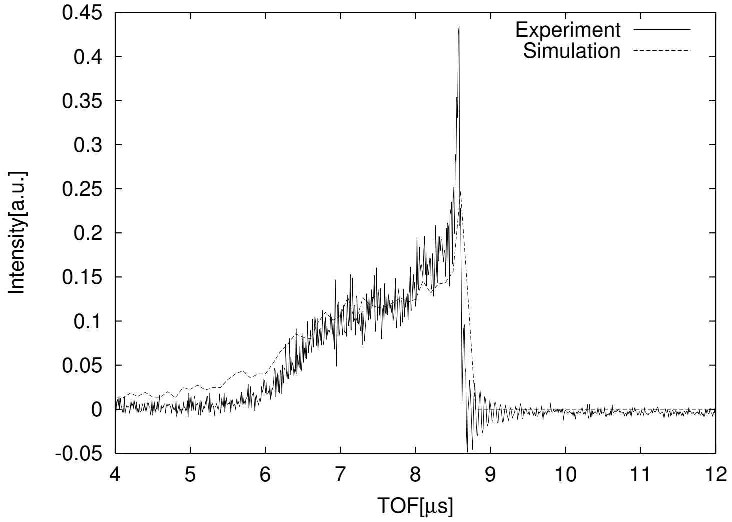

Figure 4.16 – *Experimental and simulated time of flight of the ions for a detector placed 400 mm after the PDT. The PDT high voltage V_{PDT} was 24 kV and the low voltage V_{neg} was -6 kV. Further details are given in the text.*

the electrostatic 90° bender.

The size of the bunch at the location of the detector was also measured using a strip with a 5 mm diameter hole mounted in front of the MCP (Fig. 4.17). This strip was moved through the beam in 2 mm steps while the area of the signal induced on the MCP was measured.

The simulations which best reproduce this experimental profile indicate that 43% of the incident ions reach the detector with a beam profile corresponding to the dashed line in Fig. 4.17. About 72% of these (i.e. 31% of the incident ions) have a final energy deviating less than 50 eV from the minimal value.

4.8 Discussion and outlook

It has been shown that a 30 keV bunched ion beam can be retarded and pulsed down over a range of 30 kV. The method has been successfully applied to different ion beams with masses ranging from ^{20}Ne up to ^{128}Xe using the WITCH setup at ISOLDE/CERN. Good qualitative agreement was found between the simulated TOF-spectra and those observed with an MCP detector. The time constant of the switching system, obtained from the analysis of the experimental TOF spectrum, agrees well with the expected value.

Inclusion of the phase space combined with the time spread explains the experimental results very well. The efficiency of the PDT can be estimated to be approximately the product of the efficiency induced by the time spread and the one induced by the phase space. However, because the size of the ion

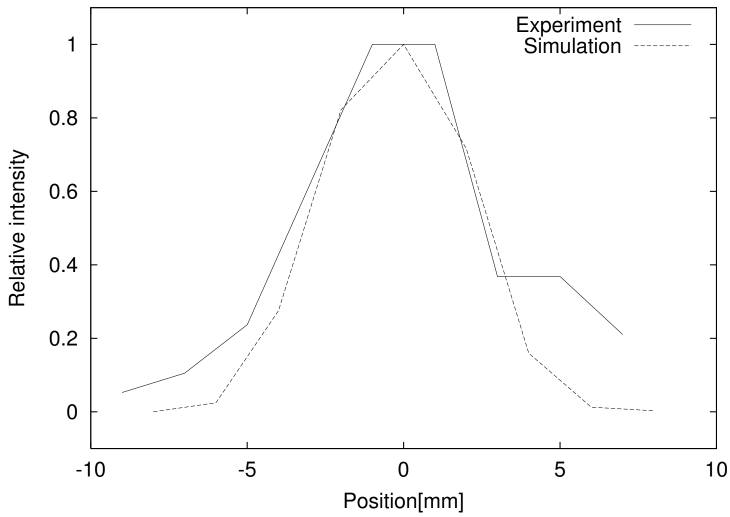

Figure 4.17 – *Radial profile of the ion bunches at the location of the detector.*

bunches increases for higher values of the PDT voltage, the voltage providing the highest efficiency is not necessarily the optimal one as ions can become difficult to manipulate after being slowed down. In order to further increase the efficiency of the PDT, additional tests are therefore planned to find the optimal PDT voltages taking into account both time spread and phase space related effects. A faster switching system could also improve the efficiency. The gain would, however, be much less. Furthermore, the gain decreases when the ions are slowed down more before reaching the pulsed drift tube.

A solution to reduce the radial blow up could be to redesign the electrode section in front of the WITCH pulsed drift tube, e.g. by introducing more electrodes or by changing the shape of the current one. A more challenging solution would be to try to perform focussing inside the pulsed drift tube by dividing it into different sections.

The WITCH switching system is now being upgraded to contain two HV switches in series as is already implemented at the ISOLTRAP setup [Bla04]. This will solve the leakage current problem which limits the current system from going to 60 kV.

4.9 Acknowledgements

This work is supported by the European Union grants FMRX-CT97-0144 (the EUROTRAPS TMR network), HPRI-CT-2001-50034 (the NIPNET RTD network) and the EURONS I3 project (TRAPSPEC Joint Research Activity), by the Flemish Fund for Scientific Research FWO and by the projects GOA 99-02 and GOA/2004/03 of the K.U. Leuven. This research was also in part funded with a specialization fellowship of the Flemish Institute for the stimulation of Scientific-Technological Research in the Industry (IWT).

4.10 Additional comments

4.10.1 Increased efficiency

Following the investigation of the ejection from REXTRAP, the time structure of the ion pulse has been made significantly shorter (see section 2.2). This means that now (nearly) all ions can be pulsed down over the full voltage range, increasing the efficiency of the PDT to (nearly) 100%. In addition, a beam-gate was installed in the horizonal beamline, which makes it possible to remove any ions that can not be pulsed down fully, before they reach the vertical beamline. This avoids high energy ions from entering the upper part of the system and possibly contaminating the recoil detector.

4.10.2 New design for the High Voltage switching system

To improve the switching speed of the PDT and more importantly to avoid problems of leakage currents through the switch, a new switching system has been developed. The electronic scheme of this new system is shown in Fig. 4.18. It uses two high voltage switches in series to switch the full range of 60 kV. Although each switch individually is rated at 65 kV, other users have observed that over time the switches develop a leakage that creates an offset in the potentials that are applied to the electrode. By using two switches in series, each individual switch only sees a 30 kV potential difference, thereby avoiding leakage problems.

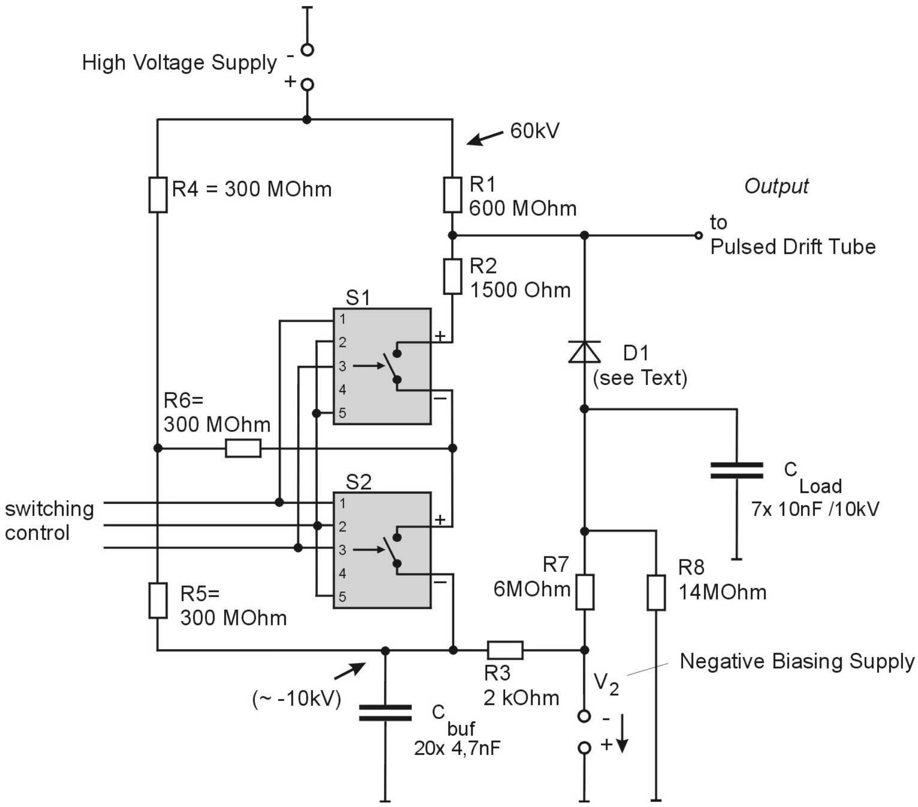

Figure 4.18 – *Electronic scheme for the new and improved HV-switch for the WITCH Pulsed Drift Tube [Sta04].*

Chapter 5

One particle in a Penning trap

In this chapter the theory behind one of the main components of the WITCH system will be discussed: the Penning traps. First the single particle case will be studied and the equations describing the motion of a single particle will be derived analytically under several, experimentally interesting circumstances. Although the WITCH experiment usually deals with ion clouds containing a large number of particles (typically of the order of 10^6, see chapter 6), the study of the single particle behavior gives a good feeling for the possibilities of Penning traps and the motion of the particles under different circumstances.

5.1 Introduction

When one wants to perform precision measurements of particle properties, one has to observe the particles of interest for a sufficiently long time under suitable conditions. To study the properties of charged particles like electrons, positrons, ions, *etc.*, charged particle traps were developed. In these traps particles can in principle be confined indefinitely in a vacuum environment. The Penning trap [Bro86], a special example of such a trap, uses a strong magnetic field

$$\mathbf{B} = B \cdot \hat{\mathbf{e}}_z \tag{5.1}$$

to confine the charged particles in a plane perpendicular to the axis (conventionally chosen as the z-axis). To also confine the particles along the magnetic field axis it is in principle sufficient to apply a sufficiently large electrostatic potential at both ends of the trap. More commonly an electrostatic field of the form

$$\mathbf{E} = \frac{U_0}{2d^2}(x\hat{\mathbf{e}}_x + y\hat{\mathbf{e}}_y - 2z\hat{\mathbf{e}}_z) \tag{5.2}$$

is used, where U_0/d^2 is a measure for the potential depth of the trap. To reproduce the shape of this potential, a hyperbolic trap, where the electrode surfaces follow the equipotential lines of equation 5.2, can be used. In this

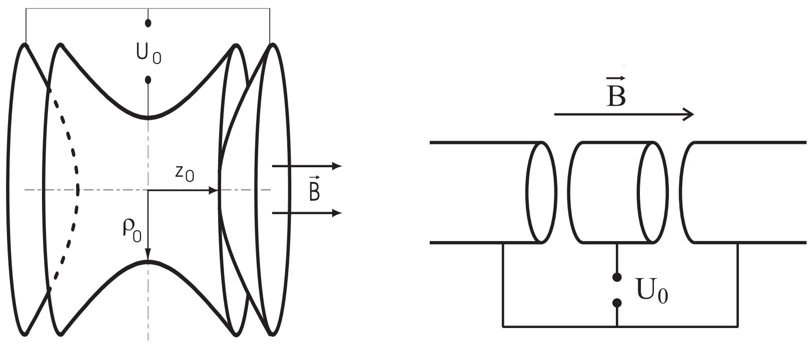

Figure 5.1 – *(left) A hyperbolical Penning trap. (right) A simple example of a cylindrical Penning trap.*

case U_0 is the potential difference between the central electrode and the endcap electrodes and the size parameter d is given by

$$d = \sqrt{\frac{z_0^2 + \rho_0^2/2}{2}} \tag{5.3}$$

with z_0 and ρ_0 as defined in Fig. 5.1.

The quadrupolar electrostatic field can also be produced by a set of cylindrical electrodes leading to a cylindrical Penning trap. The main advantage of a cylindrical Penning trap is the open access to it from the top and bottom. A simple example of a cylindrical Penning trap is also shown in Fig. 5.1.

5.2 Basic motion

Considering the forces acting on a particle trapped in a Penning trap due to the magnetic and electric field leads to the following equation of motion for the particle:

$$\ddot{\mathbf{r}} = \frac{q}{m}(\mathbf{E} + \dot{\mathbf{r}} \times \mathbf{B}) \tag{5.4}$$

or written explicitly in components

$$\begin{pmatrix} \ddot{x} \\ \ddot{y} \\ \ddot{z} \end{pmatrix} - \omega_c \begin{pmatrix} \dot{y} \\ -\dot{x} \\ 0 \end{pmatrix} - \frac{\omega_z^2}{2} \begin{pmatrix} x \\ y \\ -2z \end{pmatrix} = 0 \tag{5.5}$$

where the frequencies

$$\omega_c = \frac{qB}{m} \tag{5.6}$$

and

$$\omega_z = \sqrt{\frac{qU_0}{md^2}} \tag{5.7}$$

have been introduced. As can be seen, the axial motion is completely uncoupled from the radial motion. The equation for the axial motion reduces to

$$\ddot{z} + \omega_z^2 z = 0 \Leftrightarrow z(t) = A_z cos(\omega_z t + \phi_z) \tag{5.8}$$

which is nothing but an harmonic oscillator along the magnetic field axis. By introducing the radial vector $\boldsymbol{\rho}$

$$\boldsymbol{\rho} = \begin{pmatrix} x \\ y \\ 0 \end{pmatrix} \tag{5.9}$$

the radial part of the equation of motion can be written as

$$\ddot{\boldsymbol{\rho}} = \omega_c \dot{\boldsymbol{\rho}} \times \hat{\mathbf{e}}_z + \frac{\omega_z^2}{2} \boldsymbol{\rho}. \tag{5.10}$$

To solve this equation a transformation according to

$$\mathbf{V}^{\pm} = \dot{\boldsymbol{\rho}} - \omega_{\mp} \boldsymbol{\rho} \times \hat{\mathbf{e}}_z \tag{5.11}$$

is made. Here the rotation frequencies ω_- and ω_+ were introduced

$$\omega_{\pm} = \frac{1}{2}\Big(\omega_c \pm \sqrt{\omega_c^2 - 2\omega_z^2}\Big). \tag{5.12}$$

To make the inverse transformation one can use the relation

$$\boldsymbol{\rho} = \frac{\left(\mathbf{V}^- - \mathbf{V}^+\right) \times \hat{\mathbf{e}}_z}{\omega_+ - \omega -}. \tag{5.13}$$

Using the transformation of equation 5.11, equation 5.10 transforms into

$$\dot{\mathbf{V}}^{\pm} = \omega_{\pm}(\mathbf{V}^{\pm} \times \hat{\mathbf{e}}_z), \tag{5.14}$$

or when written in components

$$\begin{pmatrix} \dot{V}_x^{\pm} \\ \dot{V}_y^{\pm} \end{pmatrix} = \omega_{\pm} \begin{pmatrix} V_y^{\pm} \\ -V_x^{\pm} \end{pmatrix}. \tag{5.15}$$

Using the assumption that the ion motions are circular

$$V_y^{\pm} = \pm i \cdot V_x^{\pm} \tag{5.16}$$

one finally arrives to the solution of the equation of motion

$$\begin{aligned} V_x^{\pm} &= A^{\pm} \cdot e^{\pm i(\omega_{\pm} t + \phi_{\pm})} \\ V_y^{\pm} &= \pm i A^{\pm} \cdot e^{\pm i(\omega_{\pm} t + \phi_{\pm})}. \end{aligned} \tag{5.17}$$

Transforming equation 5.17 back into normal Cartesian coordinates using equation 5.13 finally gives

$$\begin{aligned} x(t) &= R_+ \cdot sin(\omega_+ t + \phi_+) - R_- \cdot sin(\omega_- t + \phi_-) \\ y(t) &= R_+ \cdot cos(\omega_+ t + \phi_+) - R_- \cdot cos(\omega_- t + \phi_-). \end{aligned} \tag{5.18}$$

This shows that the radial motion of the particle in a Penning trap consists of a superposition of two separate circular motions: the magnetron motion with rotation frequency ω_- and the cyclotron motion with rotation frequency ω_+. The complete motion is illustrated in Fig. 5.2.

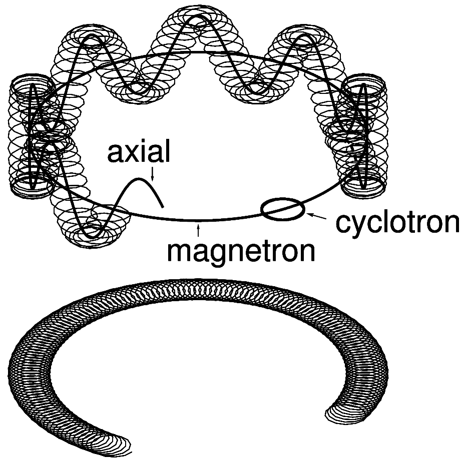

Figure 5.2 – *The motion of a charged particle in an ideal Penning trap consists of three separate motions: the axial motion, the magnetron motion and the cyclotron motion. The full motion and a projection of the motion in the radial plane are shown.*

From equation 5.12 one can deduce the following additional relations:

$$\begin{aligned} \omega_+ + \omega_- &= \omega_c && (5.19)\\ \omega_-^2 + \omega_+^2 + \omega_z^2 &= \omega_c^2 && (5.20)\\ 2 \cdot \omega_- \cdot \omega_+ &= \omega_z^2. && (5.21) \end{aligned}$$

Additionally the first order approximations

$$\begin{aligned} \omega_+ &\approx \omega_c \\ \omega_- &\approx \frac{U_0}{2Bd^2} \end{aligned} \qquad (5.22)$$

are often quite convenient. With the parameters typically used when trapping ions in a Penning trap the hierarchy

$$\omega_c \approx \omega_+ \gg \omega_z \gg \omega_- \qquad (5.23)$$

is obtained for the different frequencies of the particle motion. For instance for the WITCH Penning traps (discussed in more detail further on in the text), where $B = 9$ T and $U_0/d^2 = 1.8 \cdot 10^4$ V/m^2, the frequencies of a $^{39}K^+$ ion are given by

$$\begin{aligned} \nu_c &= 3.547020 \cdot 10^6 \text{ Hz} \\ \nu_+ &= 3.546861 \cdot 10^6 \text{ Hz} \\ \nu_z &= 3.360136 \cdot 10^4 \text{ Hz} \\ \nu_- &= 1.5916 \cdot 10^2 \text{ Hz.} \end{aligned}$$

The rest of the text will concentrate on the motions of ions as this is the case of interest for the WITCH experiment. All figures presented in this chapter will be for a particle of mass 39 u and charge $1 \cdot e$, in a magnetic field of 9 T and $U_0/d^2 = 1.8 \cdot 10^4$ V/m^2.

5.3 Frictional damping

When ions are injected into a Penning trap, they often have a lot of kinetic energy. To remove this kinetic energy one can insert a gas, often referred to as a *buffer gas*, into the trap. The ions in the trap will then be slowed down by the successive collisions with the buffer gas particles. Although this process is in reality a discrete one, it can to first order be described as a continuous drag acting on the ions. To describe this, the term

$$\mathbf{F_D} = -\delta m \dot{\mathbf{r}} \tag{5.24}$$

is added to the equations of motion. The damping coefficient δ is given by

$$\delta = \frac{q}{m} \frac{1}{K_0} \frac{p/p_N}{T/T_n} \tag{5.25}$$

where K_0 is the so-called standard ion mobility, the pressure p of the gas is given in units of the normal pressure $p_N = 1.013 \cdot 10^5$ Pa and the temperature T is expressed in units of the normal temperature $T_n = 273.15$ K. In this way the equation of motion becomes

$$\begin{pmatrix} \ddot{x} \\ \ddot{y} \\ \ddot{z} \end{pmatrix} - \begin{pmatrix} \omega_c \dot{y} - \delta \dot{x} \\ -\omega_c \dot{x} - \delta \dot{y} \\ -\delta \dot{z} \end{pmatrix} - \frac{\omega_z^2}{2} \begin{pmatrix} x \\ y \\ -2z \end{pmatrix} = 0. \tag{5.26}$$

As can be seen the axial motion is still decoupled from the radial motion and this part of the equation can thus be solved separately:

$$\ddot{z} + \delta \dot{z} + \omega_z^2 z = 0 \Leftrightarrow z(t) = A_z e^{-(\delta/2)t} cos(\omega_z t + \phi_z). \tag{5.27}$$

The axial motion thus is a damped harmonic oscillator where the amplitude reduces exponentially with a time constant $\delta/2$.

To solve the radial part of the equation of motion the following transformation is made

$$u(t) = x(t) + i \cdot y(t) \tag{5.28}$$

turning equation 5.26 into

$$\ddot{u} = -(i\omega_c + \delta)\dot{u} + \frac{\omega_z^2}{2} u. \tag{5.29}$$

The solution of this is then given by

$$\begin{aligned} u(t) = \quad & u_-(0) \cdot e^{(-\frac{i\omega_c}{2} - \frac{\delta}{2} + \frac{i}{2}\sqrt{(\omega_c - i\delta)^2 - 2\omega_z^2})t} \\ + \quad & u_+(0) \cdot e^{(-\frac{i\omega_c}{2} - \frac{\delta}{2} - \frac{i}{2}\sqrt{(\omega_c - i\delta)^2 - 2\omega_z^2})t} \end{aligned} \tag{5.30}$$

which after transformation into normal cartesian coordinates results into

$$\begin{aligned} x(t) &= R_- e^{\alpha_- t} cos(\omega'_- t + \phi_-) + R_+ e^{\alpha_+ t} cos(\omega'_+ t + \phi_+) \\ y(t) &= -R_- e^{\alpha_- t} sin(\omega'_- t + \phi_-) - R_+ e^{\alpha_+ t} sin(\omega'_+ t + \phi_+). \end{aligned} \tag{5.31}$$

The new frequencies $\omega'_\pm$ are given by

$$\begin{aligned}\omega'_\pm &= \omega_\pm \pm \Delta\omega \\ \Delta\omega &= \frac{\delta^2}{16}\cdot\frac{8\omega_z^2+\delta^2}{(\omega_c^2-2\omega_z^2)^{3/2}}\end{aligned} \tag{5.32}$$

while the damping coefficients $\alpha_\pm$ are given as

$$\alpha_\pm = -\frac{\delta}{2}\left(1 \pm \left(1+\frac{\omega_z^2+(\delta/4)^2}{\omega_c^2-2\omega_z^2}\right)\right). \tag{5.33}$$

Typically the frequency shifts are small and can to first order be neglected. The decay constants α_+ and α_- can to first order be approximated as $-\delta$ and $(\delta/2)(\omega_z/\omega_c)^2$. For the damping coefficients α it is important to notice that $\alpha_- > 0$ while $\alpha_+ < 0$, meaning that the magnetron motion expands when the ions are cooled while the cyclotron motion decreases in radius. This expansion of the magnetron orbit can be understood by looking again at the electric field defined in equation 5.2: radially this field points outwards, thus when the ions lose energy they will automatically move to the outside of the trap. Luckily α_- is typically much smaller in absolute value than $\delta/2$ and α_+ so that the axial and cyclotron motions can be cooled on a much shorter time scale than the typical time scale important for the expansion of the magnetron motion. Typical values for the WITCH Penning traps are ($^{39}K^+$ ions):

$$\begin{aligned}p &= 10^{-7}\cdot p_N \; (10^{-4}\text{ mbar}) \\ T &= T_N \\ K_0 &= 21.5\cdot 10^{-4}\text{ m}^2/\text{Vs (He buffer gas)} \\ \delta &= 1.15176\cdot 10^{2}\text{ s}^{-1} \\ \Delta\omega &= 2.671\cdot 10^{-8}\text{ s}^{-1} \\ \alpha_+ &= -1.15181\cdot 10^{2}\text{ s}^{-1} \\ \alpha_- &= 5.1689\cdot 10^{-3}\text{ s}^{-1}.\end{aligned}$$

5.4 Dipolar excitations

In a Penning trap, ions can not only be trapped and cooled but their motion can also be excited in various ways. This can for instance be achieved by applying a time dependent electric field. For the remainder of this chapter we will focus on azimuthal excitations (x,y directions but not z) as they are of the biggest use for the WITCH experiment. The simplest form of this type of excitation is a dipolar excitation where the time varying electric field for an ideal Penning trap is given by

$$\mathbf{E_d} = \frac{U_d}{r_0}cos(\omega_{rf}t+\phi_{rf})\hat{\mathbf{e}}_x. \tag{5.34}$$

To simplify the calculations we introduce the constant k_0 as

$$k_0 = \frac{qU_d}{mr_0}. \tag{5.35}$$

First the situation where there is a dipole excitation but no damping force present will be discussed.

5.4.1 Without damping

Adding the electric field of equation 5.34 to the equation of motion 5.5 leads to

$$\begin{pmatrix} \ddot{x} \\ \ddot{y} \\ \ddot{z} \end{pmatrix} - \omega_c \begin{pmatrix} \dot{y} \\ -\dot{x} \\ 0 \end{pmatrix} - \frac{\omega_z^2}{2} \begin{pmatrix} x \\ y \\ -2z \end{pmatrix} - k_0 cos(\omega_{rf}t + \phi_{rf}) \begin{pmatrix} 1 \\ 0 \\ 0 \end{pmatrix} = 0. \quad (5.36)$$

Obviously the axial motion remains uncoupled from the radial motion and still is a simple harmonic oscillator. The radial part of equation 5.36 will again be solved by making the substitution of equation 5.11 leading to

$$\begin{pmatrix} \dot{V}_x^\pm \\ \dot{V}_y^\pm \end{pmatrix} = \omega_\pm \begin{pmatrix} V_y^\pm \\ -V_x^\pm \end{pmatrix} + k_0 cos(\omega_{rf}t + \phi_{rf}) \begin{pmatrix} 1 \\ 0 \end{pmatrix}. \quad (5.37)$$

By using the ansatz

$$\mathbf{V}^\pm = \mathbf{A}^\pm \cdot e^{\pm i(\omega_\pm t + \phi_\pm)} \quad (5.38)$$

this can be written as

$$\begin{aligned} \dot{A}_y^\pm &= \mp i\omega_\pm A_y^\pm - \omega\pm A_x^\pm \\ \dot{A}_x^\pm &= \mp i\omega_\pm A_x^\pm + \omega\pm A_y^\pm + k_0 cos(\omega_{rf}t + \phi_{rf}) \cdot e^{\mp i(\omega_\pm t + \phi_\pm)} \end{aligned} \quad (5.39)$$

or by using

$$cos(\omega_{rf}t + \phi_{rf}) = \frac{e^{i(\omega_{rf}t + \phi_{rf})} + e^{-i(\omega_{rf}t + \phi_{rf})}}{2} \quad (5.40)$$

as

$$\begin{aligned} \dot{A}_x^+ = \quad & -i\omega_+ A_x^+ + \omega_+ A_y^+ \\ & + \frac{k_0}{2}\left(e^{i\left((\omega_{rf} - \omega_+)t - \phi_+ + \phi_{rf}\right)} + e^{-i\left((\omega_{rf} + \omega_+)t + \phi_+ + \phi_{rf}\right)}\right) \\ \\ \dot{A}_x^- = \quad & i\omega_- A_x^- + \omega_- A_y^- \\ & + \frac{k_0}{2}\left(e^{i\left((\omega_{rf} + \omega_-)t + \phi_- + \phi_{rf}\right)} + e^{-i\left((\omega_{rf} - \omega_-)t - \phi_- + \phi_{rf}\right)}\right) \end{aligned} \quad (5.41)$$

and analogous for the y component. Under the assumption that

$$A_y^\pm = \pm i \cdot A_x^\pm \quad (5.42)$$

equation 5.41 simplifies to

$$\begin{aligned} \dot{A}_x^+ &= \frac{k_0}{2}\left(e^{i\left((\omega_{rf} - \omega_+)t - \phi_+ + \phi_{rf}\right)} + e^{-i\left((\omega_{rf} + \omega_+)t + \phi_+ + \phi_{rf}\right)}\right) \\ \dot{A}_x^- &= \frac{k_0}{2}\left(e^{i\left((\omega_{rf} + \omega_-)t + \phi_- + \phi_{rf}\right)} + e^{-i\left((\omega_{rf} - \omega_-)t - \phi_- + \phi_{rf}\right)}\right). \end{aligned} \quad (5.43)$$

This can now easily be solved

$$\begin{aligned}
A_x^+ = \quad & A_x^+(0) - \frac{k_0}{2}\Bigg[\frac{-i}{\omega_{rf} - \omega_+}\left(e^{i(\phi_{rf}-\phi_-)} - e^{i\left((\omega_{rf}-\omega_+)t-\phi_+ +\phi_{rf}\right)}\right) \\
+ \quad & \frac{i}{\omega_{rf}+\omega_+}\left(e^{-i(\phi_{rf}+\phi_-)} - e^{-i\left((\omega_{rf}+\omega_+)t+\phi_+ +\phi_{rf}\right)}\right)\Bigg]
\end{aligned}$$

$$\begin{aligned}
A_x^- = \quad & A_x^-(0) - \frac{k_0}{2}\Bigg[\frac{-i}{\omega_{rf} + \omega_-}\left(e^{i(\phi_{rf}+\phi_-)} - e^{i\left((\omega_{rf}+\omega_-)t+\phi_- +\phi_{rf}\right)}\right) \\
+ \quad & \frac{i}{\omega_{rf}-\omega_-}\left(e^{-i(\phi_{rf}-\phi_-)} - e^{-i\left((\omega_{rf}-\omega_-)t-\phi_- +\phi_{rf}\right)}\right)\Bigg]
\end{aligned} \tag{5.44}$$

and after transformation into cartesian coordinates through the substitution of equation 5.13 one finally obtains the full solution to equation 5.36

$$\begin{aligned}
x(t) = \quad & i\Bigg(A_x^-(0) - \frac{k_0}{2}\Bigg(-\frac{i(e^{i(\phi_{rf}+\phi_-)} - e^{i((\omega_{rf}+\omega_-)t+\phi_-+\phi_{rf})})}{\omega_{rf}+\omega_-} \\
& +\frac{i(e^{-i(\phi_{rf}-\phi_-)} - e^{-i((\omega_{rf}-\omega_-)t-\phi_-+\phi_{rf})})}{\omega_{rf}-\omega_-}\Bigg)\Bigg)\cdot\frac{e^{-i(\omega_-t+\phi_-)}}{\omega_+-\omega_-} \\
& +i\Bigg(A_x^+(0) - \frac{k_0}{2}\Bigg(-\frac{i(e^{i(\phi_{rf}-\phi_+)} - e^{i((\omega_{rf}-\omega_+)t-\phi_++\phi_{rf})})}{\omega_{rf}-\omega_+} \\
& +\frac{i(e^{-i(\phi_{rf}+\phi_+)} - e^{-i((\omega_{rf}+\omega_+)t+\phi_++\phi_{rf})})}{\omega_{rf}+\omega_+}\Bigg)\Bigg)\cdot\frac{e^{-i(\omega_+t+\phi_+)}}{\omega_+-\omega_-}
\end{aligned}$$

$$\begin{aligned}
y(t) = \quad & -\Bigg(A_x^-(0) - \frac{k_0}{2}\Bigg(-\frac{i(e^{i(\phi_{rf}+\phi_-)} - e^{i((\omega_{rf}+\omega_-)t+\phi_-+\phi_{rf})})}{\omega_{rf}+\omega_-} \\
& +\frac{i(e^{-i(\phi_{rf}-\phi_-)} - e^{-i((\omega_{rf}-\omega_-)t-\phi_-+\phi_{rf})})}{\omega_{rf}-\omega_-}\Bigg)\Bigg)\cdot\frac{e^{-i(\omega_-t+\phi_-)}}{\omega_+-\omega_-} \\
& +\Bigg(A_x^+(0) - \frac{k_0}{2}\Bigg(-\frac{i(e^{i(\phi_{rf}-\phi_+)} - e^{i((\omega_{rf}-\omega_+)t-\phi_++\phi_{rf})})}{\omega_{rf}-\omega_+} \\
& +\frac{i(e^{-i(\phi_{rf}+\phi_+)} - e^{-i((\omega_{rf}+\omega_+)t+\phi_++\phi_{rf})})}{\omega_{rf}+\omega_+}\Bigg)\Bigg)\cdot\frac{e^{-i(\omega_+t+\phi_+)}}{\omega_+-\omega_-}.
\end{aligned} \tag{5.45}$$

To enable easy plotting of these functions, a C++ code *snippet* using these formulas was added in Appendix A.

When inspecting equation 5.45 one can notice that there are two excitation frequencies ω_{rf} that lead to a special behavior: the magnetron frequency ω_- and the reduced cyclotron frequency ω_+.

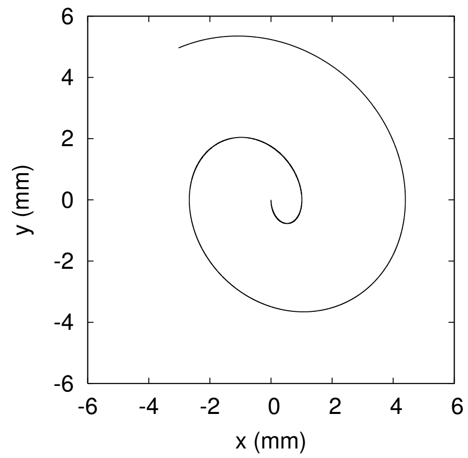

Figure 5.3 – *Ion motion under the influence of a 10 ms ω_- dipolar excitation at 10 V/m.*

Magnetron excitation

When using $\omega_{rf} \approx \omega_-$, the term containing the factor

$$\frac{e^{-i(\omega_{rf}-\omega_-)t}}{\omega_{rf}-\omega_-} \tag{5.46}$$

in equation 5.45, gives rise to a term that describes a linear increase of the radius of the magnetron motion with time. This means that during an electric dipole excitation at the magnetron frequency the particle is shifted away from the center and as ω_- is nearly mass independent, the shift from the center is also nearly mass independent (the importance of this will become clear during the discussion of mass selective cooling). The motion of an ion subjected to a dipolar excitation with an amplitude of 10 V/m at the magnetron frequency ω_- for a 10 ms timescale is depicted in Fig. 5.3 and its radius versus time is given in Fig. 5.4. As for all figures in this section the ions start at rest in the trap center in these plots. The slope of this linear increase is given by

$$\frac{k_0}{2(\omega_+-\omega_-)} \tag{5.47}$$

and thus linearly depends on the excitation amplitude.

Upon close inspection of these figures one can see that the orbit is in fact not fully circular anymore but rather somewhat flattened, an effect that is most easily seen as the oscillation on top of the linear increase in Fig. 5.4. This effect is caused by the term in equation 5.45 containing the factor

$$\frac{e^{i(\omega_{rf}+\omega_-)t}}{\omega_{rf}+\omega_-} \tag{5.48}$$

which leads to an oscillation at $2\omega_-$ in the case of resonance. The amplitude of this oscillation also linearly depends on the excitation amplitude and is given

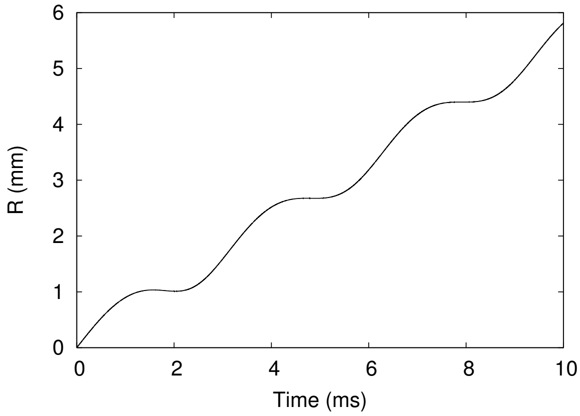

Figure 5.4 – *Distance of the ion from the trap center, R, as a function of time for a 10 ms ω_- dipolar excitation at 10 V/m.*

by

$$\frac{k_0}{4\omega_-(\omega_+ - \omega_-)}. \tag{5.49}$$

The terms containing

$$\frac{e^{\mp i(\omega_{rf} \pm \omega_+)t}}{\omega_{rf} \pm \omega_+} \tag{5.50}$$

have no effect on time scales important for the magnetron motion but do show up at small time scales, leading to the peculiar motion shown in Fig. 5.5 and Fig. 5.6.

Cyclotron excitation

Similar effects occur when using an excitation where $\omega_{rf} \approx \omega_+$. Now the terms containing

$$\frac{e^{\mp i(\omega_{rf} \pm \omega_+)t}}{\omega_{rf} \pm \omega_+} \tag{5.51}$$

lead to a linear increase of the cyclotron radius with slope

$$\frac{k_0}{2(\omega_+ - \omega_-)} \tag{5.52}$$

and oscillations at frequency $2\omega_+$ and amplitude

$$\frac{k_0}{4\omega_+(\omega_+ - \omega_-)} \tag{5.53}$$

on top of this linear increase. This is illustrated in Fig. 5.7 and Fig. 5.8. The terms with

$$\frac{e^{\pm i(\omega_{rf} \pm \omega_-)t}}{\omega_{rf} \pm \omega_-} \tag{5.54}$$

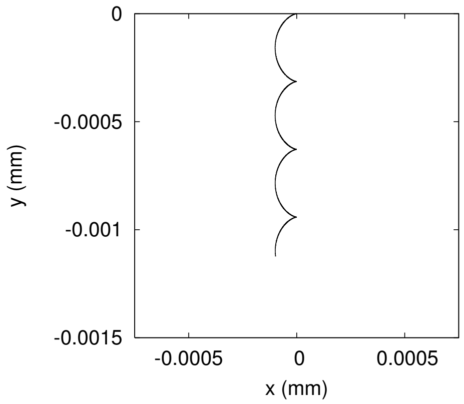

Figure 5.5 – *Ion motion under the influence of a 1 μs ω_- dipolar excitation at 10 V/m.*

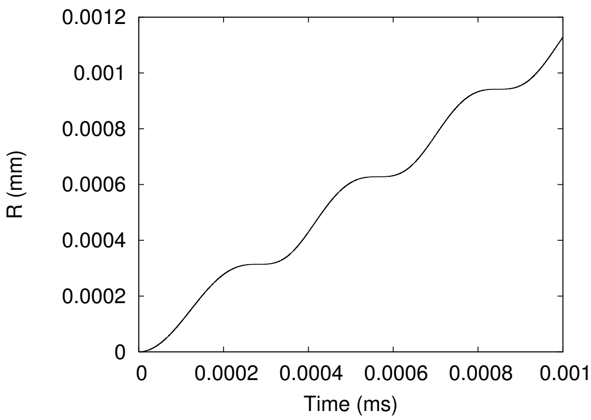

Figure 5.6 – *Distance of the ion from the trap center, R, as a function of time for a 1 μs ω_- dipolar excitation at 10 V/m.*

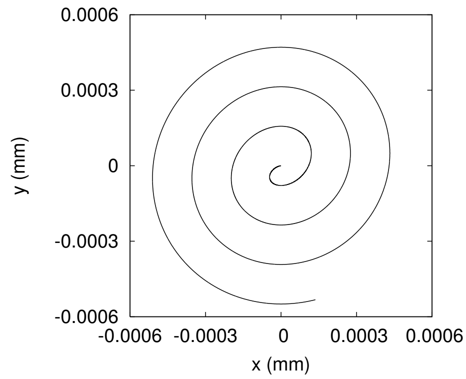

Figure 5.7 – *Ion motion under the influence of a 1 μs ω_+ dipolar excitation at 10 V/m.*

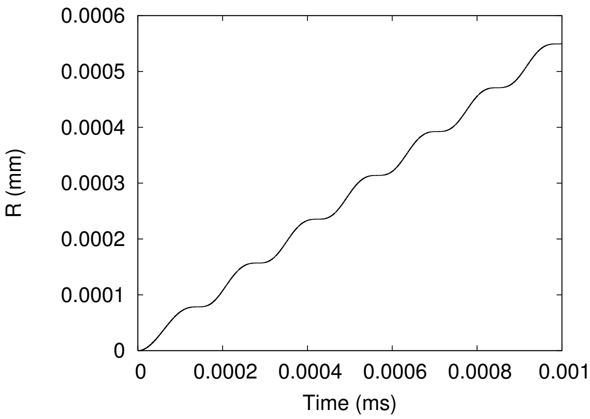

Figure 5.8 – *Distance of the ion from the trap center, R, as a function of time for a 1 μs ω_+ dipolar excitation at 10 V/m.*

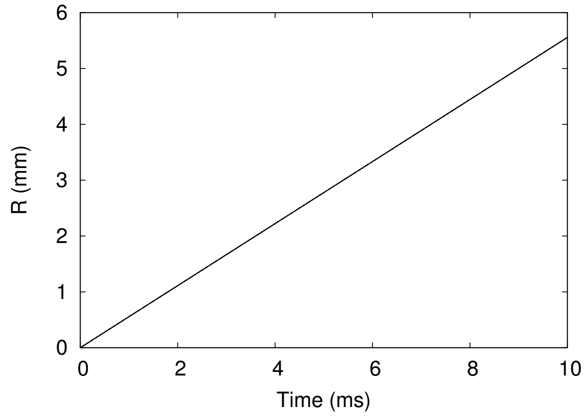

Figure 5.9 – *Distance of the ion from the trap center, R, as a function of time for a 10 ms ω_+ dipolar excitation at 10 V/m.*

have no pronounced effect on the motion. In Fig. 5.9 the motion is plotted on a longer time scale showing only a linear increase of the radius with time. Note that the reduced cyclotron frequency ω_+ is mass dependent, and almost equals the cyclotron frequency $\omega_c = qB/m$, and thus all the effects caused by an electric dipole excitation at the reduced cyclotron frequency do depend on the exact mass of the ion.

Static excitation

When some electrical imperfection is present in a real Penning trap, it could lead to a small electric field in the center of the trap. This situation can also be described as a dipole excitation with $\omega_{rf} = 0$. This mainly results in a magnetron motion for which the center is offset from the trap center with radius

$$R_-^{static} = \frac{k_0}{\omega_-(\omega_+ - \omega_-)}. \tag{5.55}$$

A small cyclotron motion is also induced with radius

$$R_+^{static} = \frac{k_0}{\omega_+(\omega_+ - \omega_-)} \tag{5.56}$$

which is typically much smaller than R_-^{static} since ω_+ is typically much larger than ω_-. This is illustrated in Fig. 5.10.

5.4.2 With damping

To solve the equation of motion with the electrical dipole excitation and damping added, we first need to express the velocity from equation 5.24 in terms of the vector from equation 5.11:

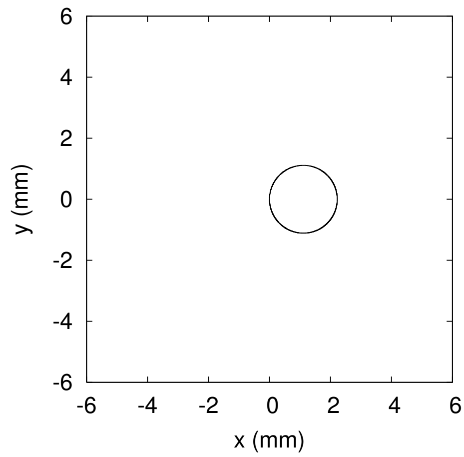

Figure 5.10 – *Ion motion under the influence of a 10 ms static dipolar excitation at 10 V/m.*

$$\begin{aligned}
\dot{x} &= \frac{\omega_+ V_x^+ - \omega_- V_x^-}{\omega_+ - \omega_-} \\
\dot{y} &= \frac{\omega_+ V_y^+ - \omega_- V_y^-}{\omega_+ - \omega_-}.
\end{aligned} \tag{5.57}$$

To simplify the calculation, the notation

$$\gamma = \frac{\delta}{\omega_+ - \omega_-} \tag{5.58}$$

is used. Now the equation of motion becomes

$$\begin{aligned}
\begin{pmatrix} \dot{V}_x^\pm \\ \dot{V}_y^\pm \end{pmatrix} = & \quad \omega_\pm \begin{pmatrix} V_y^\pm \\ -V_x^\pm \end{pmatrix} - \gamma \begin{pmatrix} \omega_+ V_x^+ - \omega_- V_x^- \\ \omega_+ V_y^+ - \omega_- V_y^- \end{pmatrix} \\
& + k_0 cos(\omega_{rf} t + \phi_{rf}) \begin{pmatrix} 1 \\ 0 \end{pmatrix}.
\end{aligned} \tag{5.59}$$

By again making the substitution of equation 5.38 and using assumption 5.42 this can be written as

$$\begin{aligned}
\dot{A}_x^+ &= \frac{k_0}{2} cos(\omega_{rf} t + \phi_{rf}) e^{-i(\omega_+ t + \phi_+)} - \gamma(\omega_+ A_x^+ - \omega_- A_x^- e^{-i\omega_c t + \phi}) \\
\dot{A}_x^- &= \frac{k_0}{2} cos(\omega_{rf} t + \phi_{rf}) e^{i(\omega_- t + \phi_-)} - \gamma(\omega_+ A_x^+ e^{i\omega_c t + \phi} - \omega_- A_x^-).
\end{aligned} \tag{5.60}$$

To first order we can now neglect the high frequency terms containing $e^{\pm i\omega_c t + \phi}$. This then leads to a set of equations

$$\dot{A}_x^+ = \frac{k_0}{2} cos(\omega_{rf} t + \phi_{rf}) e^{-i(\omega_+ t + \phi_+)} - \gamma \omega_+ A_x^+$$

$$\dot{A}_x^- = \frac{k_0}{2} cos(\omega_{rf} t + \phi_{rf}) e^{i(\omega_- t + \phi_-)} + \gamma \omega_- A_x^- \tag{5.61}$$

that can easily be solved yielding

$$\begin{aligned}
A_x^+ = & \quad e^{-\gamma\omega_+ t}\left(A_x^+(0) - \frac{k_0 e^{-i\phi_+}\Big(\omega_+(\gamma - i)cos(\phi_{rf}) + \omega_{rf} sin(\phi_{rf})\Big)}{\gamma^2\omega_+^2 - \omega_+^2 + \omega_{rf}^2 - 2i\gamma\omega_+^2}\right) \\
& + \frac{k_0 e^{-i(\omega_+ t + \phi_+)}\Big(\omega_+(\gamma - i)cos(\omega_{rf} t + \phi_{rf}) + \omega_{rf} sin(\omega_{rf} t + \phi_{rf})\Big)}{\gamma^2\omega_+^2 - \omega_+^2 + \omega_{rf}^2 - 2i\gamma\omega_+^2} \\
A_x^- = & \quad e^{\gamma\omega_- t}\left(A_x^-(0) + \frac{k_0 e^{-i\phi_-}\Big(\omega_-(\gamma - i)cos(\phi_{rf}) - \omega_{rf} sin(\phi_{rf})\Big)}{\gamma^2\omega_-^2 - \omega_-^2 + \omega_{rf}^2 - 2i\gamma\omega_-^2}\right) \\
& - \frac{k_0 e^{i(\omega_- t + \phi_-)}\Big(\omega_-(\gamma - i)cos(\omega_{rf} t + \phi_{rf}) - \omega_{rf} sin(\omega_{rf} t + \phi_{rf})\Big)}{\gamma^2\omega_-^2 - \omega_-^2 + \omega_{rf}^2 - 2i\gamma\omega_-^2}.
\end{aligned} \tag{5.62}$$

Making all substitutions back to the cartesian coordinates finally leads us to the (somewhat lengthy) result:

$$\begin{aligned}
x(t) = & \quad \frac{i}{\omega_+ - \omega_-}\Bigg[e^{\gamma\omega_- t - i(\omega_- t + \phi_-)} \\
& \left(A_x^-(0) + \frac{k_0 e^{-i\phi_-}\big(\omega_-(\gamma - i)cos(\phi_{rf}) - \omega_{rf} sin(\phi_{rf})\big)}{\gamma^2\omega_-^2 - \omega_-^2 + \omega_{rf}^2 - 2i\gamma\omega_-^2}\right) \\
& - \frac{k_0\Big(\omega_-(\gamma - i)cos(\omega_{rf} t + \phi_{rf}) - \omega_{rf} sin(\omega_{rf} t + \phi_{rf})\Big)}{\gamma^2\omega_-^2 - \omega_-^2 + \omega_{rf}^2 - 2i\gamma\omega_-^2}\Bigg] \\
& + \frac{i}{\omega_+ - \omega_-}\Bigg[e^{-\gamma\omega_+ t + i(\omega_+ t + \phi_+)} \\
& \left(A_x^+(0) - \frac{k_0 e^{-i\phi_+}\Big(\omega_+(\gamma - i)cos(\phi_{rf}) + \omega_{rf} sin(\phi_{rf})\Big)}{\gamma^2\omega_+^2 - \omega_+^2 + \omega_{rf}^2 - 2i\gamma\omega_+^2}\right) \\
& + \frac{k_0\Big(\omega_+(\gamma - i)cos(\omega_{rf} t + \phi_{rf}) + \omega_{rf} sin(\omega_{rf} t + \phi_{rf})\Big)}{\gamma^2\omega_+^2 - \omega_+^2 + \omega_{rf}^2 - 2i\gamma\omega_+^2}\Bigg]
\end{aligned}$$

$$\begin{aligned}
y(t) = & \quad \frac{-1}{\omega_+ - \omega_-}\Bigg[e^{\gamma\omega_- t - i(\omega_- t + \phi_-)} \\
& \left(A_x^-(0) + \frac{k_0 e^{-i\phi_-}\big(\omega_-(\gamma - i)cos(\phi_{rf}) - \omega_{rf} sin(\phi_{rf})\big)}{\gamma^2\omega_-^2 - \omega_-^2 + \omega_{rf}^2 - 2i\gamma\omega_-^2}\right) \\
& - \frac{k_0\Big(\omega_-(\gamma - i)cos(\omega_{rf} t + \phi_{rf}) - \omega_{rf} sin(\omega_{rf} t + \phi_{rf})\Big)}{\gamma^2\omega_-^2 - \omega_-^2 + \omega_{rf}^2 - 2i\gamma\omega_-^2}\Bigg]
\end{aligned}$$

$$+\frac{1}{\omega_+ - \omega_-}\Bigg[e^{-\gamma\omega_+ t + i(\omega_+ t + \phi_+)}$$
$$\left(A_x^+(0) - \frac{k_0 e^{-i\phi_+}\Big(\omega_+(\gamma - i)cos(\phi_{rf}) + \omega_{rf}sin(\phi_{rf})\Big)}{\gamma^2\omega_+^2 - \omega_+^2 + \omega_{rf}^2 - 2i\gamma\omega_+^2}\right)$$
$$+\frac{k_0\Big(\omega_+(\gamma - i)cos(\omega_{rf}t + \phi_{rf}) + \omega_{rf}sin(\omega_{rf}t + \phi_{rf})\Big)}{\gamma^2\omega_+^2 - \omega_+^2 + \omega_{rf}^2 - 2i\gamma\omega_+^2}\Bigg]. \tag{5.63}$$

Three separate situations described by these equations can be distinguished and are discussed in the following:

Case 1: $\mathbf{k_0 = 0}$, $\gamma \neq \mathbf{0}$

Here there is no excitation but only damping of the ion motion. Only the terms

$$e^{\mp\gamma\omega_\pm t \pm i(\omega_\pm t + \phi_\pm)} A_x^\pm(0) \tag{5.64}$$

remain in the equations of motion. This corresponds to the exponential damping discussed in section 5.3 with the damping coefficients given by

$$\alpha_\pm = \mp\gamma\omega_\pm. \tag{5.65}$$

These coefficients to first order approximate the coefficients given in equation 5.33. The small difference can be traced back to the neglecting of the higher frequency terms in equation 5.63. Note that also the small frequency shift $\Delta\omega$ given in equation 5.32 is not present due to the neglecting of these terms.

Case 2: $\mathbf{k_0 \neq 0}$, $\gamma = \mathbf{0}$

This is the case of a dipole excitation without damping that was already discussed in detail in section 5.4.1.

Case 3: $\mathbf{k_0 \neq 0}$, $\gamma \neq \mathbf{0}$

Under these conditions the magnetron and cyclotron motion remain uncoupled and thus excitations at those frequencies will be discussed separately.

Magnetron excitation As can be observed in Fig. 5.11 the addition of the damping force has no significant influence on the properties of the magnetron dipole excitation provided the buffer gas pressure is not excessively high (almost no increase in magneton radius without excitation).

Cyclotron excitation The addition of a damping force has a very pronounced effect when applying a dipole excitation at the reduced cyclotron frequency as can be seen in Fig. 5.12. The cyclotron radius no longer increases linearly with time but rather becomes *saturated* at some point.

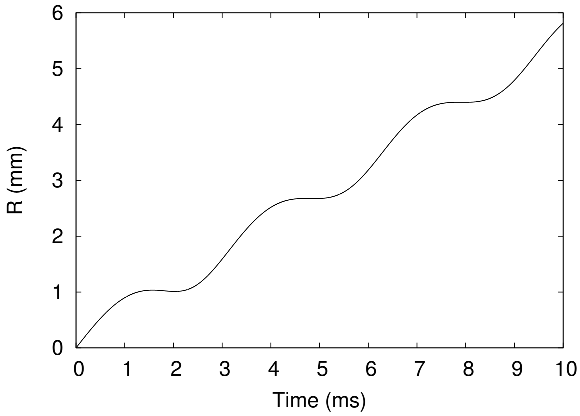

Figure 5.11 – *Distance of the ion from the trap center, R, as a function of time for a 10 ms ω_- dipolar excitation at 10 V/m and with a 10^{-4} mbar He buffer gas pressure.*

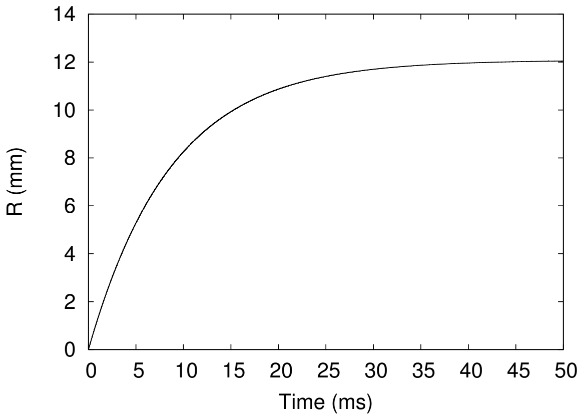

Figure 5.12 – *Distance of the ion from the trap center, R, as a function of time for a 50 ms ω_+ dipolar excitation at 25 V/m and with a 10^{-4} mbar He buffer gas pressure.*

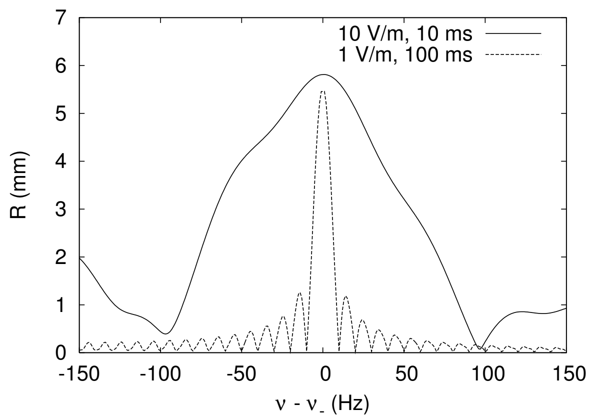

Figure 5.13 – *Distance of the ion from the trap center, R, as a function of excitation frequency for two different excitation times and amplitudes.*

The radius to which the cyclotron radius evolves can be calculated by setting $\omega_{rf} = \omega_+$ in formula 5.63 and then letting t evolve to ∞. This leads to

$$R_+^\infty \approx \frac{E_d}{2\delta B}. \tag{5.66}$$

This saturating behavior is a result of the drastic increase in the kinetic energy of a particle when it is subjected to the dipole excitation at the reduced cyclotron frequency. The higher the ion velocity, the bigger the contribution of the damping becomes, at some point leading to a situation where the driving force of the excitation is canceled by the damping force of the gas. As an excitation at the magnetron frequency doesn't lead to this increase in kinetic energy, it also doesn't give rise to this type of *saturating* behavior.

5.4.3 Frequency scans and mass resolving power

Magnetron

When applying an electric dipolar excitation and letting the frequency vary around the magnetron frequency, a resonance like the ones shown in Fig. 5.13 is obtained. First notice that the particle moves farthest from the trap center when the excitation frequency equals the magnetron frequency ω_-. The excitation time has a clear influence on the width of the excitation resonance: the longer the excitation time the narrower the resonance. For short excitation times the resonance is not symmetric, an effect that is caused by the oscillations seen in Fig. 5.4.

Although some resolution is obtained in the excitation frequency, this resolution doesn't give rise to any mass selectivity as the magnetron frequency is almost not mass dependent (see equation 5.22). Such a resonance could however be used to experimentally determine some trap parameters if they are not exactly known.

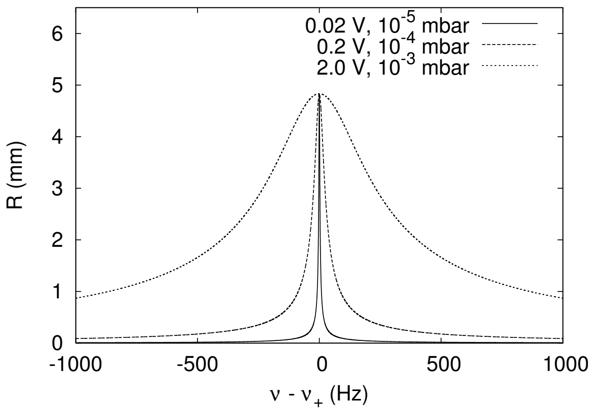

Figure 5.14 – *Distance of the ion from the trap center, R, as a function of excitation frequency for three different excitation amplitudes U_d and buffer gas pressures. All plots are for an excessively long excitation time of 10 s.*

As the result of a dipolar magnetron excitation is not influenced by the presence of a buffer gas, the shape of the resonance curve will obviously also remain unaffected.

Cyclotron

Without damping When no damping is present the width of the resonance curve, and thus the mass resolving power, is only determined by the Fourier limit and thus equals $1/t_{ex}$, where t_{ex} is the excitation time. Note that this is only true for an ideal Penning trap and that the mass resolution in a real trap will eventually be limited by for instance magnetic and electric field imperfections.

With Damping As was shown in section 5.4.2 and Fig. 5.12, the motion of the ion undergoing an electric dipole excitation at the reduced cyclotron frequency is clearly influenced by the presence of the buffer gas. This is also reflected in the resonance shape when making a frequency scan around ω_+. This is illustrated in Fig. 5.14. The width of the resonance is no longer solely determined by the excitation time (all resonances in Fig. 5.14 are for an excessively long excitation time of 10 s) but also by the buffer gas pressure since it is the buffer gas pressure that determines how soon the distance from the trap center reaches its maximal value. Obviously the width of the resonance in the presence of a gas is always larger than the width without buffer gas. The buffer gas thus also negatively affects the mass selectivity that can be obtained by performing an electric dipole excitation at the reduced cyclotron frequency.

5.4.4 Modulations

The shape of the resonance curve (for instance Fig. 5.13) shows fringes at n/t_{ex} spacings with $n = 1, 2, ...$ and t_{ex} the excitation time. These fringes are caused by the fact that a rectangular amplitude modulation is used (off - full power - off) and can be suppressed by using other types of amplitude modulation. One such modulation that can be used is the Gaussian amplitude modulation. The Fourier spectrum of two 100 ms excitations at ν_{ex}, one with rectangular amplitude modulation (no modulation) and one with Gaussian amplitude modulation, are shown in Fig. 5.15. The fringes can be suppressed by the Gaussian modulation. The Gaussian amplitude modulation also reduces the total amount of RF power added to the ion motion for the same excitation amplitude. This can be compensated by increasing the excitation amplitude by a factor

$$\frac{t_{ex}}{\sigma\sqrt{\pi}} \tag{5.67}$$

with t_{ex} the excitation time and σ the width of the modulation, as is demonstrated in Fig. 5.15 (scaled Gaussian).

Especially when using a dipolar excitation at the reduced cyclotron frequency to remove contaminant ions from the trap, using a Gaussian amplitude modulation can reduce the risk of also exciting the motion of the ions of interest except when the two masses are so close together they can not completely be resolved anyway. Note that in Fig. 5.14 no fringes are observed in the resonance due to the excessively long excitation time, but they will be present if shorter, more realistic, excitation times are used.

Other modulation schemes are possible as well. One can for instance combine two (or more) separate frequencies in a dipolar excitation at the reduced cyclotron frequency to remove two (or more) species of contaminant ions (with known mass) at once from the trap. One could even go further and apply a whole band of frequencies, a technique known as SWIFT[1] excitation. More on this technique and tests with it that where performed at ISOLTRAP can be found in Ref. [Kuc02].

5.5 Quadrupolar excitations

Another possible way of exciting the particles inside a Penning trap is through the use of a time dependent quadrupolar electric field of the form

$$\mathbf{E}(t) = -2\frac{U_q}{r_0^2} \cdot cos(\omega_q t + \phi_q) \cdot (y\hat{\mathbf{e}}_y - x\hat{\mathbf{e}}_x). \tag{5.68}$$

Again the constant

$$k_0 = \frac{2qU_q}{mr_0^2} \tag{5.69}$$

is introduced to simplify the notation for the calculations.

[1]Stored Waveform Inverse Fourier Transform

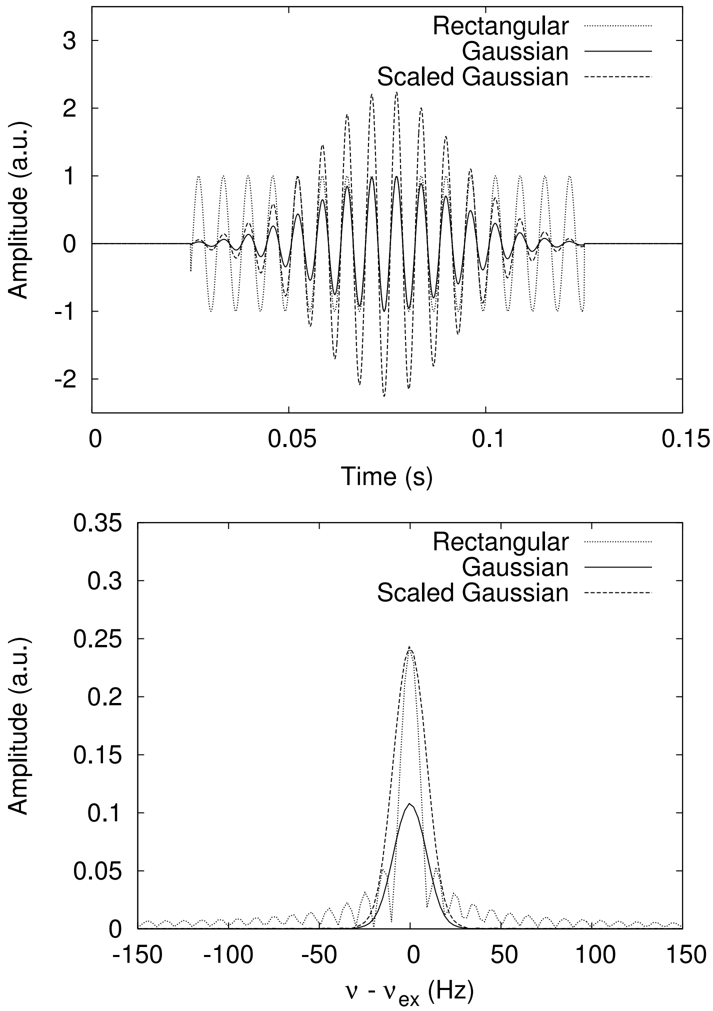

Figure 5.15 – *Effect of a Gaussian amplitude modulation on the frequencies at which the ion motions are excited.*

5.5.1 Without damping

Adding this electric field to the forces in equation 5.5 results in

$$\begin{pmatrix} \ddot{x} \\ \ddot{y} \\ \ddot{z} \end{pmatrix} - \omega_c \begin{pmatrix} \dot{y} \\ -\dot{x} \\ 0 \end{pmatrix} - \frac{\omega_z^2}{2} \begin{pmatrix} x \\ y \\ -2z \end{pmatrix} + k_0 cos(\omega_{rf} t + \phi_{rf}) \begin{pmatrix} -x \\ y \\ 0 \end{pmatrix} = 0. \quad (5.70)$$

By noting that

$$\begin{aligned} x &= -\frac{V_y^+ - V_y^-}{\omega_+ - \omega_-} \\ y &= +\frac{V_x^+ - V_x^-}{\omega_+ - \omega_-} \end{aligned} \quad (5.71)$$

the transformation according to equation 5.11 can again be made yielding

$$\begin{pmatrix} \dot{V}_x^\pm \\ \dot{V}_y^\pm \end{pmatrix} = \omega_\pm \begin{pmatrix} V_y^\pm \\ -V_x^\pm \end{pmatrix} - \frac{k_0 cos(\omega_{rf} t + \phi_{rf})}{\omega_+ - \omega_-} \begin{pmatrix} V_y^+ - V_y^- \\ V_x^+ - V_x^- \end{pmatrix} \quad (5.72)$$

which is, through the substitution of equation 5.38 and assumption 5.42, transformed into

$$\begin{aligned} \dot{A}_x^+ = & \frac{-ik_0}{2(\omega_+ - \omega_-)} \Big(A_x^- e^{-i((\omega_c - \omega_{rf})t + \phi_- + \phi_+ - \phi_{rf}))} \\ & + A_x^- e^{-i((\omega_c + \omega_{rf})t + \phi_- + \phi_+ + \phi_{rf}))} \\ & + A_x^+ e^{i(\omega_{rf} t + \phi_{rf}))} + A_x^+ e^{-i(\omega_{rf} t + \phi_{rf}))} \Big) \end{aligned}$$

$$\begin{aligned} \dot{A}_x^- = & \frac{-ik_0}{2(\omega_+ - \omega_-)} \Big(A_x^+ e^{i((\omega_c + \omega_{rf})t + \phi_- + \phi_+ + \phi_{rf}))} \\ & + A_x^+ e^{i((\omega_c - \omega_{rf})t + \phi_- + \phi_+ - \phi_{rf}))} \\ & + A_x^- e^{i(\omega_{rf} t + \phi_{rf}))} + A_x^- e^{-i(\omega_{rf} t + \phi_{rf}))} \Big). \end{aligned} \quad (5.73)$$

Now we can already see that for this type of excitation the resonance will appear at $\omega_{rf} = \omega_c$. On top of the terms leading to this resonance behavior (the ones containing $\omega_c - \omega_{rf}$) there are terms present which give rise to high frequency modulations at frequencies $\omega_{rf} + \omega_c$ and ω_{rf}. These terms will to first order be neglected leading to

$$\dot{A}_x^\pm = \frac{-ik_0}{2(\omega_+ - \omega_-)} \Big(A_x^\mp e^{\pm i((\omega_c - \omega_{rf})t + \phi_- + \phi_+ - \phi_{rf}))} \Big). \quad (5.74)$$

As the resonance case is of highest interest the focus will be on this case only.

Resonance: $\omega_{\mathbf{rf}} = \omega_{\mathbf{c}}$

Inserting $\omega_{rf} = \omega_c$ into equation 5.74 gives

$$\dot{A}_x^\pm = \frac{-ik_0}{2(\omega_+ - \omega_-)} \Big(A_x^\mp e^{\pm i(\phi_- + \phi_+ - \phi_{rf})} \Big) \quad (5.75)$$

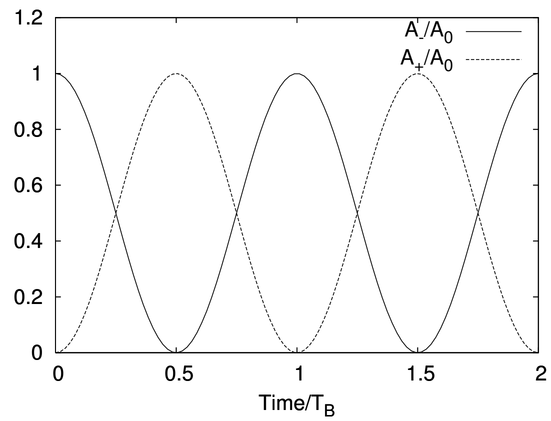

Figure 5.16 – *Conversion between the magnetron and cyclotron motion as the result of the application of a quadrupolar excitation at the cyclotron frequency* ω_c.

the solutions of which are given by

$$\begin{aligned} A_x^+ &= A_x^+(0)cos\left(\frac{k_0 t}{2(\omega_+ - \omega_-)}\right) - iA_x^-(0)e^{i\Delta\phi}sin\left(\frac{k_0 t}{2(\omega_+ - \omega_-)}\right) \\ A_x^- &= -iA_x^+(0)e^{-i\Delta\phi}sin\left(\frac{k_0 t}{2(\omega_+ - \omega_-)}\right) + A_x^-(0)cos\left(\frac{k_0 t}{2(\omega_+ - \omega_-)}\right) \end{aligned} \tag{5.76}$$

with the notation

$$\Delta\phi = \phi_+ + \phi_- - \phi_{rf}. \tag{5.77}$$

It can now easily be seen that the application of a quadrupolar excitation leads to the coupling of the magnetron and cyclotron motions, periodically converting one into the other. The time needed to make one full conversion is given by

$$T_B = \frac{2\pi(\omega_+ - \omega_-)}{k_0}. \tag{5.78}$$

This conversion is illustrated in Fig. 5.16 where it was assumed that originally only a magnetron component is present in the motion. The corresponding distance of the particle from the trap center is shown in Fig. 5.17 (the reduced cyclotron frequency is too high to correctly visualize the cyclotron motion).

Please note again that the resonance frequency ω_c is given by qB/m and as such depends in a clear way on the mass of the particle under investigation.

5.5.2 With Damping

It is also possible (and interesting) to apply such quadrupolar excitation in the presence of a buffer gas. The inclusion of the damping force caused by the buffer gas to equation 5.70 gives

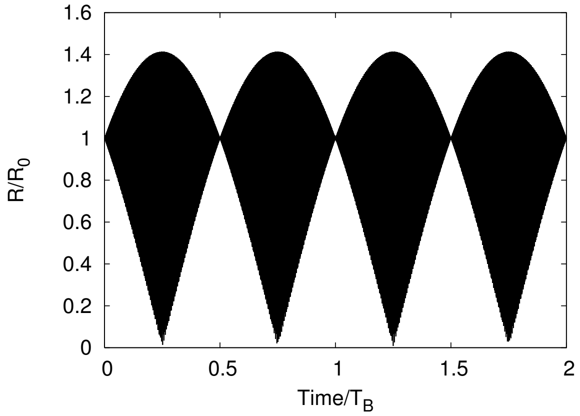

Figure 5.17 – *Distance of the ion from the trap center, R, as a function of time for a quadrupolar excitation at the cyclotron frequency ω_c. The particle started with a pure magnetron motion. Note that the reduced cyclotron frequency is too high to correctly visualize the cyclotron motion.*

$$\begin{aligned}\begin{pmatrix} \dot{V}_x^{\pm} \\ \dot{V}_y^{\pm} \end{pmatrix} = \quad & \omega_{\pm}\begin{pmatrix} V_y^{\pm} \\ -V_x^{\pm} \end{pmatrix} - \gamma\begin{pmatrix} \omega_+ V_x^+ - \omega_- V_x^- \\ \omega_+ V_y^+ - \omega_- V_y^- \end{pmatrix} \\ & - \frac{k_0 cos(\omega_{rf} t + \phi_{rf})}{\omega_+ - \omega_-}\begin{pmatrix} V_y^+ - V_y^- \\ V_x^+ - V_x^- \end{pmatrix} \end{aligned} \tag{5.79}$$

or written in terms of the magnetron and cyclotron amplitudes

$$\begin{aligned} \dot{A}_x^+ = \quad & -\gamma\Big(\omega_+ A_x^+ - \omega_- A_x^- e^{-i(\omega_c t + \phi_+ + \phi_-)}\Big) \\ & - \frac{ik_0}{2(\omega_+ - \omega_-)}\Big(A_x^- e^{-i((\omega_c - \omega_{rf})t + \phi_- + \phi_+ - \phi_{rf}))} \\ & + A_x^- e^{-i((\omega_c + \omega_{rf})t + \phi_- + \phi_+ + \phi_{rf}))} \\ & + A_x^+ e^{i(\omega_{rf} t + \phi_{rf}))} + A_x^+ e^{-i(\omega_{rf} t + \phi_{rf}))}\Big) \end{aligned}$$

$$\begin{aligned} \dot{A}_x^- = \quad & -\gamma\Big(\omega_+ A_x^+ e^{i(\omega_c t + \phi_+ + \phi_-)} - \omega_- A_x^-\Big) \\ & - \frac{ik_0}{2(\omega_+ - \omega_-)}\Big(A_x^+ e^{i((\omega_c + \omega_{rf})t + \phi_- + \phi_+ + \phi_{rf}))} \\ & + A_x^+ e^{i((\omega_c - \omega_{rf})t + \phi_- + \phi_+ - \phi_{rf}))} \\ & + A_x^- e^{i(\omega_{rf} t + \phi_{rf}))} + A_x^- e^{-i(\omega_{rf} t + \phi_{rf}))}\Big). \end{aligned} \tag{5.80}$$

Also here a resonance is present at $\omega_{rf} = \omega_c$. As before the higher frequency terms ($\omega_{rf} + \omega_c$, ω_c and ω_{rf}) are neglected:

$$\dot{A}_x^{\pm} = \mp\gamma\omega_{\pm}A_x^{\pm} - \frac{ik_0}{2(\omega_+ - \omega_-)}\left(A_x^{\mp}e^{\pm i((\omega_c-\omega_{rf})t+\phi_-+\phi_+-\phi_{rf}))}\right). \tag{5.81}$$

Resonance: $\boldsymbol{\omega_{rf} = \omega_c}$

In the case of resonance the equations of motion have now been transformed into

$$\dot{A}_x^{\pm} = \mp\gamma\omega_{\pm}A_x^{\pm} - \frac{ik_0}{2(\omega_+ - \omega_-)}A_x^{\mp}e^{\pm i\Delta\phi}. \tag{5.82}$$

With the notations

$$\eta = \sqrt{(\omega_+ - \omega_-)^2\omega_c^2\gamma^2 - k_0^2} \tag{5.83}$$

and

$$\sigma_{\pm} = -\frac{1}{2}\left(\gamma(\omega_+ - \omega_-) \pm \sqrt{\omega_c^2\gamma^2 - \frac{k_0^2}{(\omega_+ - \omega_-)^2}}\right) \tag{5.84}$$

the solutions of this system of differential equations (for $\eta \neq 0$) are given by

$$\begin{aligned} A_x^+ = &\quad C_1e^{\sigma_-t} + C_2e^{\sigma_+t} \\ A_x^- = &\quad \frac{ie^{-i\Delta\phi}}{k_0}\Big(C_1\gamma\omega_+^2e^{\sigma_-t} + C_2\gamma\omega_+^2e^{\sigma_+t} \\ &\quad -C_1\gamma\omega_-^2e^{\sigma_-t} - C_2\gamma\omega_-^2e^{\sigma_+t} + C_1\eta e^{\sigma_-t} - C_2\eta e^{\sigma_+t}\Big) \end{aligned} \tag{5.85}$$

where the integration constants C_1 and C_2 are determined by the starting conditions

$$\begin{aligned} C_1 &= \frac{-ik_0A_x^-(0)e^{i\Delta\phi} - \gamma A_x^+(0)(\omega_+^2 - \omega_-^2) + A_x^+(0)\eta}{2\eta} \\ C_2 &= A_x^+(0) - C_1. \end{aligned} \tag{5.86}$$

Two separate situations can be distinguished here: when $\sigma_{\pm}$ are real the amplitudes of the magnetron and cyclotron motions are purely exponential functions whereas they are oscillatory functions when $\sigma_{\pm}$ are imaginary.

$\underline{k_0 = \omega_c\gamma(\omega_+ - \omega_-)}$

This is equivalent to $\eta = 0$. In this situation there is a balance in the amount of kinetic energy that is added to the particle due to the conversion of the magnetron motion into the cyclotron motion, and the amount of energy that can be absorbed by the buffer gas. In this situation the reduction of the magnetron motion is optimal and thus we can define the optimal excitation amplitude as

$$U_{q,opt} = \frac{r_0^2\delta B}{2} \tag{5.87}$$

which linearly depends on the buffer gas pressure through the parameter δ. The solution of equation 5.82 under these conditions is given by

$$\begin{aligned} A_x^+ &= e^{-\frac{\gamma}{2}(\omega_+-\omega_-)t}(C_1 + C_2 t) \\ A_x^- &= \frac{ie^{-\frac{\gamma}{2}(\omega_+-\omega_-)t-i\Delta\phi}}{\gamma\omega_c}(C_1\gamma\omega_c + C_2\gamma\omega_c t + 2C_2) \end{aligned} \tag{5.88}$$

with the integration constants

$$\begin{aligned} C_1 &= A_x^+(0) \\ C_2 &= \frac{\gamma\omega_c}{2}(-ie^{i\Delta\phi}A_x^-(0) - A_x^+(0)). \end{aligned} \tag{5.89}$$

Both the magnetron and cyclotron radius thus decrease in radius with a time constant equal to $-\frac{\delta}{2}$ (the same damping coefficient as for the axial motion) although an initial increase is possible depending on the starting conditions.

$\underline{k_0 < \omega_c\gamma(\omega_+ - \omega_-)}$

Here the amplitude of the excitation is too low to provide efficient conversion of magnetron into cyclotron motion. As a result the magnetron motion only shrinks slowly.

$\underline{k_0 > \omega_c\gamma(\omega_+ - \omega_-)}$

If the amplitude rises above the optimal amplitude the conversion between the two motions becomes faster, but the buffer gas can not absorb the additional kinetic energy fast enough. The cyclotron motion created is eventually converted back into magnetron motion and the whole process can start again. Overall the magnetron motion is only dissipated at the same rate as when $k_0 = \omega_c\gamma(\omega_+ - \omega_-)$. The difference however lies in the fact that the constants $\sigma_\pm$ also have an imaginary part leading to an oscillating behavior of the magnetron and cyclotron radii. The frequency of the oscillation between the two motions is now given by

$$\omega_B = \sqrt{\frac{k_0^2}{(\omega_+ - \omega_-)^2} - \omega_c^2\gamma^2}. \tag{5.90}$$

Examples of excitations at different amplitudes are shown in Fig. 5.18 and Fig. 5.19.

The combination of a quadrupolar excitation and the presence of a buffer gas can be used to mass selectively clean an ion ensemble. By first bringing all ions of all masses to a large magnetron radius by using a dipole excitation at the magnetron frequency and then applying a quadrupolar excitation at the cyclotron frequency of the mass of interest only ions of the correct mass will remain in the center of the trap.

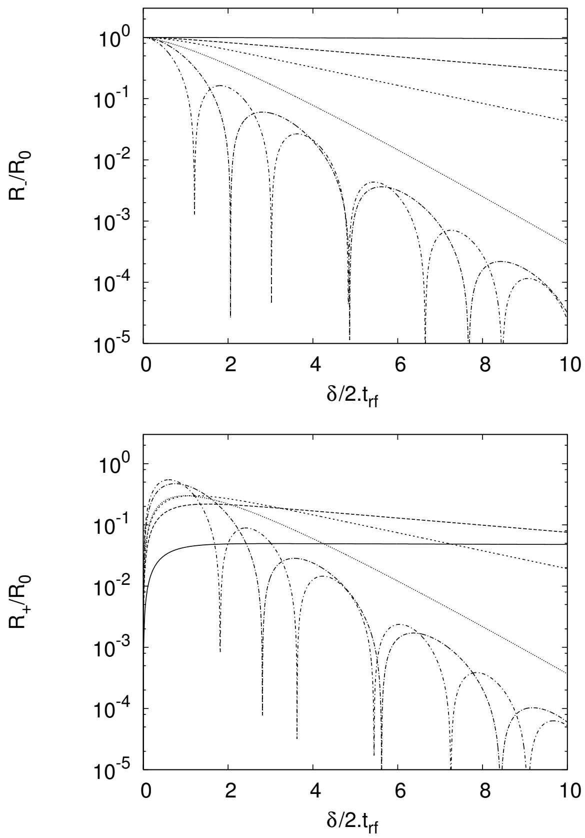

Figure 5.18 – *Amplitudes of the magnetron (top) and cyclotron (bottom) motions under the influence of a quadrupolar excitation at* ω_c *in the presence of a buffer gas. The particle starts with a magnetron component in the motion only. Different excitation amplitudes are shown: (from top to bottom)* $0.1 \cdot U_{q,opt}$, $0.5 \cdot U_{q,opt}$, $0.75 \cdot U_{q,opt}$, $1.0 \cdot U_{q,opt}$, $1.5 \cdot U_{q,opt}$ *and* $2.0 \cdot U_{q,opt}$.

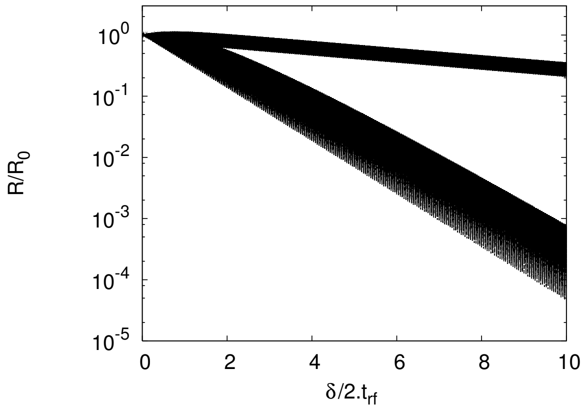

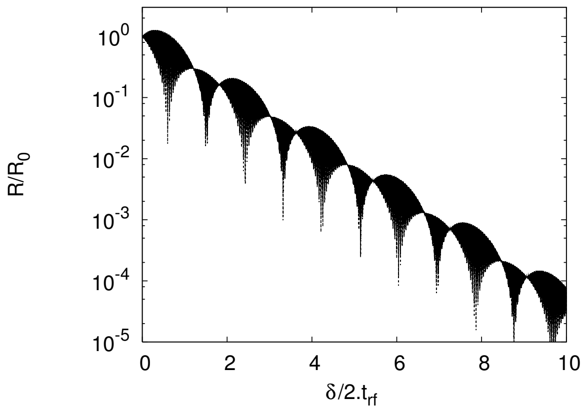

Figure 5.19 – *Distance of the ion from the trap center, R, as a function of time under the influence of a quadrupolar excitation at ω_c in the presence of a buffer gas. The particle starts with a magnetron component in the motion only. Different excitation amplitudes are shown:* $0.5 \cdot U_{q,opt}$ *and* $1.0 \cdot U_{q,opt}$ *(top) and* $2.0 \cdot U_{q,opt}$ *(bottom).*

5.5.3 Frequency scans and mass resolving power

The non-resonant case for the quadrupolar excitation will not be explicitly calculated here, instead the reader is referred to Ref. [Kön95] [2]. In this reference it is shown that the highest mass selectivity with the quadrupolar excitation can be obtained for low buffer gas pressures due to the long cooling times needed for these low pressures.

Also when using a quadrupolar excitation, fringes can be observed when performing frequency scans around the resonance frequency, ω_c in this case. These fringes can again be avoided by using a Gaussian modulation scheme for the excitation amplitude. Applying a combination of different excitation frequencies at once is again possible if one would want to bring different masses to the center of the trap simultaneously.

5.6 Octupolar excitations

Even higher order excitation schemes than the quadrupolar excitations can be used. An excitation scheme that has recently received a lot of interest is the octupolar excitation [Rin07, Eli07] where the exciting field is given by

$$\mathbf{E}(t) = -4\frac{U_o}{r_0^4} \cdot cos(\omega_o t + \phi_o) \cdot \left((x^3 - 3xy^2)\hat{\mathbf{e}}_x + (y^3 - 3x^2 y)\hat{\mathbf{e}}_y\right). \tag{5.91}$$

This type of excitation has been shown to be potentially very useful for precise mass determinations. Despite some systematic investigations using simulations, no analytical solution has been found for the equations of motion under the influence of this excitation. The usefulness of this type of excitation for the case of WITCH is still under investigation [Van07], although the complex nature of this type of excitation definitely complicates matters.

[2] Note that in this reference there is a factor 4 mistake in the definition of the quadrupolar excitation field.

Chapter 6

Penning trap simulations

In this chapter the article *Ab initio simulations on the behavior of small ion clouds in the WITCH Penning trap system* is presented. It discusses computer simulations conducted to understand the behavior of a cloud of ions in the Penning traps. This work should be considered as a first step towards understanding the behavior of larger ion clouds and as a starting point for a full Monte Carlo simulation based analysis of WITCH experimental data. At the end of the chapter additional simulations on the possibility of performing isobaric purification in the cooler trap are presented.

Ab initio simulations on the behavior of small ion clouds in the WITCH Penning trap system

S. Coeck[a], B. Delauré[a], M. Herbane[a], V. Yu. Kozlov[a], I.S. Kraev[a], M. Tandecki[a], F. Wauters[a], M. Beck[b], P. Delahaye[c], A. Herlert[c], S. Sturm[c], N. Severijns[a]

[a] *K.U.Leuven, Instituut voor Kern- en Stralingsfysica, Celestijnenlaan 200D, B-3001 Leuven, Belgium*
[b] *Westfälische Wilhelms-Universität Münster, Institut für Kernphysik, Wilhelm-Klemm Str. 9, D-48149 Muenster, Germany*
[c] *Physics Department, CERN, 1211 Geneva 23, Switzerland*

Published in: *Nuclear Instruments and Methods in Physics research A **574** (2007) 370-384*

6.1 Introduction

The advent of various types of ion traps during the last decades has opened up new opportunities for improved access to a wide range of observables for atomic physics, nuclear physics, and low energy weak interaction research [Klu04]. Thus a number of experiments are on their way to measure the so called $\beta-\nu$ angular correlation coefficient a which is sensitive to the precise nature of the weak interaction [Bec03, Ban05, Gor05, Ber03, Sci04]. Ion or atom traps are used for such experiments since the kinematics of the neutrino emitted in β-decay is usually inferred from the recoiling nucleus which has an energy of the order of a few tens to a few hundred eV only. Because of the low energies involved, the source cannot be produced by implantation into a foil since this would greatly disturb a precise measurement on the recoiling nucleus. The WITCH-experiment (Weak Interaction Trap for CHarged particles [Bec03]) aims to measure the energy spectrum of the recoil ions after β-decay. Therefore it was opted to use ions stored in a Penning trap as radioactive source for this experiment. The energy of the ions recoiling after β-decay in the Penning trap is determined with a retardation spectrometer [Bec03]. Since the number of detected events is crucial for the precision that can eventually be reached it is advantageous to have a source that is as strong as possible. However, it is clear that effects caused by ion clouds containing a large number of ions inside the Penning trap, that would influence the precision of the measurements, have to be avoided or at least investigated in detail. This paper presents results of ab initio simulations that were performed to study the behavior of such ion clouds in a Penning trap. These simulations were performed for the WITCH setup, but apply to other Penning trap experiments as well.

6.2 Penning traps

A Penning trap is a device in which charged particles can be stored and manipulated [Bro86]. A strong magnetic field $\mathbf{B} = B \cdot \hat{\mathbf{e}}_z$ confines the particles in the radial direction while an electrostatic field of the form

$$\mathbf{E} = \frac{U_0}{2d^2}(x\hat{\mathbf{e}}_x + y\hat{\mathbf{e}}_y - 2z\hat{\mathbf{e}}_z) \tag{6.1}$$

with the potential difference U_0 between the ring and endcap electrodes and the trap dimension $d = \sqrt{(z_0^2 + r_0^2/2)/2}$, r_0 being the radius of the ring electrode and $2z_0$ being the axial separation between the endcap electrodes in the case of a hyperbolic trap, confines the particles in the axial direction. Note that for other trap geometries the trap dimension d differs slightly from the ideal case [Gua95].

The combination of these two fields leads to a separation of the motion of a particle with mass m and charge q into three independent modes:

- The axial motion: a harmonic oscillation along the trap axis with frequency

$$\nu_z = \frac{\omega_z}{2\pi} = \frac{1}{2\pi}\sqrt{\frac{qU_0}{md^2}}. \tag{6.2}$$

- The magnetron motion: a rotation at the magnetron frequency ν_- of the particle around the trap center in a plane perpendicular to the magnetic field axis.

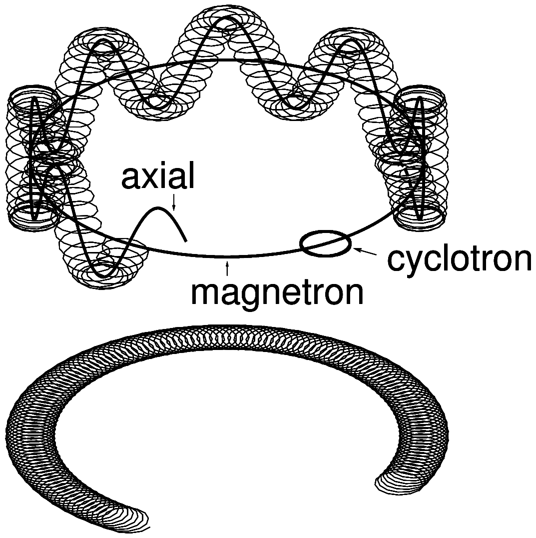

Figure 6.1 – *The motion of a charged particle in an ideal Penning trap consists of three separate motions: the axial motion, the magnetron motion and the cyclotron motion. The full motion and a projection of the motion in the radial plane are shown.*

- The cyclotron motion: a fast rotation of the charged particle around the magnetic field lines with the reduced cyclotron frequency ν_+.

The magnetron frequency and the reduced cyclotron frequency are given by

$$\omega_\pm = 2\pi\nu_\pm = \frac{1}{2}\left[\omega_c \pm \sqrt{\omega_c^2 - 2\omega_z^2}\right] \tag{6.3}$$

with the cyclotron frequency

$$\omega_c = \frac{qB}{m}. \tag{6.4}$$

The overall motion of a charged particle inside a Penning trap is shown in Fig. 6.1.

The presence of an inert buffer gas in the trap allows the removal of kinetic energy from the particles that are stored in the trap. In this way the axial and cyclotron motions can be cooled. The buffer gas cooling is often described by adding a well known Stokes damping force to the equations of motion

$$\mathbf{F}_D = -\delta m\dot{\mathbf{r}} \tag{6.5}$$

since it allows an analytical description of the particle's motion. In the simulations presented here, a different approach is followed and more realistic collisions with the neutral buffer gas particles are taken into account (see section 6.5). For a complete analytical description of the equations of motion of a single particle inside a Penning trap the reader is referred to for instance the review paper by Brown and Gabrielse [Bro86].

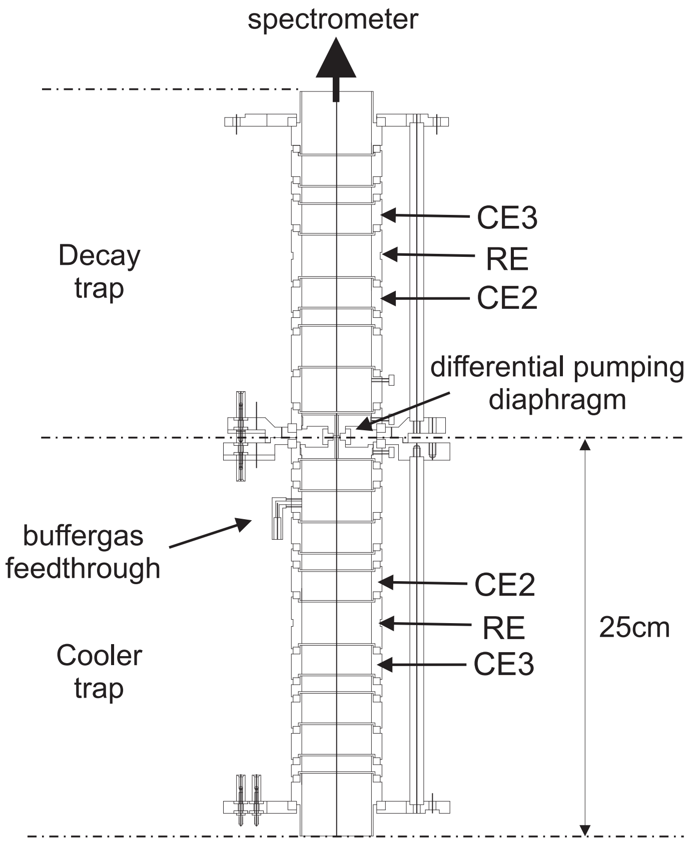

Figure 6.2 – *The two WITCH Penning traps and the main parameters for the traps. RE refers to the central ring electrode while CE marks the correction electrodes.*

6.3 Overview of the WITCH Penning trap system

The WITCH-setup uses two separate Penning traps located in the same 9 T magnetic field. The use of two traps permits to separate the functions of cooling/purification on the one hand and storage for radioactive decay on the other hand. Both Penning traps, which are almost exact copies of the trap described in [Rai97], are of cylindrical shape (see Fig. 6.2) with an inner diameter of 4 cm and are used with a characteristic depth $U_0/d^2 = 1.8 \cdot 10^4$ V/m^2. The first trap, referred to as the cooler trap, is used to capture, cool, and purify the beam of particles that is received from ISOLDE [Kug92] via the REXTRAP cooler and buncher Penning trap [Ame05]. For this purpose helium buffer gas at room temperature can be subjected to the trap volume, at a typical pressure of $10^{-3} - 10^{-5}$ mbar. The second trap, the decay trap, constitutes the real radioactive source of the experiment and as such a minimum of scattering effects

B	9 T
U_0/d^2	$1.8 \cdot 10^4$ V/m^2
T	294 K
buffer gas (cooler)	He
$p_{gas}(cooler)$	$10^{-3} - 10^{-5}$ mbar
$N_{particles}$	$10^5 - 10^7$

Table 6.1 – *Overview of the main parameters for the WITCH Penning traps.*

should occur here. To limit the gas pressure in the decay trap, a differential pumping diaphragm is installed between both traps. The central ring electrode of both traps (marked RE) is eight-fold segmented while all correction electrodes (CE) are four-fold segmented, thus permitting the application of various azimuthal excitation schemes related to the different eigenmotions of the ions inside the trap (discussed in more detail in sections 6.6.4 and 6.6.5). For the WITCH experiment the properties of the ion cloud have to be known for both traps to enable a precise measurement of the $\beta - \nu$ angular correlation through the shape of the recoil-ion energy spectrum. Typical trap parameters for the WITCH Penning trap system are also given in table 6.1.

6.4 Motivation for simulations

The equations of motion of a single particle inside a Penning trap, also in the presence of excitation fields, are well known and can be solved analytically [Bro86]. Ion clouds with high densities and low temperatures can be described as non-neutral plasmas and their properties are also well understood [Dub99]. At the typical densities and temperatures which apply to the WITCH Penning traps or similar Penning trap systems, e.g. REXTRAP [Ame05], one is far from the one particle picture but also still not in the plasma regime. As the equations of motion for a large number of interacting particles that do not form a plasma cannot be solved analytically, one has to resort to computer simulations to understand the behavior of such ion clouds.

The problem with such simulations is that, due to the inclusion of the Coulomb interaction, the complexity of the direct simulations is at least of $\mathcal{O}(N^2)$, N being the number of particles, leading to a very fast increase in computing times for ion clouds containing a large number of particles. Several solutions have been proposed to remedy this, for instance by using a scaled Coulomb force [Bec01]. For this work we have opted to first use the direct simulation of the cloud in order to avoid any effects induced by these approximations. As a consequence only clouds with a limited number of particles (up to about 1000) could be simulated instead of the expected $10^5 - 10^7$ particles. This still results in many days (weeks) of CPU time. Note that due to the adaptive stepsize used the timestep becomes smaller and simulations take longer as the motion becomes more complex (increased cyclotron motion for instance). It is clear that the results presented here can not just be extrapolated to these higher ion numbers. Nevertheless, a number of effects important for the WITCH experiment become apparent already with these clouds containing a limited number of particles. In section 6.6.8 of this paper a number of simulations is presented where the scaled Coulomb force approach is used to obtain the size of the ion cloud for larger numbers of particles.

The focus of this investigation will be on properties of the ion cloud that influence the precision that can be obtained in the WITCH experiment:

- The size of the cloud. This parameter determines in how far the ions can be manipulated to form a good radioactive source (section 6.6.3).
- The possibility of mass selectively purifying the cloud. This is of importance for the preparation of the cloud as a clean radioactive source (sections 6.6.4 and 6.6.5).
- The transfer of the cloud from one trap to the other (section 6.6.6). Low energy transfer is needed to obtain a low thermal energy ion cloud, which is of major importance for the resolution of the experiment.
- The thermal motion of the ions inside the cloud. This is one of the major factors determining the achievable experimental precision (section 6.6.7).

6.5 Simulation method and parameters

The simulation code used was developed in C++ and contains specific SSE (Streaming SIMD Extensions) coding to optimize it for speed on Pentium4® machines. The heart of the simulation code is a fifth order Runge-Kutta integration routine with adaptive stepsize adopted from [Pre92]. In addition, the code has the important feature of including collisions with the buffer gas instead of using a simple drag force approach.

First all particles are generated randomly (uniformly) inside a centered spheroid with random, but small, velocity components (see section 6.6.2). Then the equations of motion of all particles are solved simultaneously with the Coulomb force being included. Several radial excitations of the ions are possible as well and can be included at this stage of the simulations. Finally buffer gas collisions were simulated at the end of each time step using the following three-step procedure within for each ion:

- Was there a collision? Within the Langevin theory [Gio58] the probability P of having an ion-buffer gas collision is calculated as

  $$P = 1 - \exp\left(- \frac{e}{2\epsilon_0}\sqrt{\frac{\alpha_e}{\mu}}\frac{p}{kT} \cdot \Delta t\right) \tag{6.6}$$

  with e the unit of charge, ϵ_0 the permittivity of free space, α_e the polarizability of the buffer gas atoms, μ the reduced mass of the ion and buffer gas atom, p the pressure of the buffer gas, T its temperature, k the Boltzmann constant and Δt the step size in the integration routine which is typically $10^{-8} - 10^{-9}$ s [Lon93].

B	9 T
U_0/d^2	$1.8 \cdot 10^4$ V/m^2
T	294 K
buffer gas (cooler)	He
$p_{gas}(cooler)$	10^{-3} mbar
q	$1 \cdot e$
m	39 u
$N_{particles}$	500
ν_z	$3.358572 \cdot 10^4$ Hz
ν_c	$3.543718 \cdot 10^6$ Hz
ν_-	$1.592 \cdot 10^2$ Hz
ν_+	$3.543559 \cdot 10^6$ Hz

Table 6.2 – *Overview of the main parameters used in the simulations.*

- If a collision has occurred a gas atom is generated with an energy drawn randomly according to the Maxwell-Boltzmann distribution.

- Finally the new velocity components are calculated assuming a hard sphere collision.

By including buffer gas collisions a realistic temperature of the buffer gas can be taken into account. This is of major importance for the WITCH-experiment since the temperature of the ion cloud determines to a great extent the resolution of the retardation spectrometer (see section 6.6.7).

In all simulations the pressure of the buffer gas, where applicable, was set to 10^{-3} mbar. The magnetic field B was chosen along the z-axis and was set to 9 T. No field inhomogeneities or imperfections were taken into account. All simulations were performed for a cloud of 500 singly charged positive ions ($q = 1 \cdot e$) of mass $m = 39$ u, but results are applicable to other masses as well. As an overview, all parameters used in the simulations and the respective motional frequencies are summarized in table 6.2.

6.6 Simulation results and discussion

6.6.1 Buffer gas collisions

Before using the routine for simulating interactions with the buffer gas, it was first tested by comparing its output with experimental data. To this end, ions were simulated to be drifting through a gas under the influence of an applied electric field E. After some time the velocities of all ions converged to the velocity v_d. The standard ion mobility K_0 under these conditions is then given by

$$K_0 = \frac{v_d}{E} \cdot \frac{p/p_N}{T/T_N} \tag{6.7}$$

where the pressure of the buffer gas p is expressed in units of the normal pressure $p_N = 1.013 \cdot 10^5$ Pa and the temperature T in units of the normal temperature

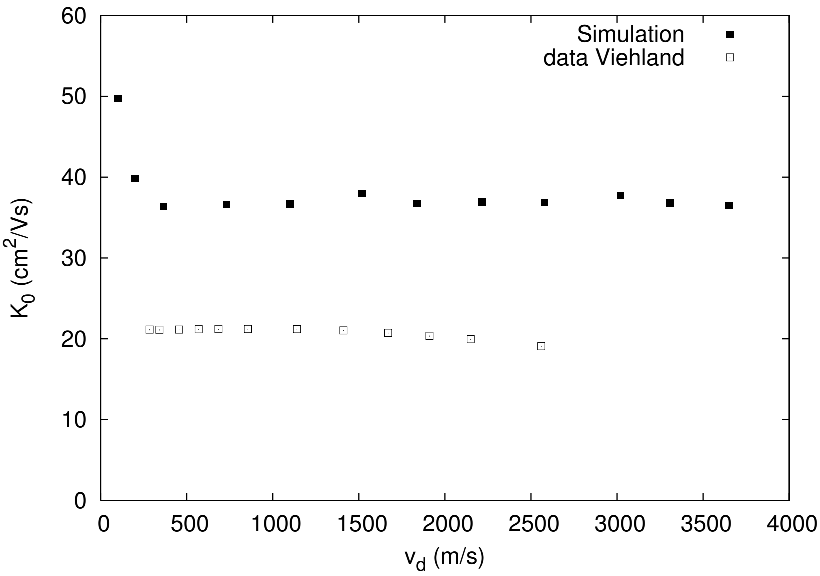

Figure 6.3 – *Comparison of the standard ion mobility K_0 obtained from simulations with experimental results taken from Viehland and Mason [Vie95].*

$T_N = 273$ K [Vie95]. In Fig. 6.3 the simulated standard ion mobility K_0 is plotted for different drift velocities v_d for $^{39}K^+$ ions in a He buffer gas at 294 K and compared to data from [Vie95]. Neglecting a factor of about two in the resulting mobility, which would correspond to a factor of two difference in pressure, the overall agreement between simulation and experiment is good. However, at low drift velocities the simulations start to deviate from the experimental data. The deviation of the simulated values at lower drift velocities is probably due to the fact that the equilibrium conditions for Langevin collisions are not fulfilled. The origin of the overall offset (about a factor 2) is not known. The deviation has been consistently seen in several tests and is thus not believed to be a statistical fluctuation. Since the ion velocities are usually larger than this, no deviation is expected in the simulations. More sophisticated routines permitting a more accurate description of the ion-buffer gas collisions do exist (see e.g. Ref. [Sch06]), but this more simple routine was used here for reasons of computational simplicity and speed.

6.6.2 Initial parameters

The initial spatial coordinates and velocity components for all ions were chosen such that after letting the system evolve for a long time (60 ms in these simulations) the distribution of the ions became independent of the exact starting conditions. Two points have to be carefully considered in this respect:

- The initial cloud size has to be smaller than the final one since buffer gas cooling alone cannot reduce the cloud size.

- The initial velocities have to be chosen low enough because the magnetron component of the radial motion cannot be reduced by buffer gas collisions.

If the initial radial velocities are chosen too large the cloud appears larger in the radial direction. This would for instance experimentally correspond to off-axis injection of the ions into the Penning trap. This larger cloud size can be remedied by applying a ν_c quadrupolar excitation, which allows the magnetron motion to be reduced (see section 6.6.5).

For the simulations presented here the ions started randomly distributed inside a sphere of 0.05 mm radius and all three velocity components randomly chosen between 0 and 10 m/s. The ion parameters obtained after the equilibration (60 ms) where subsequently used as input parameters for the rest of the simulations discussed below.

6.6.3 Cloud size

The general points of importance for the size of the ion cloud inside a Penning trap are:

- The magnetic field is most homogeneous near the trap center.
- In a cylindrical trap the quadrupole shape of the trapping potential is only achieved near the trap center.

For instance for the WITCH magnet a homogeneity of $< 1 \cdot 10^{-5}$ is obtained in a volume of 40 × 10 mm around the trap center but it rapidly worsens outside of this volume. Any deviation from the magnetic field strength in the center of the trap leads to frequency shifts and can thus disturb the mass-selective selection of ions, which is required to produce a purified ion ensemble for the β-decay.

Especially for the WITCH setup there are two other important points:

- The energy spread caused by the transfer of the ions between the cooler trap and the decay trap depends on the size of the cloud in the cooler trap and has a large impact on the response function of the retardation spectrometer (this will be discussed in section 6.6.6).
- The spatial distribution of the particles inside the decay-trap affects the response function of the spectrometer [Del04].

The size of the cloud is obtained from the simulations by assuming that the cloud has a prolate spheroid shape with size a in the radial direction (semi-minor axis) and size c in the axial direction (semi-major axis). The error bars given in, e.g., Fig. 6.4 or Fig. 6.5 represent the fit error when fitting the cloud to the assumed spheroidal shape although the statistical precision of these results is most often worse than the quoted fitting error. Although the description of the cloud as a uniform-density spheroid is strictly speaking only correct when the Debye length in the plasma is much smaller than the size of the plasma (which is not the case in the simulations presented here) and the plasma itself

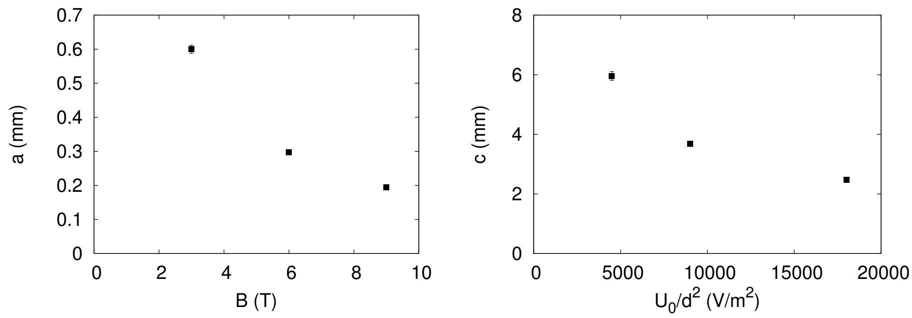

Figure 6.4 – *The influence of the magnetic field on the radial size of the cloud (left) and the influence of the electric field on the axial size of the cloud (right).*

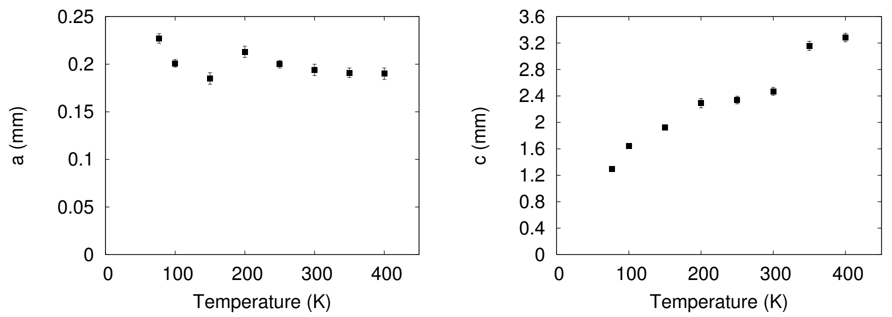

Figure 6.5 – *Plot of the influence of the buffer gas temperature on the radial (left) and axial (right) size of the cloud.*

is much smaller than the size of the trap (which is the case here) [Dub99], it allows one to quantitatively describe the simulation results. The fact that the ion cloud is much smaller than the dimensions of the Penning trap justifies the neglecting of image charges induced in the electrodes by the ion cloud for these simulations.

The size of the ion cloud depends on the strength of both the electric and magnetic field in the Penning trap. The magnetic field primarily influences the radial size of the cloud, which becomes smaller as the magnetic field strength increases, while the size of the electric field primarily influences the axial size of the cloud, which in turn becomes larger as the electric potential well becomes more shallow (see Fig. 6.4). As the temperature of the buffer gas is changed the axial size of the cloud of 500 particles in the cooler trap also changes while the radial size is mostly unaffected, as can be seen from Fig. 6.5.

Note that the axial size c is of the order of millimeters while the radial size a is only of the order of a few tenths of a millimeter for the electric and magnetic fields typically used in the WITCH Penning trap system. Thus, the cloud is typically very elongated along the axis of the magnetic field.

6.6.4 Dipolar excitations of the ion cloud

Radiofrequency excitations are required to manipulate the ion motion either for mass selection or cooling of the stored ions. Electric dipolar excitations with an electric field of the form

$$\mathbf{E}(t) = E_d \cdot cos(\omega_d t + \phi) \cdot \hat{\mathbf{e}}_i \tag{6.8}$$

with $i = x, y, z$, can be used to excite one of the three eigenmotions of the ions as defined in section 6.2. The influence of all three excitations on a small cloud of ions containing a small number of ions will now be discussed separately.

ν_- excitations

For the case of a single particle inside a Penning trap, azimuthal ($i = x$ or y in equation 6.8) dipolar excitations at the magnetron frequency ν_- cause an enlargement of the particle's magnetron radius. If an ion cloud is considered, each particle enlarges its magnetron orbit. This, however, happens in a synchronized way so that the overall effect observed is a shift of the center of the ion cloud and neither an enlargement of the cloud, nor the creation of a ring like cloud, as would be the case for an asynchronous motion of the particles. The increase in distance of the cloud's center of mass from the center of the trap (figure 6.6) is empirically described by a linear function with a sinusoidal modulation

$$R(t) = At + Bsin(\omega_m t + \phi_m). \tag{6.9}$$

The slope of the linear increase, A, depends linearly on the excitation amplitude as does the amplitude of the modulation, B:

$$\begin{aligned} A &= A_0 \cdot E_d \\ B &= B_0 \cdot E_d. \end{aligned} \tag{6.10}$$

In the case of a single particle [Coe07] the parameter A_0 is described by equation 6.11.

$$A_0 = \frac{q}{m} \frac{1}{2(\omega_+ - \omega_-)} \tag{6.11}$$

The fitted value of A_0 for the simulations with a ion cloud with a small number of ions is given by $A_0 = 5.582(1) \cdot 10^{-2}$ m^2/Vs and agrees well with the one calculated with equation 6.11: $A_0 = 5.556 \cdot 10^{-2}$ m^2/Vs. This indicates that the motion of the center of mass of the ion cloud of 500 particles is well described by the single particle picture. The parameter B_0 is described by the following equation:

$$B_0 = \frac{q}{m} \frac{1}{4\omega_-(\omega_+ - \omega_-)}. \tag{6.12}$$

In resonance the frequency of the modulation is exactly equal to twice the magnetron frequency

$$\omega_m = \omega_d + \omega_- = 2\omega_- \tag{6.13}$$

indicating that the motion of the center of mass is not a circular spiral but rather an elliptical spiral (flattened spiral). If a dipolar excitation is applied along the

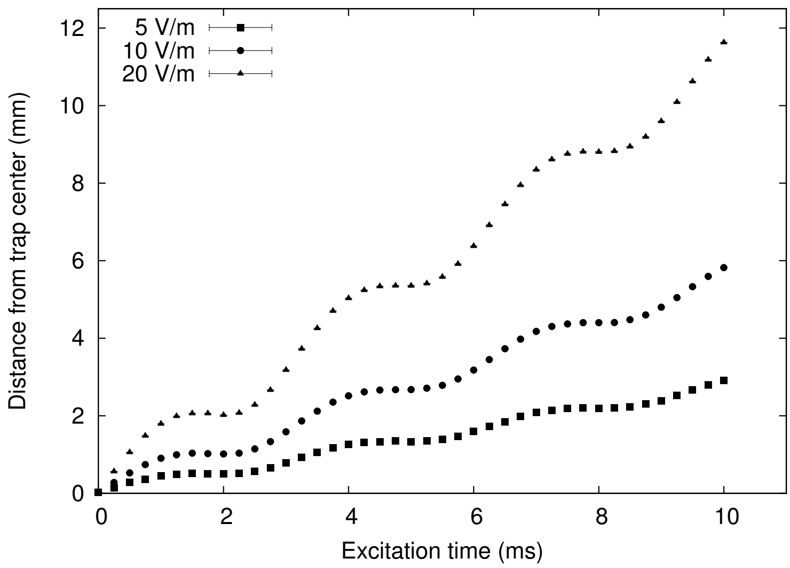

Figure 6.6 – *Shift of the center of mass of the ion cloud from the trap center due to a radial dipolar excitation at the magnetron frequency for different excitation times and amplitudes.*

x-axis the spiralling motion is flattened along the $x = y$ line and extended along the $x = -y$ line, independently of the phase of the exciting dipole field. When the excitation is stopped, the cloud starts a circular motion at the radius it obtained from the excitation. During the whole excitation no change in the cloud size or the velocity distribution of the ions inside the cloud is seen. The influence of the buffer gas on this excitation is negligible and the same result is obtained without buffer gas collisions.

The radial distance from the center after an excitation of 10 ms at 10 V/m as a function of the excitation frequency is plotted in Fig. 6.7. Also plotted is a calculated spectrum for a single particle were the phase difference between the particle's magnetron motion and the excitation field is set to zero, and the particle starts from the center of the trap without any initial velocity [Coe07]. The cloud moves farthest out of the center if the excitation frequency exactly equals the magnetron frequency $\nu_- = 159.2$ Hz and the motion of the center of the cloud is well described by the single particle picture.

ν_+ excitations

When the frequency for the azimuthal dipolar excitation equals the reduced cyclotron frequency, $\nu_+ = 3.543559 \cdot 10^6$ Hz, the situation is quite different. Although an excitation of this type also leads to a shift of the ion cloud away from the trap center, it at the same time gives rise to an expansion of the cloud in both the radial and axial directions as well as to an increase in the average

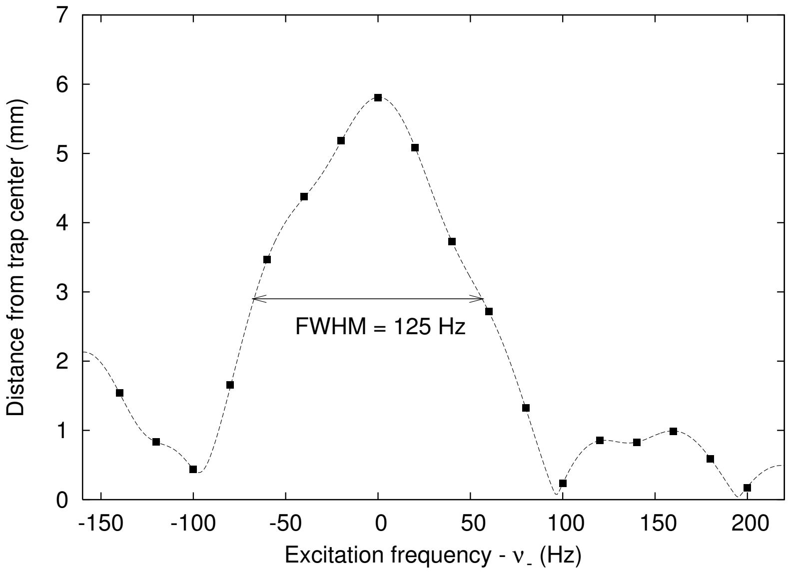

Figure 6.7 – *Radial distance of the ion cloud's center of mass from the trap center after an excitation of 10 ms at 10 V/m as a function of the excitation frequency. Simulations for a cloud of 500 particles (points) and an analytical calculation for the case of a single particle with the same parameters (line) are shown.*

radial and axial velocities (see Fig. 6.8). The expansion of the cloud and the increase in average axial velocity are caused by the increased radial velocity combined with the collisions with the buffer gas particles. These effects depend on the collision kinematics and as such are strongly depending on the mass of both the ions and the buffer gas particles. Without buffer gas, the cloud would only shift from the center and the average radial velocity of the particles would be increased (see Fig. 6.9). It seems that a periodic beating is present in the axial size and velocity. This oscillation cannot be followed with the present simulation, since the frequency is much larger than the possible sampling rate of the simulation. Note again that in these simulations the collisions with the buffer gas particles are approximated by hard sphere collisions and therefore represent only a crude approximation of reality for this type of effects that strongly depend on the exact collision kinematics.

After applying the excitation for some time the axial size of the cloud and the distance from the trap center as well as the mean axial and mean radial velocity become constant even though the exciting electric field is still applied (see Fig. 6.8). This is caused by the buffer gas damping of the ion's motion. For a single particle the maximal distance from the trap center [Coe07, Sch01] is given by

$$R_\infty^+ \approx \frac{E_d}{2\delta B}. \tag{6.14}$$

Taking into account the factor of about two by which the buffer gas collision routine overestimates the ion mobility, equation 6.14 agrees quite well with the data given in Fig. 6.8 showing that the motion of the center of mass of the ion cloud is again well described by the single particle picture.

Since the reduced cyclotron frequency ν_+ is mass dependent all effects discussed here in relation to ν_+-excitations are mass dependent, too, and can thus be used to distinguish between ions of different mass inside the trap. An example of a simulated frequency scan around the reduced cyclotron frequency is given in Fig. 6.10 together with a fit to the data by a Lorentzian peak function. For excitation durations longer than 20 ms as shown in the example neither the width nor the amplitude of the resonance is changed. This indicates that for all excitation frequencies the amplitude of the ion motion has saturated. This leads to a FWHM of the resonance that is no longer dependent on the excitation time, t_{ex}, i.e. $\Delta\nu(FWHM) = 1/t_{ex}$ (e.g. $t_{ex} = 20\text{ms} \rightarrow FWHM = 50\text{Hz}$). Rather the FWHM is mainly determined by the buffer gas pressure, since it determines when the increase in cyclotron motion is balanced by the cooling of this motion by the buffer gas. The same effect is observed in the case of a single particle [Coe07, Sch01]. This has to be taken into account when using this excitation for mass selection as in the presence of a buffer gas the resolution obtained can be severely reduced.

The mass dependence of this excitation was for instance already used in the WITCH cooler trap to determine the main contaminants in the buffer gas [Koz06] by looking for the loss of ions when the excitation frequency equals their reduced cyclotron frequency.

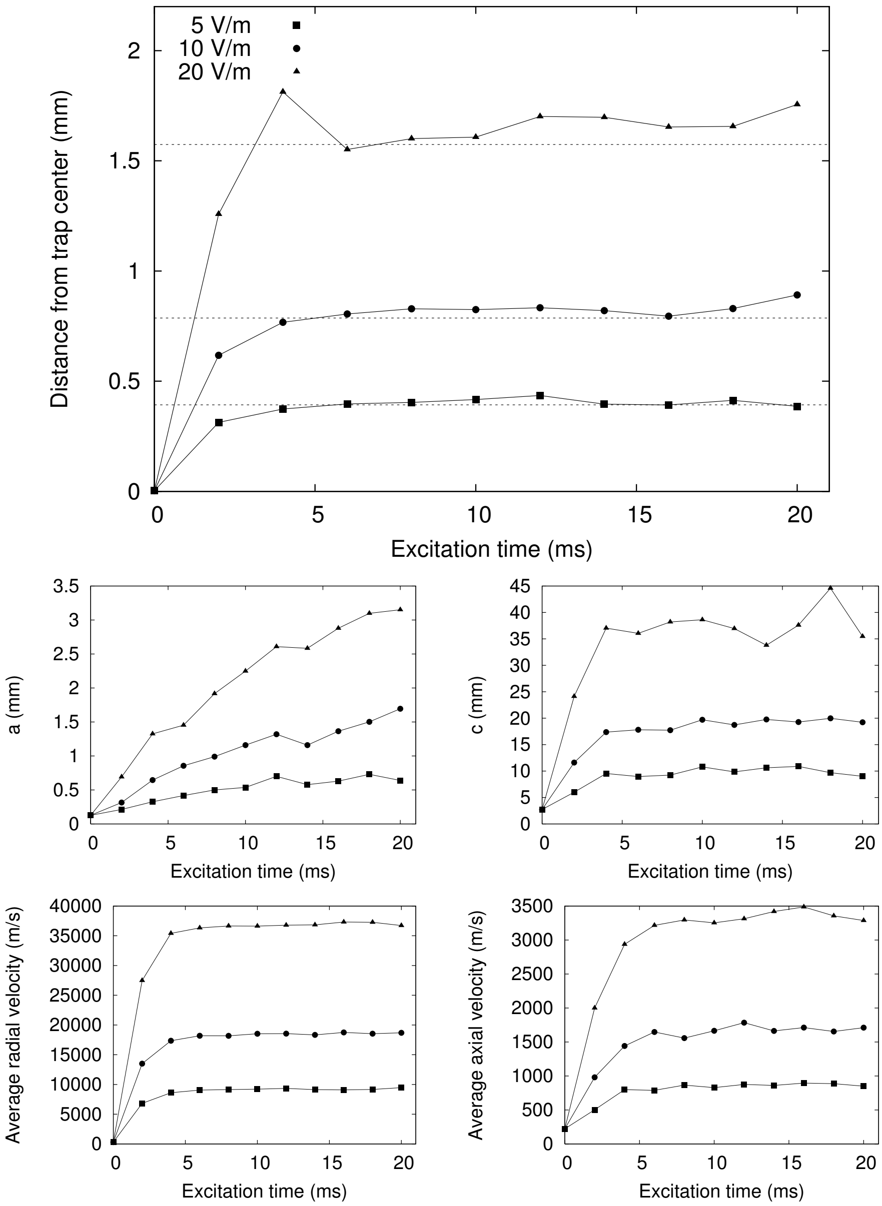

Figure 6.8 – *The influence of an electric dipolar excitation at the reduced cyclotron frequency ν_+ on the particle motion in the presence of a buffer gas. Results are shown as a function of excitation time and for different excitation amplitudes. For every plot the same symbols as for the top figure are used for the excitation amplitude. The dashed lines in the top figure indicate the value of R^+_∞ calculated from equation 6.14. Lines connecting the data points were added to guide the eye.*

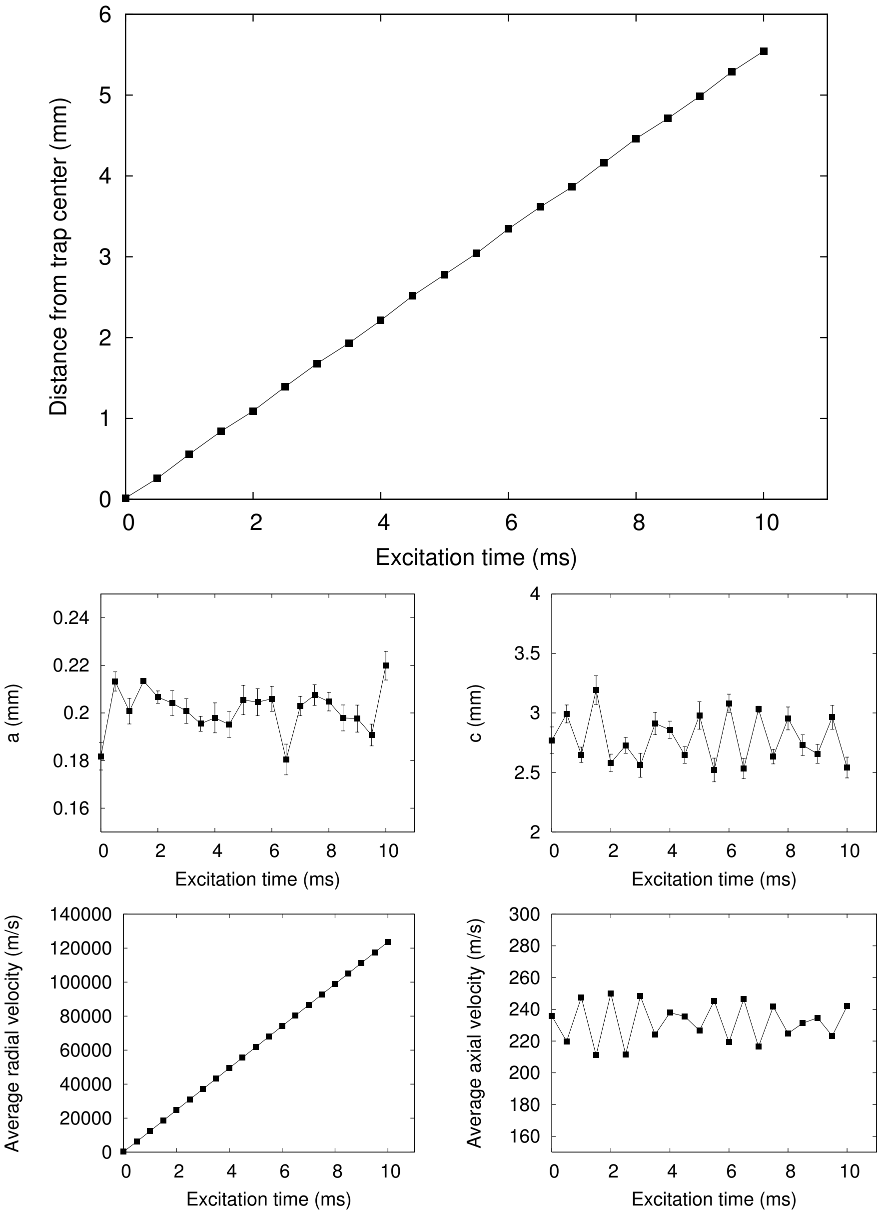

Figure 6.9 – *The influence of an electric dipolar excitation at the reduced cyclotron frequency ν_+ (10 V/m) on the particle motion without buffer gas.*

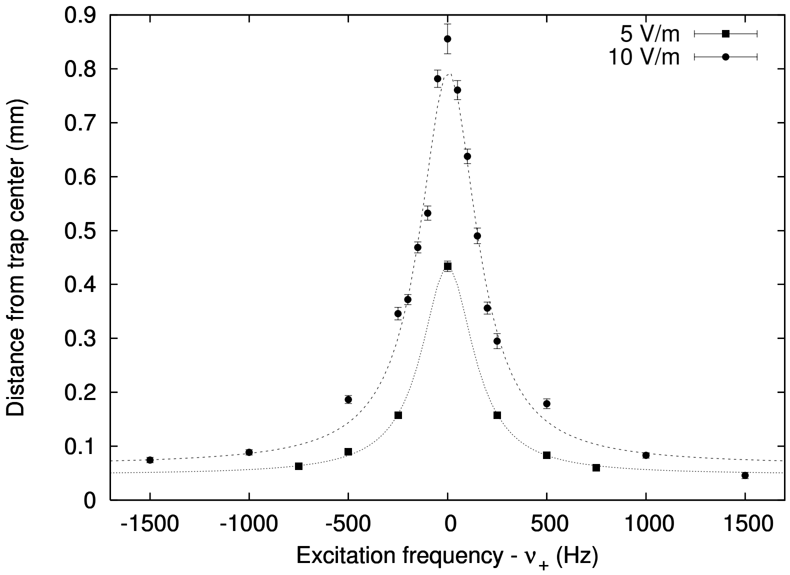

Figure 6.10 – *Example of a frequency scan of the electric dipolar excitation around the expected reduced cyclotron frequency ν_+. The ion motions were excited with a field of 5 V/m and 10 V/m for 20 ms. Lorentzian peaks with 319(11) Hz FWHM and 0.39 mm amplitude and 349(8) Hz FWHM and 0.73 mm amplitude, respectively, are fitted to the data.*

ν_z excitations

Using a longitudinal ($i = z$ in equation 6.8) dipolar excitation at the axial oscillation frequency, ν_z, for 10 ms at 10 V/m has a large effect on the cloud. The center of mass of the cloud rapidly starts oscillating over the trap axis as it is driven by the dipole electric field. In this process the cloud expands in all directions, again due to collisions with the buffer gas. The center of the trap is, like for any harmonic oscillation, the point where the average energy of the particles is highest. It is interesting to note that the axial size of the cloud appears to be minimal, but still considerably larger than before the excitation, when the cloud is in the trap center. These effects are shown in Fig. 6.11 for two simulations with a $\frac{\pi}{2}$ phase difference for the driving electric field.

6.6.5 Radial sideband cooling of the ion cloud

As was shown in Ref. [Sav91] a radial electric quadrupolar excitation of the form

$$\mathbf{E}(t) = 2\frac{U_q}{r_0^2} \cdot cos(\omega_q t + \phi_q) \cdot (y\hat{\mathbf{e}}_y - x\hat{\mathbf{e}}_x) \tag{6.15}$$

with r_0 the radius of the trap electrodes to which the excitation with amplitude U_q is applied, can be used to mass-selectively cool ions inside a Penning trap if the excitation frequency is set to the cyclotron frequency, $\omega_q = \omega_c = \omega_+ + \omega_-$. This process is called *sideband cooling* as it cools the magnetron motion of the ions by coupling it to the cyclotron motion. The technique was however only described analytically for the case of one particle [Sav91].

In section 6.6.2 the application of a radial quadrupolar excitation at the cyclotron frequency was mentioned to result in a shrinking of the radial size of the ion cloud if the initial magnetron orbit of the ions is large and the motion of the particles is not synchronized. Such an excitation also results in an increase in the particle density inside the cloud since the axial size of the cloud is almost unaffected. This is illustrated in Fig. 6.12. During the excitation the cloud is no longer a spheroid but rather also becomes elliptical in the radial plane. This can be seen in the middle left graph of Fig. 6.12 where the fitted radial size of the cloud projected on both the x and y-axis is shown. The fact that they are not the same indicates that the cloud is elliptical in the radial plane. This plot also shows that the cloud is rotating along it's longitudinal axis (oscillating behavior of projection size). These effects persist even when the cloud has achieved it's maximal density but only while the excitation is still applied. During the cooling process both the average radial and axial velocities are initially increased but they are cooled again exponentially to a value close to their original value.

If the cloud's center of mass was brought to a larger radius by applying a radial dipolar excitation at the magnetron frequency, the quadrupolar excitation can be used to (mass-selectively) re-center the ion cloud (see Fig. 6.13). The difference with the aforementioned application of the quadrupolar excitation is that due to the application of the dipolar excitation at the magnetron frequency the magnetron motion of all particles has the same phase and thus the motions are synchronized. The combination of both the dipolar and quadrupolar excita-

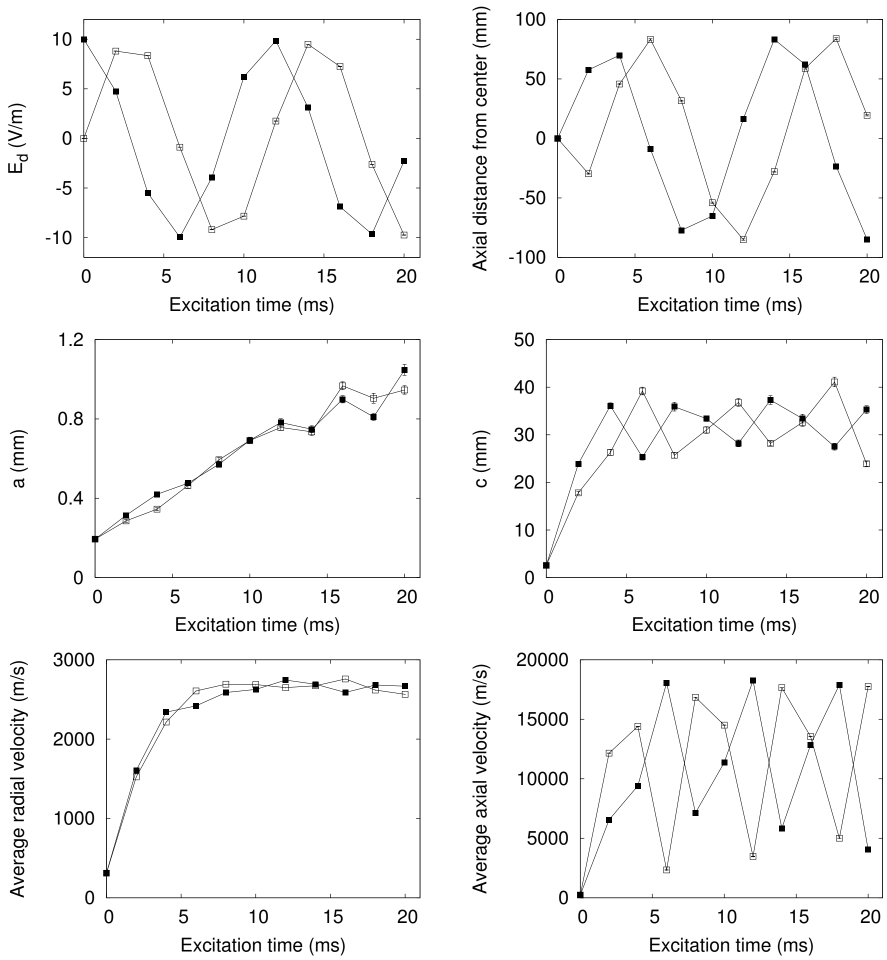

Figure 6.11 – *The influence of an axial electric dipolar excitation at the frequency ν_z (here two separate simulations with a phase shift of $\frac{\pi}{2}$ with respect to each other are shown). Note that the motion is not sampled at the full frequency required by the Nyquist - Shannon sampling theorem (i.e. at $2 \cdot \nu_z = 67.1714$ kHz) here. For this reason the dipolar field strength at this sampling frequency is shown as well (top left).*

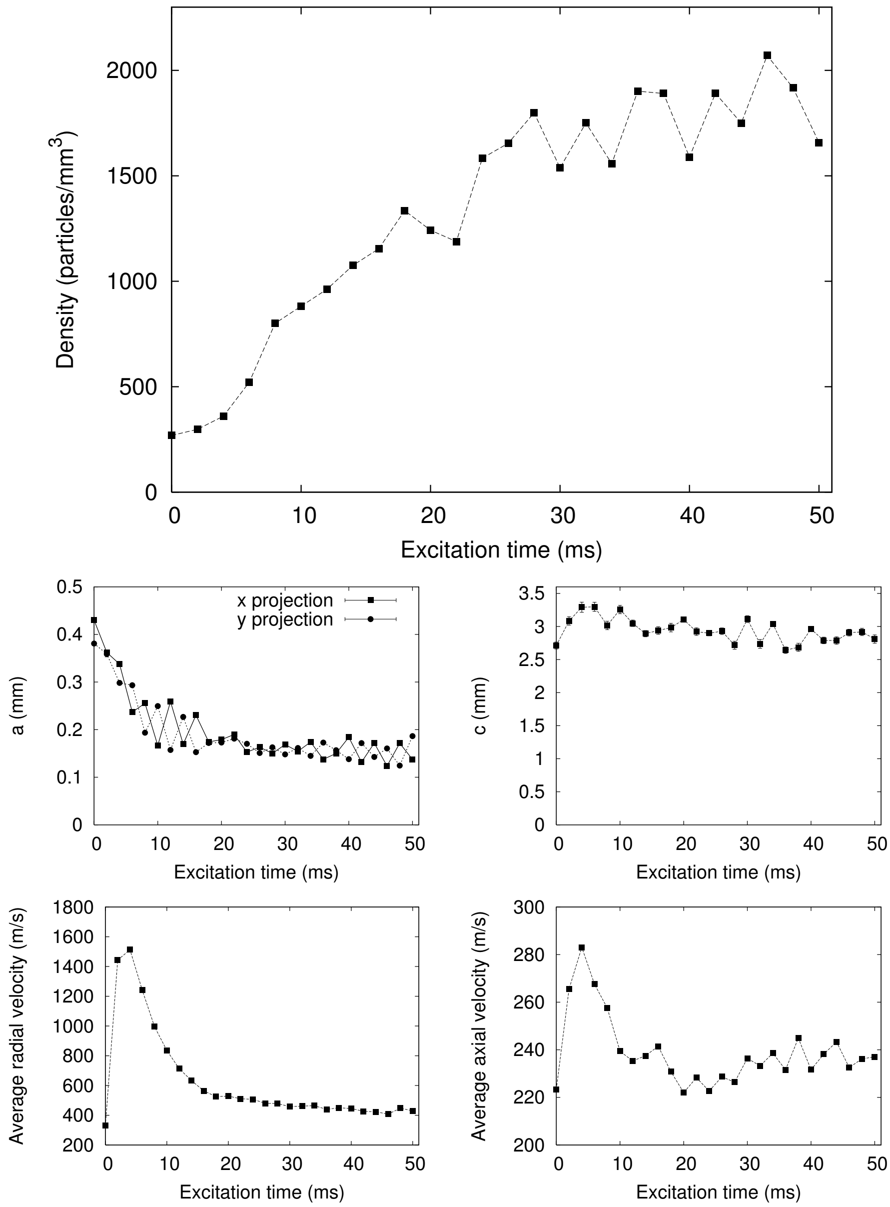

Figure 6.12 – *The influence of a radial electrical quadrupolar excitation at the true cyclotron frequency ν_c (1 V) when the magnetron motion of the particles is not synchronized.*

Electrode	Trapping voltage (V)	Transfer voltage (V)
EE8	20	20
EE7	20	20
EE6	20	20
EE5	20	20
CE4	13.5	20
CE3	3.3	1.1
RE	0	1.3
CE2	3.3	1.3
CE1	13.5	1.3
EE4	20	-5
EE3	20	-5
EE2	20	-5
EE1	20	-5

Table 6.3 – *Voltages applied to the different trap electrodes of the WITCH setup during trapping (taken from Ref. [Rai97]) and transfer. The voltages for the cooler trap are given and the voltages of the decay trap should be set as an exact mirror of these voltages. (EE: endcap electrode, CE: correction electrode, RE: ring electrode. For the direction of numbering see Fig. 6.2 and note that the numbering already takes into account the fact that voltages on the second trap should be the mirror image of the voltages on the first trap.)*

tion is often used to mass-selectively re-center the ion cloud in a Penning trap and is also used in the WITCH cooler trap for this purpose. Note that while applying this excitation the cloud first expands and then starts to shrink again as the excess energy is cooled away. Finally, the cloud cools exponentially to the same conditions as before the dipolar excitation was started, but does so only for ions of one specific mass. Also during this form of quadrupolar excitation the projection of the shape of the cloud in the radial plane becomes elliptical and is rotating (Fig. 6.13 middle left).

6.6.6 Transfer between traps

In the double Penning trap system of WITCH, the ion cloud in the second trap constitutes the actual source of the experiment and thus has to be transferred from the first to the second trap. Since the ion cloud has a certain size in the first trap, some ions will experience a shift in their potential energy during ejection from this trap whereas other ions will experience an opposite shift during injection in the second trap. This could induce an extra energy spread of the ions inside the second trap. For the special case of the WITCH setup this would lead to a broadening of the spectrometer response function. Therefore, a set of electrode voltages that minimizes this effect was chosen for the first trap (table 6.3), while the voltages on the second trap were set as an exact mirror of the voltages on the first trap. The potential along the trap axis during trapping and ejecting created by these voltages is shown in Fig. 6.14. The ejection/injection potential on the side of the trap that remains closed is as close as possible to the quadrupolar trapping potential so as to minimize the

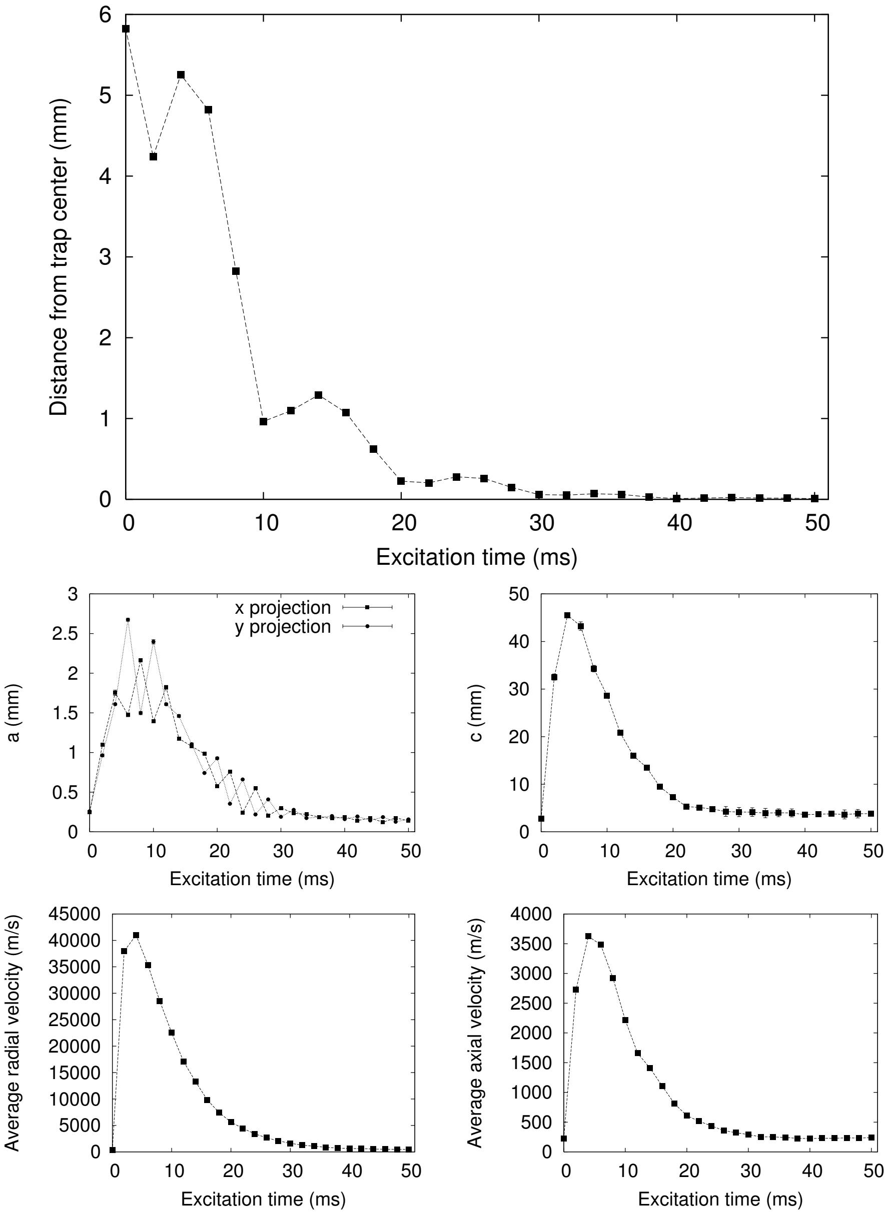

Figure 6.13 – *Example simulation of a cloud of 500 particles that was first subjected to a dipolar excitation at frequency ω_- during 10 ms at 10 V/m (not shown) and then to a quadrupolar excitation at the cyclotron frequency for 50 ms at 1V.*

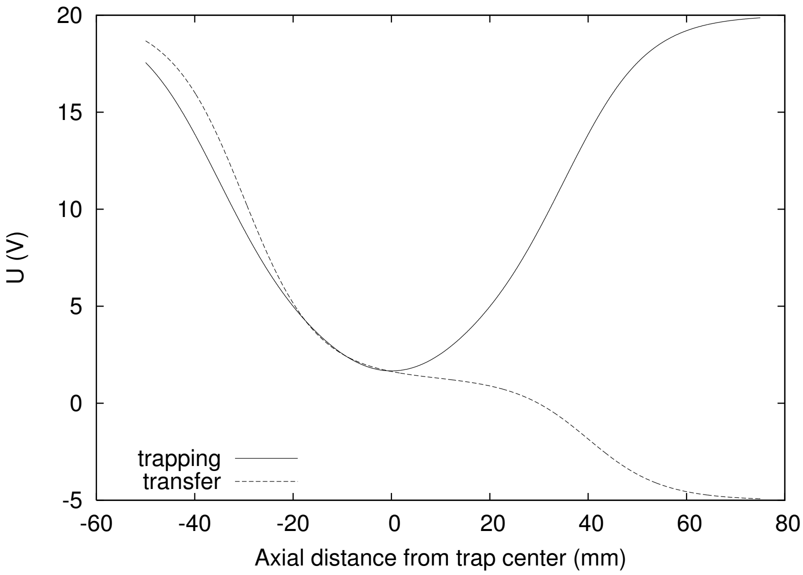

Figure 6.14 – *The potential created along the trap axis during trapping and transfer by the electrode voltages given in table 6.3.*

shift in energy of the ions located in this section of the trap during transfer. The potential on the other side of the trap has to be lower than the potential in the trap center to allow the ions to escape and it is the ions located here during transfer that will experience an energy shift. By increasing the voltage gradient in this region one can reduce the width in time of the ejected ion bunch, but this at the same time leads to an increase in energy spread inside the bunch.

Simulations of the transfer of a cloud of 500 particles at a temperature of 294 K from the first to the second trap were performed by using the coordinates and velocities of the ions obtained from previous simulations as starting conditions for simulations of the traps in SIMION [Dah00] where the actual transfer was simulated. The velocity distribution inside the ion cloud is shown in Fig. 6.15 for different times between the opening of the first trap and the closing of the second. If this time is chosen correctly (i.e. around 66 μs in this case) the cloud can be transferred without inducing a large additional spread or increase in energy. If the second trap is closed too early or too late a large fraction of the ions will experience a shift in energy introducing an additional spread or increase in energy in the cloud.

6.6.7 Inside the decay trap

The ion cloud in the decay trap is the actual radioactive source of the WITCH-experiment. When a radioactive ion decays inside this trap it recoils and can leave the trap. Its energy can be measured using the electrostatic retardation spectrometer [Bec03]. The recoil ion energy spectrum is measured by changing

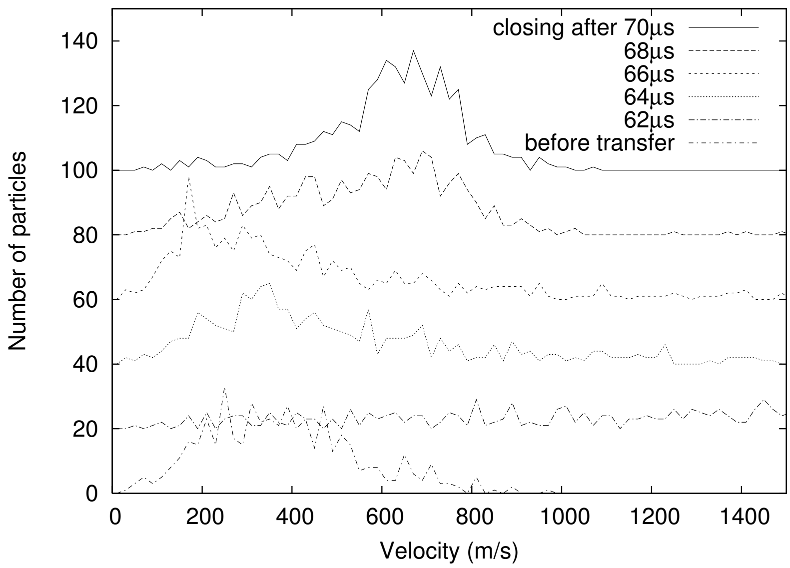

Figure 6.15 – *Simulations of the velocity distribution of an ion cloud of 500 particles transferred from the first to the second trap for different closing times of the second trap. Note that a different offset was used for the different curves (in steps of 20) to clarify the figure.*

the voltage on the retardation electrode in steps and registering each time the ions that pass over the retardation barrier. In the WITCH setup an MCP detector is used for this [Lie05]. Since the typical energy of a recoil ion after β-decay is only of the order of several hundreds of eV, the Doppler broadening due to the initial ion motion cannot be neglected for a cloud at room temperature [Koz06].

To study this effect with a simulation, all particles were supposed to experience a decay with the same energy and to recoil into a random direction. This was repeated 100 times to gather sufficient statistics. The resulting response function for an ideal spectrometer is bell-shaped but not necessarily Gaussian. The width of the response function, defined as half the width of the interval around the center which contains 68.3% of the particles, equivalent to σ in the case of a Gaussian response function, is found to be proportional to the square root of the decay energy. Since the spectrum of recoil energies is continuous, the width shall therefore always be divided by the square root of the recoil energy (in eV) to get a measure of the quality of the response function (quoted as the *normalized sigma* σ_n which has units $eV^{1/2}$).

The width of the response function is also depending on the temperature of the ion cloud as shown in Fig. 6.16. The width $\sigma_n = \sigma_\epsilon/\sqrt{E_{recoil}}$ of the distribution of the energy shift ϵ due to the Doppler broadening was calculated in Ref. [Del04] and Ref. [Koz06]. Assuming a Mawellian ion velocity distribution in the trap and taking into account that the energy at typical thermal energies

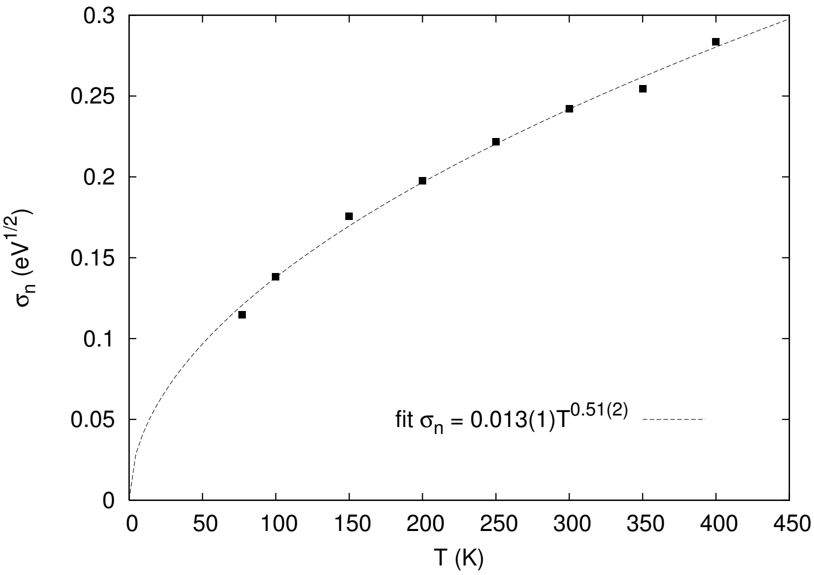

Figure 6.16 – *Relation between the temperature of the ions inside the decay trap and the expected width of the WITCH spectrometer response function σ_n (see text), together with the best fit to the simulated data.*

(77 k to 400 K here) is much smaller than the recoil energy

$$\sigma_n = \sqrt{2k_bT} = 0.0131T^{1/2} \tag{6.16}$$

was obtained. The fit shown in Fig. 6.16 gives

$$\sigma_n = 0.013(1)T^{0.51(2)} \tag{6.17}$$

showing that the width of the response function is indeed well described by equation 6.16. To minimize the width of the spectrometer's response function, it could be advantageous for the WITCH-experiment to minimize the temperature of the buffer gas in the first trap. This could be realized by installing a cryogenically cooled Penning trap comparable to the one described in [Web03]. However, even with a cryogenic trap, it is clear that the width of the response function would still depend on a possible increase of the ion's energy caused by the transfer between the two traps.

When storing the ion cloud for 100 ms in a buffer gas free environment, as the decay trap should ideally be, no significant changes in the cloud's parameters were observed.

6.6.8 Larger number of ions

As was already stressed, the size of the ion cloud inside both Penning traps is of major importance for the WITCH-experiment. Therefore a number of simulations using a scaled Coulomb force approach [Bec01] have been performed

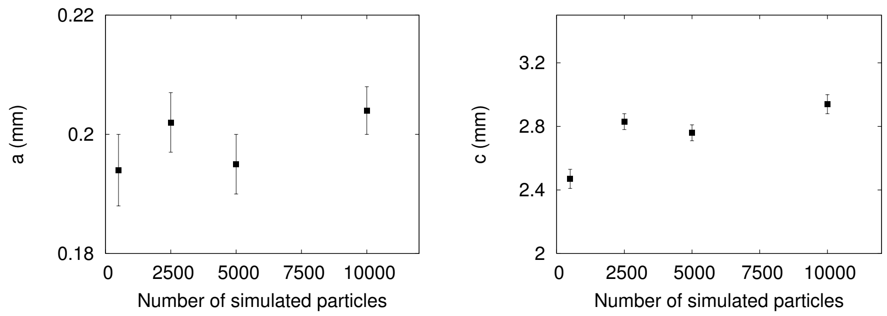

Figure 6.17 – *Size of the ion cloud for larger numbers of particles. The cloud was allowed to evolve in the presence of the buffer gas for 60ms. Simulations used a scaled Coulomb force approach on a cloud of 500 particles (see text).*

to also obtain information on the size of the cloud for larger numbers of particles. In this technique a limited number of particles is simulated (the exact number is limited by computing time only) but the Coulomb force between the particles is scaled to mimic the presence of more particles such that

$$n_{tot} \cdot F_C = n_{comp} \cdot F_{Ccomp} \tag{6.18}$$

where n_{tot}, F_C, n_{comp} and F_{Ccomp} represent respectively the desired number of particles for the simulation, the normal Coulomb interaction between two ions, the number of particles actually used in the simulation and the scaled Coulomb interaction used. In [Bec01] it was shown that this technique gives rather good qualitative agreement with the experimental values from REXTRAP discussed in [Ame01] for the frequency shift and resonance broadening observed when using sideband cooling on ion clouds with a large number of ions. The dependence of the ion cloud size on the number of particles simulated in this way is shown in Fig. 6.17.

This simulation technique is however also limited in the number of particles that can be taken into account since it is expected that the approximation becomes successively worse as the ratio between the scaling factor and n_{comp} increases. Other possibilities include using other approximations or possibly specialized computer hardware [Mak98].

6.7 Conclusion

A computer code was developed permitting to simulate ion clouds containing typically 500 particles, inside a gas-filled Penning trap. Simulations showed the expected size of these clouds inside the WITCH cooler Penning trap. Under the influence of a radial electric dipolar excitation at the magnetron frequency the cloud was seen to shift from the trap center while the size of the cloud remained unchanged. For a radial electric dipolar excitation at the reduced cyclotron frequency, however, the cloud was seen to both shift from the center and expand. It was shown that through the application of a radial electric quadrupolar excitation the cloud could either be reduced in size or re-centered depending on the starting conditions. Specifically for the case of the WITCH-experiment a set of voltages to be applied to the different electrodes of the cylindrical Penning traps was given which, according to the simulations, does not drastically increase the average velocity of the ions during the transfer from one Penning trap to the other. Furthermore, the influence of the cloud temperature on the expected response function of the WITCH retardation spectrometer was discussed. Finally, it was shown how scaled Coulomb force simulations can reveal the size of the ion cloud also for large numbers of particles. Even with these simulations the total number of ions that can be simulated is rather limited. In addition much more systematic experimental investigations have to be performed to compare the simulations to and/or find additional experimental effects for ion numbers that lie beyond the simulation capabilities.

6.8 Acknowledgements

This work is supported by the European Union grants FMRX-CT97-0144 (the EUROTRAPS TMR network) and HPRI-CT-2001-50034 (the NIPNET RTD network), the European Union Sixth Framework through RII3-EURONS (contract no. 506065), the Flemish Fund for Scientific Research FWO and project GOA 99-02 of the K.U. Leuven.

6.9 Additional simulations

Using the same routine as the one described above, several simulations have been performed to check the influence of the simultaneous presence of two ion species with nearly equal mass in the trap. For the simulations ^{35}Ar and ^{35}Cl were considered as ^{35}Ar is the prime candidate for a physics measurement and ^{35}Cl is expected to be the main contaminant in the beam. To allow the simulation of large ion numbers, for which space charge effects are expected to be observed, the scaled Coulomb force approach was again used. 100 particles of each mass were followed in the simulation and the interaction was scaled.

In Fig. 6.18 an example of a 80 ms quadrupolar excitation at 0.5 V and a buffer gas pressure of $5 \cdot 10^{-4}$ mbar is shown for different scaling factors. As can be seen the influence of the presence of the ^{35}Cl is quite pronounced for large ion numbers. Not only does the resonance curve for ^{35}Ar shift, the cloud is no longer fully recentered for these excitation parameters. Also the motion of ^{35}Cl is greatly influenced for larger ion numbers. Other strange effects of the presence of contaminant ions of similar mass than the ions of interest on the shape of the quadrupolar resonance curve have been experimentally observed at ISOLTRAP [Sch05].

In Fig. 6.19 an example of a 20 ms dipolar excitation at a buffer gas pressure of $5 \cdot 10^{-4}$ mbar is shown for different scaling factors. Clearly the influence of the total number of particles or the number of contaminant ions is much smaller. This would indicate that a dipolar excitation at the reduced cyclotron frequency could be much more efficient in performing a mass selective cleaning of the ion cloud when one is dealing with large ion numbers. This result is consistent with experimental results that have been observed at REX-TRAP [Stu06]. Note again that if high mass resolution is to be obtained from a cyclotron dipolar excitation, the buffer gas pressure should be low enough, increasing the time that is needed to cool the ions upon injection. For optimal performance one has to balance both parameters and this will depend on the specific application which one is using.

Further experimental testing will be required to check these effects in the WITCH cooler trap.

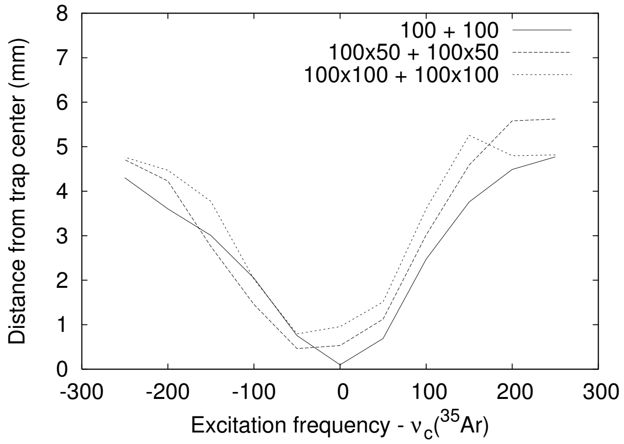

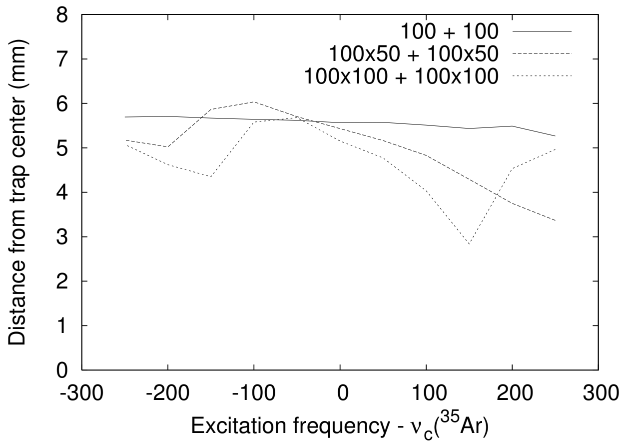

Figure 6.18 – *Influence of the number of ions on the shape of the resonance curve for a quadrupolar excitation when the ion cloud contains two ions species of different mass. The top graph shows the influence on the* ^{35}Ar *ions while the bottom graph shows the influence on the* ^{35}Cl *ions.*

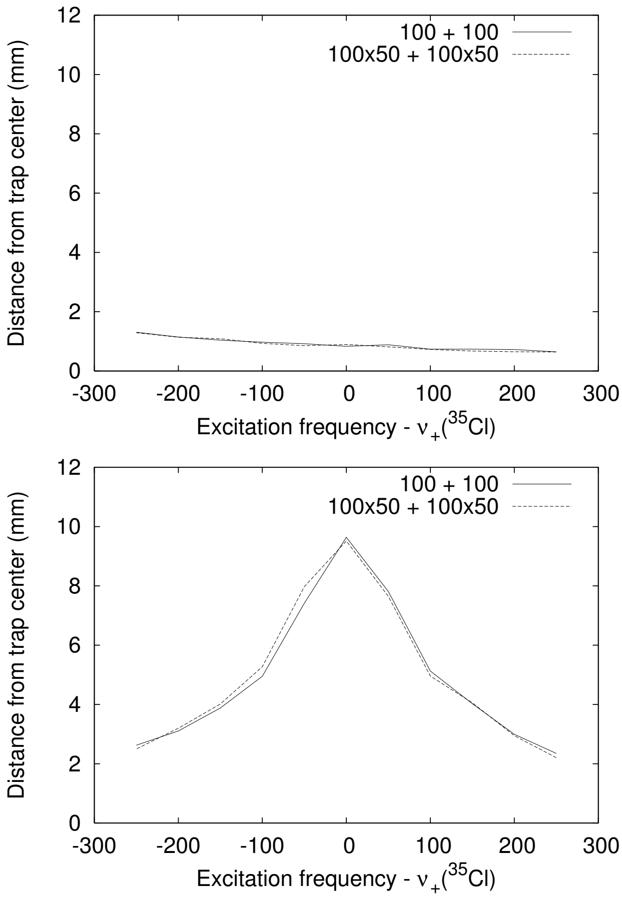

Figure 6.19 – *Influence of the number of ions on the shape of the resonance curve for a dipolar excitation when the ion cloud contains two ions species of different mass. The top graph shows the influence on the ^{35}Ar ions while the bottom graph shows the influence on the ^{35}Cl ions.*

Chapter 7

WITCH Penning trap system

An overview of the possibilities of Penning traps was already given in chapters 2, 5 and 6. In this chapter the focus will be on the technical implementation of the Penning traps at WITCH, the electronics needed to run them and the trapping cycle as it is used in the experiment.

7.1 Technical implementation

The WITCH Penning traps are made from High Conductivity Oxygen Free Copper. The electrodes were first plated with a thin layer of Silver and subsequently Gold plated. The Silver layer in between the Gold and Copper avoids the Copper from diffusing through the Gold layer to the surface where it could oxidize. The electrodes are electrically insulated from each other by Macor spacers. Both traps are of the cylindrical type. The equipotential lines in the center of the WITCH cooler trap, which are plotted in Fig. 7.1, show that indeed a hyperbolically shaped electrical potential can be obtained with this configuration when the correct potentials are applied (see chapter 6 and Ref. [Rai97]).

To be able to apply the different excitation schemes discussed in chapters 5 and 6, the central electrode of the trap has to be segmented. In Fig. 7.2

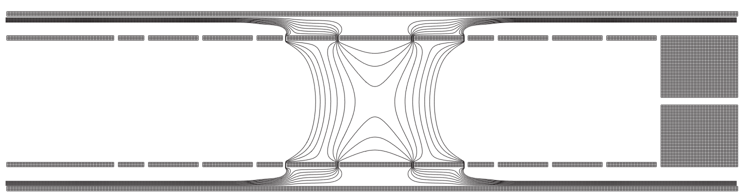

Figure 7.1 – *Equipotential lines in the center of the WITCH cooler trap.*

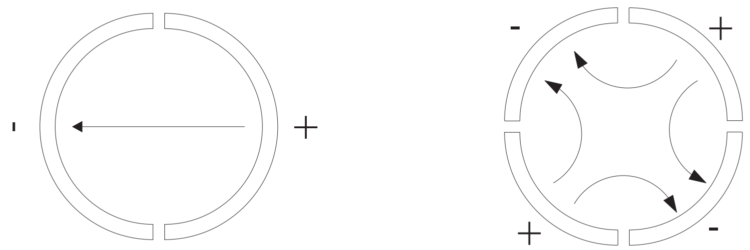

Figure 7.2 – *Segmenting the central electrode of a Penning trap in two (four) segments allows the application of a dipolar (quadrupolar) electric field in the center of the trap.*

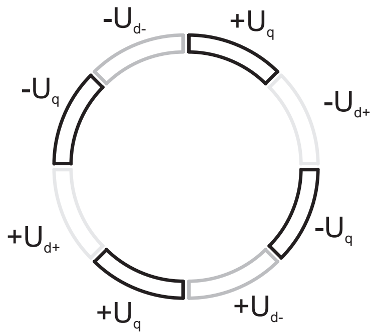

Figure 7.3 – *By segmenting the central electrode of a Penning trap into eight pieces, each excitation mode can have its dedicated segments and octupolar excitations become possible.*

it is shown how this allows the creation of a dipolar and quadrupolar electric field in the center of the Penning trap. By segmenting the central electrode in eight pieces, each excitation mode can have its dedicated segments and octupolar excitations become possible. This is demonstrated in Fig. 7.3. Although excitation of the ion motion is only planned to be done in the cooler trap, the central electrodes of both Penning traps are segmented in eight pieces. This renders the system more flexible for other measurements.

The high purity helium buffer gas is inserted into the cooler trap through a Teflon tube that is connected to the gas bottle through an electronically controlled gas dosing valve. Although the vacuum properties of Teflon are not bad, it would probably be advantageous for the purity of the buffer gas to eventually switch to a metal gas tube. In this respect it would also be interesting to foresee a cold trap or other gas purification device at the point were the gas feeding tube enters the main vacuum to further limit the amount of impurities that are present in the buffer gas. On the inside of the trap structure, a narrow and long channel (often referred to as a pumping diaphragm) is foreseen to limit the gas flow from the cooler trap into the decay trap. On the outside of the trap

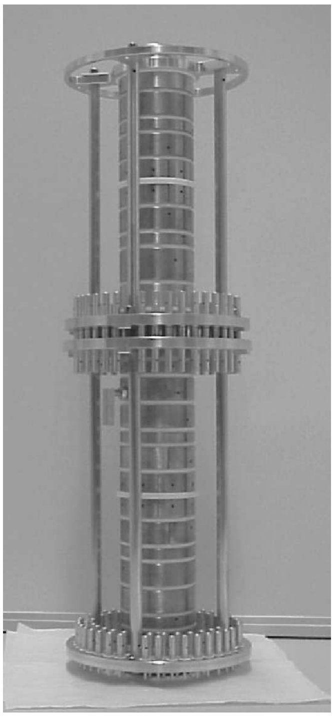

Figure 7.4 – *Picture of the assembled WITCH Penning traps. The electrical connections and buffer gas feeding line are not shown.*

structure several rings in Capton foil are foreseen between the cooler and decay trap to avoid large quantities of gas seeping into the decay trap or spectrometer section. The pressure of the buffer gas can not directly be measured in the cooler trap, but instead has to be deduced from the pressure in the gas feeding line and other pressure measuring points in the system. Typical operating pressures for the buffer gas in the cooler trap are of the order of 10^{-4} - 10^{-5} mbar.

A picture of the assembled trap structure is shown in Fig. 7.4. Note that the electrical connections and buffer gas feeding line are not shown.

7.2 Trapping cycle

The WITCH trapping cycle consist of 6 steps (illustrated in Fig. 7.5):

a) The bottom endcap of the cooler trap (CEE8) is set to a low voltage allowing the ions which have a typical kinetic energy of the order of 100 eV to enter the trap. The top endcap of the cooler trap (CEE1) is at a sufficiently high potential to reflect the ions.

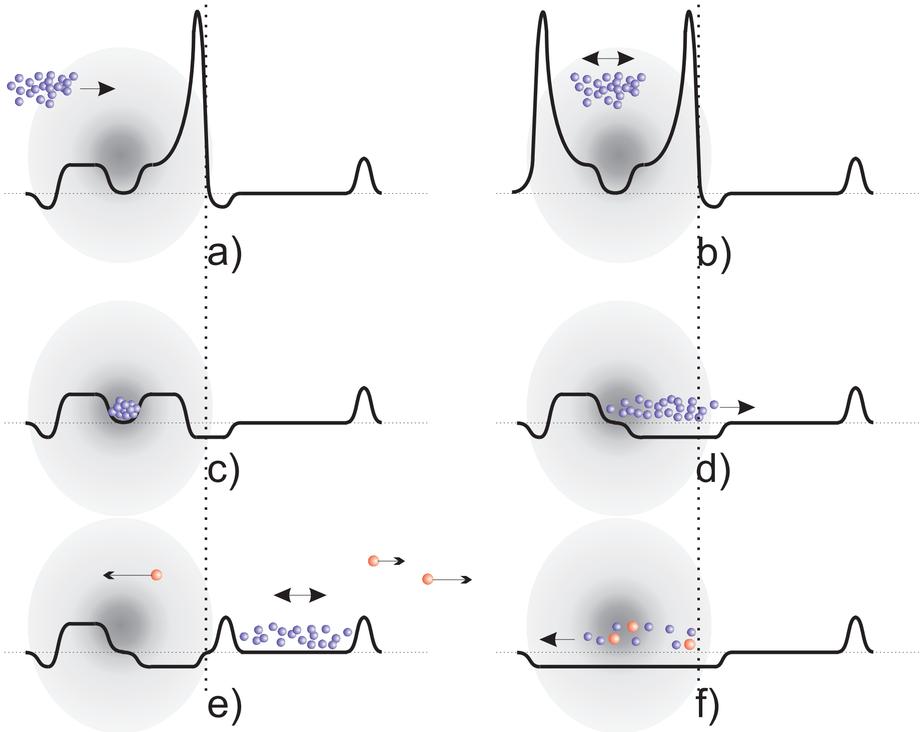

Figure 7.5 – *Schematic picture of the electric potential in the Penning trap system during the different stages of the experimental cycle. The vertical lines indicate the separation between the cooler trap on the left hand side and the decay trap on the right hand side.*

b) The bottom endcap is again raised to a higher potential while the ion bunch is inside the trap effectively trapping the ions between the two endcaps of the cooler trap.

c) After some time the ions have lost so much kinetic energy due to their collisions with the buffer gas particles that the endcaps are no longer required and the quadrupolar field in the center of the trap is enough to trap them. The bottom endcap is best lowered before the top endcap to prevent ions that have not lost sufficient energy from entering the spectrometer volume. Several bunches can be accumulated at this stage as lowering the bottom endcap to accept more bunches does not result in a loss of ions. Finally the top endcap is lowered and if required any excitations can be performed at this stage.

d) The cooled ion cloud is transferred from the cooler to the decay trap by lowering the upper half of the trapping potential in the cooler trap and making sure the bottom of the decay trap is at low voltage. It can be advantageous to have the top endcap of the decay trap at a higher potential during this transfer, again to avoid ions with excess energy from reaching the spectrometer section.

e) The bottom endcap of the decay trap is raised and the ion bunch is trapped in the decay trap. Now a measurement on the recoil ions can start.

f) When the measuring time is over all ions that remain in the decay trap (ions that have not decayed yet or ions that remained trapped after they decayed) are shot back down to empty the trap and prepare it for a new ion bunch. The ions are shot downwards and not upwards to avoid contaminating the spectrometer and the main detector with radioactivity.

The corresponding cycle in terms of timing signals is shown Fig. 7.6. Alternative timing schemes are presented in Appendix B. Although Fig. 7.5 shows the trapping cycle when the decay trap is used as a box trap the same principle also holds when it is used with a full quadrupolar potential. Note that to be able to do transfer in the way that is suggested in chapter 6 and empty the traps towards the bottom of the system, some of the electrodes need to be switched between three separate levels. With the present electronics this is not possible but a device that is able of achieving this is currently being conceived.

7.3 Trap electronics

To be able to operate the traps for storage, cooling and manipulation of the ions a number of electronic devices are needed. A schematic overview of the electronics used for the operation of the WITCH Penning traps is shown in Fig. 7.7. A more detailed description of the electronic devices is listed below.

- The Gate and Delay unit. This is the timing unit that controls the whole experimental cycle including the different stages of the trap operation. More details can be found in Ref. [Lin04].

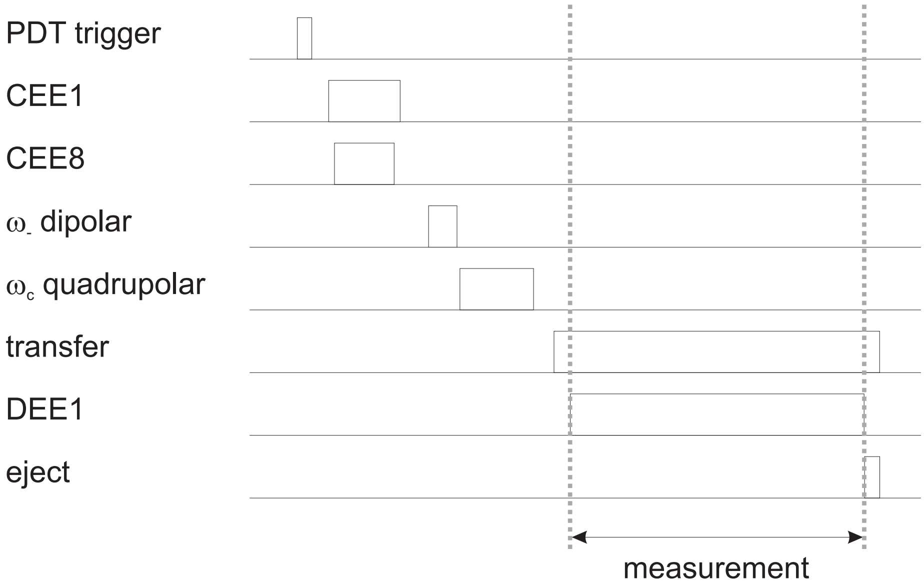

Figure 7.6 – *The timing signals for the trap cycle shown in Fig. 7.5.*

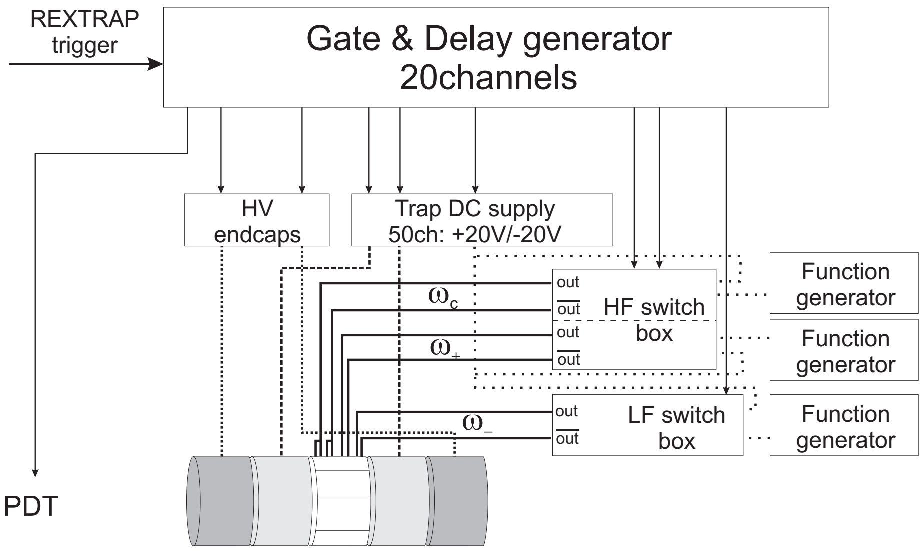

Figure 7.7 – *Schematic drawing of the electronics connected to the cooler Penning trap.*

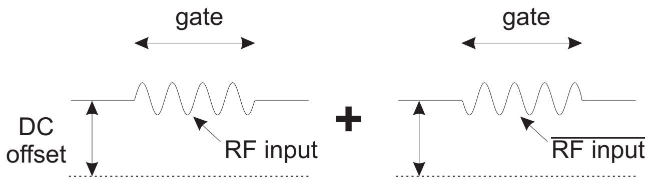

Figure 7.8 – *Schematic representations of the operation of the HF and LF switch boxes.*

- The HV endcap switches. These switchable voltage supplies provide the voltages needed for the endcaps that trap the ions in the cooler trap when they are injected. For this they can switch between a positive voltage, adjustable between 0 V and +450 V, and a negative voltage that can be set between 0 V and -20 V. The switching can be performed on a time scale of about 100 ns.
- The DC supply. Contrary to what the name might suggest, this supply can actually switch between two voltages that can be set between -20 V and +20 V independently of each other. The entire unit consists of 50 independent channels like this. All electrodes, except the endcaps, are connected to this supply, be it not always directly (see Fig. 7.7).
- The HF (High Frequency) and LF (Low Frequency) switch boxes. The main purpose of these devices is to gate, invert and DC offset the oscillating voltage coming from the frequency generator. Their operation is illustrated in Fig. 7.8. The DC offset is generated by the DC supply and is thus strictly speaking not necessarily a true DC voltage.
- The function generators. The DS345 Stanford Research Systems function generators are used to supply the rf-voltages needed for the different excitations in the cooler trap. They can deliver up to 30 MHz with a resolution of 1 μHz and a peak-to-peak amplitude up to 10 V on 50 Ω.

Instead of using the LF switch box for applying the magnetron (ω_-) dipolar excitation, one can use two separate function generators, each connected directly to one segment of the central electrode of the cooler trap, that are triggered by the same signal and have a relative phase of 180°. This way of working has as advantage that the excitation is *phase-locked* [Bla03], meaning it has the same well known phase for all trap cycles. This is not the case when using the RF switch boxes as they merely gate the RF signal coming from the function generators. The disadvantage is that no DC offset can be superimposed on them. By combing the use of a triggered function generator and the LF switch box, a *phase-locked* magnetron excitation with DC offset can be obtained. For this one can just use as trigger for the function generator the same signal as the one that is used for the gate of the LF switch box.

An example of a frequency scan around the cyclotron frequency for a quadrupolar excitation on $^{133}Cs^+$ is shown in Fig. 7.9. Two separate tests were

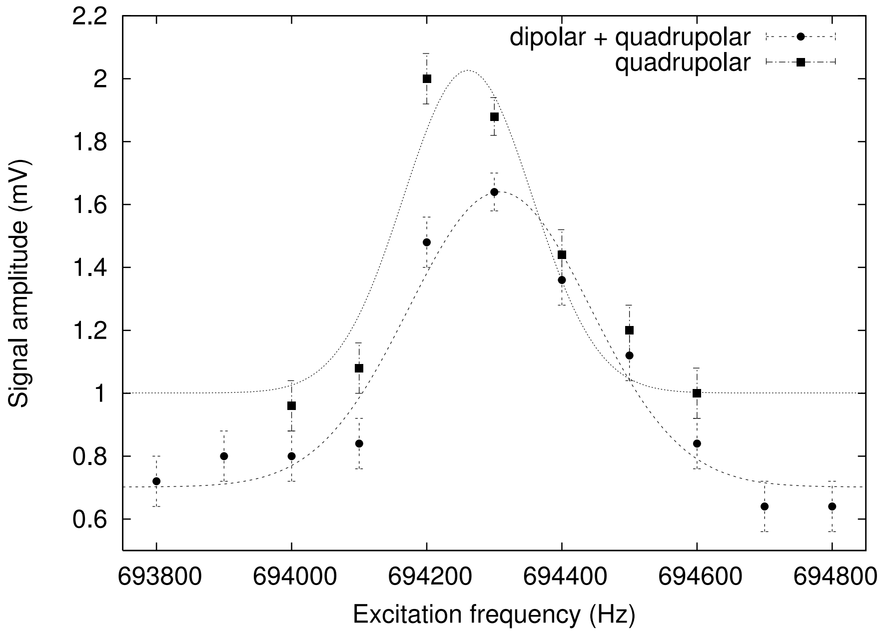

Figure 7.9 – *Example of a frequency scan around the cyclotron frequency for a quadrupolar excitation on $^{133}Cs^{+}$. The result corresponds mass resolution of 2000-3000.*

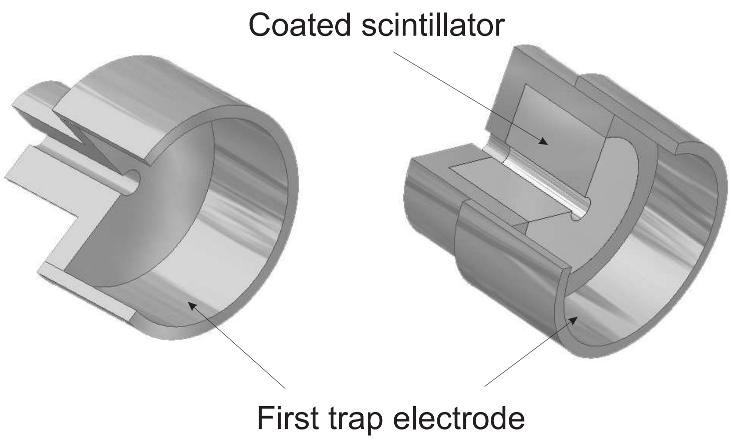

Figure 7.10 – *Cutaway view of the pumping diaphragm separating the two traps (only decay trap side is shown). (left) The system as it was originally designed. (right) The planned implementation of the β-detector.*

performed:

- A quadrupolar excitation without prior dipolar excitation.
- A quadrupolar excitation preceded by a dipolar excitation at the magnetron frequency.

The first shrinks the ion cloud before the transfer to the decay trap and the second first brings all ions to a larger radius and then only re-centers those with the chosen mass. A mass resolution of 2000-3000 is already obtained. Further tests will have to show how much the mass resolution can still be improved.

7.4 β-detector

As was described in [Koz06] many of the β-particles coming from the ions that decay in the decay trap hit the pumping diaphragm separating the two traps. For this reason part of the diaphragm will be replaced by a β-detector as shown in Fig. 7.10. This detector can then be used for normalizing the total number of particles present in the decay trap for each trap load (see section 2.8). The detector itself is a plastic scintillator coated on the outside with a light tight conducting layer. The coating is needed as part of the detector serves as part of the endcap electrodes of the traps. In addition the conductive coating helps to prevent charging effects that could disturb the electrical field inside the traps.

The light output from the scintillator will be guided to a photodiode or MCP based photomultiplier by a set of optical fibers. The photodiode or photomultiplier converts the light signal into an electric pulse that can be brought outside the vacuum. The signals are then amplified and guided to a discriminator connected to a scaler that is integrated into the data acquisition system.

Chapter 8

First on-line measurements

Before starting with precision measurements to determine the β-ν-angular correlation coefficient, the principle of the WITCH system still had to be proven as it had only been tested in simulations. For this a radioactive beam from ISOLDE was needed and the aim was to observe recoil ions for the first time and possibly measure a recoil energy spectrum.

8.1 Choice of isotope

To prove the principle of the setup one of the prime requirements for the isotope to be used, was that is should provide sufficient detected events in a relatively short amount of time. Therefore several requirements had to be met:

1. The production yield at ISOLDE should be sufficiently high, preferably of the order of 10^6 or more particles per second.

2. The half-life of the isotope should be of the order of 1 s.

3. The ionization potential of the element should be quite low to avoid problems with neutralization in both REXTRAP and the WITCH cooler trap.

4. The isotope should preferably be β^--decaying as in this case the number of recoils that keeps some electric charge is not of the order of 10% but rather of the order of 100% since one does not depend on the *shake-off* effect.

5. The daughter isotope after decay should be stable.

6. Isobaric contamination from any other isotope should be minimal and if present preferably the contaminant is a stable isotope.

7. To eventually extract physics from the measurement the decay scheme of the isotope should be as simple as possible since all different decay branches will produce a different recoil spectrum and these will all overlap in the measured spectrum.

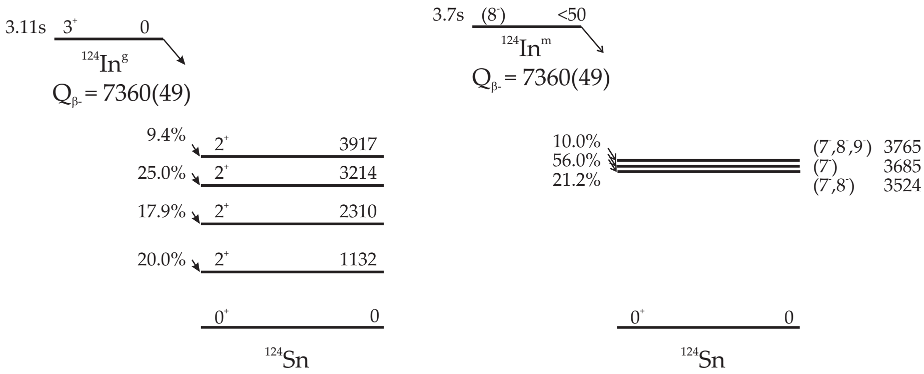

Figure 8.1 – *The simplified decay schemes of $^{124}In^g$ (left) and $^{124}In^m$ (right). Only the branches with the highest intensities are shown.*

Sadly the prime physics candidate ^{35}Ar doesn't meet all these requirements (more specifically 3 and 4) and could thus not be used in the first experiment.

The isotope ^{122g}In does meet all these requirements and was therefore selected for a first measurement. Although listed in the ISOLDE yield book as being produced at a promising rate of $2.5 \cdot 10^8$ particles/μC on a U-carbide target, spectroscopic measurements preceding the actual beamtime showed that ^{122g}In is actually not produced but instead only the two isomeric states of ^{122}In are formed.

Another interesting isotope produced on the same target is ^{124g}In. The disadvantage of this isotope compared to ^{122g}In is its more complicated decay scheme (shown in Fig. 8.1, for complete decay schemes see Appendix C). In addition ^{124}In also has an isomeric state of which the exact contribution to the beam was not exactly known but was determined to be roughly as intense as the ground state in a previous measurement on an identical target. Note that for this isotope the β-decays are mainly pure Gamow-Teller transitions, for which $a = -1/3$.

8.2 Setup

For this measurement, one out of every four or more proton pulses was used, resulting in a total cycle time for WITCH of 4.8 s. This gives sufficient time for preparing the ions in the cooler trap and measuring their decay in the decay trap (the half-lives of the groundstate and isomer are 3.11 s and 3.7 s).

During the measurement large discharges where observed when switching the spectrometer voltage. No conclusive explanation for this has been found up to now. Later off-line tests suggest, however, that the large number of γ-rays produced by the decay of $^{124g,m}In$ plays an important role in this process. This meant that the spectrometer could no be used as intended. Instead another electrode was used as retardation electrode as indicated in Fig. 8.2.

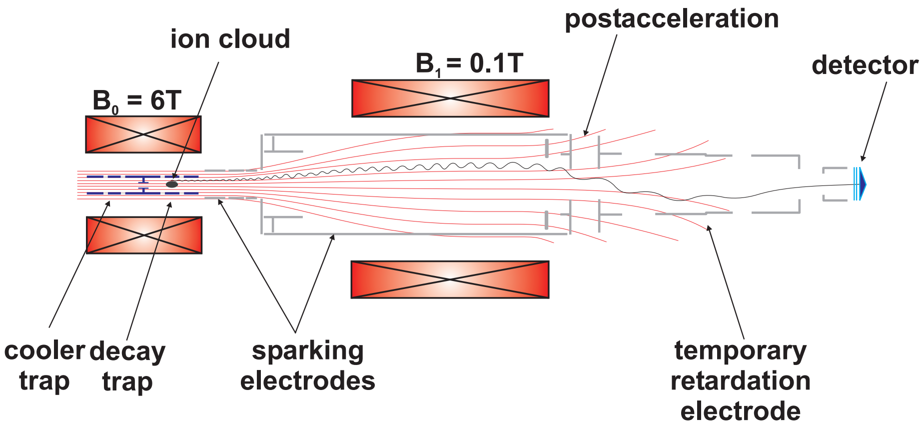

Figure 8.2 – *The spectrometer set-up as it was used during the measurement with radioactive ^{124}In.*

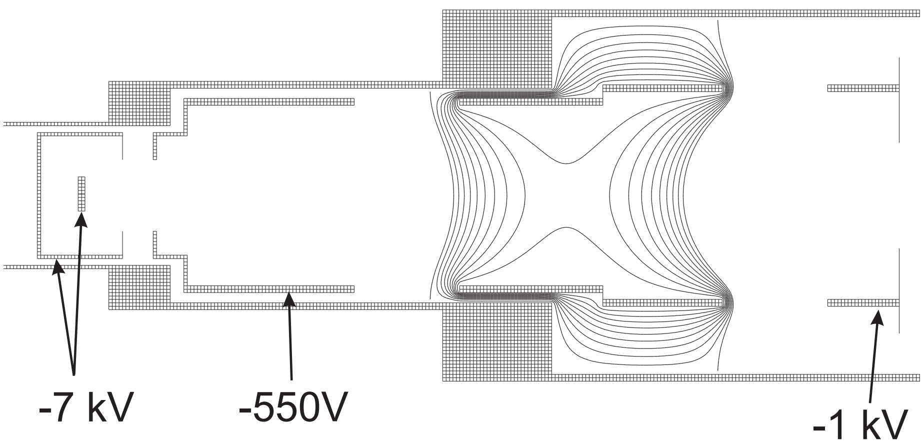

Figure 8.3 – *Equipotential lines for the electrode that was used as temporary retardation electrode. The electrode is at a potential of +100 V and equipotential lines with 10 V spacing are drawn. In the center of the electrode a potential of only +88 V is present.*

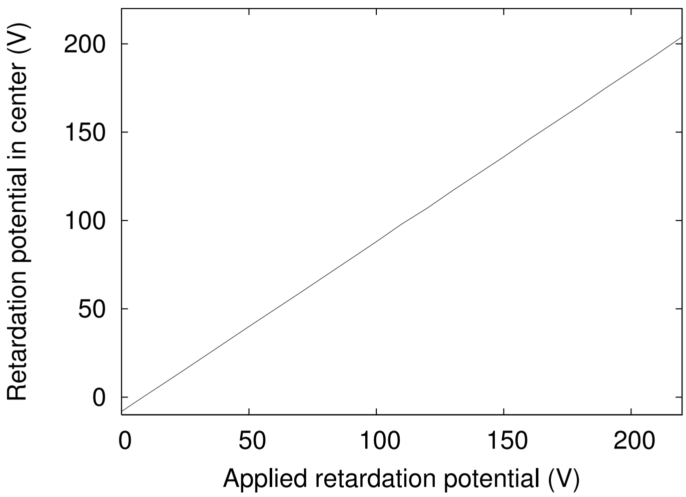

Figure 8.4 – *Potential in the center of the temporary retardation electrode volume as a function of the applied retardation potential.*

Because this electrode was not designed for this purpose and is rather small compared to the normal retardation section of the spectrometer, the potentials of the adjacent electrodes penetrate rather deeply into the electrode volume as can be seen in Fig. 8.3. As a result the potential in the center of the volume is lower than the applied one and the retardation potential is not uniform over the electrode volume. In Fig. 8.4 the potential in the center of the volume is plotted as a function of the applied retardation potential. This correction has to be taken into account when interpreting the recoil spectrum, unless this is done through full particle tracking simulations in which this effect is automatically included.

Not only in the spectrometer sparking was observed, also in the cooler trap sparking sometimes appeared, especially when using high buffer gas pressures combined with high endcap voltages. Because of this the buffer gas pressure had to be limited during the experiment, implying that the ion cloud could not be cooled efficiently in the cooler trap.

8.3 On-off

With an on-off measurement we mean a measurement in which the retardation is switched between two extreme voltages: 0 V letting all ions through, and 200 V stopping all ions (this voltage is obviously isotope dependent). If a significant decrease in count rate is observed when going from the off-state (0 V) to the on-state (200 V) one has shown that recoil ions are present in the system. This measurement is easier to interpret than a full spectrum measurement and is therefore perfectly suited as a first step in a *proof of principle* measurement.

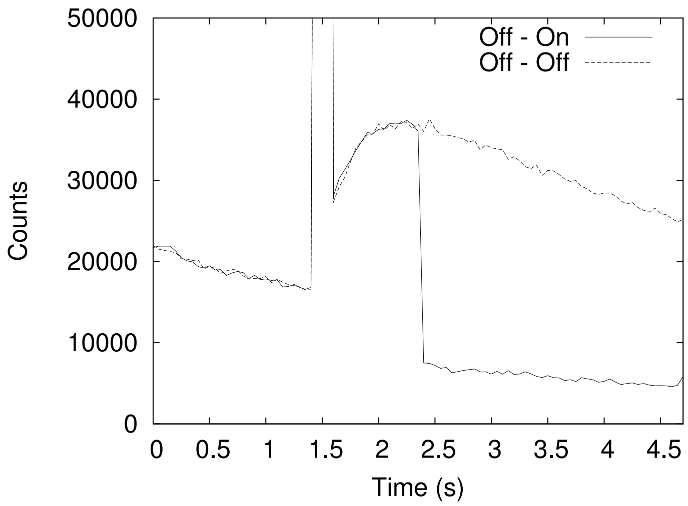

Figure 8.5 – *The count rate measured throughout the measuring cycle during an on-off measurement .*

8.3.1 Spectrum shape

During the retardation on period all ions are blocked and only β-particles can reach the detector. During the retardation off period both ions and β-particles reach the detector and there is no easy way to distinguish between them.

Figure 8.5 shows the result of such on-off measurement. The curve marked *off-on* shows the real measurement. The figure shows the count rate observed by the recoil detector throughout the whole experimental cycle starting with the injection into the cooler trap. After 1.6 s the ions are transferred from the cooler trap into the decay trap. At this moment a big increase in count rate is observed indicating that not all ions were stopped in the decay trap but some got shot through the trap. After 2.4 s the retardation was switched on. A significant decrease in count rate is clearly observed at this point. A separate measurement, marked *off-off* in Fig. 8.5 shows the same experimental cycle but now the retardation is not actually switched on. The count rates in both graphs were normalized to the total number of counts in the first 1.4 s. The comparison between the two curves clearly shows that there are indeed recoil ions in the system and that they can be stopped by using a retardation of 200 V. This was the first time ever that ions recoiling from a Penning trap after β-decay were observed.

The normalization of the count rate as it was done here, i.e. on the basis of the number of β-particles that reach the main detector while the radioactive ions are in the cooler trap, could also provide a way of normalizing the trap loads when the retardation voltage of the spectrometer is only changed in between cycles (section 2.8). However, as was shown in section 2.11, it would be beneficial for the obtainable precision of the experiment to significantly reduce the number

Fitting region	Fitted half-life (s)
0.0 s $< t <$ 1.4 s	3.44 (13)
2.4 s $< t <$ 4.7 s, retardation off	4.06 (7)
2.4 s $< t <$ 4.7 s, retardation on	3.52 (12)

Table 8.1 – *Decay half-life fitted for different measurement regions and supposing that there is no background that is not caused by the radioactive decays in the system.*

of β-particles reaching the main detector, in which case the normalization is no longer optimal.

8.3.2 Half-life

The half-life of the radioactive ensemble can be fitted from the on-off spectrum in three different regions:

- 0.0 s $< t <$ 1.4 s: β-particles escaping from the cooler trap and the decay of ions that where implanted on the detector;
- 2.4 s $< t <$ 4.7 s, retardation off: β-particles and ions escaping from the decay trap and the decay of ions that where implanted on the detector;
- 2.4 s $< t <$ 4.7 s, retardation on: β-particles escaping from the decay trap and the decay of ions that where implanted on the detector.

The results of the half-life fitting in these regions are given in table 8.1.

The fitted half-lives from fitting regions 1 and 3 are consistent with a ratio groundstate/isomer of about 1/2. The fact that the half-life measured during the period that the ions are in the decay trap without any retardation (fitting region 2) is not shorter than the expected half-life indicates that there is no significant loss of ions in the decay trap. There is, however, no clear explanation as yet for the fact that this lifetime is significantly larger than the two other results.

8.3.3 Position information

Although in principle the shape of the recoil energy spectrum is all that is needed to extract the β-ν-angular correlation coefficient a, an investigation of other event parameters can be interesting to study the behavior of the setup and to understand systematic effects. For the analysis that follows two separate measurements were actually used: one where the retardation was switched between 0 V and 200 V (the *off-on* curve in Fig. 8.5) and one where the retardation was not switched but the rest of the cycle was the same (the *off-off* curve in Fig. 8.5). Only the data after the trigger for the retardation switching (after 2.4 s) were included in the analysis.

Firstly we can have a look at the distribution of the events over the detector surface. This is done separately for the retardation on and off states in

Fig. 8.6, where all events are plotted and in Fig. 8.7 where a 2D intensity map is shown.

Several observations can be made:

- The beta particles seem to hit the detector more or less uniformly except for the central region. The increased intensity in this central part is believed to be caused by radioactive ions that where implanted into the detector (probably during the transfer of the ions from the cooler trap to the decay trap; see the peak at 1.6 s in Fig. 8.5) and are subsequently decaying.
- The recoil ions seem to all fall within the detector surface and the distribution of the ions is not cylinder symmetric.

8.3.4 Pulse Height Distributions

In Fig. 8.8 the pulse height distributions of the events that where detected for the retardation off and retardation on periods are plotted. The shapes of these pulse height distributions clearly differ: the β-particles hitting the detector during the retardation on period produce an exponential pulse height distribution, consistent with offline measurements, while during the retardation off period a bell shape pulse height distribution of the ions is added on top of the exponential pulse height distribution of the β-particles, consistent with the data from [Lie05]. Because both pulse height distributions overlap, unfortunately no *event by event* separation between ions and β-particles can be made on this basis.

8.3.5 Introducing cuts

Since for all the events registered by the *event-daq* both the pulse height and the position are known, both parameters can be combined. Useful information can be obtained by imposing certain limits on one parameter and looking at the effect on the other.

Cuts in the pulse height distribution

Firstly, certain events are selected on the basis of their pulse height and their position is plotted. In Fig. 8.9 the positions of the events are plotted for four different regions in the pulse height distribution for no retardation (i.e. when both ions and β-particles reach the detector) while in Fig. 8.10 the same is done for a retardation of 200 V (only β-particles).

- $0 \rightarrow 50$: for the retardation on period (Fig. 8.10) a similar position distribution as the one from Fig. 8.6 (bottom) is observed with a uniform distribution and a brighter central region. For the measurement without retardation (Fig. 8.9) a large central spot of ion events is seen, but still the outside of the detector detects only beta particles.
- $50 \rightarrow 100$: for both the retardation on and off measurements the result in this pulse height distribution region is much the same as in the region $0 \rightarrow 50$, but with less intensity.

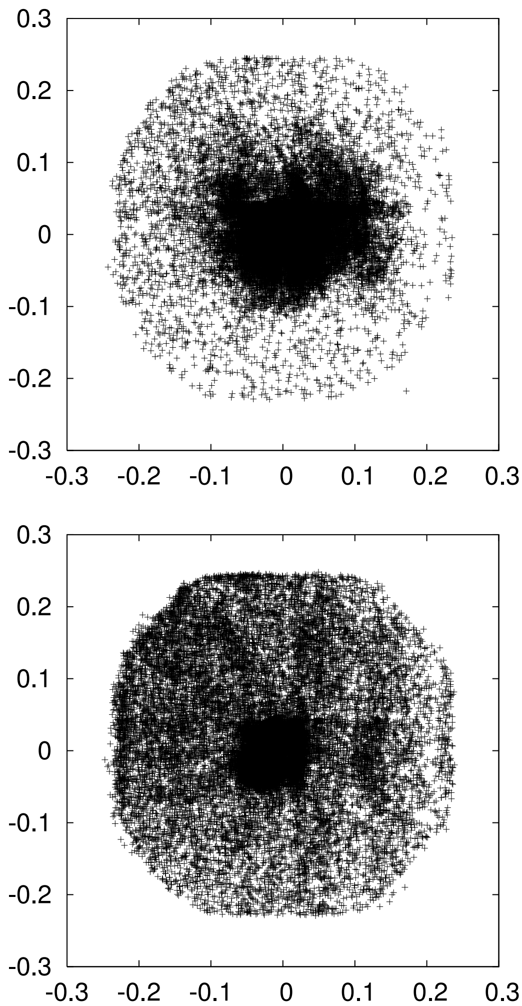

Figure 8.6 – *Distribution of the events over the detector surface (top) retardation off (bottom) retardation on. Note that the counting time for the top and bottom plots was different.*

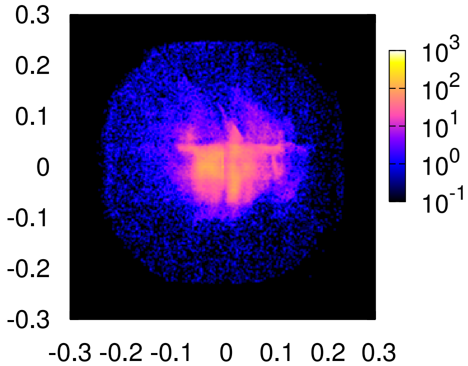

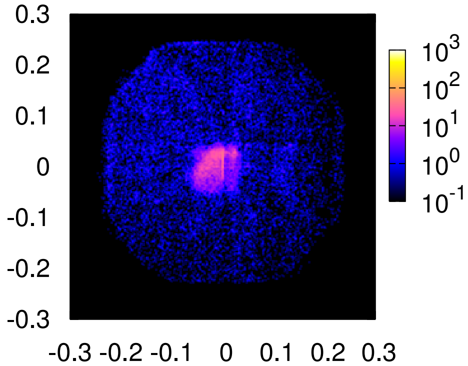

Figure 8.7 – *2D histograms of the event distribution over the detector surface (top) retardation off (bottom) retardation on.*

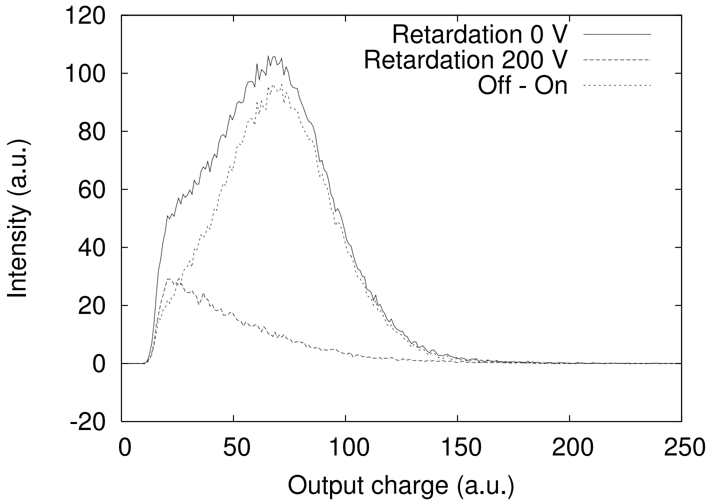

Figure 8.8 – *Normalized pulse height distributions for retardation off and retardation on and the difference between both, showing the pulse height distribution as it is caused by the ions.*

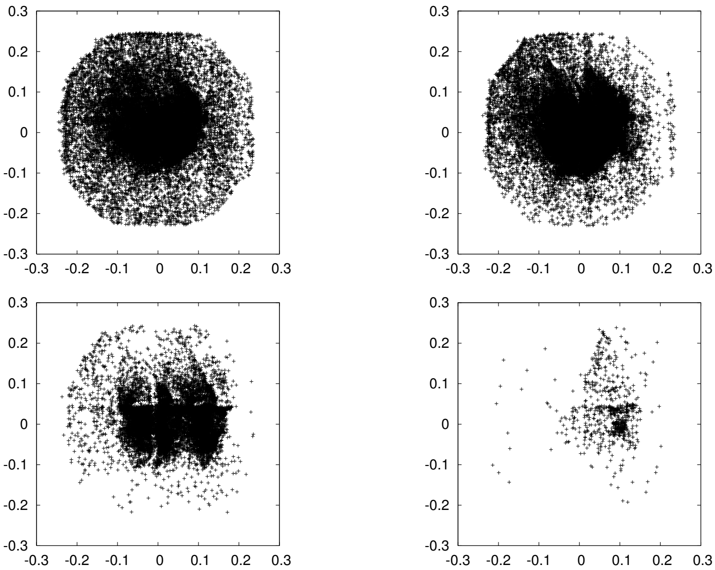

Figure 8.9 – *Positions of the events with no retardation for four different pulse height distribution regions in Fig. 8.8: from left to right, top to bottom: channels* $0 \rightarrow 50$, $50 \rightarrow 100$, $100 \rightarrow 150$, $150 \rightarrow 250$.

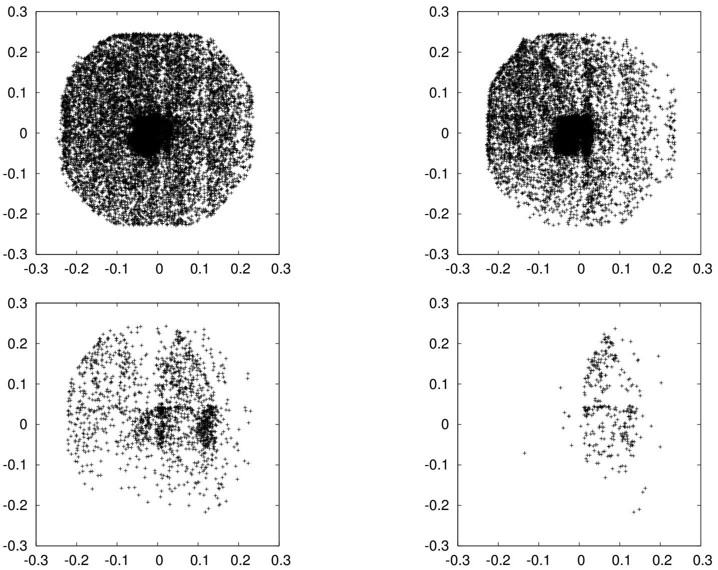

Figure 8.10 – *Positions of the events with 200 V retardation for four different pulse height distribution regions in Fig. 8.8: from left to right, top to bottom: channels* 0 → 50, 50 → 100, 100 → 150, 150 → 250.

- 100 → 150: here in both retardation off and on measurements interesting structures appear. For the retardation off a completely asymmetric profile is seen. For retardation on an extra bright spot (around x = 0.13 and y = 0) is observed.

- 150 → 250: all events with very high pulse height seem to lie to one side of the detector, both for retardation on and off. This could be caused by a non-uniform efficiency of the detector.

Cuts in position

Secondly, a selection in position of the events will take place and for this detection region the pulse height distribution will be plotted.

Firstly, we can look at the pulse height distribution of the events that fall on the outer perimeter (outer 0.6 cm) of the detector during the retardation off period. As can be seen in Fig. 8.11 the pulse height distribution of these events has the characteristic exponential shape associated with the β-particles, indicating that all ion events are situated at the inside of the outer perimeter and thus supporting the claim that all ion-events fall within the detector surface.

Secondly, we can concentrate on one of the asymmetric areas seen in the retardation off distribution. For a very specific region of the events of Fig. 8.6 where $-0.1 < y < 0.1$ and $0.1 < x < 0.15$ (the brighter spot mentioned above) the resulting pulse height distribution is shown in Fig. 8.12. The pulse height

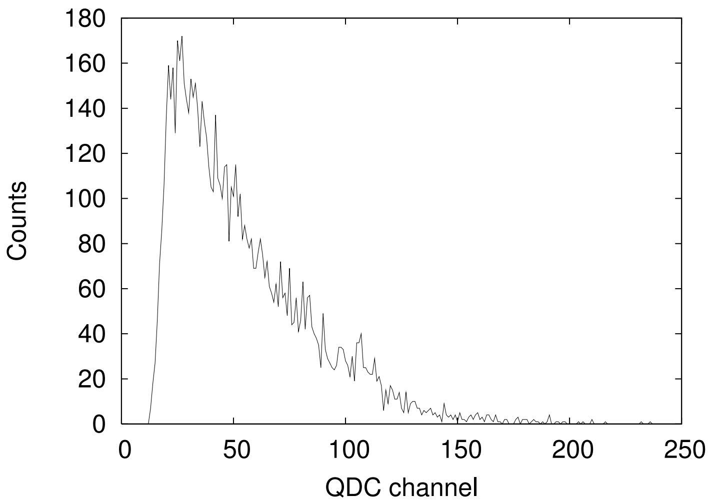

Figure 8.11 – *Pulse height distributions for the events that hit the detector at a radius larger than 0.17 (1.7 cm) during the retardation off period.*

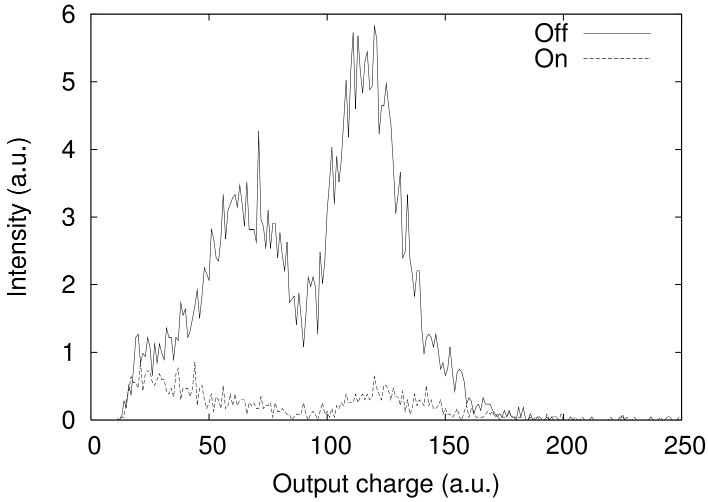

Figure 8.12 – *Normalized pulse height distributions for the events that hit the detector at a location where* $-0.1 < y < 0.1$ *and* $0.1 < x < 0.15$.

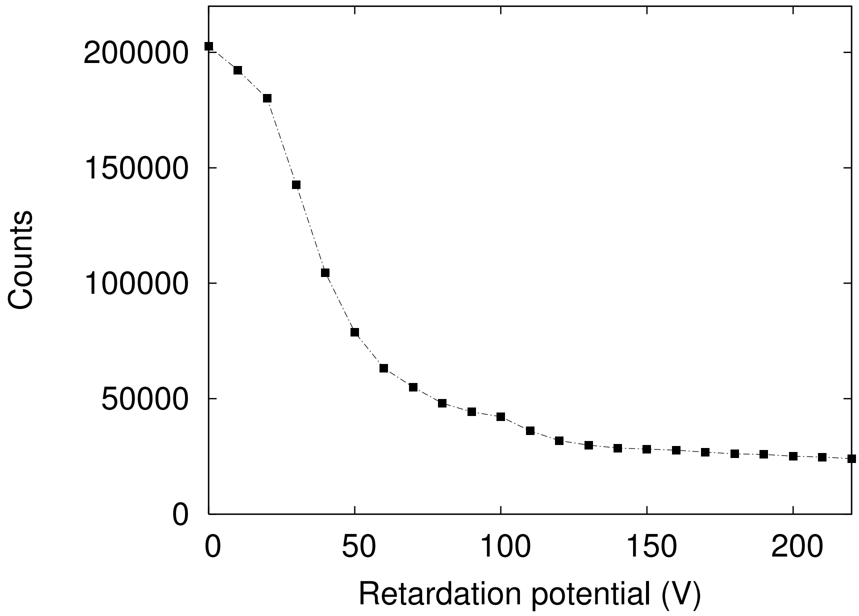

Figure 8.13 – *Integral energy spectrum of the recoiling ions after the ^{124}In β-decay. The data points were connected to guide the eye and the statistical error bars fall within the symbols.*

distribution clearly shows a second bell shaped peak between QDC channels 100 and 150, in addition to the structures that were already visible in Fig. 8.8. This structure is observed in both the on and off data. No conclusive explanation for this effect has been found yet. Precise off-line tests with the detector will have to show whether it is a detector related effect, e.g. caused by a non-uniform detection efficiency over the detector surface.

8.4 First recoil spectrum

With the on-off measurement discussed above, clear evidence was given that recoil ions were indeed seen to escape the decay trap after β-decay. The next step was trying to measure the energy spectrum of the recoiling ions. For this the same setup as for the previous measurement was used but instead of switching the retardation from 0 V to 200 V in one step, it was now switched from 0 V to 220 V in steps of 10 V. The recoil spectrum obtained in this way is shown in figure 8.13.

8.4.1 Spectrum shape

To understand the shape of the recoil spectrum as it was measured, many factors have to be included in the analysis. Several of these are known, i.e.

- the lifetimes of ^{124g}In and ^{124m}In (3.11 s and 3.7 s);
- their decay schemes (Appendix C), needed for the determination of the recoil energy due to γ-ray emission following the β-decay (section 1.4.4);
- the actual retardation potential (section 8.2);
- the potential of the decay trap, important for the determination of the trapped-after-decay fraction (section 2.5.2).

However, some have to be inferred from the spectrum itself. To start the analysis the following assumptions were made:

- the charge state distribution is the same for all decay branches and for both the ground and isomeric state and is not energy dependent;
- the a parameter was assumed to be equal to -1/3 (the value for a pure Gamow-Teller decay) for all decay branches, although for some levels the spins are not exactly known and thus also first forbidden β-transitions are possible. This is a valid assumption since for allowed decays the isospin selection rule forbids Fermi transitions for ^{124}In (contribution due to isospin-mixing being at most of the percent level). Further the a-parameter for a first forbidden transition can be approximated by the value for an allowed transition;
- because of the complexity of the decay schemes the weakest decay branches (i.e. branching ratio <1%) were not taken into account;
- the temperature of the ion cloud in the decay trap was fixed at 100000 K corresponding to an average kinetic energy of about 8.5 eV in accordance with the potential needed on the upper endcap of the decay trap to trap the particles.

The recoil spectra for all decay branches and charge states were then generated separately in a much simplified simulation of the setup. Later all these spectra were combined to form the total spectrum in a fitting routine that varied the following parameters:

- an offset on the retardation potential as presented in section 8.2 (*offset*);
- the contribution of ^{124m}In to the beam (*isomer*);
- an overall scaling factor that is a measure for the total amount of recoil ions that reached the MCP detector (*scaling*);
- a scaling factor for the exponentially decreasing β-background (β*-scaling*).

In addition the charge state distribution was assumed to consist of two separate parts:

- a pure β^--recoil part. For this a scaled charge state distribution measured for the pure ground state to ground state β^--decay of ^{85}Kr (see Fig. 8.14 [Sne57]) was used which was additionally shifted by 1 unit of charge. Only an overall scaling factor was varied for this distribution (β^-*-charge*);

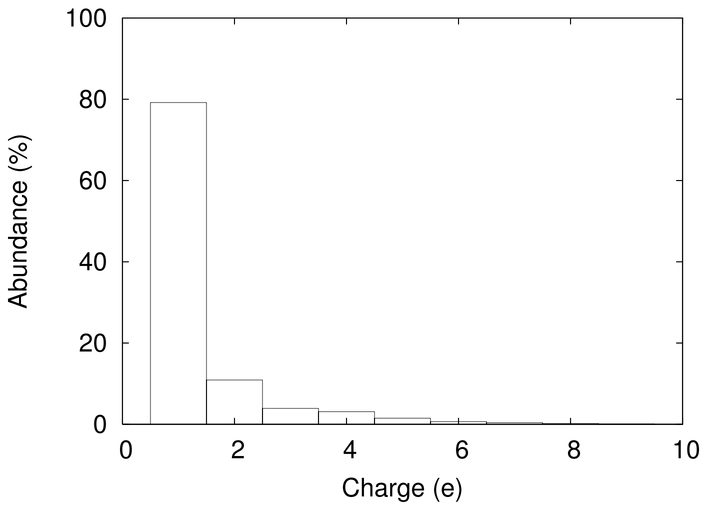

Figure 8.14 – *Charge state distribution of the recoil ions after the ground state to ground state β^--decay of ^{85}Kr [Sne57]. The distribution for the higher charge states is simply determined by the statistical chance of shaking off several electrons at the moment of the decay and not by any cascading mechanism.*

- a Gaussian charge state distribution at higher charge states. Both the position of this Gaussian distribution and its width were left as free parameters (G_μ and G_σ).

This type of charge state distribution was used to allow for a distribution like the one that was observed in Ref. [Sne58] for the decay of ^{133}Xe (see Fig. 8.15). In this reference the measured charge state distribution is explained as being the combination of the monotonically decreasing β^--decay charge state distribution observed for ^{85}Kr [Sne57] (Fig. 8.14), but also for ^{23}Ne [Car63] and ^{41}Ar [Car63], and the charge state distribution caused by internal conversion, which is peaked at higher charge states, as was observed for $^{131}Xe^m$ [Ple57] (Fig. 8.15).

The resulting simulated recoil spectrum that agrees best with the measured data is shown in Fig. 8.16. As can be seen the overall agreement is reasonably good, although some specific features of the measured spectrum are not reproduced, i.e. the sharp decrease in the beginning of the spectrum and the small bump around a retardation potential of 100 V.

Fitting the experimental data yielded the charge state distribution for the decay of $^{124g,m}In$ 1^+ ions, which is shown in Fig. 8.17 and table 8.2. This fit has a high χ^2/ν of 1131/16, but omitting the first data point as well as the three points of the bump at 100 V retardation potential improves the reduced χ^2 by a factor of more than two, to a χ^2/ν of 362/12. Despite of this high reduced χ^2 and the fact that the present data set is too limited to obtain rigid constraints for all parameters mentioned above, the most striking

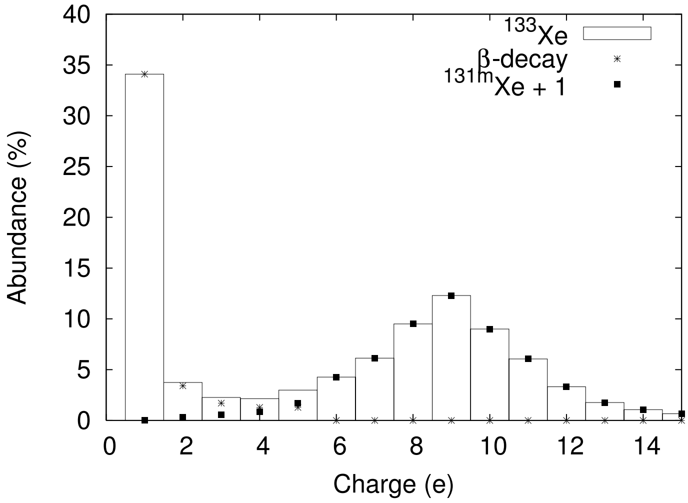

Figure 8.15 – *Charge state distribution of the recoil ions after the decay of ^{133}Xe [Sne58]. The pure β^- contribution and internal conversion (Auger cascade) contribution to the charge state distribution are indicated separately. The shape of the β^- contribution was previously observed for* ^{85}Kr

, while the contribution of the internal conversion processes was previously measured for ^{131m}Xe, but was shifted by one unit of charge in this case.

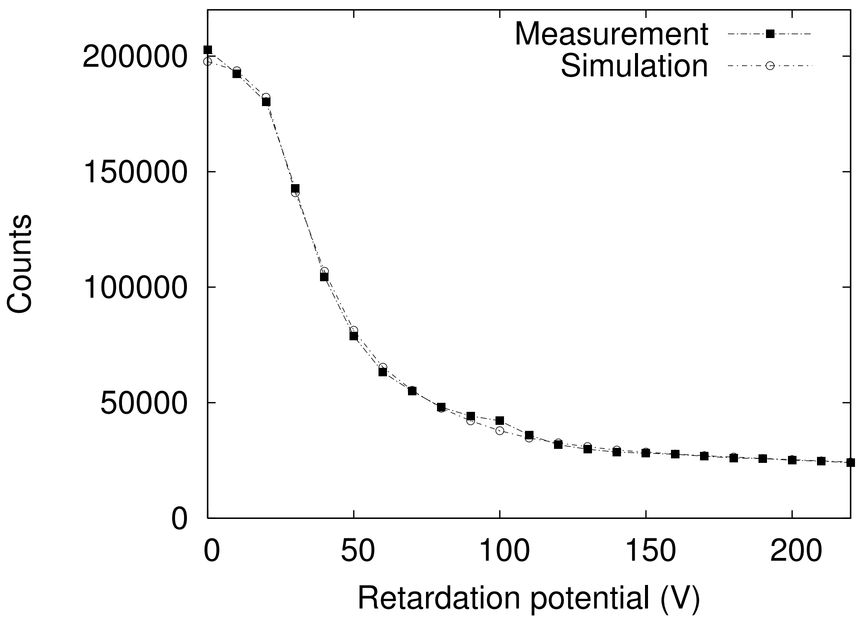

Figure 8.16 – *Comparison between the simulated and measured recoil spectrum.*

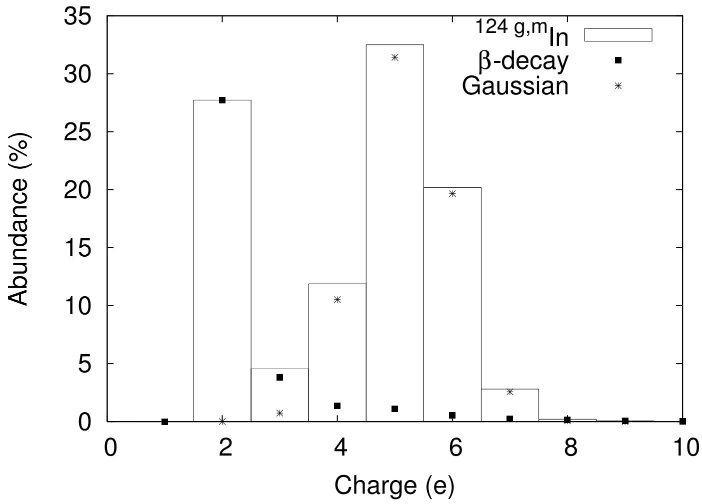

Figure 8.17 – *Charge state distribution of the recoil ions after the decay of $^{124}In/^{124m}In$ as obtained from fitting the experimental recoil ion energy spectrum shown in Fig. 8.13.*

Charge state	Abundance (%)
1^+	0
2^+	28
3^+	5
4^+	12
5^+	33
6^+	20
7^+	3

Table 8.2 – *Charge state distribution of the recoil ions after the decay of $^{124}In/^{124m}In$ as obtained from fitting the experimental recoil ion energy spectrum. See also Fig. 8.17.*

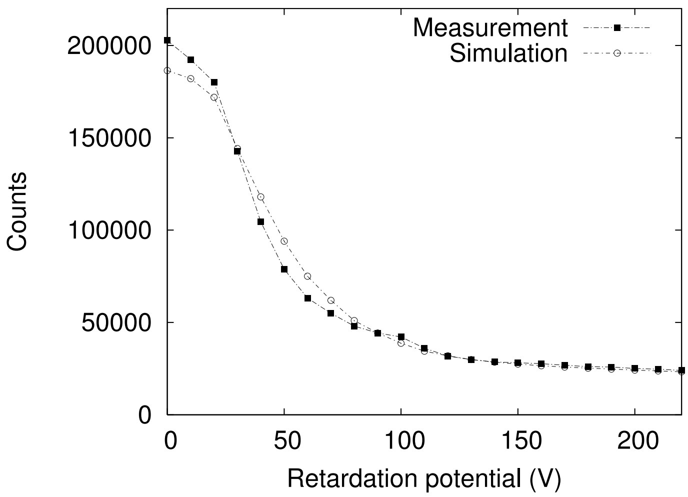

Figure 8.18 – *Best fit to the measured recoil spectrum of Fig. 8.13, when omitting the higher charge states and only taking into account the β^- charge state distribution.*

feature, namely the double peak structure of the recoil charge state distribution, is needed to satisfactorily explain the measured recoil spectrum. If the broad distribution at higher charge states is omitted, even the best fit strikingly misses almost all of the data points. This is demonstrated in table 8.3 where χ^2/ν is given as a function of the contribution of the β^- charge state distribution to the total charge state distribution. To further illustrate this graphically, the best fit that could be obtained when omitting the higher charge states and only taking into account the β^- charge state distribution, is shown in Fig. 8.18. This shows that the contribution of the β^- charge state distribution to the total charge state distribution is determined to be only $35 \pm 10\%$ with the error bar a mere estimate based on the data presented in table 8.3 and not a 1σ error bar.

As mentioned before this type of double peaked charge state distribution was also observed for the decay of (neutral) ^{133}Xe, a pure β^--decay followed by internal conversion in about 65% of the cases. In Ref. [Sne58] the presence of the higher charge states was ascribed to the presence of this large internal conversion component in the decay. In the case of our measurement, however, only a limited number of the decays gives rise to internal conversion processes (about 10% of the decays, see for instance table 8.4) but a significant contribution (i.e. about 65%) of the second broad distribution at higher charge states is nevertheless observed. This factor of 6 larger contribution from Auger cascades compared to what is expected from the internal conversions in the decay of $^{124g,m}In$ is striking.

Our result thus seems to suggest that an orbital electron that does not originate from the outer shells is more frequently (i.e. in about 65% of the decays) lost in the decay of $^{124g,m}In$ 1^+ ions than in the decay of ^{85}Kr. By this

β^--*charge* (%)	20	25	30	35	40	45	50
χ^2/ν	113	90	74	71	75	88	117
χ^2/ν'	59	40	33	30	54	67	102
offset (V)	3	3	3	3	5	5	5
isomer (%)	50	50	50	50	50	55	55
scaling	96755	97800	105585	99315	96254	93740	88495
β-*scaling*	38850	38450	38450	38150	38050	37800	37450
G_μ	4.5	4.8	5.5	5.3	5.2	5.2	5.1
G_σ	1.25	1.35	1.25	0.80	0.80	0.80	0.80

Table 8.3 – *χ^2/ν for the best fit for different values of the contribution of the β^- charge state distribution (^{85}Kr) to the total charge state distribution. χ^2/ν' denotes the reduced χ^2 when omitting the first data point as well as the three points of the bump at 100 V retardation potential. The other fit parameters varied little, except the width of the Gaussian contribution in the charge state distribution which varied within ±30%. These data clearly indicate that the higher charge states are needed to satisfactorily explain the measured data. Note that the scaling factor as given here, can not directly be translated into the number of observed recoil ions.*

the ^{124}Sn daughter ends up in a higher charge state through the subsequent Auger cascades in which additional orbital electrons are removed. It is however striking that this process is not caused by internal conversion, which occurs in less than about 12% of the decays. Comparison of the position of the maximum of the Gaussian component in the charge state distribution with the one that was previously observed for the internal conversion in the decay of ^{133}Xe [Sne58] and $^{83}Kr^m$ [Dec90], additionally indicates that in the case of $^{124g,m}In$ an electron from an intermediate shell is lost as the loss of an electron from the lowest lying shells would give rise to even higher charge states. It should be noted that the data presented here are for decays that started with a charged mother ion, certainly explaining a shift of one unit in the charge state distribution, and that the electronic structures of *Sn* (the daughter of ^{124}In) and the singly ionized alkali *Rb* (the daughter of ^{85}Kr) are quite different. Another possible reason that could explain the difference is the fact that the previously mentioned measurements were performed with a gaseous source in which collisions, and thus charge exchange, of the daughter ions can not be excluded, although the mean free paths are considerably longer than the size of the measurement apparatus [Sne57]. One last point that could explain the observed contribution of higher charge states is the difference in decay energy which is of the order of several MeV in the case of $^{124g,m}In$ but only of the order of 0.7 MeV for ^{85}Kr and 0.35 MeV for ^{133}Xe. To be able to formulate a definite conclusion in this respect, a dedicated measurement or dedicated calculations would have to be performed.

8.4.2 Position and pulse height

For a correct measurement of a recoil spectrum it is important to be sure that during the entire measurement all recoil ions fall within the surface area of the

Isotope	γ-energy (keV)	multipolarity	branching ratio (%)	internal conversion (N_{IC}/N_{tot})
^{124g}In	/	/	/	/
^{124m}In	102.91	E1	45(5)	0.142
	120.34	E2	38(4)	0.456
	243.12	M1 (+E2)	11(1)	<0.1

Table 8.4 – *Low energy γ-transitions in the decay of $^{124g,m}In$ [NNDC] and their corresponding internal conversion coefficients [Ban02].*

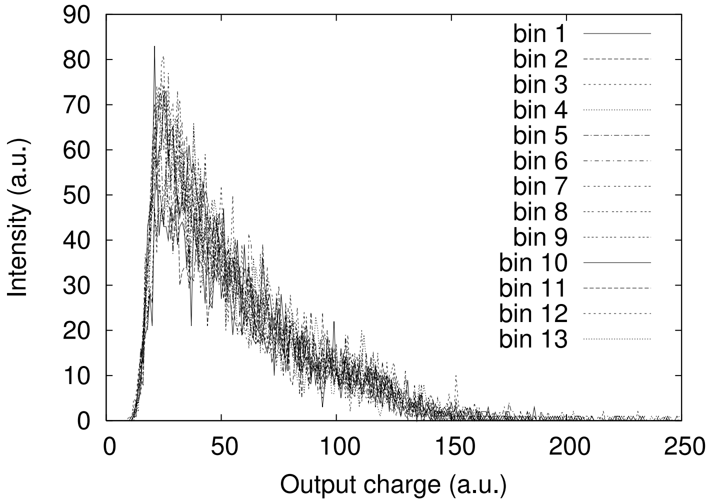

Figure 8.19 – *Pulse height distributions for the outer rim of the detector (r > 1.7 cm) for the first 13 retardation steps of the recoil spectrum shown in Fig. 8.13.*

detector. For this reason the pulse height distribution for the first 13 measuring bins, after which the spectrum is dominated by β-particles, is shown in figure 8.19. All pulse height distributions show a characteristic exponential shape indicating that for none of these retardation steps the recoil ions have moved to the edge of the detector, giving confidence that all recoil events were correctly detected.

8.5 Conclusion

The first measurements at the WITCH setup have convincingly proven the principle of the experiment. For the first time a Penning trap was used as a scattering free radioactive source for ions that recoil after β-decay. The analysis of this first experiment has hinted towards a charge state distribution for the recoiling ^{124}Sn nuclei that consists of two separate parts: a low charge state part (2^+ and 3^+) and a high charge state part (4^+ to 7^+). This should be considered as the first *physics* result produced by the WITCH experiment after several years of primarily technical development and testing [Koz05, Del04].

Although the measurements have convincingly proven the principle of the experiment, several problems in the interpretation of the results are still present. These are both of a technical (e.g. MCP behavior and spectrometer sparking) as well as of a physical nature (e.g. complex decay scheme of ^{124}In and its isomer $^{124}In^m$). Especially the points of technical nature have to be addressed thoroughly before proceeding to the next measurement and systematic investigations of several of these points are already ongoing. In this respect a full systematic investigation of the recoil ion MCP's response has been shown to be imperative. Furthermore the analysis lacks the input of a full particle (recoil ions and β-particles) tracking simulation to include as many of the systematic effects caused by the setup as possible.

In view of a precision experiment, the analysis of the first *proof of principle* experiment has also shown how important it is to determine as many as possible of the free parameters like the charge state distribution, the temperature of the ion cloud or any isobaric contamination, independently from the actual spectrum measurement. Luckily for a measurement of the β-ν-angular correlation coefficient a on ^{35}Ar no radioactive isobaric contamination is expected and the full charge state distribution is of less importance as only the upper half of the recoil spectrum will be used.

Chapter 9

Evaluation of current status

Although many of the challenges that have to be faced at the WITCH experiment to come to a precision measurement of the β-ν-angular correlation coefficient a have already been mentioned throughout the text, in this chapter they will be listed and discussed in more detail to provide an overview of the current status of the experiment.

9.1 First results

In the previous chapter, the first results obtained with the WITCH setup were discussed. It was shown how for the first time ions recoiling from an electromagnetic Penning trap were detected and how, through the use of an electromagnetic retardation spectrometer, their recoil energy could be determined. Also for the first time the charge state distribution for the decay of a charged mother ion was studied. In addition, it was the first time that β-recoils were observed from the decay of an element that is neither an alkali nor a noble gas. This experiment concluded the first testing and setting up phase of WITCH and paved the road for future precision experiments.

9.2 Technical issues

Before coming to a final measurement, several technical issues that were encountered throughout the years and especially during the first measurement have to be considered in more detail. Some key issues will be discussed separately here.

9.2.1 Beamline tuning

It is clear that a continuous effort has to be made to improve the efficiency of the WITCH beamlines and to maintain this efficiency. This requires a lot of time actually working with the setup and this in term requires the WITCH experiment to be independent from ISOLDE and especially REX. A first step in this direction has been taken through the installation of a new high voltage ion source in the WITCH beamline (chapter 2) but full independence also requires the magnetic field to be shielded (chapter 10).

9.2.2 REXTRAP optimization

As was mentioned in chapter 2, the parameters used at REXTRAP for REX operation are not always optimal when using REXTRAP in combination with WITCH. That is why a detailed study of the REXTRAP parameters is needed to ensure optimal working conditions at WITCH. These parameters include collection/cooling times, excitation amplitudes, buffer gas pressure *etc.* and their dependence on the number and species of trapped ions. These tests require a lot of offline testing with REXTRAP which was in the past and still is now not always possible due to the large amount of beamtime REX experiments take up. Important work in this respect was performed recently [Van07].

9.2.3 Penning trap operation

Not only the REXTRAP Penning trap has to be optimized, also the WITCH Penning traps require an intensive study.

Optimal parameters

First of all the optimal operation parameters have to be found, like in the case of REXTRAP. Not only high efficiency should be obtained but the Penning traps should enable us to obtain a well prepared source for an experiment. This includes the removal of isobaric contaminants from the ion beam that is obtained from ISOLDE. It is clear that it is almost impossible to optimize all parameters at once (for instance longer excitation times lead to better mass resolution but also result in more losses due to the radioactive decay) and therefore a good compromise has to be found through experimental testing. In this respect a lot can still be learned from other experiments using Penning traps like for instance ISOLTRAP, SHIPTRAP or JYFLTRAP.

Ion cloud temperature

Even if a well prepared ion cloud can be obtained in the cooler trap, it still has to be transferred to the decay trap at very low energy. In chapter 6 it was shown that this is in principle possible but it has yet to be tested experimentally. Not only is this important to limit the amount of kinetic energy the ions have in the decay trap, but it is also crucial for the analysis of the experimental data that the temperature of the ion cloud is known with good precision. It is unclear for the moment how this can be tested experimentally without using a radioactive beam.

Charge exchange

Because of the use of buffer gas to cool the ions, charge exchange processes, in which the ion of interest attracts an electron from a buffer gas particle (or more importantly a contaminant in the buffer gas) are likely to occur. It has yet to be tested experimentally how important this is for WITCH, but as one of the prime isotope candidates to be used is the ionized noble gas ^{35}Ar these effects are not likely to be negligible.

Sparking

At several occasions the endcap electrodes of the cooler trap have been seen to produce some sparking, especially when high buffer gas pressures are used. This problem will hopefully be solved after the installation of the newly coated Penning traps. Once this issue has been resolved the cooling power in the cooler trap can be optimized to obtain an as cold as possible cloud in the decay trap.

9.2.4 Spectrometer

Sparking

Another issue that has to be investigated in more detail is the sparking of the spectrometer electrodes. Although some off-line tests have already been performed, a more in depth investigation with $\beta^{\pm}$- and γ-sources is needed. For β^{+}-particles not only the particles themselves might cause problems, but also the 511 keV γ-ray background created by their annihilation might be an issue. Even if the major sparking is solved, one has to make sure that no *false counts* end up in the recoil spectrum falsifying the result. To avoid electrons that are created when γ-rays strike the electrodes from entering the main spectrometer volume, a shield consisting of a grid mounted on the inside of the spectrometer electrodes and biased at a slightly lower voltage might be needed.

In this respect it is also necessary to check the effect of ions or β-particles that remain trapped somewhere in the spectrometer volume as they could induce discharges when a large amount of charged particles builds up. To avoid this effect it might be necessary to install a system that removes trapped charges when required. This could be achieved by momentarily creating a large electric field that deflects all trapped particles towards one of the electrodes.

Response function

As for the first experiment the full retardation spectrometer could not be used, its response function could not be checked yet. Preferentially this is done by using the mono energetic recoils from an electron capture decay. As will be shown in chapter 11 short lived EC-decay isotopes are difficult to find and if one needs decays with different recoil energies to fully test the spectrometer the task becomes even harder. Possible usable isotopes include ^{140}Eu, ^{140}Pm and ^{144}Eu (see chapter 11 and note that ^{140}Eu could possible suffer from isobaric contamination of ^{140}Pm). Therefore it might be necessary to find other ways for testing the spectrometer response function. This could include ejecting the ions from the decay trap with a strong electric field, or applying an excitation in the decay trap to increase the kinetic energy of the ions.

9.2.5 Recoil detector

One of the steps that has to be undertaken before proceeding to a final measurement is the systematic investigation of the behavior of the recoil ion detector. The analysis of the first data presented in the previous chapter clearly indicate that there are potentially numerous systematic effects that can be caused by this detector. One of the tests that certainly has to be performed is a detailed measurement of the efficiency for the different regions of the detector surface as this might have severe consequences for the analysis of data from a precision measurement.

Although the data presented in chapter 8 show that all recoiling ions arrive well within the detector surface, the possibility that some 1^+ ions (which where not present in that measurement but will be when using ^{35}Ar decays) miss the detector can not yet be excluded. If this would be the case, one will have to invest in a bigger MCP detector, preferably again of the type described in Ref. [Lie05] (DLD80).

9.2.6 Alignment

Not only for the beamline but also for the Penning traps and the spectrometer, alignment is an important issue. Although the beamline was aligned mechanically, the alignment with respect to the magnetic field was never checked in detail neither for the beamline nor for the Penning traps or the spectrometer. It is clear that to avoid asymmetries in the setup this issue deserves some attention in a future phase of the experiment.

9.3 Principle issues

Besides several issues of technical nature, there are also some issues that are of a more principle nature that have to be addressed.

9.3.1 Charge state distribution

The charge state distribution of the recoiling ions has already been mentioned several times as being an important parameter in the interpretation of many results that can (or have been) obtained with the WITCH setup. It immediately also shows how interdisciplinary the experiment is, as this distribution finds its origin in atomic physics effects. Therefore if this effect is to be investigated theoretically, cooperation with physicists specialized in atomic physics will become important. In chapter 10 several possibilities for experimentally determining the charge state distribution after the decay will be presented.

9.3.2 Particle tracking simulations

Experimental data from a technically complex experiment like WITCH can not be analyzed by using some theoretical description of all of its components.

Rather the data can only be analyzed by repeating the experiment in a simulation routine that reproduces the experimental conditions as closely as possible. As the experiment deals with particles flying through a combination of electric and magnetic fields, it is clear that such simulations should be full particle tracking simulations. Such simulation routine is currently being developed at the university of Münster [Fri07].

Penning traps

In chapter 6 some simulations on the behavior of ion clouds containing a relatively small number of ions were already discussed. It has to be stressed again how important this type of simulations is with respect to a full description of the experimental setup in a simulation routine. It is therefore also imperative that simulations for ion clouds containing more ions are performed and that they are checked against experimental data, preferentially obtained with the WITCH Penning traps. To increase the range of the amount of particles that can be simulated, new simulation methods will have to be used as the computing power becomes insufficient quite fast, unless specialized hardware can be used.

Spectrometer response

Besides the Penning traps, the spectrometer is also a section of the setup that deserves a lot of attention in simulations, as the particles execute a complex motion due to the changing magnetic and electric field in this section. Simulations together with experimental investigations will also have to point out any systematic effects caused in this part of the setup.

9.3.3 Choice of isotope

In section 2.9 a list of properties that an isotope to be used in a measurement should have, was listed. A table of several interesting isotopes was also given. Some physically interesting isotopes, notably $^{26}Al^m$ and ^{46}V, where later excluded from the list due to their low production yield at ISOLDE. If their production yields would however be increased significantly thanks to new developments in target and ion source technology, they are potentially more interesting candidates than ^{35}Ar which is the prime physics candidate for the moment.

Chapter 10

Future planning and additional improvements

10.1 Short term future plans

The principle of the experiment has been proven to work by the measurements on ^{124}In. A next step in the steady progress of the experiment will be a recoil ion spectrum measurement of ^{35}Ar. Once this has been achieved a lot of work will have to be invested in the thorough systematic investigation of the whole apparatus. Not only will many off-line tests have to be performed, a large effort will also have to be made to implement the whole system in a simulation routine that can be used to analyze the experimental data (see chapter 9).

10.2 Additional technical improvements

Many technical improvements have already been suggested throughout the text. Some more will be mentioned in this section. One topic that has not been mentioned yet but deserves to be is certainly the shielding of the WITCH magnet system.

10.2.1 Magnetic field shielding

The WITCH experiment requires a high magnetic field for the operation of the Penning traps. The magnetic field is however not shielded and can therefore influence the ion beam in other experiments. Most notably the highly charged ions in the nearby REX beamline are strongly affected by the WITCH magnetic field. Because of this, no off-line tests with the WITCH system that require the magnetic field can be performed when REX is using the ISOLDE beam. To ensure a fast and continuous progress at WITCH it is thus unavoidable that the system is shielded. Simulations have shown that this is only possible by enveloping the REX beamline section from the EBIS to the entrance of the RFQ in a material with high permeability like mumetal or supermalloy. The technical achievability of such magnetic shielding is momentarily being investigated.

10.2.2 Scintillating optical fibers

Although a scintillator setup for normalization through the detection of β-particles was already presented in chapter 7, other possible schemes using a scintillator also remain possible. One of the interesting ideas in this respect is the use of scintillating optical fibers. These fibers have the properties of an optical fiber for transporting light signals but combine this with scintillating properties. This allows one to easily shape them into different forms, without the need for complicated machining. By using separate pieces of these fibers or by using a delay line setup, they can even be used as a position sensitive scintillator. By installing such a position sensitive β-detector in the system, not only normalization is provided, but it also gives a possible check for systematic effects like asymmetries in the system.

10.2.3 Solid state detector

If a detector that can distinguish between ions with different charge states would be used to count the recoiling ions instead of a microchannel plate detector, the β-ν-angular correlation coefficient can not only be derived from the upper part of the recoil spectrum but from of a fit of the whole spectrum. It could even be determined separately for all different charge states, providing a result with much higher precision. Additionally the detector would allow a better separation of the signals resulting from ions and those from β-particles, further increasing the precision through a reduction of the background. Such detector could be for instance a Si-detector with a very thin *death layer*. By elevating the detector to high potential, one can make sure that all ions and all charge states are detected with high efficiency (possibly close to 100%). The feasibility of using such detector as recoil ion detector depends very much on the progress that is made by the manufacturers of this type of detector in decreasing the thickness of the *death layer*.

Such detector could be tested in the WITCH beamline using either REX-TRAP or the WITCH high voltage ion source, in which case there is no need to elevate the detector to high potential but different charge states can not be obtained.

10.3 Future physics goals

Although a precision measurement of the β-ν-angular correlation coefficient to investigate the contribution of Scalar currents in the Weak interaction Hamiltonian is the first goal, it is not the only physics question that can be pursued with the WITCH experiment. Thanks to the use of Penning traps, a whole range of isotopes can be used for experiments. Also its location at the ISOLDE separator, makes that many different elements can be selected.

$t_{1/2}$ (s)	yield (ions/μC)	daughter	state	$t_{1/2}$	ΔE (MeV)	$T_{R,max}$ (eV)	BR %	a_{SM}
3.0	$1.7 \cdot 10^7$	^{58}Fe	gs	stable	6.250	302	97	-1/3
65.3	$*$		ex	2.2 ps	4.117	118	76	?

Table 10.1 – *Most important properties for the isotope* ^{58}Mn.
**No information available on the same target [Isolde].*

One of those possibilities is a measurement to determine a possible contribution of a heavy neutrino in the weak interaction eigenstate of the electron neutrino. This measurement will be discussed separately in chapter 11. Some other possible measurements are described below and many can still be added to the list.

10.3.1 Tensor currents

Obviously not only limits on Scalar type currents can be derived from a precision measurement of the β-ν-angular correlation coefficient but also Tensor type currents can be searched for in the same way. Although the sensitivity for this type of physics is worse ($a = \mp 1/3$ for Tensor *vs.* $a = \pm 1$ for Scalar), a β^--decaying isotope could be used, leading to an increased detection efficiency as one does not rely on *shake-off* to obtain a charged daughter isotope (see section 1.4.3).

One possible candidate could be ^{58}Mn (most important properties listed in table 10.1), a pure Gamow-Teller β^--decaying isotope with a half-life of 3 s. Unfortunately this isotope also has a 65.3 s isomer on which no yield information is known for the same UC_x target on which the groundstate is produced most intensely ($1.7 \cdot 10^7$ particles/μC). It is, however, produced two orders of magnitude more intensely on a Nb target ($1.2 \cdot 10^7$ *vs.* $1.3 \cdot 10^5$ particles/μC). All other isobaric contaminants can be suppressed by the use of the RILIS laser ion source [Mis93].

10.3.2 Recoil charge state distribution

As was stressed before (see e.g. section 1.4.3) the charge state distribution after $\beta^\pm$-decay is poorly or not known for many isotopes. Since the retardation spectrometer can separate the recoil spectra of these charge states, the WITCH setup could be used to determine the charge state distribution after $\beta^\pm$-decay of a wide range of isotopes.

Alternatively to using the retardation spectrometer, a TOF measurement could be performed like was suggested in Ref. [Del04]. This would involve raising the endcap electrodes of the decay trap high enough that no recoils can escape the trap, and after some time ejecting all the trapped ions and measuring their TOF towards the main detector. To obtain good precision with this method, possible charge exchange effects of the multiplely charged daughter ions in the decay trap should first be investigated. These effects could be circumvented in the measurement if one would, for instance, eject the decay trap after different trapping times and extrapolate the charge state distribution ratios to time zero to obtain the real charge state distribution after the decay. Note that when using this method the daughter ions with a charge state of 1^+ can not be distinguished from the mother ions that have not decayed yet.

Yet another option is to use the solid state detector mentioned above, in which case deriving the charge state distribution after decay becomes almost trivial. When using this detector one could even perform coincidence measurements where the β-particle is detected using the scintillator discussed in chapter 7, thus improving the signal to noise ratio. It would then also be advantageous to bring the whole spectrometer section to some negative potential to limit the TOF of the recoiling ion through the spectrometer, thus increasing the count rate that can be handled successfully.

10.3.3 Spectroscopy

Not only for β-recoil measurements the use of a Penning trap as a scattering free radioactive source can be interesting, also for spectroscopic measurements it can be advantageous. Two types of experiments can be distinguished: *in trap* measurements and *trap assisted* measurements. In the first a Penning trap is used as a scattering free radioactive source, while in the second only the high mass resolving power of the trap is used to obtain a pure radioactive sample.

β-spectroscopy

Especially in high resolution electron spectroscopy the presence of the source material can often hamper a precise measurement. The possibility of performing conversion electron spectroscopy in a Penning trap has already been demonstrated in REXTRAP [Wei02] and IGISOL [Jok06].

At WITCH the feasibility of performing precision measurements of the shape of the β-spectrum is being investigated. This could be accomplished by installing an energy sensitive β-detector at the exit of the decay trap. To avoid particles that back scatter on this detector from being included in the energy spectrum, a gas filled multi wire drift chamber that detects back scattering on an event-by-event basis [Bod07], can be installed in front of the energy sensitive detector. This type of measurement will for instance allow a precise determination of the contribution of the *weak magnetism* in the nuclear β-decay [Hol74]. In addition a contribution of a heavy neutrino in the weak eigenstate of $\overline{\nu}_e$ could be researched by looking for subtle *kinks* in the spectrum [Deu90] (see also chapter 11). In a first stage, the principle of this measurement will be tested offline with a long lived radioactive source (e.g. ^{60}Co) prepared on a mylar foil. Such source is *nearly* scattering free and can be used for first measurements.

γ-spectroscopy

Also γ-ray spectroscopy can benefit from a scattering free radioactive source. In WITCH γ-spectroscopy could be performed if the central electrode of the decay trap is opened up and detectors are installed around the center of the trap.

Trap assisted spectroscopy

Lastly trap assisted spectroscopy, where a Penning trap is no longer used as a radioactive source but rather to obtain a pure source [Rin07a], is a possibility at WITCH. This is especially useful if isobarically pure ion samples are needed for for instance life time measurements. This type of measurements requires that the mass resolution of the cooler trap is sufficiently high to separate the isotope of interest from its isobaric contaminants, a condition which is aimed for also for weak interaction studies.

The purified ion ensemble can then directly be ejected from the cooler trap and deposited on a moving collection tape system. The radioactive source is then transported to the detectors where spectroscopic studies can be performed.

Chapter 11

Search for heavy neutrino admixture

The WITCH system is not only limited to measuring the β-ν-angular correlation coefficient a, but can also be used for precision measurements on different observables. One field in which high precision measurements could be performed, is the search for an admixture of a heavy neutrino to the electron neutrino.

11.1 Introduction

Experiments on neutrino oscillations have convincingly shown that the neutrino's are not massless as was long thought. Experiments on ^3H have also shown that the mass of the electron-neutrino ν_e is below 2.3 eV [Wei06]. However a small admixture of a heavy neutrino (with a mass of $\mathcal{O}$(MeV)) into the weak eigenstate of ν_e has not fully been excluded experimentally. The weak eigenstate $|\nu_e\rangle$ can be written in terms of the light neutrino mass eigenstate $|\nu_0\rangle$ and a possible heavy neutrino mass eigenstate $|\nu_x\rangle$ as

$$|\nu_e\rangle = \sqrt{1-|U_{ex}|^2}|\nu_0\rangle + U_{ex}|\nu_x\rangle \tag{11.1}$$

where $|U_{ex}|^2$ determines the admixture probability.

Although traditionally the presence of a high mass neutrino admixture has been researched in β-decay by looking for distortions in the continuous β-spectrum [Deu90], recent measurements have shown that the full reconstruction of the neutrino momentum [Tri03] provides an equally valid method for determining any heavy neutrino admixture. Instead of determining the neutrino momentum for a β^+-decaying isotope, it can also be determined in a measurement with an isotope that undergoes electron capture (EC). The advantage of EC over β^+-decay is the much simpler kinematics, thanks to the fact that in the final state only two particles (neutrino and daughter nucleus) are present instead of three (neutrino, β and daughter nucleus). This was already described in Ref. [Hin98] were the recoils from the ^{37}Ar EC decay were observed.

Present limits on heavy (anti-)neutrino admixture are shown in Fig. 11.1.

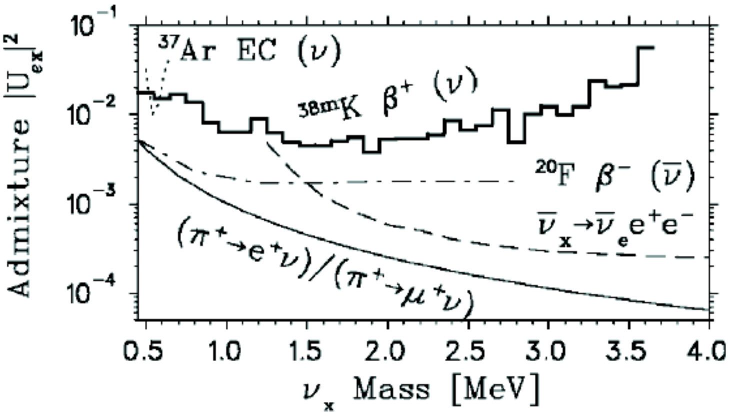

Figure 11.1 – *Present experimental limits on heavy (anti-) neutrino admixture (from Ref. [Tri03] and references cited therein).*

The limits imposed by the ^{38m}K experiment [Tri03] are the best direct limits on admixture for ν_e for $m_{\nu_x} = 0.7 - 3.6$ MeV and the best model independent limits for $m_{\nu_x} = 2.9 - 3.6$ MeV. For antineutrinos more strict direct limits exist from measurements on ^{20}F [Deu90].

11.2 Heavy neutrino signature in EC decay

In an electron capture process the neutrino is produced through the reaction

$$p + e^- \rightarrow n + \nu_e$$

or in terms of nuclei

$$^A_Z X + e^- \rightarrow ^A_{Z-1} X + \nu_e.$$

As only two particles are present in the final state, the neutrino and the recoiling daughter nucleus each have a well defined energy. In case the neutrino is massless, the kinetic energy of the recoiling nucleus can to good order be approximated as

$$E_R = \frac{(Q - B_i)^2}{2Mc^2} \tag{11.2}$$

with Q the Q-value of the decay, B_i the binding energy of the electron that was captured and M the mass of the daughter atom $^A_{Z-1}X$. When including the neutrino mass one obtains

$$E_R = Q - B_i + Mc^2 - \sqrt{2(Q - B_i)Mc^2 + M^2c^4 + m_\nu^2c^4}. \tag{11.3}$$

For a massive neutrino the recoil energy of the daughter will thus be smaller than in the case of a massless neutrino. This dependency is plotted in Fig. 11.2 for the specific case of ^{144}Eu (see sections 11.3 and 11.5). In this plot the binding energy of the captured electron was neglected as it is typically much

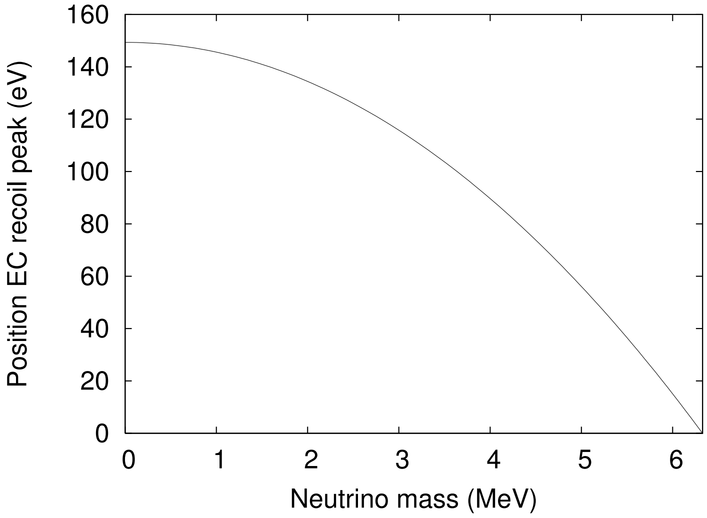

Figure 11.2 – *The position of the EC recoil peak as a function of the neutrino mass for* ^{144}Eu.

smaller than Q. Thus, by looking for a small EC contribution with a recoil energy lower than the one expected for a massless neutrino EC-decay, limits could be set on the presence of a heavy neutrino mass eigenstate admixing in the ν_e weak eigenstate. The interpretation of these limits would not depend on theoretical predictions and thus this type of experiment could provide model independent and direct limits on the admixture of a heavy neutrino.

11.3 Candidate isotopes

An isotope should meet certain conditions to enable a measurement of this type:

- Production yield at ISOLDE more than 10^5 - 10^6 particles per second.
- The half-life of the isotope should be of the order of seconds.
- The daughter isotope should be stable or sufficiently long but not too long lived (order hours/days).
- Minimal isobaric or isomeric contamination should be present.
- The decay should have a high probability for electron capture.

Except for the last point these points are general requirements for isotopes to be used at WITCH. The difficulty in finding a suitable isotope for this experiment lies in the combination of the relatively short half-life and the high EC probability. Two isotopes that appear to be suitable are ^{144}Eu and ^{140}Pm. Their most important properties are listed in table 11.1. As can be seen, most of their properties render them well suited for this type of experiment although a few

	^{144}Eu	^{140}Pm
Production yield (particles/μC)[a]	$5.6 \cdot 10^8$	$1.7 \cdot 10^8$
Target material	Ta	Ta
Half-life (s)	10.2 (1)	9.2 (2)
Daughter isotope	^{144}Sm (stable)	^{140}Nd (3.37 days)
EC in highest energy branch (%)	9.68(19)	9.90(24)
β^+ in highest branch (%)	79.7(7)	83.7(7)
total β^+(%)	87.1	88.8
Q (MeV)	6.328(30)	6.047(23)
EC_0 recoil peak position (eV)	149.0	139.9
β recoil endpoint (eV)	124.9	116.3

Table 11.1 – *Main properties of the two prime candidates for a measurement on the admixture of a heavy neutrino.*

[a] Old SC yields are shown. No data available for the PSB [Isolde].

inconveniences might have to be taken into account for both isotopes. These points are discussed separately below.

11.3.1 ^{144}Eu

The main problem with this isotope is the possible contamination of the beam with ^{144}Pm. Although ^{144}Pm can be mass selectively removed in either REXTRAP or the WITCH cooler trap this isotope with a half-life of 1 year could contaminate the whole system for years to come. No information on the presence of this isotope in the beam is available from ISOLDE [Isolde] but it is clear that this issue has to be investigated before proceeding with a measurement on this isotope. The contribution of stable ^{144}Sm or ^{144}Nd to the ion beam also has to be checked. Chemical selectivity in the ion beam taken from ISOLDE could also be obtained by using the RILIS laser ion source [Mis93]. An ionization scheme for Eu isotopes has already been developed at PNPI, Gatchina, but has not been used at ISOLDE yet. Because of the risk of ionizing Pm through surface ionization a thin Nb ion source could be used to obtain a better selectivity [Fed07].

11.3.2 ^{140}Pm

Although the daughter isotope ^{140}Nd of ^{140}Pm is not stable, it does not disturb a measurement due to its long half-life of 3.37 days. Also for ^{140}Pm isobaric contamination of the beam is a major issue. The isotope ^{140}Sm is produced at $2 \cdot 10^8$ particles/μC and has a half-life of 14.82(12) minutes. It does however not pose a risk in the form of contaminating the setup thanks to its relatively short half-life. Additionally this contaminant can be mass selectively removed from the beam, but it will occupy space in REXTRAP and the WITCH traps, limiting the amount of ^{140}Pm that can be trapped. ^{140}Pm also has a 7^- isomeric state with a half-life of nearly 6 minutes for which no yield information is available from the ISOLDE yield database [Isolde]. Also here the contribution of stable contaminants in the beam has to be checked.

11.4 Data analysis

Examples of integral recoil spectra for the conditions that

- roughly 10% of the β^+ events gives rise to a β^+-particle being detected in the recoil detector;
- only roughly 10% of the β^+ recoils has a charge state 1^+ while (almost) all EC events have a 1^+ charge state;

are plotted in Fig. 11.3. Plots without heavy neutrino and with a heavy neutrino at 138.3 eV recoil energy with $|U_{ex}|^2 = 0.005$ and $|U_{ex}|^2 = 0.01$ are shown. In the left part of the spectrum the continuous recoil spectrum of the β-recoils is clearly visible while the big step on the right side indicates the massless neutrino EC peak. The difference between the spectra with heavy neutrino and the one without heavy neutrino is shown in Fig. 11.4.

When performing a measurement like this, the most interesting range of retardation voltages to be scanned is between the endpoint of the continuous β recoil spectrum and the massless neutrino EC peak. It can be advantageous to include part of this continuous spectrum and especially the massless neutrino EC peak in the measurement to enable complete analysis of the data. In this way a mass region for the heavy neutrino between $\sim$0.5 and $\sim$3 MeV can be covered.

The analysis of the measured data can then proceed through the comparison of the measured spectrum to the expected spectrum that was obtained from MC simulations in the same way as was explained in section 2.10. The different contributions in the simulated spectrum are generated separately and are then recombined to form the idealized spectrum. By first fitting the height, width and offset of the EC_0 peak one obtains information on the contribution of the EC events to the spectrum, the temperature of the ion cloud and background from β^+-particles, thereby limiting the parameter space that has to be checked through MC simulations.

11.5 Feasibility study

To check the feasibility of performing such a measurement some idealized assumptions about the WITCH system have to be made:

- Roughly 10% of the β^+ events gives rise to a β^+-particle being detected in the recoil detector. This estimate is based on the measurements that were performed with ^{124}In.
- Only roughly 10% of the β^+ recoils has a charge state 1^+ while (almost) all EC events have a 1^+ charge state.

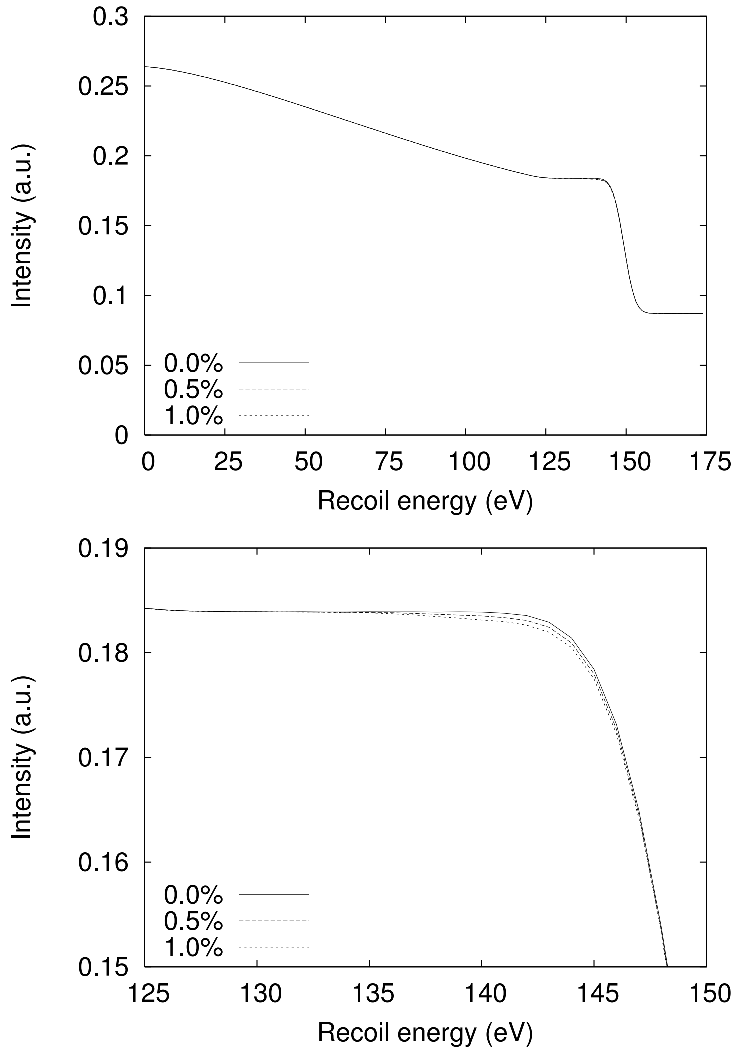

Figure 11.3 – *Example integral recoil spectra for ^{144}Eu under the conditions mentioned in section 11.5 without heavy neutrino and with 0.5% and 1% heavy neutrino admixture at 138.3 eV recoil energy. Only the highest intensity branch in the decay has been taken into account.*

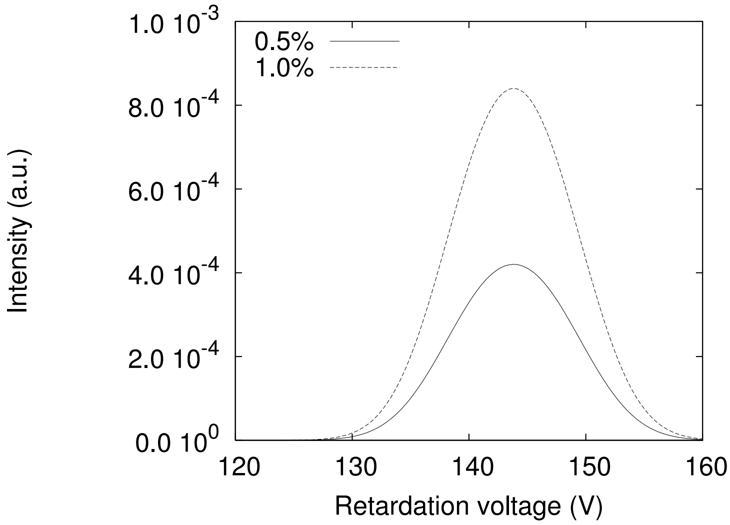

Figure 11.4 – *Difference between the recoil spectrum with only a massless neutrino and one in which a heavy neutrino admixture at 138.3 eV recoil energy is allowed.*

Again a large number of spectra were simulated through simplified Monte Carlo simulations of the setup. All these spectra were then fitted and the spread on the fit results was checked. In all fits a large number of parameters has to be included:

- The total number of events.
- The temperature of the ion cloud in the decay trap.
- The contribution of β-recoils.
- The background of β-particles.
- The contribution of electron capture.
- The heavy neutrino contribution.
- The position of the heavy neutrino EC peak (if present).

although the parameter space for some can be greatly limited thanks to the first step in the analysis routine mentioned above. Because so many parameters have to be fitted also for this type of measurements high statistics is of the utmost importance. In Fig. 11.5 the precision that can be obtained as a function of the number of events is plotted. Here the number of events is quoted as the number of decays that give a signal in the detector per bin if the retardation potential is 0 V. A measurement region from 120 eV to 155 eV separated in steps of 1 eV was assumed (35 bins), although a smaller measuring range would probably also suffice (e.g. 125 - 150 eV). For this analysis the width of the

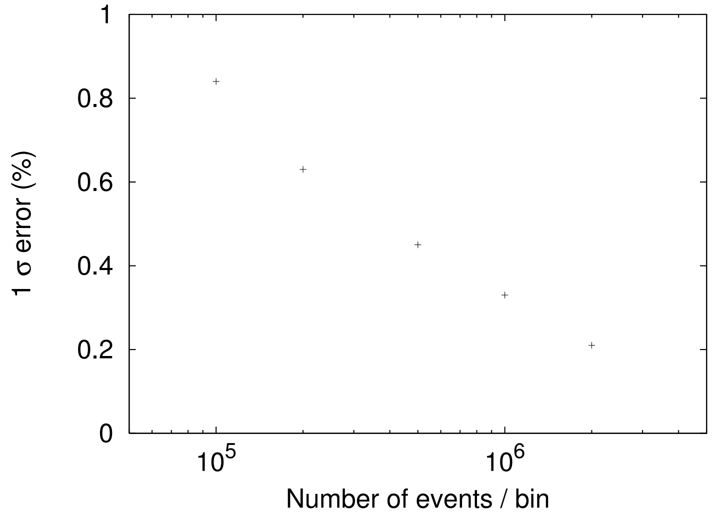

Figure 11.5 – *Obtainable precision on a contribution of a heavy neutrino for a measurement using the isotope* ^{144}Eu.

spectrometer response was assumed to be known and corresponded to an ion cloud at room temperature in the decay trap. A limit of about 0.5% on the heavy neutrino contribution should be obtained to be competitive with presently known data. For a moderate rate of 10^5 decays in the decay trap per cycle of 10 s, a total measuring time of about 3 hours would be required to obtain the necessary precision under the assumption that no other effects interfere with the measurement.

Note that if the contribution of the 1^+ charge state for the EC decays would substantially differ from 100%, as was shown in previous measurements [Hin98, Sne59], the number of decays needed to obtain a certain precision should be scaled accordingly. For the rest, the charge state distribution will not affect the measurement as only the upper part of the recoil spectrum is included in the measurement anyway, unless a large dependence of the shake-off probability on the recoil energy would be present. Assuming only 20% of the EC events has a 1^+ charge state the total measuring time to obtain a 0.5% limit on the contribution of a heavy neutrino would increase by roughly a factor of 5 to 10.

Conclusion

In this work the WITCH experiment, which in the first place aims for precision measurements of the β-ν-angular correlation coefficient, was presented in detail.

First a theoretical description of the β-decay process was presented and it was shown how measurements of correlation coefficients can reveal the exact nature of the weak interaction. Although many experiments have already been conducted in this field, there is still considerable room for additional phenomena that are not included in the Standard Model. At WITCH the β-ν-angular correlation coefficient will be obtained from precision measurements of the energy spectrum of the nuclei that recoil after β-decay, thus avoiding the need to observe the neutrino.

To enable a measurement of the recoiling ions, the setup uses a combination of two electromagnetic Penning traps and a retardation spectrometer. This allows one to construct the scattering free radioactive source that is needed as the recoiling ions only have a very small kinetic energy.

To obtain good efficiency when transporting the beam to the Penning traps a new set of diagnostics detectors was developed and their properties were studied in detail. Before the radioactive ions that are obtained from ISOLDE through REXTRAP, can be injected into the Penning traps, they first have to be slowed down by means of a pulsed drift cavity. The behavior of this system was also researched in detail both experimentally and through the use of simulations.

The behavior of single ions and ion clouds in the Penning traps was discussed in detail both through analytical calculations and Monte Carlo simulations. These simulations will finally have to provide the necessary input that is needed to analyze the experimental data that will be obtained with the setup.

The first ever measurement of recoil ions in the system was presented and the available data were thoroughly analyzed. Although not all effects are under control yet, this measurement proved that the principle of the experiment is sound and that data contributing to the present physics knowledge can be obtained with this system. Additionally these first data hinted that the charge state distribution of the ions after the β-decay, could be different from what was observed in previous measurements if one starts with initially charged particles that are in addition not alkali metal or noble gas elements.

Several alternative measurements were also suggested. A possible search for the contribution of a heavy neutrino to the weak eigenstate of the electron-neutrino through a measurement of the recoil ion energy spectrum from an electron capture decay, was discussed in detail and the feasibility of such measurement was shown.

Although the principle of the experiment was shown to be sound within the framework of this thesis, a lot of work remains to be done before one can proceed to a precision measurement. Most of this work is of technical nature and many problems are already being addressed. A first measurement on the isotope of interest, ^{35}Ar, still has to be performed, and possible technical challenges accompanying the use of this isotope have to be investigated. Another area where a lot of work remains to be done is the complete simulation of the setup. This is needed because the data that will be obtained during radioactive beam times will have to be interpreted through such simulations.

In parallel with this work, first preparations for performing other types of measurements (see chapter 10) are being started. For most of these measurements both the technical and principal problems still have to be studied in detail, but interesting physics outcome is certainly expected to be obtained with the WITCH setup over the coming few years.

Appendix A

C++ code samples

A.1 Dipolar excitation without damping

Below a code sample is given that can be used for calculating the trajectories of particles for a dipolar excitation without damping according to equation 5.45.

```
#include <cstdlib>
#include <iostream>
#include <fstream>
#include <math.h>
#include <complex>

using namespace std;

double time_tot = 10E-3; \\total excitation time
double time_step = 2E-6; \\time step

complex<double> wrf (0.0,0.0);
complex<double> wc (0.0,0.0);
complex<double> wm (0.0,0.0);
complex<double> wp (0.0,0.0);
complex<double> q (0.0,0.0);
complex<double> B (0.0,0.0);
complex<double> m (0.0,0.0);
complex<double> k0 (0.0,0.0);
complex<double> Ud (0.0,0.0);
complex<double> a (0.0,0.0);
complex<double> Amx0 (0.0,0.0);
complex<double> Apx0 (0.0,0.0);
complex<double> D (0.0,0.0);
complex<double> wz (0.0,0.0);
complex<double> prf (0.0,0.0);
complex<double> pm (0.0,0.0);
complex<double> pp (0.0,0.0);
complex<double> i(0.0,1.0);
```

```
complex<double> gamma (0.0,0.0);
complex<double> delta (0.0,0.0);
complex<double> p (0.0,0.0);
complex<double> pn (0.0,0.0);
complex<double> T (0.0,0.0);
complex<double> Tn (0.0,0.0);
complex<double> u (0.0,0.0);

complex<double> rx(double t){ //calculate x coordinate

 complex<double> result (0.0,0.0);
 result = (i*(Amx0-0.5*k0*(-i*(exp(i*(prf+pm))
-exp(i*((wrf+wm)*t+pm+prf)))/(wrf+wm)
+i*(exp(-i*(prf-pm))-exp(-i*((wrf-wm)*t-pm+prf)))/(wrf-wm)))
*exp(-i*(wm*t+pm))+i*(Apx0-0.5*k0*(-i*(exp(i*(prf-pp))
-exp(i*((wrf-wp)*t-pp+prf)))/(wrf-wp)+i*(exp(-i*(prf+pp))
-exp(-i*((wrf+wp)*t+pp+prf)))/(wrf+wp)))
*exp(i*(wp*t+pp)))/(wp-wm);
 return result;
 }

complex<double> ry(double t){ //calculate y coordinate

 complex<double> result (0.0,0.0);
 result= ((Apx0-0.5*k0*(-i*(exp(i*(prf-pp))
-exp(i*((wrf-wp)*t-pp+prf)))/(wrf-wp)
+i*(exp(-i*(prf+pp))-exp(-i*((wrf+wp)*t+pp+prf)))/(wrf+wp)))
*exp(i*(wp*t+pp))-(Amx0-0.5*k0*(-i*(exp(i*(prf+pm))
-exp(i*((wrf+wm)*t+pm+prf)))/(wrf+wm)+i*(exp(-i*(prf-pm))
-exp(-i*((wrf-wm)*t-pm+prf)))/(wrf-wm)))
*exp(-i*(wm*t+pm)))/(wp-wm);
 return result;
 }

int main(int argc, char *argv[]) {
    ofstream out("output.txt");

    q=1.6E-19;                  //charge (C)
    m=39.0*1.66E-27;            //mass (kg)
    B=9;                        //magnetic field (T)
    D=1.8E4;                    //U0/d^2 (V/m^2)
    a=0.02;                     //exciation radius (m)
    Ud=0.2;                     //excitation amplitude (V)
    prf=0.0;                    //rf phase
    u=21.5E-4;                  //reduced ion mobility (m^2/Vs)
    pn=1.013E5;Tn=273.15;
    p=1E-7*pn;                  //buffer gas pressure
    T=Tn;                       //buffer gas temperature

    Amx0=0.0;Apx0=0.0;          //initial coordinates
```

```
    pm=0.0;pp=0.0;

    wc=q*B/m;
    wz=sqrt(q*D/m);
    wp=wc*0.5+sqrt((wc*wc*0.25)-(wz*wz*0.5));
    wm=wc*0.5-sqrt((wc*wc*0.25)-(wz*wz*0.5));
    k0=q*Ud/(m*a);
    delta=(q/m)*(1.0/u)*((p/pn)/(T/Tn));
    gamma=delta/(wp-wm);

    wrf = wm*1.0000000000001;

    double t=0.0;
    double x=0.0,y=0.0;

    while(t<time_tot){
        x = real(rx(t));y=real(ry(t));
        out<<t<<"    "<<x<<"    "<<y<<"    "<<sqrt(x*x+y*y)
            <<endl;
        t+=time_step;
         }

    out.close();

    system("PAUSE");
    return EXIT_SUCCESS;

}
```

Note that in this code the excitation frequency ω_{rf} (wrf) can not be set exactly equal to ω_- or ω_+ (wm or wp). Doing this will result in an error since a division by zero takes place.

A.2 Dipolar excitation with damping

```
complex<double> rx(double t){
    complex<double> result (0.0,0.0);
    result =(i*(exp(gamma*wm*t)*(Amx0+k0*exp(i*pm)
    *((wm*gamma-i*wm)*cos(prf)-wrf*sin(prf))/
    (gamma*gamma*wm*wm-wm*wm+wrf*wrf-2.0*i*gamma*wm*wm))
    -k0*exp(i*t*wm+i*pm)*(wm*cos(t*wrf+prf)*gamma-
    i*wm*cos(t*wrf+prf)-wrf*sin(t*wrf+prf))/
    (gamma*gamma*wm*wm-wm*wm+wrf*wrf-2.0*i*gamma*wm*wm))
    *exp(-i*(t*wm+pm))+i*(exp(-gamma*wp*t)*(Apx0-k0*exp(-i*
        pp)
    *((wp*gamma-i*wp)*cos(prf)+wrf*sin(prf))/
    (gamma*gamma*wp*wp-wp*wp+wrf*wrf-2.0*i*gamma*wp*wp))+
    k0*exp(-i*t*wp-i*pp)*(cos(t*wrf+prf)*gamma*wp-
    i*cos(t*wrf+prf)*wp+wrf*sin(t*wrf+prf))/
    (gamma*gamma*wp*wp-wp*wp+wrf*wrf-2.0*i*gamma*wp*wp))
```

```
        *exp(i*(t*wp+pp)))/(wp-wm);
        return result;
        }

complex<double> ry(double t){
        complex<double> result (0.0,0.0);
        result=((exp(-gamma*wp*t)*(Apx0-k0*exp(-i*pp)
        *((wp*gamma-i*wp)*cos(prf)+wrf*sin(prf))/
        (gamma*gamma*wp*wp-wp*wp+wrf*wrf-2.0*i*gamma*wp*wp))
        +k0*exp(-i*t*wp-i*pp)*(cos(t*wrf+prf)*gamma*wp-
        i*cos(t*wrf+prf)*wp+wrf*sin(t*wrf+prf))/
        (gamma*gamma*wp*wp-wp*wp+wrf*wrf-2.0*i*gamma*wp*wp))
        *exp(i*(t*wp+pp))-(exp(gamma*wm*t)*(Amx0+k0*exp(i*pm)
        *((wm*gamma-i*wm)*cos(prf)-wrf*sin(prf))/
        (gamma*gamma*wm*wm-wm*wm+wrf*wrf-2.0*i*gamma*wm*wm))
        -k0*exp(i*t*wm+i*pm)*(wm*cos(t*wrf+prf)*gamma
        -i*wm*cos(t*wrf+prf)-wrf*sin(t*wrf+prf))/
        (gamma*gamma*wm*wm-wm*wm+wrf*wrf-2.0*i*gamma*wm*wm))
        *exp(-i*(t*wm+pm)))/(wp-wm);
        return result;
        }
```

A.3 Quadrupolar excitation with damping

```
#include <cstdlib>
#include <iostream>
#include <fstream>
#include <math.h>
#include <complex>

using namespace std;

double time_tot = 2E-1; \\total excitation time
double time_step=1E-5; \\time step


complex<double> wrf (0.0,0.0);
complex<double> wc (0.0,0.0);
complex<double> wm (0.0,0.0);
complex<double> wp (0.0,0.0);
complex<double> q (0.0,0.0);
complex<double> B (0.0,0.0);
complex<double> D (0.0,0.0);
complex<double> m (0.0,0.0);
complex<double> k0 (0.0,0.0);
complex<double> Uq (0.0,0.0);
complex<double> a (0.0,0.0);
complex<double> Apx0 (0.0,0.0);
complex<double> Amx0 (0.0,0.0);
complex<double> wz (0.0,0.0);
```

```
complex<double> I(0.0,1.0);
complex<double> pm(0.0,0.0);
complex<double> pp(0.0,0.0);
complex<double> prf(0.0,0.0);
complex<double> dp(0.0,0.0);

complex<double> gamma (0.0,0.0);
complex<double> delta (0.0,0.0);
complex<double> p (0.0,0.0);
complex<double> pn (0.0,0.0);
complex<double> T (0.0,0.0);
complex<double> Tn (0.0,0.0);
complex<double> u (0.0,0.0);

complex<double> sp(0.0,0.0);
complex<double> sm(0.0,0.0);
complex<double> s(0.0,0.0);
complex<double> C1(0.0,0.0);
complex<double> C2(0.0,0.0);
complex<double> Apx(0.0,0.0);
complex<double> Amx(0.0,0.0);
complex<double> Apy(0.0,0.0);
complex<double> Amy(0.0,0.0);
complex<double> Vpx(0.0,0.0);
complex<double> Vmx(0.0,0.0);
complex<double> Vpy(0.0,0.0);
complex<double> Vmy(0.0,0.0);

complex<double> rx(double t){
        complex<double> result (0.0,0.0);

        Apx=C1*exp(-sm*t)+C2*exp(-sp*t);
        Amx=I/k0*exp(-I*dp)*(C1*gamma*wp*wp*exp(-sm*t)
        + C2*gamma*wp*wp*exp(-sp*t) - C1*gamma*wm*wm*exp(-sm*t)
        - C2*gamma*wm*wm*exp(-sp*t) + C1*s*exp(-sm*t) - C2*s*
            exp(-sp*t));
        Apy=I*Apx;
        Amy=-I*Amx;

        Vpy=Apy*exp(I*(wp*t));
        Vmy=Amy*exp(-I*(wm*t));
        Vpx=Apx*exp(I*(wp*t));
        Vmx=Amx*exp(-I*(wm*t));

        result =(Vmy-Vpy)/(wp-wm);
        return result;
        }

complex<double> ry(double t){
        complex<double> result (0.0,0.0);
```

```
        result=(Vpx-Vmx)/(wp-wm);
        return result;
        }

int main(int argc, char *argv[]) {
    ofstream out("output.txt");

    q=1.6E-19;m=39.0*1.66E-27;B=9;D=1.8E4;a=0.02;
    Apx0=0.0;Amx0=1.0;Uq=0.2069099294*2.0;
    pm=0.0;pp=0.0;prf=0.0;

    u=21.5E-4;pn=1.013E5;Tn=293.0;p=1E-7*pn;T=Tn;

    wc=q*B/m;
    wz=sqrt(q*D/m);
    wp=wc*0.5+sqrt((wc*wc*0.25)-(wz*wz*0.5));
    wm=wc*0.5-sqrt((wc*wc*0.25)-(wz*wz*0.5));
    k0=2.0*q*Uq/(m*a*a);
    delta=(q/m)*(1.0/u)*((p/pn)/(T/Tn));
    gamma=delta/(wp-wm);
    dp=pp+pm-prf;

    sp=(gamma*(wp-wm)+sqrt(wc*wc*gamma*gamma-(k0/(wp-wm))
    *(k0/(wp-wm))))/2.0;
    sm=(gamma*(wp-wm)-sqrt(wc*wc*gamma*gamma-(k0/(wp-wm))
    *(k0/(wp-wm))))/2.0;
    s=sqrt((wp*wp-wm*wm)*(wp*wp-wm*wm)*gamma*gamma-k0*k0);
    C1=(-Amx0*exp(I*dp)*I*k0
    - gamma*Apx0*(wp*wp-wm*wm)+Apx0*s)/(2.0*s);
    C2=Apx0-C1;

    double t=0.0;
    double x=0.0,y=0.0;
    double r0 = 0.0;

    out.precision(12);

    x = real(rx(t));y=real(ry(t));
    r0 = 1000.0*sqrt(x*x+y*y);

    while(t<time_tot){
                    x = real(rx(t));y=real(ry(t));
                    out<<t<<"        "<<1000.0*x<<"        "
                        <<1000.0*y
                    <<"        "<<1000.0*sqrt(x*x+y*y)/r0<<endl;
                    t+=time_step;
          }

    out.close();
```

```
    cout<<"Done"<<endl;
    system("PAUSE");
    return EXIT_SUCCESS;

}
```

Appendix B

Alternative trapping cycles

B.1 Additional quadrupolar cooling

Especially when the injection into the cooling trap is not ideal, it can be beneficial to apply a quadrupolar excitation at the cyclotron frequency to obtain a smaller cloud before starting the real mass dependent purification (see chapter 6). This excitation can already start while the endcap electrodes are still at high voltage. The timing scheme for this is shown in Fig. B.1.

B.2 Magnetron dipolar excitation as diagnostic

If some misalignment is present in the trap system, it is possible that the cooled and centered ion cloud hits the pumping diaphragm when it is transferred from the cooler trap to the decay trap. As was shown in chapter 6, the application of a dipolar excitation at the magnetron frequency ν_- can shift the whole ion cloud away from the trap center without changing the cloud size. By using a phase locked magnetron excitation with fixed frequency, phase and length, the cloud can always be brought to exactly the same off-center position in the trap prior to the transfer through the pumping diaphragm. When the phase of the magnetron excitation can not be chosen (it has to be the same for each cycle though), or it is difficult to do so, an alternative is to wait a certain time after the application of the excitation until the cloud comes into the correct position. This is possible because when the excitation stops, the cloud starts rotating around the trap center at the magnetron frequency ν_-. A possible timing scheme that implements this is shown in Fig. B.2. Note that when doing this the cloud will still have a large magnetron component in the decay trap, which can possibly induce systematic errors during precision measurements. The best solution for this problem is of course a better alignment of the trap structure itself and of the traps with respect to the magnetic and mechanical axis of the system.

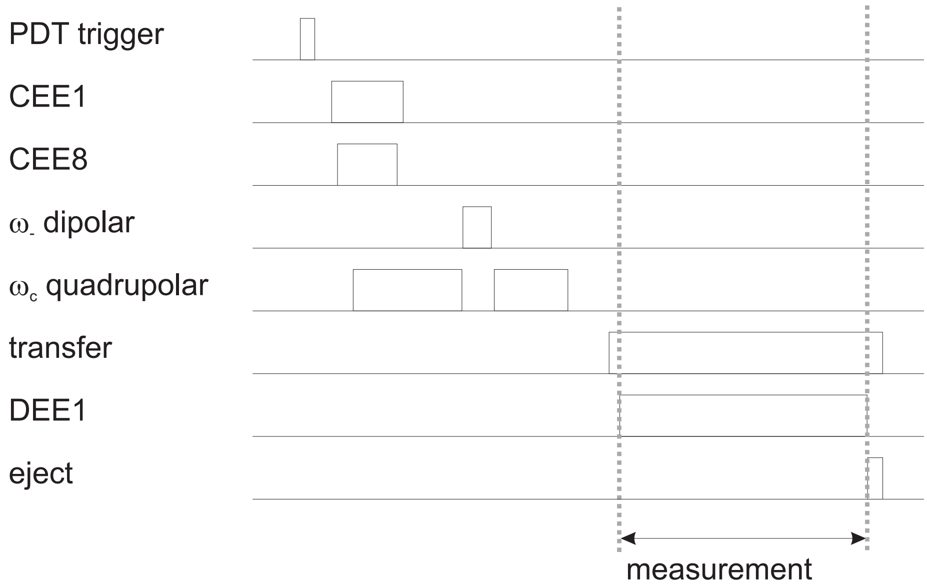

Figure B.1 – *Timing scheme for shrinking the ion cloud prior to mass selective purification.*

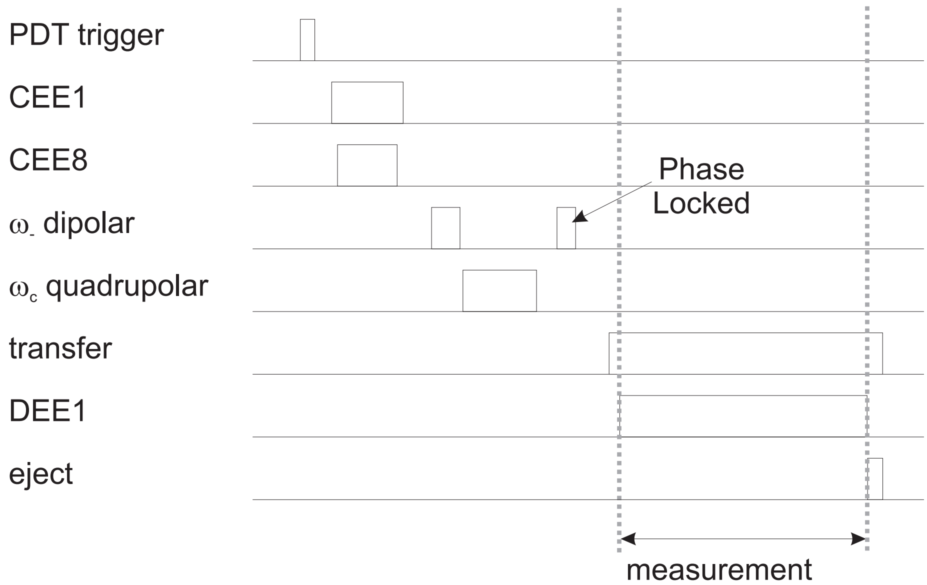

Figure B.2 – *Possible alternative timing scheme that shifts the ion cloud away from the trap center, but to an exactly known location, prior to making the transfer through the pumping diaphragm.*

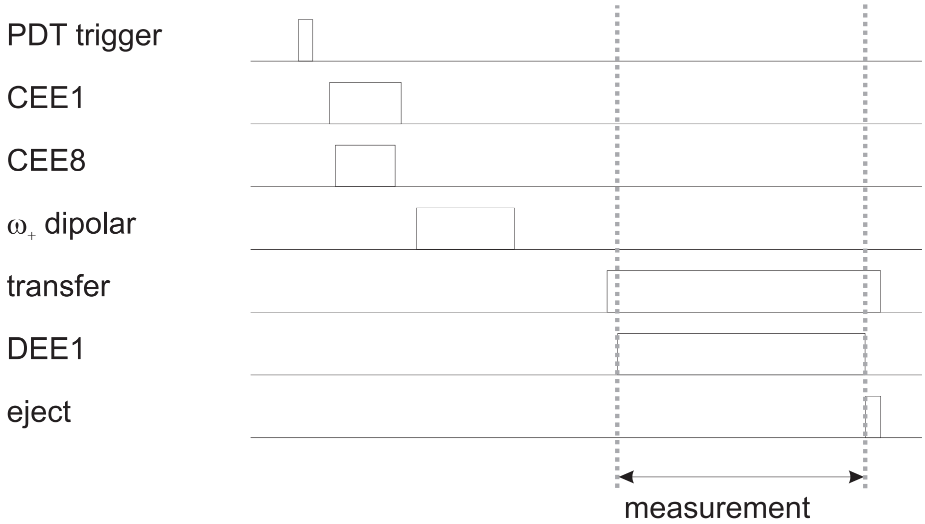

Figure B.3 – *Trap timing scheme when using a dipolar excitation at the reduced cyclotron frequency ν_+ to remove unwanted ions from the trap.*

B.3 Cyclotron dipolar excitation

Instead of using a quadrupolar excitation for mass selectively purifying the ion cloud, one can also use a dipolar excitation at the reduced cyclotron frequency ν_+ to remove unwanted ions from the trap. If contaminants of several different masses are present one can either apply separate excitations at the different frequencies, or combine the frequencies through a Fourier transformation. The timing scheme for this is shown in Fig. B.3. A cooling time is foreseen after the excitation to allow the motion of the ions of the desired mass to cool again in case they were partially excited as well.

Appendix C

Decay schemes

In this appendix the full decay schemes of ^{124}In and ^{124m}In and those of ^{144}Eu and ^{140}Pm can be found.

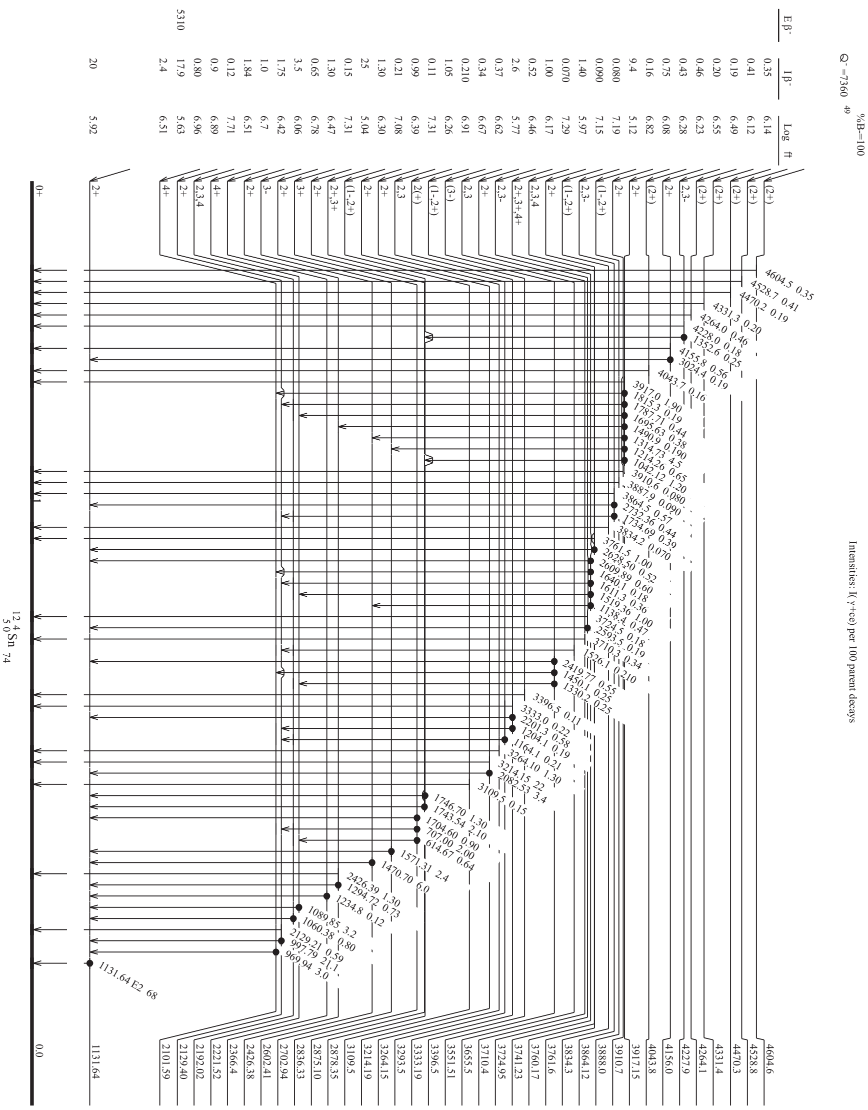

Figure C.1 – *Complete decay scheme of ^{124}In (taken from Ref. [NNDC]).*

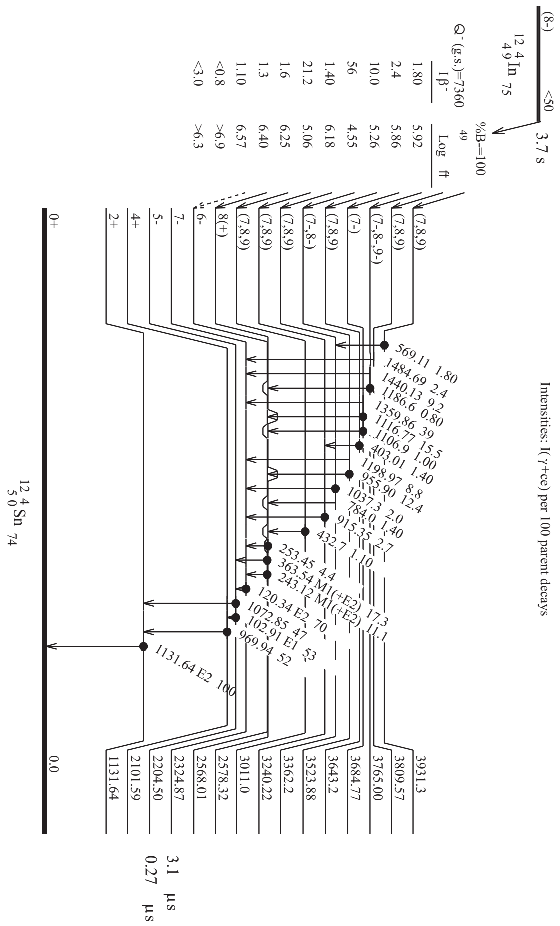

Figure C.2 – *Complete decay scheme of ^{124m}In (taken from Ref. [NNDC]).*

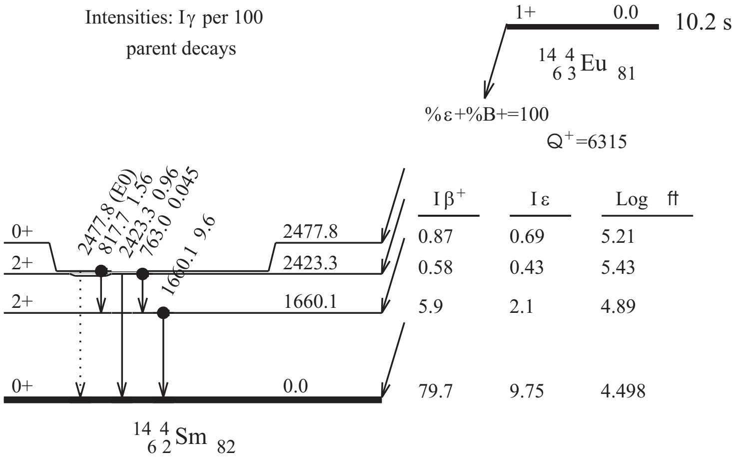

Figure C.3 – *Complete decay scheme of* ^{144}Eu *(taken from Ref. [NNDC]).*

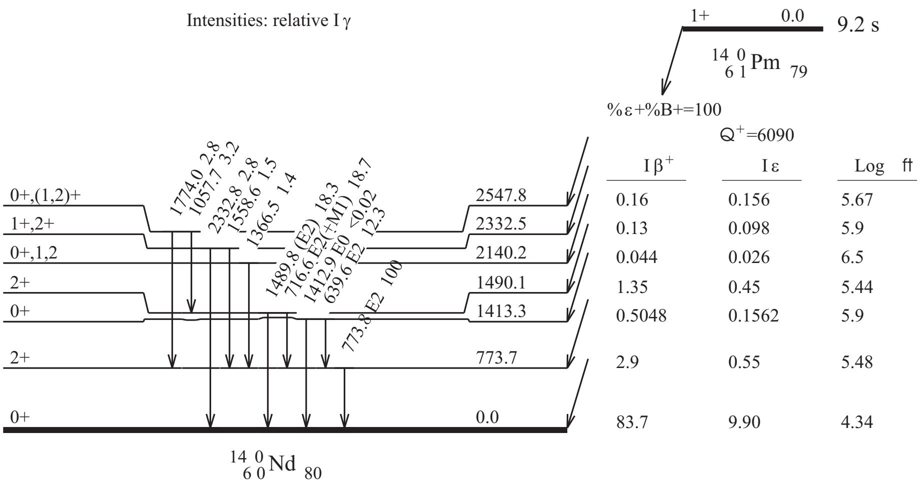

Figure C.4 – *Complete decay scheme of* ^{140}Pm *(taken from Ref. [NNDC]).*

Samenvatting

Van de vier gekende krachten die waargenomen worden in de natuur, is de zwakke kernkracht voor vele fysici nog de meest mysterieuze hoewel de fenomenen die er door veroorzaakt worden reeds geruime tijd bekend zijn. De WITCH-opstelling (een acroniem voor **W**eak **I**nteraction **T**rap for **CH**arged particles, *zwakke interactie val voor geladen deeltjes*) werd speciaal geconcipiëerd om met hogere nauwkeurigheid de eigenschappen van de zwakke interactie te bepalen. Dit werk geeft een beschrijving van de zwakke interactie fysica die onderzocht wordt en de opstelling die hiervoor gebruikt wordt. Een aantal cruciale onderdelen van de opstelling worden in detail besproken. Ook een eerste meting die werd uitgevoerd wordt uitvoerig beschreven. Daarbuiten worden een aantal nieuwe ideeën aangereikt voor hoe de opsteling verder kan geperfectioneerd worden en alternatieve metingen die met de opstelling verwezenlijkt kunnen worden.

In de tekst werden drie artikels verwerkt zoals ze gepubliceerd werden:

- **Microchannel plate response to high intensity ion bunches**
  S. Coeck, M. Beck, B. Delauré, V.V. Golovko, M. Herbane, A. Lindroth, S. Kopecky, V.Yu. Kozlov, I.S. Kraev, T. Phalet, N. Severijns,
  Nuclear Instruments and Methods in Physics research A, **557** (2006) 516-522 [Coe06].

- **A Pulsed Drift Cavity to capture 30 keV ion bunches at ground potential**
  S. Coeck, B. Delauré, M. Herbane, M. Beck, V.V. Golovko, S. Kopecky, V.Yu. Kozlov, I.S. Kraev, A. Lindroth, T. Phalet, B. Vereecke, S. Versyck, D. Beck, P. Delahaye, F. Wenander, N. Severijns,
  Nuclear Instruments and Methods in Physics research A, **572** (2007) 585-595 [Coe07a].

- **Ab initio simulations on the behavior of small ion clouds in the WITCH Penning trap system**
  S. Coeck, B. Delauré, M. Herbane, V.Yu. Kozlov, I.S. Kraev, M. Tandecki, F. Wauters, M. Beck, P. Delahaye, A. Herlert, S. Sturm, N. Severijns,
  Nuclear Instruments and Methods in Physics research A, **574** (2007) 370-384 [Coe07b].

Zwakke Interactie

Theoretisch gezien kan de Hamiltoniaan van de zwakke interactie bestaan uit vijf verschillende termen die zich verschillend gedragen onder Lorentz transformatie. Hoewel slechts twee van deze termen (Axiale-vector en Vector) weerhouden werden binnen het zogenaamde Standaard Model zijn de Scalaire en Tensoriële bijdragen experimenteel nog niet volledig uitgesloten.

Om de verschillende bijdragen in de zwakke interactie Hamiltoniaan experimenteel te kunnen waarnemen dient men op zoek te gaan naar observabelen waarvan de waarde afhangt van de sterkte van de verschillende termen. Eén van de mogelijke observabelen is de β-ν-angulaire correlatie coëfficiënt a. Om deze coëfficiënt rechtstreeks te kunnen bepalen dient men het uitgezonden neutrino waar te nemen, hetgeen quasi onmogelijk is. Om de coëfficiënt toch te kunnen bepalen wordt daarom gekeken naar de na het verval terugstotende kern. In het geval van WITCH gebeurt dit door nauwkeurig de vorm van het terugstoot energie spectrum te bepalen.

Omdat de kinetische energie van de terugstotende kern typisch erg klein is, kan de radioactive bron niet op een standaard manier gemaakt worden. In plaats daarvan moet men op zoek gaan naar een manier om een bron te maken waar er zich geen verstrooiing voordoet.

Experimentele opstelling

Een schematische voorstelling van de gehele WITCH-opstelling is getoond in Fig. 1. Om de zwakke interactie te bestuderen aan de hand van kernen die β-vervallen, heeft de WITCH opstelling een groot antal radioactieve ionen nodig. Hiervoor werd de opstelling gebouwd aan de ISOLDE isotopen separator waar een hele waaier aan radioactieve ionenbundels geproduceerd wordt met hoge intensiteit. De ionen worden eerst gebunched in de REXTRAP ionen koeler en buncher Penning trap alvorens ze in de WITCH bundellijnen geïnjecteerd worden. In het vertikale gedeelte van de bundellijn worden de ionen vertraagd van 30 of 60 keV naar enkele honderden eV om ze vervolgens te kunnen invangen in de eerste van twee elektro-magnetische ionenvallen. In de ionenvallen kunnen de radioactieve ionen worden vastgehouden tot ze vervallen. Aangezien de ionen niet door materiaal omgeven worden kunnen de terugstotende ionen zonder verstrooiing waargenomen worden. Hun energie kan daarna opgemeten worden met behulp van de retardatie spectrometer. Dit type spectrometer gebruikt een elektrische potentiaal barrière om na te gaan hoeveel ionen een kinetische energie boven een bepaalde drempel hebben. De ionen die door de spectrometer doorgelaten worden, bereiken vervolgens de microchannel plate (MCP) detector waar ze uiteindelijk geregistreerd worden.

Praktisch

Vooraleer over te gaan tot een eerste meting diende de gehele opstelling grondig afgeregeld te worden. Vooral het transport van de bundel van REXTRAP tot in de WITCH Penningvallen werd hier voor met de nodige aandacht behandeld. Reeds in een vroege fase van dit werk werd duidelijk dat er een grondige studie nodig was van de MCP detectoren die voor het afregelen van de bundel gebruikt worden. Verschillende off-line tests toonde hoe verzadiging het signaal van deze detectoren kan vervormen, hetgeen tot een foute interpretatie van de afregeling van de bundel kan leiden. Bovendien werd er een nieuw type positiegevoelige diagnose detector, die het toelaat snel een idee te krijgen van de positie en de grootte van de ionenbundel, ontwikkeld.

Niet alleen op het gebied van de diagnosedetectoren maar ook op het gebied van het begrijpen van het gedrag van de gepulste driftsectie (PDT) werd belangrijke vooruitgang geboekt. Simulaties toonden hoe de, op het eerste zicht zeer complexe, tijdstructuur van de ionenpuls geïnterpreteerd dient te worden. Samen met de betere diagnosedetectoren en een systematische manier van het afregelen van de bundel, leidde dit tot een totale efficientie van het bundeltransport die hoog genoeg is voor het uitvoeren van een eerste meting. Een overzicht van de behaalde efficiënties wordt getoond in tabel 1.

Ook aan het begrijpen van het gedrag van de ionen in de Penningvallen werd veel aandacht besteed, zowel met behulp van analytische berekeningen als met Monte Carlo simulaties voor het gedrag van ionenwolken in een Penningval. Dit onderzoek laat toe optimale parameters voor de Penningvallen te bepalen en de simulaties vormen tevens een eerste stap in het volledig simuleren van de opstelling, hetgeen nodig is voor de analyse van de data die met de WITCH opstelling vekregen worden.

Eerste metingen

Hoewel de beste kandidaat voor een meting van de β-ν-angulaire correlatie coëfficiënt a het isotoop ^{35}Ar is, diende het gehele principe van de opstelling eerst getest te worden alvorens over te schakelen op dit technische meer veeleisende isotoop. Hiervoor werd het isotoop ^{124}In gekozen. Dit isotoop is door zijn β^--vervallend karakter en de hoge productie aan ISOLDE, uitstekend geschikt om een eerste test meting op uit te voeren.

Eerst werd er getracht een zogenaamde *on-off* meting uit te voeren. Hierbij wordt de spanning op de spectrometer in een keer van 0 V (*off*) naar 200 V (*on*, voldoende om al terugstotende ionen te stoppen) gebracht. Een plotse vermindering in het aantal tellingen dat waargenomen wordt op de detector wijst dan op de aanwezigheid van terugstootionen. Dit is inderdaad wat waargenomen werd zoals getoond is in Fig. 2. Zo werd voor de eerste maal aangetoond dat er terugstootionen kunnen waargenomen worden in de WITCH opstelling.

Niet alleen werden voor het eerst terugstootionen waargenomen, er werd ook voor de eerste maal een terugstootspectrum opgemeten. Het opgemeten terugstootspectrum wordt samen met een gesimuleerd terugstootspectrum getoond in Fig. 3. Zoals te zien is, wordt de globale vorm van het spectrum goed gerepoduceerd door de simulatie maar zijn er nog enkele details die niet volledig begrepen zijn. Om deze overeenkomst te bekomen moest echter wel gebruik gemaakt worden van een ladingsverdeling van de terugstotende ionen,

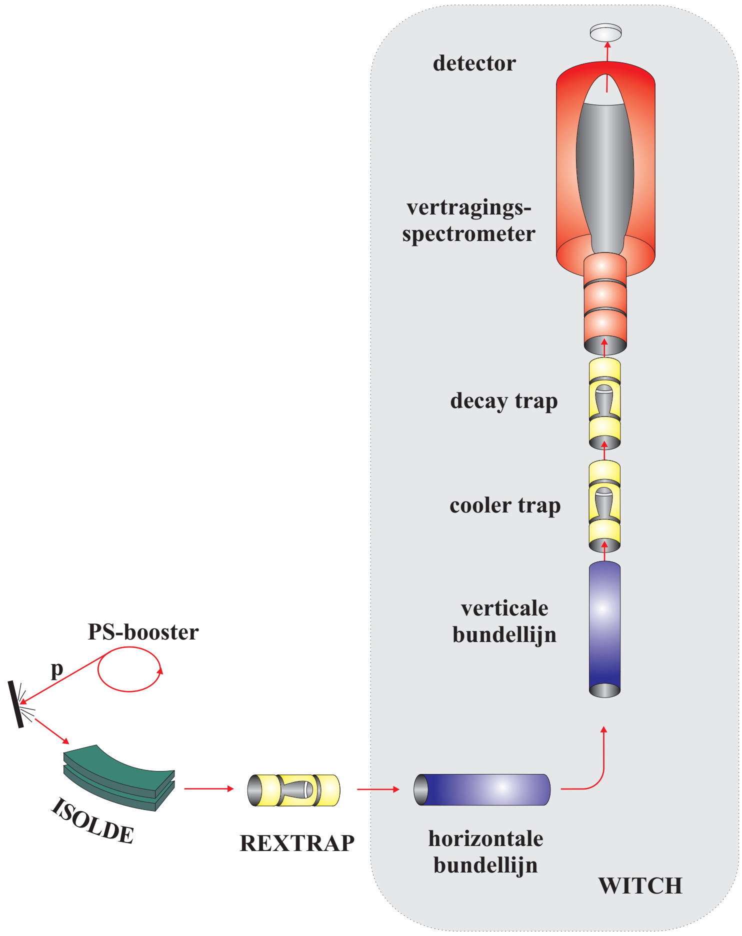

Figuur 1 – *Schematisch overzicht van de gehele WITCH opstelling. De belangrijkste onderdelen van de opstelling zijn aangegeven.*

Parameter	Ideaal	2004	2007
Horizontale bundellijn, ϵ_{HBL} (%)	100	100	100
Pulsed Drift Tube, ϵ_{PDT} (%)	100	8	50-100
Injectie in magneetveld, ϵ_{inj} (%)	100	1-10	~10
Cooler trap, ϵ_{cool} (%)	100	~45	~45
Transfer tussen traps, ϵ_{trans} (%)	100	~80	~80
Opslag in decay trap, ϵ_{decay} (%)	100	100	100
Fractie van trap naar spectrometer (ruimtehoek, gevangen na verval), $\epsilon_{2\pi/4\pi} \cdot \epsilon_{tad}$ (%)	40	/[a]	/
Shake-off naar 1^+ ladingstoestand voor β^+, ϵ_{s-0} (%)	~10[b c]	/	/
Transmissie door de spectrometer, ϵ_{spectr} (%)	100	/	/
MCP, ϵ_{MCP} (%)	60	52.3	52.3
Totaal (%)	~1	$\sim 0.6 \cdot (10^{-3} - 10^{-2})$	~0.05

Tabel 1 – *Overzicht van de efficiënties voor de verschillende onderdelen van de WITCH opstelling. Ideale en 2004 data werden overgenomen uit Ref. [Koz06].*

[a] Deze efficienties werden nog niet experimenteel bestudeerd. De ideale waarde werd gebruikt voor het berekenen van de totale efficientie.

[b] Dit kan verhoogd worden tot ~80% als er gebruik wordt gemaakt van een isotoop dat via β^- vervalt.

[c] Dit zijn slechts schattingen aangezien de verdeling in ladingstoestand na het verval van $^{35}Ar^+$ niet gekend is.

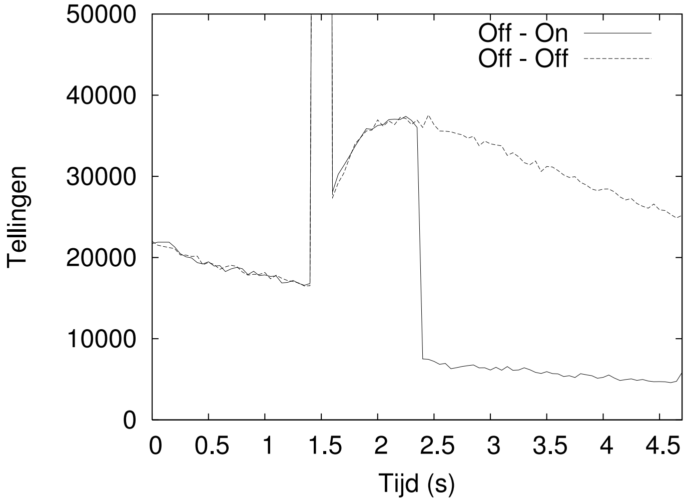

Figuur 2 – *Aantal waargenomen tellingen gedurende de gehele meetcyclus tijdens een on-off meting.*

die afwijkt van wat vroeger reeds werd waargenomen. Het verschil kan mogelijks verklaard worden door het feit dat voor deze metingen naar het verval van ionen gekeken werd en dat het element dat bestudeerd werd voor het eerst geen alkali metaal of edelgas was.

Alternatieve metingen

Omdat WITCH gekoppeld is aan de ISOLDE faciliteit, waar een groot gamma aan radioactieve bundels geproduceerd wordt, blijven de mogelijkheden van de opstelling niet beperkt tot het meten van de β-ν-angulaire correlatie coëfficiënt a op ^{35}Ar. Ook het gebruik van penningvallen laat toe de opstelling veelzijdiger te gebruiken. Andere metingen die mogelijk zijn met de opstelling zijn onder andere:

- Het bepalen van de ladingstoestanden van terugstotende kernen na β-verval.

- Verstrooiingsvrije spectroscopie in de ionenvallen, zowel β-spectroscopie als γ-spectroscopie.

- Spectroscopie waarbij een zuivere bron verkregen wordt door middel van de penningvallen.

- Het zoeken naar een bijdrage van een massief neutrino in de zwakke interactie eigentoestand van het elektron-neutrino.

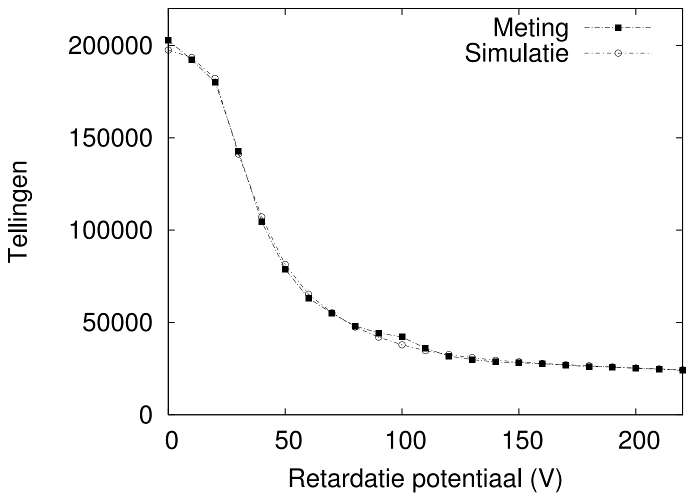

Figuur 3 – *Integraal terugstootspectrum voor het β-verval van ^{124}In en $^{124}In^m$.*

Vooruitblik

Hoewel het principe van het WITCH experiment werd aangetoond binnen het kader van dit doctoraatsonderzoek, dienen er nog enkele, vaak technische, problemen opgelost te worden alvorens kan worden overgegaan tot een precisiemeting van de β-ν-angulaire correlatie coëfficiënt.

In de loop van het jaar 2007 worden de eerste metingen verwacht op het isotoop ^{35}Ar. Deze metingen zullen wederom een schat aan informatie opleveren in verband met gedrag van de experimentele opstelling en hoe deze kan verbeterd worden om de verhoopte nauwkeurigheid te bereiken. Ook de manier van analyseren van experimentele data begint stilaan vorm te krijgen naarmate er meer ervaring wordt opgedaan met het systeem. Er blijft echter nog veel test- en simulatiewerk nodig om het volledige gedrag van de opstelling te doorgronden.

Ook andere metingen, die fysisch relevante informatie kunnen opleveren, beginnen steeds meer vorm te krijgen en het valt dan ook te verwachten dat in de komende jaren enkele interessante metingen zullen plaatsvinden met dit systeem.

Bibliography

[Ade99] Adelberger, E.G., *et al.*, Phys. Rev. Lett. **83** (1999) 1299.

[Ame98] Ames, F., *et al.*, AIP conference proceedings **445** (1998) 927.

[Ame01] Ames, F., *et al.*, Hyp. Int. **132** (2001) 469.

[Ame03] Ames, F., Private Communication 2003.

[Ame05] Ames, F., *et al.*, Nucl. Instrum. and Meth. A **538** (2005) 17.

[Ban02] Band, I.M., *et al.*, Atomic Data and Nuclear Data Tables 81 (2002) 1.

[Ban05] Ban, G., *et al.*, Nucl. Phys. A **752** (2005) 67.

[Bec01] Beck, D., *et al.*, Hyp. Int. **132** (2001) 473.

[Bec03] Beck, M., *et al.*, Nucl. Instrum. and Meth. A **503** (2003) 567.

[Bec03b] Beck, M., *et al.*, Nucl. Instrum. and Meth B **204** (2003) 521.

[Ber03] Berg, G.P., *et al.*, Nucl. Instrum. and Meth. B **204** (2003) 532.

[Bla03] Blaum, K., *et al.*, J. Phys. B **36** (2003) 921.

[Bla04] Blaum, K., Private Communication 2004.

[Bod07] Bodek, K., Private Communication 2007.

[Bol96] Bollen, G., *et al.*, Nucl. Instr. and Meth. A **368** (1996) 675.

[Bre95] Brehm, B., *et al.*, Meas. Sci. Technol. **6** (1995) 953.

[Bro86] Brown, L.S. and G. Gabrielse, Rev. Mod. Phys. **58** (1986) 233.

[Car63] Carlson, T.A., Phys. Rev. **130** (1963) 2361.

[Car63] Carlson, T.A., Phys. Rev. **131** (1963) 676.

[Coe03] Coeck, S., Karaktersering van detector en ionebron voor het WITCH-experiment, 2003, Master Thesis, Katholieke Universiteit Leuven.

[Coe06] Coeck, S., *et al.*, Nucl. Instrum. and Meth. A **557** (2006) 516.

[Coe07] Coeck, S., Ph.D. Thesis, Katholieke Universiteit Leuven, this work.

[Coe07a] Coeck, S., *et al.*, Nucl. Instrum. and Meth. A **572** (2007) 585.

[Coe07b] Coeck, S., *et al.*, Nucl. Instrum. and Meth. A **574** (2007) 370.

[DaC05] Da Costa, G., *et al.*, Rev. Sci. Instrum. **76** (2005) 013304.

[Dah00] Dahl, D.A., Int. J. Mass Spectrom. **200** (2000) 3.

[Dec90] D.J. Decman and W. Stoeffl, Phys. Rev. Lett. **64** (1990) 2767.

[Del] Del Mar Ventures http://www.sciner.com

[Del04] Delauré, B., Development of a Penning trap based setup for precision tests of the Standard Model, 2004, Ph.D. Thesis, Katholieke Universiteit Leuven.

[Deu90] Deustch, J., M. Lebrun and R. Prieels, Nucl. Phys. A **518** (1990) 149.

[Dub99] Dubin, D., and T.M. O'Neil, Rev. Mod. Phys. **71** (1999) 87.

[Eli07] Eliseev, S., *et al.*, Int. Journ. of Mass Spectr. **262** (2007) 45

[Fed07] Fedosseev, V., Private Communication 2007.

[Fra83] Fraser, G.W., Nucl. Instr. and Meth. **206** (1983) 445.

[Fra91] Fraser, G.W., *et al.*, Nucl. Instrum. and Meth. A **306** (1991) 247.

[Fra93] Fraser, G.W., *et al.*, Nucl. Instrum. and Meth. A **327** (1993) 328.

[Fri07] Friedag, P., to be published 2007, Master Thesis, Westfälische Wilhelms-Universität Münster.

[Gao84] Gao, R.S., *et al.*, Rev. Sci. Instrum. **55** (1984) 1756.

[Gha96] Ghalambor Dezfuli, A.M., Injection, Cooling and Extraction of Ions from a very Large Paul Trap, 1996, Ph.D. Thesis, McGill University Montreal.

[Gha96b] Ghalambor Dezfuli, A.M., *et al.*, Nucl. Instrum. and Meth. A **368** (1996) 611.

[Gha02] Ghalambor Dezfuli, A.M., *et al.*, AIP Conference proceedings **610** (2002) 932.

[Glu05] Gluck, F., *et al.*, Eur. Phys. J. A **23** (2005) 135.

[Gio58] Gioumousis, G., *et al.*, J. Chem. Phys. **29** (1958) 294.

[Gor05] Gorelov, A., *et al.*, Phys. Rev. Lett. **94** (2005) 142501.

[Gua95] Guan, S., and A.G. Marshall Int. J. Mass Spectrom. Ion Proc. **146/147** (1995) 261.

[Har05] Hardy ,J.C., and I.S. Towner, Phys. Rev. C **71** (2005) 055501.

[Hel85] Hellsing, M., *et al.*, J. Phys. E **18** (1985) 920.

[Her01] Herfurth, F., *et al.*, Nucl. Instrum. and Meth. A **469** (2001) 254.

[Hin98] Hindi, M.M., *et al.*, Phys. Rev. C **58** (1998) 2512.

[Hol74] Holstein, B.R., Rev. Mod. Phys. **46** (1974) 789.

[Isolde] Online ISOLDE yield database, http://isolde.web.cern.ch/ISOLDE/.

[Jac57] Jackson, J.D., S.B. Treiman and H.W. Wyld, Nucl. Phys. **4** (1957) 206.

[Jac75] Jackson, J.D., Classical electrodynamics, Wiley (1975).

[Joh63] Johnson, C.H., F. Pleasanton and T.A. Carlson, Phys. Rev. **132** (1963) 1149.

[Jok06] Jokinen, A., *et al.*, Int. J. Mass Spectrom. Ion. Proc. **251** (2006) 204.

[Kat04] Report by the KATRIN Collaboration 2004, FZKA7090 NPI ASCR Rez EXP-01/2005 MS-KP-0501.

[Klu04] Kluge, H.J., and K. Blaum, Nucl. Phys. A **746** (2004) 200c.

[Kön95] König, M., *et al.*, Int. J. Mass Spectrom. Ion. Proc. **142** (1995) 95.

[Koz05] Kozlov, V.Yu., WITCH, a Penning trap for weak interaction studies, 2005, Ph.D. Thesis, Katholieke Universiteit Leuven.

[Koz06] Kozlov, V.Yu., *et al.*, Int. J. Mass Spectrom. **251** (2006) 159.

[Kuc02] Kuckein, M., Phase-locked magnetron excitation and implementation of a SWIFT cleaning mechanism at ISOLTRAP, 2002, Master Thesis, Technische Universität München.

[Kug92] Kugler, E., *et al.*, Nucl. Instrum. and Meth. **70** (1992) 41.

[Kug00] Kugler, E., Hyp. Int. **129** (2000) 23.

[Lee56] Lee, T.D., and C.N. Yang, Phys. Rev. **104** (1956) 254.

[Lie05] Liénard, E., *et al.*, Nucl. Instrum. and Meth. A **551** (2005) 375.

[Lin04] Lindroth, A., *et al.*, Nucl Instrum. and Meth. A **534** (2004) 551.

[Lob85] Lobashev, V.M., and P.E. Spivak, Nucl. Instrum. and Meth. A **240** (1985) 305.

[Lon93] Londry, F.A., *et al.*, J. Am. Soc. Mass Spectrom. **4** (1993) 687.

[Mak98] Makino, J., and M. Taiji, Scientific Simulations with Special-Purpose Computers the GRAPE Systems, Wiley (1998)

[Mis93] Mishin, V.I., *et al.*, Nucl. Instrum. and Meth. B **73** (1993) 550.

[Nav91] Navilat-Cuncic, O., *et al.*, J. Phys. G, **17** (1991) 919.

[Nie01] Nieminen, A., *et al.*, Nucl. Instrum. and Meth. A **469** (2001) 244.

[NNDC] http://www.nndc.bnl.gov

[Obe97] Oberheide, J., *et al.*, Meas. Sci. Technol. **8** (1997) 351.

[Pic92] Picard, A., *et al.*, Nucl. Instrum. and Meth. B **63** (1992) 345.

[Ple57] Pleasonton, F. and A.H. Snell, Proc. Roy. Soc. (London) A **241** (1957) 141.

[Pod04] Podadera Aliseda, I., *et al.*, Nucl. Phys. A **746** (2004) 647c.

[Pre92] Press, W.H., *et al.*, Numerical Recipes in C: The Art of Scientific Computing, 2nd. ed. , Cambridge university press (1992).

[Rai97] Raimbault-Hartmann, H., *et al.*, Nucl. Instrum. and Meth. B **126** (1997) 378.

[Rep07] Reponen, M., The WITCH experiment off-line tuning ion source, 2007, Master Thesis, University of Jyväskylä.

[Rex05] REXTRAP Team, Private Communication 2005.

[Rin07] Ringle, R., *et al.*, Int. Journ. of Mass Spectr. **262** (2007) 33.

[Rin07a] Rinta-Antila, S., *et al.*, Eur. Phys. J. A **31** (2007) 1.

[Sav91] Savard, G., *et al.*, Phys. Lett. A **158** (1991) 247.

[Sch01] Schmidt, P., Rextrap: Ion Accumulation and Bunching for REX-ISOLDE, 2001, Ph.D. Thesis, Johannes Gutenberg Universität Mainz.

[Sch05] Schweikhard, L., *et al.*, Eur. J. Mass Spectrom. **11** (2005) 457.

[Sch06] Schwarz, S., Nucl. Instrum. and Meth. A **566** (2006) 233.

[Sci03] Scielzo, N.D., *et al.*, Phys. Rev. A **68** (2003) 022716.

[Sci04] Scielzo, N.D., *et al.*, Phys. Rev. Lett. **93** (2004) 102501-1.

[Sev06] Severijns, N., M. Beck and O. Naviliat-Cuncic, Rev. Mod. Phys. **78** (2006) 991.

[Sik03] Sikler, G., *et al.*, Nucl. Instrum. and Meth. B **204** (2003) 482.

[Sne55] Snell, A.H. and F. Pleasonton, Phys. Rev. **100** (1955) 1396.

[Sne57] Snell, A.H. and F. Pleasonton, Phys. Rev. **107** (1957) 740.

[Sne58] Snell, A.H. and F. Pleasonton, Phys. Rev. **111** (1958) 1338.

[Sne59] Snell, A.H., F. Pleasonton and J.L. Need, Phys. Rev. **116** (1959) 1548.

[Sta04] Stahl, S., Possible Improvements of the Witch-ISOLDE-60kV switch, 2004.

[Stu06] Sturm, S., Private Communication 2006.

[Tan07] Tandecki, M., Private Communication 2007.

[Tri03] Trinczek, M., *et al.*, Phys. Rev. Lett. **90** (2003) 012501.

[Van07] Van Gorp, S., Beweging van ionen in de WITCH Penningvallen, to be published 2007, Master Thesis, Katholieke Universiteit Leuven.

[Ver06] Verheyden, R., Karakterisatie van een positiegevoelige MCP detector voor het WITCH-experiment, 2006, Master Thesis, Katholieke Universiteit Leuven.

[Vie95] Viehland, L.A., and E.A. Mason, Atomic Data and Nuclear Data Tables **60** (1995) 37.

[Vog83] Vogel, P. and B. Werner, Nucl. Phys. A **404** (1983) 345.

[Web03] Weber, C., Konzeption eines kryogenen Penningfallenaufbaus für SHIPTRAP und Massenbestimmungen von Radionukliden um den Z = 82 Schalenabschluss an ISOLTRAP, 2003, Ph.D. Thesis, Ruprecht-Karls-Universität Heidelberg.

[Wei02] Weissman, L., *et al.*, Nucl. Instrum. and Meth. A **492** (2002) 451.

[Wei06] Weinheimer, Ch., Prog. Part. Nucl. Phys. **57** (2006) 22.

[Wiz79] Wiza, J.L., Nucl. Instrum. and Meth. **162** (1979) 587.

[Wu57] Wu, C.S., *et al.*, Phys. Rev. **105** (1957) 1413.

[Yaz06] Yazidjian, Ch., *et al.*, Hyp. Int. **173** (2006) 181.